Quantum Properties in Hybrid Nanowire Devices

Xu, D.

DOI
10.4233/uuid:26c9e59f-5d64-40a4-adb9-cabe2c272bcb

Publication date
2022

Document Version
Final published version

Citation (APA)
Xu, D. (2022). *Quantum Properties in Hybrid Nanowire Devices*. [Dissertation (TU Delft), Delft University of Technology]. https://doi.org/10.4233/uuid:26c9e59f-5d64-40a4-adb9-cabe2c272bcb

QUANTUM PROPERTIES IN HYBRID NANOWIRE DEVICES

QUANTUM PROPERTIES IN HYBRID NANOWIRE DEVICES

Proefschrift

ter verkrijging van de graad van doctor
aan de Technische Universiteit Delft,
op gezag van de Rector Magnificus prof. dr. ir. T.H.J.J. van der Hagen,
voorzitter van het College voor Promoties,
in het openbaar te verdedigen op donderdag 12 mei 2022 om 10:00 uur

door

Di XU

Master of Science in Physics,
RWTH Aachen University, Aken, Duitsland,
geboren te Zhangjiakou, China.

Dit proefschrift is goedgekeurd door de

promotor: prof. dr. ir. L.P. Kouwenhoven
promotor: dr. M.T. Wimmer

Samenstelling promotiecommissie:

Rector Magnificus,	voorzitter
Prof. dr. ir. L.P. Kouwenhoven,	Technische Universiteit Delft, promotor
Dr. M.T. Wimmer,	Technische Universiteit Delft, promotor
Onafhankelijke leden:	
Prof. dr. Y.M. Blanter	Technische Universiteit Delft
Prof. dr. J.M. van Ruitenbeek	Universiteit Leiden
Dr. S. de Franceschi	CEA Grenoble, Frankrijk
Dr. E. Prada	Instituto de Ciencia de Materiales de Madrid, Spanje
Prof. dr. J.M. Thijssen	Technische Universiteit Delft, reservelid
Overige leden:	
Prof. dr. E.P.A.M. Bakkers,	Technische Universiteit Eindhoven

Keywords: Majorana, hybrid device, semiconductor nanowire, InSb, superconductivity, Andreev bound state, selective area growth, Aharonov-Bohm effect

Printed by: Ipskamp Printing, Enschede

Front & Back: Bottom: Designed by D. Xu. Top: part of *View of Delft*, c. 1660-1661 by Johannes Vermeer, Credit: Mauritshuis, The Hague.

Casimir PhD Series, Delft-Leiden 2022-08

ISBN 978-90-8593-519-3

An electronic version of this dissertation is available at
`http://repository.tudelft.nl/`.

To my parents,

To my grandfather, Zhigang Xu (1939 – 2020)

CONTENTS

SUMMARY

Quantum computing is a flourishing field of scientific and technological research. The development of quantum computing in the past decades is the so-called second quantum revolution, where various aspects of quantum physics, such as entanglement and superposition, are used to form the main building block of computation — the quantum bit, or qubit. With quantum technologies rapidly growing, people have been paying attention to a few promising implementation schemes for quantum computing, including schemes based on topological protection.

Majorana bound states (MBSs) are predicted to be non-Abelian anyons that enable topological quantum computing, which uses the topological phase of matter to protect quantum information against noise from the environment. The search for MBSs has drawn enormous interests in condensed matter physics community, where hybrid semiconductor-superconductor nanowire systems are currently the most promising candidates. Great advances have been achieved in this field over the last decade, due to efforts ranging from material growth, to transport experiments and to theoretical understanding.

When a hybrid nanowire undergoes a transition to a topologically nontrivial phase, two MBSs appear at the ends of the hybrid region. As a result, zero-bias peaks (ZBPs) should appear in tunneling spectroscopy performed on normal-conductor – semiconductor-nanowire – superconductor (N-nanowire-S) junctions. In this thesis, we firstly demonstrate large ZBPs in vapor-liquid-solid (VLS) InSb nanowires with epitaxial Al with heights on the order of $2e^2/h$. Besides the original Majorana interpretation of these ZBPs, we discuss alternative explanations such as quasi-Majoranas due to a smooth potential and random disorder. (*Chapter 4*)

In the same system, we then demonstrate that the induced superconducting gap, the effective Landé g-factor and the spin-orbit coupling strength can be tuned by the electrostatic environment, i.e. applied gate voltage. The change of these quantities is dominated by the coupling between the semiconductor and the superconductor. (*Chapter 5*)

The remaining part of the thesis focuses on selective area growth (SAG) InSb nanowires with epitaxial Al. Quantum transport results on these nanowires show high-quality phase-coherence, hard superconducting gap and $2e$-Coulomb blockaded transport. We then study the properties on induced superconductivity as well as phase coherence in SAG nanowire networks. We establish a fitting model to extract the phase coherence length based on the temperature dependence of the Aharonov-Bohm (AB) effect. The SAG platform will allow scalable experiments for more complicated quantum transport, paving the way towards Majorana braiding. (*Chapters 6 – 8*)

SAMENVATTING

Het maken van berekeningen met een kwantumcomputer is een bloeiend gebied van wetenschappelijk en technologisch onderzoek. De opkomst van de kwantumcomputer in de afgelopen decennia is de zogenaamde tweede kwantumrevolutie, waarbij verschillende aspecten van de kwantumfysica, zoals verstrengeling en superpositie, worden gebruikt om de belangrijkste bouwsteen van deze berekeningen te vormen — de kwantumbit of qubit. Nu de kwantumtechnologieën snel groeien, hebben mensen aandacht besteed aan een paar veelbelovende implementatieschema's voor de kwantumcomputer, inclusief schema's op basis van topologische bescherming.

Er wordt voorspeld dat Majorana-gebonden toestanden (*en.* MBS's) niet-Abelse anyonen zijn die een topologische kwantumcomputer mogelijk maken, waarbij de topologische fase van materie wordt gebruikt om de kwantuminformatie te beschermen tegen ruis uit de omgeving. De zoektocht naar MBS's heeft enorme belangstelling gewekt in de gemeenschap van gecondenseerde materie fysici, waar hybride halfgeleider-supergeleider nanodraadsystemen momenteel de meest veelbelovende kandidaten zijn. Op dit gebied zijn de afgelopen tien jaar grote vooruitgangen geboekt, dankzij inspanningen variërend van materiële groei tot transportexperimenten en tot theoretisch begrip.

Wanneer een hybride nanodraad een transitie ondergaat naar een topologisch niet-triviale fase, verschijnen er twee MBS's aan de uiteinden van het hybride gebied. Als gevolg hiervan zouden nul-spanning pieken (*en.* ZBP's) moeten verschijnen in tunneling spectroscopie uitgevoerd op normale geleider – halfgeleider nanodraad – supergeleider (N-nanodraad-S) juncties. In dit proefschrift demonstreren we eerst grote ZBP's in damp-vloeistof-solide (*en.* VLS) InSb-nanodraden met epitaxiaal Al met de hoogten in de orde van $2e^2/h$. Naast de originele Majorana-interpretatie van deze ZBP's, bespreken we alternatieve verklaringen, zoals quasi-Majorana's vanwege een glad potentieel en willekeurige verstoringen. (*Hoofdstuk 4*)

In hetzelfde systeem demonstreren we vervolgens dat zowel de geïnduceerde supergeleidende energiekloof, als ook de effectieve Landé g-factor en de spin-baan-koppelingssterkte kunnen worden beïnvloed door de elektrostatische omgeving, d.w.z. aangelegde gatespanning. De verandering van deze grootheden wordt gedicteerd door de koppeling tussen de halfgeleider en de supergeleider. (*Hoofdstuk 5*)

Het resterende deel van het proefschrift richt zich op de op selectieve gebieden gegroeide (*en.* SAG) InSb nanodraden met epitaxiaal Al. Kwantumtransportresultaten op deze nanodraden laten een hoogwaardige fasecoherentie, een harde supergeleidende energiekloof en $2e$-Coulomb geblokkeerd transport zien. Vervolgens bestuderen we de eigenschappen van geïnduceerde supergeleiding en fasecoherentie in SAG-nanodraadnetwerken. We stellen een passend model op om de fasecoherentielengte te extraheren op basis van de temperatuurafhankelijkheid van het Aharonov-Bohm (AB) effect.

Het SAG-platform maakt schaalbare experimenten mogelijk voor meer gecompliceerd kwantumtransport, wat de weg vrijmaakt voor Majorana-vlechten. (*Hoofdstukken 6 – 8*)

1

INTRODUCTION

Contraria sunt complementa.

Niels Bohr

1

1.1. FROM QUANTUM MECHANICS TO TOPOLOGICAL QUANTUM COMPUTING

Quantum mechanics, a revolution on the way we see the world under our visual limit, was developed in the first half of the 20th century by many names which will be forever immortalized on our planet. Our protagonist Ettore Majorana (1906 – ?) is undoubtedly one of them, for his well-known theory in 1937 on the "Majorana fermion" [1], a particle that is its own anti-particle. Quantum mechanics have shaped our lives today by stimulating modern science and technology, especially the semiconductor industry, throughout the 20th century to this day. Interestingly, people already set their sights on transport phenomena even before Lord Kelvin identified two "clouds": the Drude model was introduced in 1900 as the theory of metallic conduction [2], shortly after electron was discovered in 1897 by J.J. Thomson. The Drude model is very successful as it is still used today as a practical way for rough estimations, despite other theories of quantum transport have been well developed.

As early as 1960, when it was still impossible to fabricate components at a nanometer scale, Richard Feynman suggested the possibility of manipulating and operating devices scaling down to the size of an atom in his inspiring paper "There's Plenty of Room at the Bottom" [3]. This work is considered as the first concept of current nanotechnology. In the decades that followed, the development of new sophisticated techniques made it possible to study many interesting properties of materials at the micro- and nanoscale. In 1972, Philip W. Anderson published the famous "More is Different" [4], breaking through the traditional reductionism and marking the starting point of condensed matter physics.

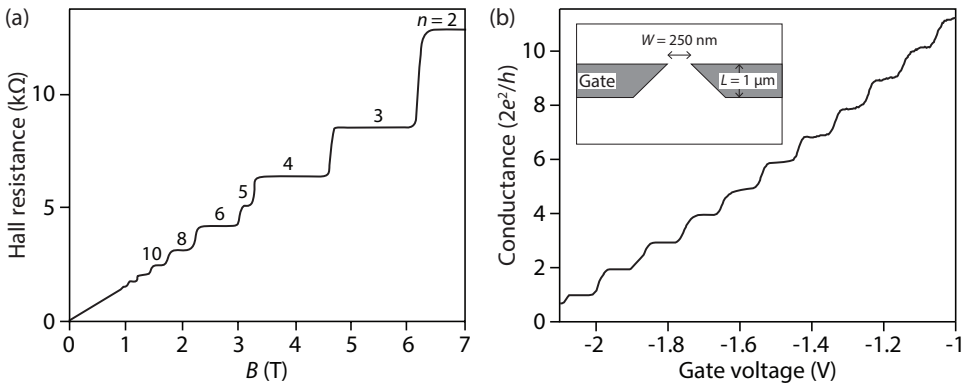

Figure 1.1: **(a) Quantum Hall effect.** The Hall resistance plotted as a function of the magnetic field perpendicular to the plane of the 2-dimensional electron gas. A sequence of plateaus is observed when the Hall resistance reaches h/ne^2, namely when the conductance is at ne^2/h. The values of n are indicated in the plot for each resistance plateau. The resistance quantum is $h/e^2 \approx 26\,\mathrm{k}\Omega$. Adapted from Ref. [5] originally based on Ref. [6]. **(b) Quantum point contact.** Conductance of a ballistic point contact as a function of gate voltage. The conductance is quantized at integer multiples of $2e^2/h$. Inset: the layout of the device fabricated on a GaAs-AlGaAs 2-dimensional electron gas. Adapted from Ref. [7] at pixel level.

With the development of nanotechnology, it became possible to synthesize and study

low-dimensional systems rather than staying in the 3-dimensional macroscopic world. In 1980, a revival of the Hall effect happened when K. von Klitzing measured quantized conductance on a 2-dimensional electron gas (2DEG) [8]. A similar measurement is shown in Fig. 1.1(a), where a sequence of plateaus with integer multiples of the conductance quantum e^2/h is measured as increasing the magnetic field. Physicists became aware that low-dimensional constrictions make the electron subband spacing large enough so that transport measurement can directly resolve the subbands. With confining a 2DEG with gate electrodes to a quantum point contact (QPC), quantized conductance plateaus at integer multiples of the spin-degenerate conductance quantum $2e^2/h$ were achieved in Delft in 1988 [7], as shown in Fig. 1.1(b). Therefore, people also expected conductance quantization in a 1-dimensional system, e.g. a semiconductor nanowire, and it was indeed measured in QPCs of InSb nanowire [9]. These findings made Delft one of the centers of quantum transport in the world.

In 2001, Kitaev showed a p-wave superconductor 1-dimensional model which hosts non-Abelian Majorana bound states (MBSs) at the ends with an energy gap in the middle which is topologically nontrivial [10], known as a Kitaev chain. He also proposed that non-Abelian anyonic system can be used for quantum computing [11], where quantum information created by exchanging the anyons is topologically protected. Physicists were then looking for condensed matter systems that meet the requirements of the Kitaev chain. Fu & Kane suggested that the topological phase can occur on an edge-state of a topological insulator proximitized by a s-wave superconductor [12]. This work broadened people's scope of mind to look for equivalent systems. Finally, Lutchyn *et al.* & Oreg *et al.* proposed the 1-dimensional hybrid semiconductor-superconductor nanowire model [13, 14]. We will introduce their model in Chapter 2 and let the journey begin.

1.2. METHODOLOGY IN CONDENSED MATTER PHYSICS

In the past two years, we not only went through the unprecedented Covid-19 pandemic with the entire world, but also witnessed the rise of the ethos of open data policy in our community of quantum computing research. In 2022, we had a QuTech-wide meeting on scientific integrity, and put QuTech's own data policy into effect. We are pleased to see this happening in our community, especially in an influential institute like QuTech.

The fact that the open data policy was raised as a topic of conversations in our daily life in QuTech, more or less, originated from a retracted work [15] from our lab, whose results are correctly re-analyzed and presented in Chapter 4 of this thesis.

As the experts quoted in the report [16] when they evaluated the retracted paper, Feynman had the expression on his philosophy of conducting scientific research: "The first principle is that you must not fool yourself — and you are the easiest person to fool. So you have to be very careful about that. After you've not fooled yourself, it's easy not to fool other scientists. You just have to be honest in a conventional way after that." Indeed, zooming in on a sweet spot in the parameter space while ignoring other signs that contradicts one's goal, is treated as self-deception that occurred in the retracted work. One should not focus only on the data that supports a certain claim and thus only present this part of the data for peer review, even though scientific researchers are entitled to have their own interpretations and we acknowledge that there has to be a curating of data for a publication. To readers who are interested, you can compare Chapter 4 with Ref. [15]

to draw your own conclusion on the key problem that occurred.

After this crisis happened in 2020, the co-authors who were still in Delft always acted with an open, strict and responsible view to our works. Our re-calibration of the experimental set-up, the decision of retracting the paper, the re-analysis, publishing the corrected work, and internal investigation on other papers should count for scientific integrity.

Unfortunately, we still found that more works in our field are filled with self-deception and wishful thinking, and it still happens for arrogating academic benefits in other places of the world. This only makes us more aware of the importance of conducting scientific research with a proper methodology.

It could well be the case that we find mistakes in previous publications or that previous conclusions no longer hold, simply because the understandings in the field has developed, e.g. new theories have been put forward. This is the normal course of scientific development. But the bottom line should be that the data contradicting the claims were not intentionally ignored.

Admittedly, I would say that we grew and were trained in such a research culture, where the methodology we read in some papers seems to indicate that confirmation-bias-influenced processes are easily accepted and endorsed. This is sometimes quite convincing for junior researchers and creates the impression that this is a norm of the field. Our field should reject such hypes. I feel glad that we have learned lessons and more people are aware of this problem in the past two years.

As we become more and more senior, we gradually find a balance on how to present our data, after we saw plenty of data in experiments and our community developed better understandings over time, but still, I feel many cases are in the gray zone and debatable. This does not naturally mean that our peers in this field developed a lower standard on scientific integrity, but can be determined by the nature of condensed matter physics. The field of condensed matter physics is quite different from those where predesigned routine of experiments can be followed, but our experiments on a device are like to explore an unknown world, where decision-making is in every step along the line of measurements. Scientific integrity still holds by consensus within the field, e.g. in the peer review process. Suppressing possible confirmation bias is definitely part of the consensus in this field. I still feel positive on our field because all the past works, negatively or positively, still deepen our scientific understandings despite ups and downs.

1.3. OUTLINE OF THE THESIS

Chapter 2 introduces the theoretical background that are useful to understand the experimental results in subsequent chapters. The chapter starts from the so-called Lutchyn-Oreg model, that is, Majorana zero modes (MZMs) emerging as quasi-particles in one-dimensional condensed matter system. From an experimental perspective, several theories on what experimental signatures should be expected for Majoranas in nanowires are reviewed, and several experimental works are also introduced. Further towards topological quantum computing, topological properties of Majoranas, measurement-based braiding and Majorana teleportation are then shown as a motivation for Chapters 6 and 8.

Chapter 3 describes the experimental techniques. At the beginning we demonstrate

the growth technique of vapour-liquid-solid (VLS) nanowires, used in Chapters 4 and 5. Then we introduce the fabrication techniques used throughout the thesis, with using a selective-area growth (SAG) device as an example. We then specifically demonstrate the selective etch of Al, an essential step to create the devices used in Chapters 6 and 7. This chapter is finished with the electrical measurement set-up.

The following chapters on quantum transport in this thesis can then be divided to two branches, based on the VLS platform (Chapters 4 and 5) and on the SAG platform (Chapters 6, 7 and 8), respectively showing experimental developments on the two nanowire platforms.

Chapter 4 is a rewritten work of the retracted paper [15]. We report electron transport studies on InSb-Al hybrid semiconductor-superconductor nanowire devices, demonstrating large zero-bias peaks (ZBPs) of the order of $2e^2/h$, and investigate their gate dependences. We discuss possible interpretations in terms of Andreev bound states and Majorana zero modes.

Chapter 5 is chronological a follow-up study of Chapter 4. After we observed large ZBPs in VLS InSb-Al nanowires, we conduct a more detailed study on this system, here namely how the external electric field, i.e. gate voltage, affects the coupling between the semiconductor and the superconductor. We find that the change of coupling strength has consequences on the induced superconducting gap, the effective Landé g-factor and the spin-orbit coupling. We then present alternative explanations of the zero-bias anomalies, mimicking Majorana behaviors.

In Chapter 6 we present the growth platform that allows in-plane InSb-Al nanowire networks, namely the SAG. The first half of the chapter introduced the growth dynamics, and the second half we demonstrate its quantum transport properties, including Aharonov-Bohm effect, superconducting gap and $2e$-Coulomb blockade, which are the building blocks towards topological qubits.

Chapters 7 and 8 follow Chapter 6, performing studies on superconducting properties and phase coherent properties. We demonstrate how the fitting model is established to extract the phase coherence length of SAG nanowire networks based on the temperature dependence of their Aharonov-Bohm (AB) effect. Finally, conclusions and outlooks are made in Chapter 9.

2

THEORY

Der Unterschied zwischen Vergangenheit, Gegenwart und Zukunft
ist für uns Wissenschaftler eine Illusion, wenn auch eine hartnäckige.

Albert Einstein

This chapter presents the theoretical background that are useful to understand the experimental results in this thesis. We start in Section 2.1 with an introduction to Majoranas emerging as quasi-particles in one-dimensional condensed matter system. Section 2.2 is about the experimental observations of Majorana zero modes (MZMs). A few theoretical works on Majoranas as well as non-Majoranas based on these experimental phenomena are reviewed. This section tries to serve as a guidance through the strides in the experimental research field of Majorana. Section 2.3 describes the role of Majoranas in topological quantum computing, the proposals to perform Majorana braiding, and near-term directions in experiments as strategic principles to proceed from the works presented in this thesis.

2.1. MAJORANAS IN CONDENSED MATTER SYSTEM

In 1937, the Italian physicist Ettore Majorana made his investigation to look for real solutions to the Dirac equation [1]. After this, the term Majorana fermion, named after the physicist, is used to describe the particle that is its own antiparticle, in other word, its creation operator $\gamma^\dagger$ is equal to its annihilation γ, thus $\gamma^\dagger = \gamma$, so they are both real.

It is still unknown where to look for Majorana fermions as one of the elementary particles. However, various quasi-particles in condensed matter physics give physicists the inspiration that there could be an exotic quasiparticle existing as a Majorana mode in the sense that $\gamma^\dagger = \gamma$.

Given the creation operators of a fermion and its antiparticle are $c^\dagger$, c, respectively, we can construct new Majorana operators γ_1 and γ_2 by splitting them into real and imaginary parts:

$$c = \frac{1}{2}\left(\gamma_1 + i\gamma_2\right),\ c^\dagger = \frac{1}{2}\left(\gamma_1 - i\gamma_2\right). \tag{2.1}$$

We then write the Majorana operators as:

$$\gamma_1 = c^\dagger + c,\ \gamma_2 = i\left(c^\dagger - c\right). \tag{2.2}$$

Here we clearly get $\gamma_i^\dagger = \gamma_i$.

If we could find quasiparticle excitations formed like $c^\dagger + c$, they would be deemed to be Majorana quasiparticles. It is natural to think of electrons as a realization of this point, where an electron and a hole state are a good analogy to a pair of particle and antiparticle. A good candidate for holding such excitations is the superconducting system, where the wavefunctions of Bogoliubov quasiparticles have both an electron and a hole component [17]. In this example, being its own antiparticle means that the Bogoliubov quasiparticle needs to be an equal superposition of an electron and a hole to be called a Majorana quasiparticle [18]. Further, these excitations will only form at zero energy due to the particle-hole symmetry of a superconducting system, thus they are called Majorana zero modes (MZMs) [19]. Also note that MZMs always have to form in pairs because we construct them by splitting the fermionic creation and annihilation operators into their real and imaginary parts as shown by Eq. 2.1.

It is worth mentioning that MZMs are called as such only because of the relation $\gamma^\dagger = \gamma$ and beyond that they are unrelated to the Majorana fermions with the context of particle physics. We will discuss the unique important properties of MZMs in Section 2.3 to show why the community of condensed matter physics are intrigued by MZMs.

It is worth notifying that we need to seek for Bogoliubov quasiparticles with the form like $\gamma = \frac{1}{\sqrt{2}}\left(c_\uparrow^\dagger + c_\uparrow\right)$, if we take into account the spin degree of freedom. In other words, it is required to be realized in a "p-wave" superconductor in which the superconducting pairing happens between electrons with the same spin species.

Kitaev has proven that MZMs need to be supported by topological systems, especially a 1-dimensional p-wave superconductor [10]. The inversion of the superconducting gap, meaning the gap closes and reopens with continuously deforming physical parameters, has a topological origin and is refereed to as "topological phase transition". Since the gap is inverted in the bulk of the 1D superconductor, we naturally find gap inversion points at the two ends of the system, indicating Majorana states are formed at the ends. Since

MZMs have to be "bounded" at the ends in the context of 1D systems, the term Majorana bound states (MBSs) is used interchangeably with MZM in the community.

With the purpose of establishing a 1D p-wave superconductor, currently the most studied system to realize MZMs is refered to as the so-called Lutchyn-Oreg model, consisting of a 1D semiconductor nanowire with strong spin-orbit coupling, with superconductivity induced by a s-wave superconductor and applying an external magnetic field [13, 14]. This system is illustrated in Fig. 2.1(a).

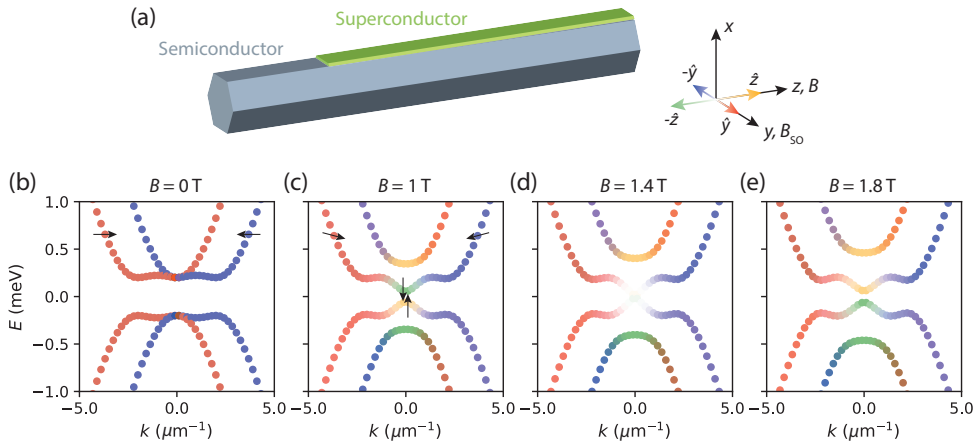

Figure 2.1: **Majorana nanowire and its energy spectra.** **(a)** Schematic of a Majorana nanowire: a semiconductor nanowire (gray) with coupled to a s-wave superconductor. The semiconductor nanowire (along z) has a large g-factor and strong spin-orbit coupling (along y). An external magnetic field is applied along the nanowire (z direction). **(b)-(e)** Energy spectra of the Majorana nanowire while increasing the magnetic field. In all panels $m^* = 0.013m_e$, $\mu = 0$, $\alpha = 2\,\text{eV}\cdot\text{Å}$, $\Delta = 0.2\,\text{meV}$ and $g = 5$. The discretization of k is due to the finite length effect with setting $l = 30\,\mu\text{m}$ and thus the interval is given by π/l. B values denote the external magnetic field along z. Colors of the plots indicate the spin orientation as shown in the coordinate system in **(a)**: red (→) and blue (←) indicate spin orientations along the spin-orbit field (y), orange (↑) and green (↓) along the external magnetic field (z). **(b)** When the external magnetic field is zero, the splitting along the k axis is due to Rashba spin-orbit interaction, and the spectra are gapped due to induced superconductivity. **(c)** When B increases, Zeeman splitting between the subbands is observed. The superconducting gap shrinks, especially around $k = 0$. The spin orientation changes gradually along the spectra. **(d)** When the Zeeman energy $E_Z = \frac{1}{2}g\mu_B B \approx \sqrt{\Delta^2 + \mu^2}$, the nanowire system undergoes a topological phase transition, the spectra cross at zero energy at $k = 0$. **(e)** When further increasing the magnetic field beyond the topological transition field, the gap reopens around $k = 0$ and an inversion is observed.

The superconducting film contacting the nanowire gives rise to a proximity effect [20], inducing superconducting pairing Δ into the semiconducting nanowire. The nanowire along the z-axis gives a momentum $\hbar k_z$, an effective mass m^* and a chemical potential μ. In order to realize the topological phase transition to generate MZMs in this system, we introduce a Rashba spin-orbit coupling α_R and apply a magnetic field B along the nanowire direction. Therefore, the spin-orbit coupling is equivalent to an effective magnetic field $B_{\text{SO}} = \alpha_R k_z \times E_x$ in the y-direction, assuming an electric field E in the x-direction [21]. Thus the directions of momentum $\hbar k_z$, the electric field E_x and the spin-orbit field B_{SO} are mutually orthogonal. Additionally the external magnetic field gives rise to a Zeeman term, $E_Z = \frac{1}{2}g\mu_B B$, with the Landé g-factor, g, and the Bohr magneton,

μ_B. The Hamiltonian that describes this system has the form [13, 14]

$$\begin{aligned} H &= \int \Psi^\dagger \mathscr{H} \Psi \mathrm{d}z, \\ \mathscr{H} &= \left(\frac{\hbar^2 k_z^2}{2m^*} - \mu\right)\tau_x - \alpha_\mathrm{R} k_z \sigma_y \tau_x + E_\mathrm{Z} + \Delta\tau_z, \end{aligned} \tag{2.3}$$

with σ and τ the Pauli matrices acting on the spin and the particle-hole space, respectively. Here we use the Nambu basis $\Psi = \left(\psi_\uparrow, \psi_\downarrow, \psi_\downarrow^\dagger, -\psi_\uparrow^\dagger\right)^T$, in which ψ_σ and $\psi_\sigma^\dagger$ denote electron and hole states, respectively.

Fig. 2.1(b) shows the spectrum of the nanowire as narrated above when the magnetic field $B = 0$. As a result of the spin-orbit coupling, the originally spin degenerate bands (here red and blue) are shifted in momentum with the amount defined as $\pm k_\mathrm{SO}$ and the spin is polarized along the spin-orbit field. Spin orientation is represented by the color scheme shown in the coordinate system in Fig. 2.1(a), and black arrows are sometimes added in the spectra for a more intuitive illustration. We also observe the particle-hole symmetry: the electron-like bands with positive energy and the hole-like bands with negative energy are gapped around zero energy by the superconducting pairing Δ.

In Fig. 2.1(c), with increasing the magnetic field B along z, the gap shrinks around $k = 0$ and the spin orientation around $k = 0$ rotates towards the external magnetic field direction. The bands at finite momentum are not influenced so strongly as around $k = 0$ by the magnetic field.

Further increasing B, the gap closes at $k = 0$ at the critical magnetic field given by

$$E_\mathrm{Z} = \frac{1}{2} g \mu_B B = \sqrt{\Delta^2 + \mu^2}. \tag{2.4}$$

Fig. 2.1(d) plots the spectra close to this critical magnetic field and the topological phase transition happens at this point. In Fig. 2.1(e) we observe a reopening of the gap with further increasing the Zeeman energy. Compared to Fig. 2.1(c), the gap around $k = 0$ is inverted. Now the device is in the topological regime: the bulk is a topological superconductor with MBSs present at both ends of the hybrid nanowire. According to Lutchyn-Oreg [13, 14], MBSs appear when and only when $\frac{1}{2} g \mu_B B \geq \sqrt{\Delta^2 + \mu^2}$. We note that the spin-orbit coupling assures that the spin orientation is perpendicular to the external B field at finite momentum and the gap only reacts weakly with respect to B, providing a protection for the inverted gap around $k = 0$. Note that these explanations are based on single subband and without disorders.

The wavefunction of MBSs in the nanowire decays exponentially away from the ends [22]:

$$\Psi(z) \propto e^{-z/\xi} e^{\pm k_F z}, \tag{2.5}$$

in which ξ is the effective coherence length of the induced superconductivity, and k_F is the effective Fermi wave vector. If the nanowire has a finite length, the two MBSs on both sides will overlap in the bulk and interestingly lead to an energy splitting around zero [22]:

$$\Delta E \approx \hbar^2 k_F \frac{e^{-2L/\xi}}{m^* \xi} \cos(k_F L), \tag{2.6}$$

with L the length of the nanowire and $L \gg \xi$. The finite energy splitting ΔE scales with $\exp(-L/\xi)$. And the cosinusoidal term indicates an oscillation of ΔE. To better illustrate this finite length effect, we plot the energy spectra of a Majorana nanowire to show their evolution as a function of the magnetic field for different wire lengths in Fig. 2.2.

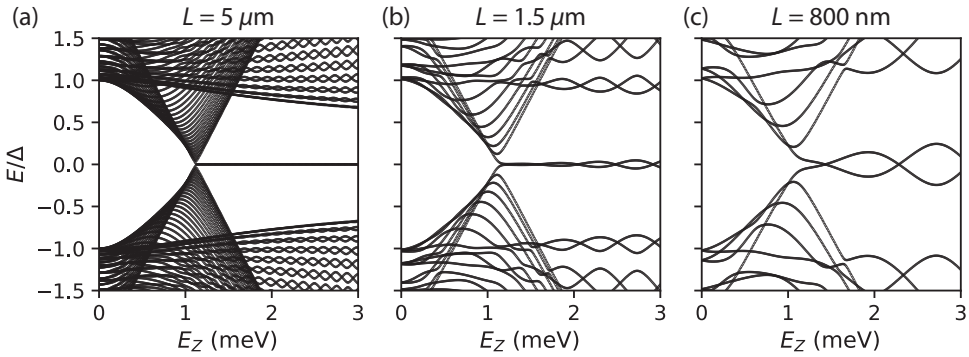

Figure 2.2: **Zeeman energy dependent energy spectra of a Majorana nanowire with different lengths. (a)** In a very long nanowire ($L = 5\,\mu$m, $L \geqslant \xi$), the MBSs stay at 0 energy after the gap reopens. **(b)** When the nanowire becomes shorter ($L = 1.5\,\mu$m), the continuum of states becomes more discretized and the MBSs oscillates due to the overlap between them showing increasing amplitude with raising Zeeman energy. **(c)** In a short wire ($L = 800\,$nm), the discretization of the continuum and the oscillation of MBSs becomes even larger. In the simulation $m^* = 0.02 m_e$, $\mu = 1\,$meV, $\alpha = 2\,$eV$\cdot$Å, $\Delta = 0.5\,$meV and the lattice constant $a = 0.648\,$nm.

For a very long nanowire ($L \gg \xi$, Fig. 2.2(a)), the above-gap states are densely distributed. When the Zeeman energy is greater than its critical point of the topological phase transition, the spectrum shows the emergence of the Majorana state very close to zero energy. When we decrease the length, in Fig. 2.2(b), we observe a significant discretization of states due to the finite length effect. The zero energy Majorana states starts to oscillate and the oscillating amplitude increases with larger E_Z. Furthering decreasing the wire length (Fig. 2.2(c)), the finite length effect is so strong that the oscillating amplitude can even reach the same order of magnitude as Δ. The previously narrated long wire approximation no longer applies.

Hereby we point out that the emergence of these states close to zero energy leads to important experimental signatures in quantum transport, which will be discussed in the following sections.

2.2. MAJORANAS FROM AN EXPERIMENTAL PERSPECTIVE

2.2.1. DETECTING MAJORANAS IN NANOWIRES

TUNNELING SPECTROSCOPY

In this section we discuss how we experimentally detect MZMs in nanowire systems in the framework of quantum transport. The primary tool, which was also first used in this field, is tunneling spectroscopy [23–27]. Tunneling spectroscopy is a well-established tool to probe the density of states (DOS) in a quantum system.

In such a measurement, a typical setup consists of a normal metal and a device under test separated by a tunnel barrier. In our nanowire system, we create a tunnel barrier

between the normal part and the proximitized part of the nanowire so that we have a so-called N-nanowire-S junction. This case is illustrated in Fig. 2.3. The proximitized region is simply treated as a superconductor (S) in the sketch. The normal part (N) and the superconducting part is separated by a tunnel barrier, which is often experimentally realized by a narrow local gate close to the nanowire with applying a negative potential. A bias voltage $-V$ is applied to the N-side and the S-side is grounded, accordingly the chemical potentials μ_1 and μ_2 on the two sides have a difference of eV. Thus a current is sent through the tunnel barrier and the resulting conductance can be measured.

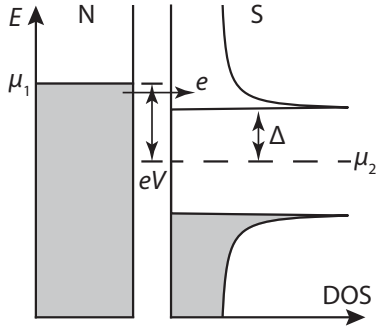

Figure 2.3: **N-S tunneling transport.** A tunnel barrier is situated between the normal section (N) and the superconducting section (S). The density of states (DOS) are plotted as a function of energy. The shaded states are occupied by electrons. The chemical potentials of the N section and the S section are respectively μ_1 and μ_2. μ_1 is lifted by eV due to a bias voltage V applied between the two parts. The DOS of S illustrates a superconducting gap Δ. Electrons tunnel to empty quasi-particle states from N to S.

Making use of the Landauer-Büttiker formalism [28, 29], we represent the transition probability from left to right with $\mathscr{T}$, for which $\mathscr{T} \ll 1$ in the tunneling scenario and thus considered constant with respect to energy E [30]. We can write the net tunneling current from the N-side to the S-side as

$$I_{\mathrm{NS}} \propto \mathscr{T} \int_{-\infty}^{\infty} DOS_{\mathrm{N}}(E+eV) DOS_{\mathrm{S}}(E) \left[f(E) - f(E+eV) \right] \mathrm{d}E, \tag{2.7}$$

in which we include the density of states $DOS_{\mathrm{L(R)}}(E)$ on both sides and $f(E)$ denotes the Fermi-Dirac distribution.

Then the differential conductance G is given by

$$G_{\mathrm{NS}} = \frac{\mathrm{d}I_{\mathrm{NS}}}{\mathrm{d}V} \propto \mathscr{T} \int_{-\infty}^{\infty} DOS_{\mathrm{N}}(E+eV) DOS_{\mathrm{S}}(E) \left[-\frac{\partial f(E+eV)}{\partial (eV)} \right] \mathrm{d}E. \tag{2.8}$$

For the normal contact, we assume the density of states is not dependent on energy close to eV and is approximated as a constant. The term $-\dfrac{\partial f(E+eV)}{\partial (eV)}$ is a δ-function at zero temperature at the energy of eV and becomes a peak with a full width at half maximum of $3.5 k_B T$[1]. Therefore, with the mentioned approximation and the zero-temperature

[1] The symbol T only represents the temperature here, while in other contexts of this chapter T is usually used as the transmission.

limit, Eq. 2.8 is simplified as

$$G_{\mathrm{NS}} \propto \mathscr{T} DOS_{\mathrm{N}} DOS_{\mathrm{S}}(eV) \tag{2.9}$$

Here we have proven that the DOS can be probed via the tunneling spectroscopy as it is directly proportional to the measured differential conductance $G \equiv \mathrm{d}I/\mathrm{d}V$ at the bias voltage, when a tunnel barrier is created next to the probed system.

When MZMs are present in a gapped system in which the DOS is normally zero, MZMs bring a finite DOS around zero energy. As a result, a conductance peak would be measured when the bias voltage is zero. This so-called zero-bias peak (ZBP) is an important experimental signature in quantum transport associated with MZM studies.

ANDREEV REFLECTION

We have introduced that charge transport happens from a normal conductor to a superconductor. We note that the superconductor has an gapped energy spectrum in which quasiparticle states do not exist inside the superconducting gap Δ, so an electron cannot simply tunnel across the N-S junction if its energy is smaller than Δ, and has to undergo other physical process instead. Besides the tunnel barrier, we now discuss what process at the N-S interface actually enables the transport.

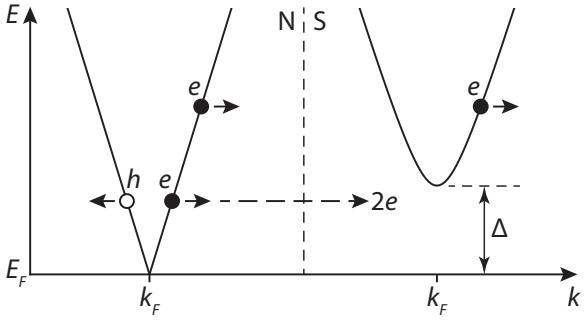

Figure 2.4: **Andreev reflection.** An electron moving from the normal (N) section to the superconducting section (S) gets reflected back as a hole at the same energy and with approximately the same momentum, while sending a Cooper pair into the superconductor, if the energy of the incident electron is small than the superconducting gap Δ. An electron with an energy greater than Δ transports into the superconductor as a quasiparticle at the same energy. Black curves are the excitation spectra centered at k_{F} on both sides.

Fig. 2.4 illustrates a N-S junction. The left side (N) shows a linear dispersion $E(k) = \hbar v_F k - E_F$ and the right side (S) shows the dispersion resulting from the Bogoliubov-de Gennes (BdG) equation [31] with the superconducting gap Δ above E_F. In the high energy limit, an incident electron is transmitted as a quasiparticle with approximately the same energy and momentum. The transport becomes identical to a N-N junction, and the conductance in the single channel case is given by

$$G_{\mathrm{NN}} = \frac{2e^2}{h} T, \tag{2.10}$$

with T the transmission of the tunnel barrier. This is a simplified version of the Landauer formula [32].

If the energy of the incident electron is lower than Δ, it undergoes the process called "Andreev reflection": the electron is reflected back as a hole at the same energy and with approximately the same momentum at the N-S interface, while sending a Cooper pair into the superconductor. The process is equivalent to that the incident electron carries another electron from the normal conductor and transfers $2e$ into the superconductor. Considering only single channel, a 1D model describing the conductance of Andreev reflection is developed as the Blonder-Tinkham-Klapwijk (BTK) theory [33]. At zero-bias voltage, the conductance is given by

$$G_{\mathrm{NS}}(V=0) = \frac{2e^2}{h}\frac{2T^2}{2-T^2}. \tag{2.11}$$

The BTK theory not only gives the zero-bias conductance, but in the entire energy spectrum [33]. With tunneling spectroscopy introduced previously, the BTK theory can be simply and directly verified in experiments.

Comparing equations 2.10 and 2.11, if $T \ll 1$, we find that the tunneling conductance inside the superconducting gap is extremely suppressed compared to the above-gap conductance, but is never completely zero. In the subsequent experimental chapters of this thesis, the term "hard gap" is used to describe that the measured conductance is consistent with the BTK theory, while a "soft gap" has a higher subgap conductance than what the BTK theory predicts. If the tunnel barrier becomes open and $T \approx 1$, we find G_{NS} reaches $2G_{\mathrm{NN}}$: the doubled subgap conductance demonstrates the so-called "Andreev enhancement".

QUANTIZED ZERO-BIAS PEAK

We've already shown that a finite zero-bias conductance is a signature that can be measured in transport when a MZM[1] presents in the experimental device for certain ranges of the chemical potential and the magnetic field. However, zero-bias anomaly is not rare in various condensed matter systems, here we introduce furthermore that a specific value is expected for the Majorana zero-bias conductance peak as a unique property to detect MZMs.

In a tunneling spectroscopy, the MZM at zero energy leads to a resonant tunneling. A resonant tunneling occurs when two tunnel barriers are combined and a resonant state occurs in the potential well between the barriers. In general, the transmission of the double barrier is approximately the product of the transmissions of each individual barrier. However, close to the resonance, the transmission through the double barrier can increase drastically to a high value regardless of the details of individual barriers. Assuming the transmission coefficients of the two individual barriers T_1 and T_2, the transmission of the double barrier is given by [34]

$$T \approx \frac{4T_1T_2}{(T_1+T_2)^2}. \tag{2.12}$$

In the tunneling experiment of a system with MZMs, an incident electron from the normal lead enters the Majorana state across the tunnel barrier, and is then reflected as

[1] Note that MZMs always occur in pairs, but the devices covered in this thesis are usually made to study only one of the ends of a hybrid nanowire.

a hole. The reflected hole tunnels back to the normal lead across the same tunnel barrier as for the incident electron, because the MZM is supposed to be at zero energy thus the incident electron and the reflected are both at the same energy. This process can be treated as a continuous tunneling of an electron (hole) across a double barrier at zero energy and is bonded to Andreev reflection. According to Eq. 2.12, if the transmission coefficients of the two barriers are identical, the resulting transmission arrives at unity. As a result of Eq. 2.10, the Majorana conductance is quantized at $2e^2/h$ at zero energy, giving an important conclusion of this section.

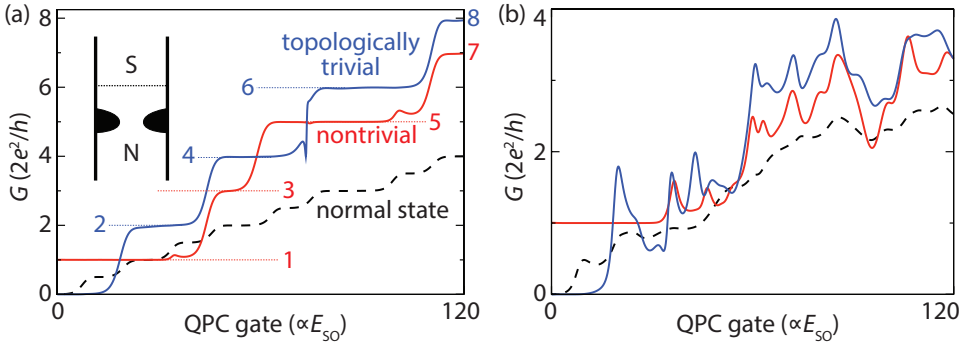

Figure 2.5: **Conductance quantization when probing a N-S tunnel junction via a quantum point contact (QPC). (a)** Conductance as a function QPC gate, equivalent to a tunnel gate. Blue curve shows the topologically trivial phase while red curve shows the nontrivial phase. In the topological nontrivial case (red), the zero-bias conductance, i.e. Majorana conductance, forms a quantized plateau at $2e^2/h$. When increasing the gate voltage, the conductance is subsequently quantized at odd time of $2e^2/h$. In a trivial case, the conductance rises from 0 to $4e^2/h$ and is subsequently quantized at even times of $2e^2/h$. The conductance through a normal QPC is shown by the black dashed line. Inset: an illustration of a N-S junction with the interface represented by the black dotted line. A QPC in the N region serves as a probe of the junction. **(b)** The presence of disorder covers up the features in the trivial (blue) and the nontrivial (red) cases, while the quantized Majorana conductance at $2e^2/h$ remains undisturbed. Adapted from Ref. [35].

Furthermore, Ref. [35] simulates the conductance due to a MZM in a N-S junction via a quantum point contact (QPC), equivalent to a tunnel barrier while being able to control the number of subbands via the QPC. Fig. 2.5(a) shows an ideal case of the zero-bias conductance of this system in the topologically trivial as well as nontrivial phases. The first zero-bias conductance plateaus have the values:

$$\left.\frac{\mathrm{d}I}{\mathrm{d}V}\right|_{V=0} = 2\left\lfloor\frac{n}{2}\right\rfloor\cdot\frac{2e^2}{h}\ \text{(trivial)}\quad\text{or}\quad\left.\frac{\mathrm{d}I}{\mathrm{d}V}\right|_{V=0} = \begin{cases}\dfrac{2e^2}{h}, & n<4\\ \left(2\left\lfloor\dfrac{n}{2}\right\rfloor-1\right)\cdot\dfrac{2e^2}{h}, & n\geq 4\end{cases}\ \text{(topological)}, \tag{2.13}$$

in which n is the number of subbands in the QPC as shown by the black dashed line. A remarkable feature of the zero-bias conductance before the QPC conductance reaches $2\cdot\frac{2e^2}{h}$ (the second subband is fully opened, $n=4$) is that it is independent of the tunneling strength and remains quantized at $2e^2/h$ in the topological phase, while in the topologically trivial phase it varies from 0 to $4e^2/h$. When the QPC is further opened, the

conductance exhibits steps of $4e^2/h$ because the Andreev reflection enhances the conductance as each subband would contribute to a conductance of $2e^2/h$ in the normal to normal case.

Focusing on the 1st conductance plateau in the nontrivial case, even when disorder is introduced into the simulation, the quantized Majorana conductance remains undisturbed as long as only one subband enters the N-S junction, as shown in Fig. 2.5(b). This stability stands in remarkable contrast to the trivial case in which the conductance quantization is destroyed by the disorder. This topological behavior of the robust quantization gives experimental physicists an indication how to distinguish MBS from other topologically trivial bound states.

2.2.2. EXPERIMENTAL SIGNATURES OF MAJORANAS

Guided by these theoretical predictions, signatures of MBS-like states have been observed in numerous experiments in the past decade [23–27, 36, 37], relying on tunneling spectroscopy introduced in Section 2.2. These experiments have opened up a whole new field of studies. Here we list a series of important experimental works in several steps of this field to make a review from the perspective of experiments, which hopefully can be used as a guidance for the potential readers of this thesis.

III-IV semiconductors with strong spin-orbit coupling such as InAs and InSb first came into views of the researchers as there have been well-developed technique for the nanowire growth [38]. In 2012, the first ZBP was observed in an InSb nanowire coupled to NbTiN [23] while applying a finite magnetic field, similar to the zero energy state that Fig. 2.2 predicts. As shown in Fig. 2.6(a), a ZBP of $\mathrm{d}I/\mathrm{d}V$ emerges in the magnetic field sweep from 100 mT and 400 mT inside a superconducting gap of 250 μeV. In 2012 this experiment was considered as a signature consistent with the Majorana theory. Shortly after this, ZBPs in similar type of devices were reproduced [24–27].

A typical device of such measurements is sketched in Fig. 2.6(c) [40]. The hexagonal semiconductor nanowire (grey) is proximitized by a superconducting film (green). A metallic contact (yellow) is deposited next to the hybrid segment to form a N-S junction. A bias voltage is applied on the contact to perform tunneling spectroscopy with a tunnel barrier induced by the tunnel gates (red), and the current is measured from the other contact. Super gates (blue) and possibly available global back gates are usually used to tune the chemical potential of the nanowire.

In these early stage ZBP experiments, finite subgap conductance indicates soft superconducting gap, which spoils Majorana signatures. The ZBP in Fig. 2.6(a) is much lower than the predicted quantized conductance and only has a height of $\sim 5\% \cdot 2e^2/h$. As another material approach, 2-dimensional electron gases (2DEGs) was also used for Majorana research in parallel with our nanowire systems. In 2017, the first "large" ZBP close to the conductance quantum was reported in InAs-Al 2DEG system (Fig. 2.6(c)).

It was believed that disorders at the semiconductor-superconductor interface are the cause of soft gap by several studies. Important material breakthrough was then made on the epitaxial growth of superconductor directly on the clean nanowire surface, producing atomic flat interfaces [41, 42]. On this generation of epitaxial hybrid nanowires, hard superconducting gap and large ZBPs were soon achieved in epitaxial InSb-Al nanowire devices. An example is shown in Fig. 2.6(d), in which a ZBP of $2e^2/h$ is present at the

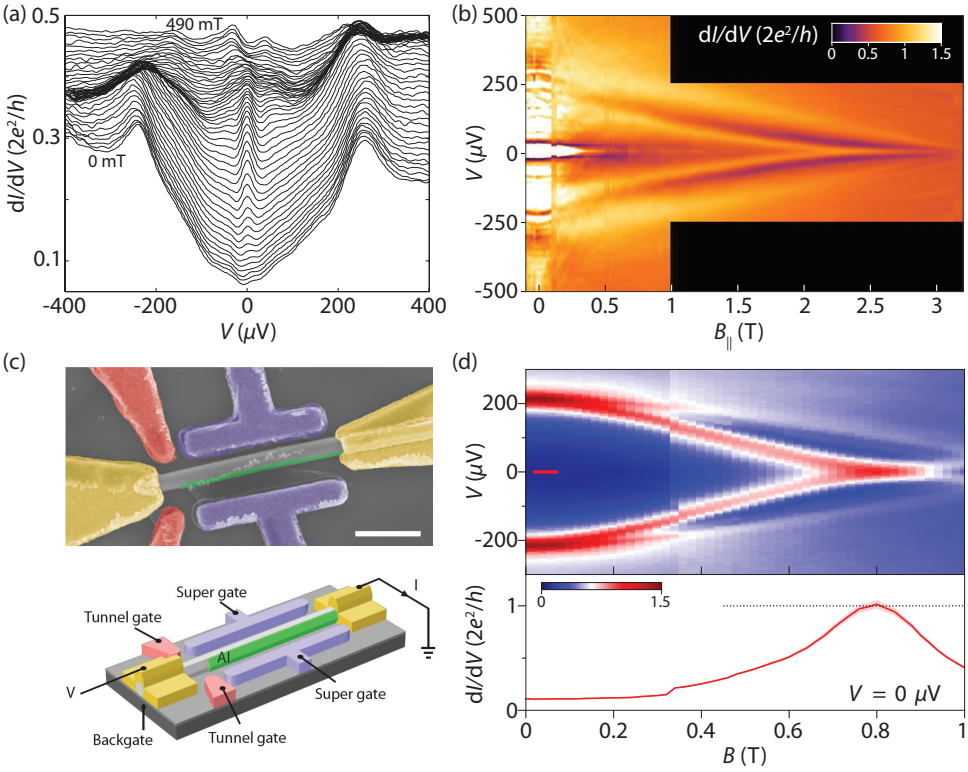

Figure 2.6: **Zero-bias peaks as a signature of MZM. (a)** One of the first zero-bias peak measurements on an InSb nanowire hybridized with NbTiN superconductor. $\mathrm{d}I/\mathrm{d}V$ is plotted against the bais voltage V at magnetic fields from 0 to 490 mT. The superconducting gap is 250 μeV. Zero-bias peaks are present between 100 mT and 400 mT. Adapted from Ref. [23]. **(b)** A large zero-bias peak close to $2e^2/h$ on a InAs-Al junction synthesized on a 2-dimensional electron gas. The color plot denotes $\mathrm{d}I/\mathrm{d}V$ as functions of bias voltage V and magnetic field B. Adapted from Ref. [39]. **(c)** A typical device for tunneling spectroscopy on a hybrid nanowire. Upper panel shows a scanning electron micrograph of a device, and its schematics is shown in the lower panel. An hexagonal semiconductor nanowire (grey) is covered by a superconducting film (green). Metallic contacts (yellow) serve as source and drain electrodes on the nanowire. Tunnel gates (red) controls a tunnel barrier in the nanowire segment not covered by the superconductor. Super gates (blue) are next to the hybrid nanowire. The scale bar is 500 nm. **(d)** Upper panel: $\mathrm{d}I/\mathrm{d}V$ versus V and B shows a large zero-bias peak in the device shown in (c). A line trace at $V = 0$ is shown in the lower panel with the shaded area showing the 2σ error. The peak of the zero-bias conductance is close to $2e^2/h$. (c) and (d) are adapted from Ref. [40].

magnetic field of ~ 0.8T [40]. This clean and robust ZBP marks a milestone among the achievements made on simple N-S devices. The significant progress was for a moment believed as a smoking-gun realization of the quantized Majorana conductance, while our later understanding on these measurements will be discussed in Section 2.2.3 and Chapter 4.

In addition, another type of Majorana studies were performed on hybrid island devices. The measurements on island devices cannot directly demonstrate MZMs but are rather treated as a minimal requirement for the devices to host MZMs. We make a conceptual introduction of this type of measurements for ease of reference to Chapter 6.

A typical hybrid island device is illustrated in Fig. 2.7(a) [43]. Two metallic contacts are made on both sides of the hybrid segment on a nanowire. Two barriers on both sides are enabled by two tunnel gates and a plunger gate tunes the charge occupation of the Coulomb blockaded region. The superconductivity and the charging energy of the island give it interesting properties. The superconductivity dictates that only Cooper pairs can be added or removed via Andreev reflections on both sides with overcoming the charging energy, unless a quasiparticle state is available in the island for electrons on the leads to move in or out. Assuming the gate-induced charge number $N_G = CV_G/e$, with C the gate capacitance and V_G the gate voltage, the energy of the island is given by [43]

$$E(N_G) = E_C (N_G - N)^2 + p_N E_0 \quad \text{with} \quad p_N = \begin{cases} 0, \text{ odd } N \\ 1, \text{ even } N \end{cases} \tag{2.14}$$

where E_C is the charging energy, N is the electron occupancy and E_0 is the lowest quasiparticle state. This energy manifests itself as a series of parabolas, as depicted in the upper panel of Fig. 2.7(b).

The odd charge states are originally lifted by E_0 (blue parabolas), which is given by the lowest quasiparticle energy that can be either the superconducting gap or a subgap state. With changing physical parameters, it is possible to lower the energy of odd charge states. In the topological phase, MZMs allow a zero energy subgap state, indicating the odd charge states (red) are evenly distributed together with the even states. Quantum transport only happens when the states have charge degeneracy, i.e. at the intersections of the parabolas. The resulting conductance peaks are shown in the lower panel. If $E_0 > E_C$, the conductance peaks occur with a period corresponding to adding $2e$ charge to the island. If the system undergoes a topological phase transition, we expect to observe a transition from $2e$-periodic to $1e$-periodic conductance peaks.

Fig. 2.7(c) and d show two typical cases in which a $2e$-to-$1e$ transition pattern can be measured [44]. Fig. 2.7(c) shows a sweep of the bias voltage V_{Bias} in which $2e$ Coulomb diamonds are clearly resolved. With $V_{Bias} > E_0 - E_C$, the period as a function of the gate voltage becomes $1e$. Fig. 2.7(d) shows a magnetic field sweep, directly resolving the $2e$-to-$1e$ transition as panel b indicates with increasing the magnetic field parallel to the nanowire.

2.2.3. ALTERNATIVE EXPLANATIONS OF ZERO-BIAS PEAKS

Soon after the first signature of Majorana ZBP was measured in experiments, researchers have been looking for alternative explanations for topologically trivial origins of zero-bias anomalies already since 2012 [45–52]. In these systems zero energy or near-zero

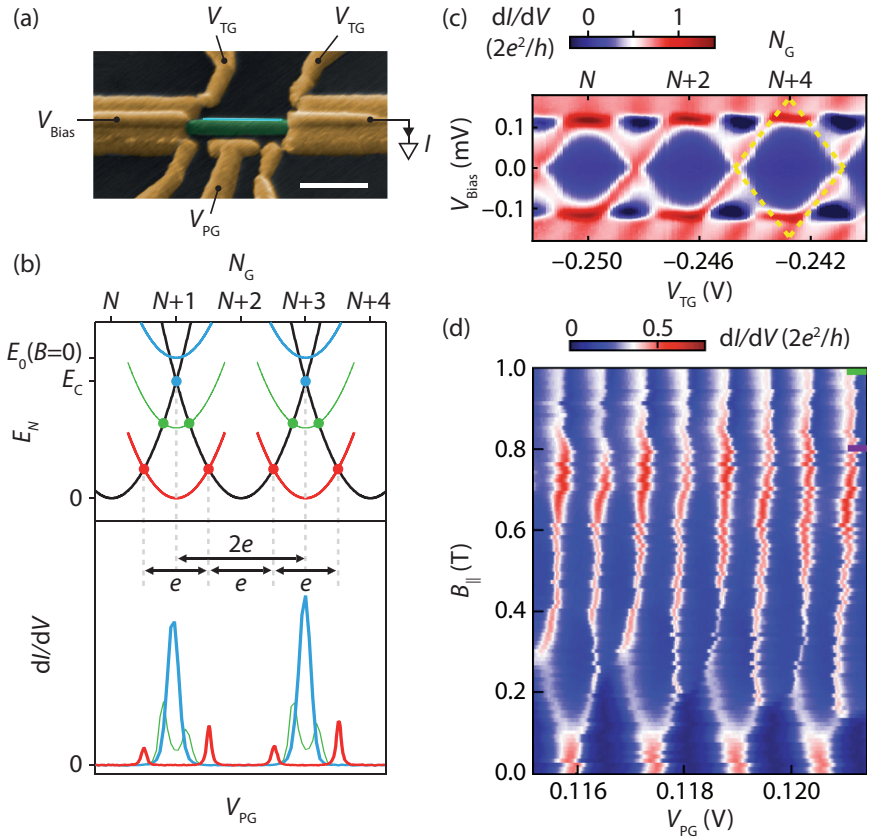

Figure 2.7: **Hybrid island device and measurements.** **(a)** Scanning electron micrograph of a typical hybrid island device based on nanowire. The nanowire (green) has a section proximitized with a superconducting film (light blue). Contacts (yellow) are deposited on the normal regions on two sides. Tunnel gates (TG) tunes tunnel barriers on both sides of the hybrid island and the plunger gate (PG) tunes charge occupation of the island. Scale bar is 500 nm. **(b)** Upper panel: energy of the island E_N (N electrons occupy the island) plotted vs the normalized gate voltage N_G. Black and blue curves represent energy spectra of even occupation and odd occupation, respectively. The energy offset of odd occupation is E_0 at zero magnetic field. When increasing the magnetic field, the odd energy descends to the green curve, and finally to the red curve if zero energy states appear in the system. Lower panel: $\mathrm{d}I/\mathrm{d}V$ vs V_{PG}, a manifestation of the energy spectra in the upper panel. The Coulomb peak positions correspond to the colored dots in teh upper panel. The Coulomb peaks is $2e$-periodic in the blue curve and $1e$-periodic in the red curve. (a) and (b) are adapted from Ref. [43]. **(c)** $\mathrm{d}I/\mathrm{d}V$ vs tunnel gate voltage V_{TG} and bias voltage V_{Bias}. $2e$-periodic Coulomb diamonds (yellow dashed lines) are visible at low bias, while around 0.1 mV $2e$-periodic Coulomb peaks transit to $1e$-periodic. **(d)** $\mathrm{d}I/\mathrm{d}V$ at zero-bias with increasing magnetic field. The $2e$-periodic Coulomb peaks splits and gradually become $1e$-periodic as the magnetic field increases. (c) and (d) are adapted from Ref. [44].

Andreev bound states (ABSs) are generally present before the topological phase transition, and they can sometimes even pin at zero energy across an extended range in the parameter space. Beyond the ideal Majorana model, it is also realized that the tunneling spectroscopy experiments are difficult to demonstrate several theoretical predictions, such as bulk-gap closing and reopening, Majorana oscillations or increasing oscillations with the magnetic field.

After the development of this field for almost a decade, people have gained more insight on the trivial origins of ZBPs. In realistic systems, these states can originate from all kinds of inhomogeneities in hybrid nanowire systems. We roughly classify the inhomogeneities in two aspects: smooth confinement and disorder. Particularly, a smooth confinement in the nanowire leads to trivial zero modes called quasi-Majoranas, or equivalently partially separated ABSs. The review article written by Prada *et al.* [53] is recommended for the readers as an extensive textbook on this matter. Additionally in 2020 to 2021, Pan and Das Sarma *et al.* performed a series of studies on disorders in hybrid nanowire systems [54–57]. A detailed discussion on disorder combined with our measurements is provided in Section 4.3.

2.3. MAJORANA DEVICES BEYOND SINGLE NANOWIRES

Now that we have introduced Majorana bound states and how they manifest themselves in condensed matter physics, we return to this point what special physical meaning they have and how they behave distinctly from other particles and quasiparticles. We will discuss how their properties can contribute to topological quantum computing. We will also see what advanced devices beyond single nanowires are of interest towards a topological qubit.

2.3.1. PROPERTIES OF MAJORANAS

From Eq. 2.2 we can derive the anticommutation relation of Majorana operators

$$\{\gamma_i, \gamma_j\} = \gamma_i\gamma_j + \gamma_j\gamma_i = 2\delta_{ij}. \tag{2.15}$$

Thus defining a Majorana number operator does not lead to any physical meaning as $n_{\mathrm{M}} = \gamma_i^\dagger\gamma_i = 1$. Instead, the number operator of fermion is expressed as

$$n = c^\dagger c = \frac{1}{2}\left(1 + i\gamma_1\gamma_2\right), \tag{2.16}$$

which can be 0 or 1 for an empty or filled fermionic state, respectively. Two Majoranas therefore form one fermionic state, which can only be filled or unfilled with one fermion (e.g. a Bogoliubov quasiparticle). Further, we define the parity operator

$$P = -i\gamma_1\gamma_2, \tag{2.17}$$

which has the value -1 or 1 for empty (even) or filled (odd) fermionic state, respectively.

Based on the nanowire model hosting MZMs (Section 2.1), a pair of Majorana states can be created nonlocally on a nanowire. Because a Majorana is only a half of a fermionic state, the two Majoranas form one fermionic state together and define one fermionic

parity while located far away from each other. Quantum information defined using parities under the nonlocal nature of Majoranas is considered to be topologically protected, and robust against local perturbations, demonstrating potential applications of Majoranas in quantum computing [10, 58–62].

Another intriguing property of Majoranas is their non-Abelian exchange statistics, differentiating them from other particles obeying Fermi-Dirac or Bose-Einstein statistics[1]. This special exchange statistics is embodied in the so-called "braiding" operation. We defined the braiding operator as [17]

$$B_{ij} = \frac{1}{\sqrt{2}}\left(1 \pm \gamma_i \gamma_j\right), \tag{2.18}$$

in which ± indicates difference forms of the operator between a clockwise (+) and a counterclockwise (−) exchange. With two pairs of Majoranas, the non-Abelian exchange statistics is expressed by [63]

$$\left[B_{i-1,i}, B_{i,i+1}\right] = \gamma_{i-1}\gamma_{i+1}, \tag{2.19}$$

meaning that the two braiding operators involving the same Majorana do not commute. The braiding operations can be designed for qubit operations in a system with at least two pairs of Majoranas.

A braid operation can be experimentally realized by physically exchanging Majoranas with certain gate operations as described in early stage proposals [63]. However, later proposals implements braiding by adiabatically tuning the couplings among MZMs with a specifically designed tuning of magnetic flux or gates [58, 59]. With Vijay and Fu introducing the concept of "braiding without braiding" [60], the measurement-based braiding becomes a more popular idea for topological qubit proposals.

2.3.2. MEASUREMENT-BASED BRAIDING

We now narrow down to the possible next step for realizing a topological qubit in a nanowire-based system. Fig. 2.8(a) illustrates a minimal setup that functions as a topological qubit, named as Majorana box qubit [61]. The qubit device consists of two parallel nanowire-based topological superconductors with 4 MBSs γ_1 to γ_4 at the ends. The length scale of the system is designed such that the overlapping effect between MBSs can be neglected. The two topological superconductors are connected by a superconducting bridge. When applying gate voltage on the normal sections to build a strong Coulomb blockade for the hybrid island, the fermionic parity is then a good quantum number, i.e. $P = \prod_{i=1}^{4} \gamma_i = \pm 1$. The two different parity states are defined as qubit states $|0\rangle$ and $|1\rangle$. The 4 Majoranas with a joint well-defined parity corresponds to a degenerate spin-1/2 degree of freedom [64–67], and the Pauli operators for the qubit are given by

$$\hat{x} = i\gamma_1\gamma_2, \quad \hat{y} = i\gamma_3\gamma_1, \quad \hat{z} = i\gamma_2\gamma_3. \tag{2.20}$$

[1] Majorana is not the only quasiparticle with non-Abelian statistics, but all elementary particles obey either Fermi-Dirac or Bose-Einstein statistics. Other candidates for non-Abelian statistics include the fractional quantum Hall state at the filling factor 5/2.

The conductance $G_z(\phi)$ measured between the two leads as a function of the applied out-of-plane magnetic flux ϕ is suppose to demonstrate an interfering pattern similar to the Aharonov-Bohm (AB) effect [68]. The research shows two possible outcomes with of $G_z(\phi)$ a π-phase shift between each other for the readout of the $\hat{z}$-eigenvalues ± 1 as the circuit loop includes γ_2 and γ_3.

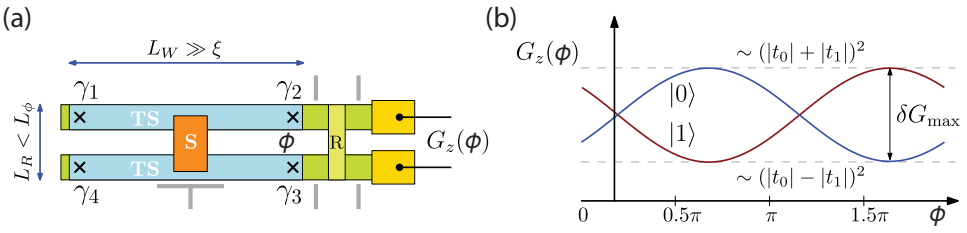

Figure 2.8: **Majorana box qubit. (a)** Schematics of a Majorana box qubit. Two topological superconducting (TS) nanowires are connected by a superconducting bridge (S), and by a semiconducting reference section (R) on the side. Four Majoranas (γ_1-γ_4) are created on the ends of the TSs. The interferometric properties of this system is measured by leads on the right involving a magnetic flux ϕ. The superconducting coherence length and the phase coherence length are ξ and L_ϕ, respectively. L_R the length of the reference arm, L_W the length of the topological nanowire. **(b)** The proposed conductance $G_z(\phi)$ measured with the read-out circuit, showing oscillatory behavior. The interference pattern has a period of 2π and show a π-phase shift between two different parity states, i.e. qubit states $|0\rangle$ and $|1\rangle$. Adapted from Ref. [61].

This method of projective measurements enables 90° rotations of the qubit states in the Bloch sphere [69, 70]. Braiding operation can be designed as sequence of such projective measurements without physically moving the Majorana states. This concept is called measurement-based braiding and lays the foundation for the latest topological quantum computing proposals [62].

2.3.3. MAJORANA TELEPORTATION

The Majorana box qubit has two core ingredients: nanowire-based 1D Coulomb blockaded topological superconductor and nanowire-loop-based AB interference. Naturally, a precursory experiment for this study is comprised of a nanowire loop with a 1D hybrid segment in the interference loop. Such an experiment is proposed by Fu as the so-called Majorana teleportation [60, 71]. We note that Fu's experiment is generally called a cotunneling, while the experiment we described in Section 2.3.2 via $\gamma_2\gamma_3$ demonstrates a more generalized anyonic teleportation in the context of measurement-based braiding [62, 69].

Fig. 2.9(a) shows a schematic of a teleportation device based on a nanowire loop with a flux ϕ. The hybrid segment on one of the interference arms can be turned into a Majorana island with applying tunnel barriers on both sides. Via the delocalized Majorana wavefunction distributed on both ends, an electron from the normal region can tunnel into the island and jump out on the other side via the same state [18, 71]. This cotunneling process via the MZMs is predicted to be phase coherent however long distance it needs to travel as a result of Majoranas' nonlocal nature.

Fu predicts the interference pattern of zero-bias conductance for different parities of the MZMs. As shown in Fig. 2.9(b), a π-phase shift is expected between the even and odd

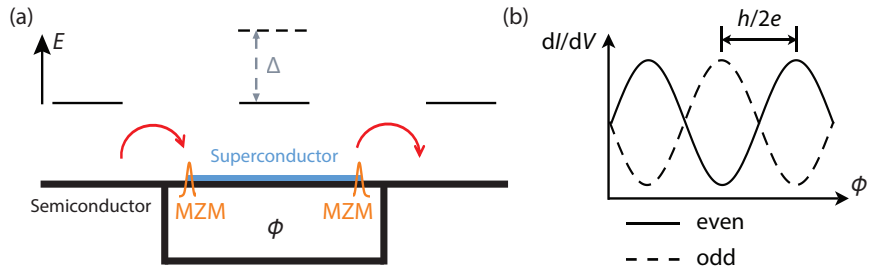

Figure 2.9: **Majorana teleportation. (a)** Schematic of a semiconductor nanowire interferometer with an arm proximitized by a superconductor. The hybrid segment is separated from the rest of the interferometer by tunnel barriers. The fermionic state of the hybrid segment is lifted by the superconducting gap Δ and MZMs are created at both ends. The arrows denote an electron teleportation process via MZMs. **(b)** The proposed zero-bias conductance as a function of the magnetic flux ϕ. A π-phase shift is expected between even and odd parity states. (b) is adapted from Ref. [71].

parity states [71]. Note that the period of the AB oscillation is h/e, indicating that single electron transport is allowed via the MZMs, while a trivial superconducting island would only allow $2e$ tunneling at zero-bias.

As a near term experimental exploration, quantum transport of nanowire loops without superconductor is studied in Chapters 6 and 8 in this thesis.

3

EXPERIMENTAL TECHNIQUES

Nanos gigantium humeris insidentes.

John of Salisbury

This chapter describes the experimental techniques used throughout the thesis, including material growth, fabrication techniques and electrical measurement set-up, unless provided in other experimental chapters. The hybrid semiconductor-superconductor nanowires used in our experiments are grown by the vapour-liquid-solid (VLS) technique and the selective area growth (SAG) technique in the group of Erik Bakkers at TU/e from a metalorganic vapour-phase epitaxy (MOVPE) system, with Al film on the nanowires grown by molecular-beam epitaxy (MBE) either in the group of Chris Palmstrøm at UCSB or in the group of Erik Bakkers at TU/e. This chapter starts from the growth of hybrid nanowires, then focuses on the fabrication techniques for InSb-Al hybrid devices which we developed in our lab in Delft, especially on the selective etch of Al on InSb SAG nanowires which has been filed as a patent.

3.1. HYBRID NANOWIRE GROWTH[1]

The experiments presented in this thesis are related to two different growth mechanisms: vapour-liquid-solid (VLS) and selective area growth (SAG). VLS forms vertically orientated nanowires on a growth substrate, which means the length direction of the nanowires is perpendicular to the surface of the growth substrate. A network of nanowires may be synthesized by connecting together two or more of VLS grown nanowires. After growing the nanowires by VLS, the nanowires need to be transferred to another substrate for device fabrication. This is done by a micromanipulator which is a movable needle made of W or In with a very sharp tip and can be integrated to an optical microscopic system or a scanning electron microscope (SEM). SAG comprises forming a mask over the substrate, then growing the nanowires using e.g. MOVPE or MBE. The mask controls the position at which the semiconductor grows. SAG is particularly useful for constructing networks of nanowires, since the nanowires and junctions between the nanowires can be conveniently formed at the same time by configuring the openings in the mask appropriately. A SAG growth wafer can be diced into suitable size for fabrication. Then a massive SEM inspection is needed to select the best grown nanowires for proceeded device fabrication. Due to the nature of SAG, the great majority of the grown structures have to be sacrificed on a chip.

This section describes the VLS growth of hybrid InSb-Al nanowires, while SAG will be discussed in detail in Chapter 6.

In 2016 our collaborators developed a technique for generic bottom-up synthesis of complex quantum devices with a special focus on nanowire networks with a predefined number of superconducting islands. Accurate control over the nanowire position and growth direction enables us to grow complicated networks of up to four crossed junctions, such as closed loops of four interconnected nanowires (referred to as 'hashtags'). Furthermore, this platform allows *in situ* growth of a predefined number of separated superconducting islands on the nanowires. This eliminates the need for metal etching during device fabrication. Therefore, the integration of semiconductors with metals (for example, niobium) is possible without an additional etching process. This guarantees that the pristine atomically flat InSb(110) facets are left intact, a key element for high device performance. At the same time a clean epitaxial superconductor-nanowire interface is established, which had been previously proven to be crucial for the quality of the induced superconducting gap [41, 72].

For the growth of the nanowire networks a substrate with trenches is first fabricated (see Fig. 3.1a). These structures are defined by electron-beam (e-beam) lithography, a reactive ion etch and a subsequent wet etch to expose (111)B facets on an InP(100) crystal surface (Fig. 3.1a). A second lithography step is then used to position gold particles, which catalyze nanowire growth via the vapor-liquid-solid mechanism, on the inclined facets. Owing to the geometry of the (111)B facets, the nanowires are forced to grow towards each other and can fuse into a network. The final size and symmetry of the networks are controlled by the dimensions of the trenches and the spacing between them, that is, the parameters a-f, as indicated in Fig. 3.1a. The left (right) trenches and wires grown from them are labelled L_1, L_2 (R_1, R_2). The offset (Δy) between the gold parti-

[1] Part of this section belongs to the publication *Epitaxy of advanced nanowire quantum devices*, S. Gazibegovic *et al.*, Nature **548**, 434-438 (2017).

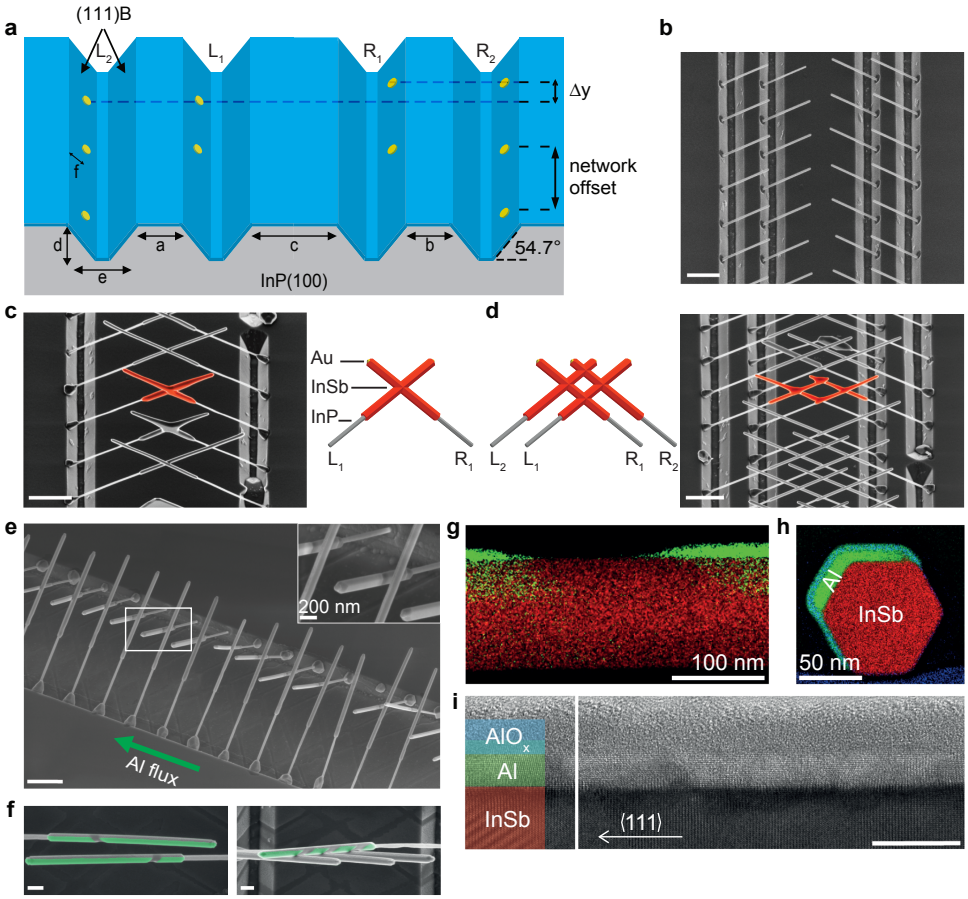

Figure 3.1: **Deterministic growth of InSb nanowire networks. a**, Schematic illustration of the substrate with etched trenches. Gold catalysts are lithographically defined on the inclined facets. The offset between the catalyst particles (Δy) is critical for the realization of nanowire networks and shadowed superconducting islands. The size and the symmetry of the networks are controlled by the dimensions of the trenches indicated in the schematic: the spacing between the left-left (L_1, L_2), a, right-right (R_1, R_2), b, and left-right (L_1, R_1), trenches, c, as well as the trench depth, d, width, e, and position of the gold particles on the inclined facets, f. **b**, A scanning electron microscopy (SEM) image of InP nanowires which serve as stems for InSb nanowire growth. **c**,**d**, SEM images and schematic illustrations of accomplished nanowire structures having one junction (**c**) or four junctions (**d**; hashtag). SEM images in **b**-**d** are taken at 30° tilt with scale bars of 1 μm. **e**, A 45°-tilted SEM image of an array of Al-InSb nanowires. The green arrow indicates the direction of Al beam flux during deposition. Scale bar is 1 μm. Inset, magnified area indicated by a white rectangle in the main panel. Each InSb nanowire is covered by two Al islands separated by a shadowed region. The number of shadows, n, and hence the number of superconducting islands, $n+1$, is determined by the number of wires directly in front of the shadowed wire. **f**, SEM images of InSb nanowires with two (left) and four (right) Al islands (pseudo-colored green). Both scale bars are 200 nm. **g**, STEM-EDX chemical composition map of an InSb nanowire (red) with Al islands (green) separated by an Al-free shadowed region. **h**, EDX chemical composition map of the nanowire cross-section. Al (green) is covering two out of the six {110} InSb side-facets. The Al-InSb interface is oxygen-free. **i**, High-resolution transmission electron microscopy image of an InSb nanowire (red) covered with a thin (about 10 nm), crystalline film of Al (green) and a layer of AlO_x (blue). InSb growth direction ⟨111⟩ is indicated by a white arrow. The image is taken along the ⟨110⟩ zone axis. The scale bar is 10 nm. Adapted from Ref. [42].

cles is an important parameter to control for two reasons. First, if $\Delta y < D$, where D is the nanowire diameter, nanowires will merge during growth (specifically, for $\Delta y \approx 0$ ($\Delta y \leq D$), resulting in the formation of a T-junction (X-junction) [73]); second, $\Delta y > D$ enables shadow growth of the superconducting islands, as discussed later in the text. In Fig. 3.1b we show a uniform array of InP nanowires that are used as stems to facilitate uniform nucleation of InSb nanowires. When InSb nanowires (highlighted in red in Fig. 3.1c,d) are grown on top of these InP stems, nanowire networks with 1 till 4 wire-wire junctions are formed, depending on the trench design (Fig. 3.1c,d). Importantly, this approach is generic and can be used to synthesize interconnected nanowires of various semiconductor materials which grow along a ⟨111⟩B direction. The number of wire-wire junctions can be increased by allowing for longer nanowire growth times and/or fabricating a larger number of left and right trenches.

Next, we combine the nanowire-network geometry with the directionality of molecular beam epitaxy (MBE) to shadow-grow aluminum superconducting islands on the InSb wires. The aluminum flux is aligned parallel to the trenches (Fig. 3.1e), such that a frontal wire casts a shadow on a wire in the background (inset of Fig. 3.1e). This causes interruptions in a uniform layer of aluminum as shown in Fig. 3.1f (left). For effective shadowing, it is important that the frontal wire does not merge with the shadowed wire, that is, $\Delta y > D$. The number of shadows, n, (and, accordingly, the number of superconducting islands, $n+1$) on any InSb nanowire is determined by the number of wires directly in front of that nanowire. For example, Fig. 3.1f (right) depict an InSb nanowire with three shadows cast by three frontal nanowires. The position and the width of the shadows are uniform for all wires examined and are set by the relative position of the wires and the solid angle of the aluminum effusion cell. The abrupt transition between the shadowed region of the nanowire and the segment covered with aluminum is evident from the chemical composition map (Fig. 3.1g) acquired by energy-dispersive X-ray spectroscopy (EDX) combined with scanning transmission electron microscopy (STEM). The line-of-sight directionality of MBE growth results in aluminum being deposited on two out of six facets of an InSb nanowire, as can be seen from a STEM-EDX map of a nanowire cross-section (Fig. 3.1h). The partial coverage of a nanowire with aluminum is essential as it allows tuning of the electron density of the proximitized nanowire by an external gate electrode, which is necessary for accessing the topological phase. The epitaxial interface between the InSb nanowire and a uniform, thin layer of aluminum is revealed by HRTEM imaging (Fig. 3.1i).

3.2. FABRICATION OF HYBRID INSB-AL NANOWIRE DEVICES

After depositing a VLS nanowire on a chip or having a SAG chip diced in a suitable size, the chip undergoes a series of fabrication steps for making nanowire devices that can be used for electrical measurements. In this section we demonstrate the fabrication process on a SAG InSb N-nanowire-S junction, with a global top gate, with InP walls on the substract enabling shadowed Al deposition. Such a device is relatively simple and representative enough as it covers almost all fabrication processes that we need.

Fig. 3.2(a) shows a tilted SEM image illustrating a SAG growth chip as what we obtained from our collaborators. An InSb nanowire is grown on an InP substrate in a groove defined by the SAG mask next to two InP walls (bright blocks) with the height of several

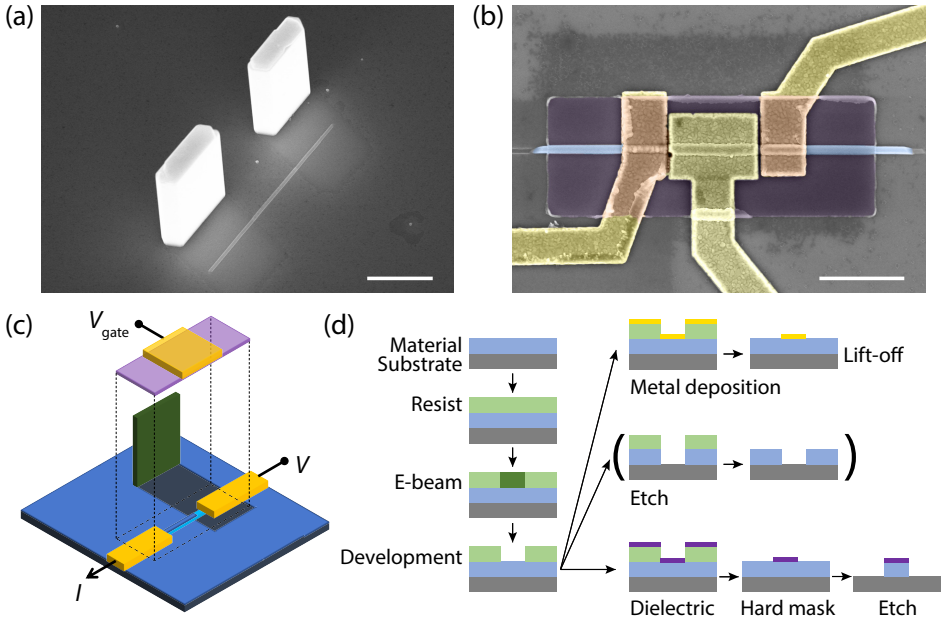

Figure 3.2: **Device fabrication.** **(a)** A tilted SEM image of a SAG chip. Two bright blobs are InP walls grown on the (111)B InP substrate. Parallel to the InP walls an in-plane SAG InSb nanowire. Al is deposited in MBE from the upper left in this image and shadows are formed next to the InP walls. Scale bar is 2µm. **(b)** SEM image of a SAG N-nanowire-S device. The InSb nanowire (blue) is contacted by two Cr/Au leads in the normal region (left, yellow) and the superconducting region (right, yellow). A Si_xN_y layer (purple) is deposited on top of the contacts and the nanowire, serving as an etch mask for Al as well as a dielectric. A top gate (middle, yellow) is deposited on the dielectric. Scale bar is 1µm. **(c)** Schematic illustration of the device in (b). The InP is shown in green and Al is shown in dark blue. Other colors stay in correspondence with (b). The dielectric and the top gate are lifted for a clear illustration. **(d)** Schematic representation of the fabrication process. Left column: electron beam (e-beam) lithography; first right row: metal deposition and lift-off; second right row: etch with the resist as the mask, parentheses indicating that this process is not involved in our fabrication flow; third right row: dielectric deposition and lift-off and etch with it as a hard mask.

micrometers. Al is deposited in the MBE chamber in TU/e from the upper in this image. Therefore, two shadowed regions can be seen on the right side of the InP walls. The normal-superconducting boundary formed naturally during the shadow deposition of Al allows us to fabricate a N-nanowire-S junction, without the necessity of creating an Al-free region with chemical etch. Because the height of the InP walls are much more than the common thickness of e-beam resists, the walls need to be broken off before any lithography steps to avoid uneven coverage of e-beam resists and difficulty of lift-off. This is done in a “waxing” style by adhering the wafer surface to a PDMS film (conveniently using a Gel-Pak) and applying a force to a direction along which the walls would not fell on nanowires.

Fig. 3.2(b) shows a final N-nanowire-S device. Two metal contacts (golden) under the semi-transparent dielectric layer (purple) serve as ohmic contacts to the nanowire, with part of the nanowire milled away to form oxigen-free contacts. Another metal layer

(golden) is deposited on top of the dielectric layer for gating the nanowire device. The dielectric layer also serves as an etching mask to remove the Al film that is not covered, to avoid short circuit between devices. Fig. 3.2(c) is a schematic of this device, with the dielectric and gate lifted up for a clear illustration of the layered structure. The dark blue region representing Al shows where it is deposited during the shadow deposition. Assuming that the SAG nanowire has a rectangular cross-section, there is one facet not covered with Al on the nanowire.

Fig. 3.2(d) shows a schematic representation of the fabrication flow in a general way. The material on the substrate can refer to the InSb nanowire, or the Al film in different specific situations. Electron-beam lithography is the primary tool to pattern the desired region for material deposition or etching. The chip is covered by an e-beam resist, e.g. PMMA as a positive resist, and is exposed to focused electron beam based on a pattern designed with AutoCAD. This is performed in a Raith EBPG 5000 or 5200, with the focused beam spot size adjustable in different situations. In the process of development, we use a developer to remove the resist exposed to e-beam (in the situation of a positive resist) thus form the desired pattern. We use a mixture of MIBK and IPA with the ratio 1:3 to develop PMMA. Then we may perform desired processing, such as metal deposition, etching with the resist as mask (not involved in our experiments) or dielectric deposition.

To form transparent ohmic contacts to the nanowire, the native oxide layer on the surface of the nanowire need to be removed before depositing metal or superconductor. It has been shown by our group that an ammonium polysulfide solution is sufficient to remove the native oxide and passivate the surface to prevent oxidation before depositing the contacts. This process is named sulfur passivation and is able to produce highly transparent ohmic contact [74], but only suitable for bare InSb nanowires without epitaxial superconductor. We use Ar ion milling or Ar plasma etching to remove the native oxide. The effect of these milling processes are similar on the nanowires, but can have different rates because they are performed in different machines. The effect of milling is shown in Fig. 3.3. Panel a shows a SEM image of a epitaxial Al-InSb nanowire before processing, while panel b shows a milled nanowire (inclucing a PMMA mask). A zoom-in in the inset shows that droplets are formed on the surface of the nanowire, which are indium droplets. We think the In droplets enables a transparent contact between the nanowire and the deposited material. These In droplets can even protect the nanowire from re-oxidation and allows a short exposure to air if transferring between instruments is needed. Ar ion milling and Ar plasma etching need to be performed intermittently to prevent overheating of the chip, otherwise heating accelerates the diffusion between InSb and Al, and turn the PMMA resist into a state not soluble by acetone. Further, any heating process should be avoided as much as possible throughout the entire fabrication flow to prevent the diffusion between InSb and Al, e.g. the PMMA resist should not be baked as a normal fabrication flow would allow, but should be pumped in vacuum to volatilize the anisole solvent before lithography instead.

We use evaporated Cr/Au for normal contacts and Ti/Au for top gates (10 nm Cr or Ti as a sticking layer for the adhesion of Au to the substrate), and use sputtered Si_xN_y as dielectric. Finally, the remaining PMMA is removed in a lift-off process using acetone, therefore, the deposited material only remain in the patterned regions by the e-beam

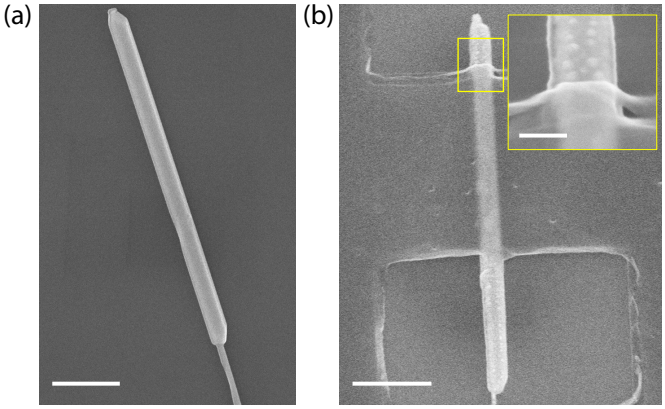

Figure 3.3: **Ar milling on InSb nanowire.** **(a)** SEM image of an epitaxial InSb-Al nanowire, transferred on a Si/SiO_2 substrate. Scale bar is 500 nm. **(b)** SEM image of the InSb-Al nanowire after Ar milling. PMMA mask is also shown. Scale bar is 500 nm. Inset: a zoom-in of the yellow region. Indium droplets are present. Scale bar is 100 nm.

lithography.

If a chemical etching process is needed to remove e.g. the Al film, it may be performed directly with the patterned PMMA as the etch mask, or using the sputtered dielectric layer as the hard mask. Selective etch of Al on SAG InSb nanowires will be discussed in Section 3.3.

To provide a visualized illustration of the fabrication processes, Fig. 3.4 shows.. The device shown in Fig. 3.4(a) is a N-nanowire-S device on which the Al is patterned with selective etch. A cross-section of the device is shown in Fig. 3.4(b). The high resolution image in Fig. 3.4(d) shows the stack of InSb-Al-Si_xN_y, and the Si_xN_y includes the mask for Al etch and the dielectric layer before depositing the top gates. We notice that the cross-section of the super contact (left side, yellow, high resolution in Fig. 3.4(c)) and the normal contact (right side, yellow, high resolution in Fig. 3.4(e)) are different. Under the normal contact, a large portion of the InSb nanowire has been removed during the Ar milling process before depositing Cr/Au, forming an oxygen-free contact interface. However, the AlO_x layer on top of Al is clearly visible in Fig. 3.4(c) under the Cr/Au, indicating that the Ar milling process is not sufficient to remove the native oxide on the Al surface. But we conclude that a sufficient super contact forms on the facet not covered by Al (schematically shown in Fig. 3.2(c)).

3.3. SELECTIVE ETCH OF AL ON SAG INSB NANOWIRES[1]

The fabrication of hybrid devices comprising an Al layer arranged on an InAs semiconductor nanowire has been reported (e.g. Ref. [41]). But we are mostly interested in devices based on InSb nanowires which has high electron mobility, strong spin-orbit coupling and a large Landé g-factor. On the SAG InSb nanowires reported in Ref. [75], the Al

[1] This section is part of the patent application filed as, *Method for selectively etching a metal component*, **Di Xu** and Hao Zhang, PCT/EP2020/087828, European Patent Office, 23 Dec 2020.

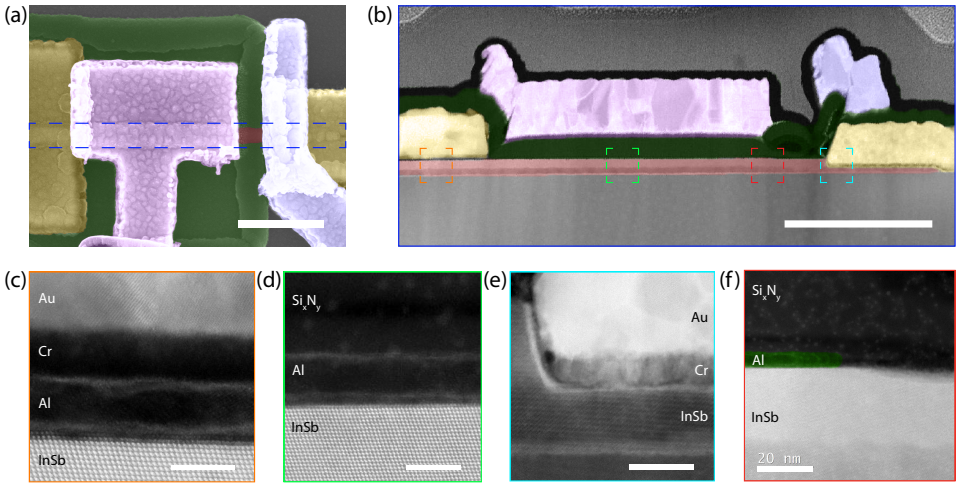

Figure 3.4: **Cross-section TEM of a SAG device.** **(a)** SEM image of a normal-nanowire-superconductor (N-nanowire-S) device. The InSb nanowire (red) is covered by an Al layer (green, covered by the etch mask). Contacts are Cr/Au (yellow). The tunnel- (blue) and super-gates are Ti/Au, deposited on top and separated from the wire by a Si_xN_y dielectric layer. Scale bar is 500 nm. The area indicated with blue dashed lines shows where the TEM specimen is made. **(b)** Cross-section transmission electron microscopy (TEM) image of the device. The structures have the same colors as those of the corresponding structures in (a), except for the Si_xN_y dielectric colored in green together with Al. Scale bar is 500 nm. **(c)** High resolution TEM image of the orange region in (b), showing the structure of the super contact. Note that the Cr/Au can contact the nanowire from the facet not covered by Al even though the AlO_x layer on top of Al is not sufficiently removed by a milling process. Scale bar is 5 nm. **(d)** STEM image of the green region in (b), showing the structure of the InSb-Al-Si_xN_y dielectric stack. Scale bar is 5 nm. **(e)** High resolution STEM image of the cyan region in (b), showing the structure of the normal contact. Note that the milling process before depositing Cr/Au has etched into the InSb sufficiently to form an oxygen-free contact interface. Scale bar is 20 nm. **(f)** High resolution STEM image of the red region in (b), showing the edge of Al (green) formed by chemical etching. The edge of Al is well defined after the chemical etch using TMAH, while the InSb surface that is exposed to the etchant is slightly degraded. Scale bar is 20 nm. Partly used in Fig. 6.18.

layer is grown over the entire surface of the chip. In order to form a usable device, areas of InSb which are not covered by Al is needed, for example to create junctions. There is therefore a need for a method for selectively patterning the Al. The ability to remove Al selectively would also be useful to allow different devices fabricated on the same chip to be electrically separated to avoid short circuits.

When fabricating a hybrid InSb-Al device on a SAG chip, we found that the etching of Al in the presence of InSb is particularly challenging. Good selectivity is desired so that the Al is able to be removed without excessively damaging the semiconductor, and high resolution is desired so that a small creeping distance underneath the mask is able to be well controlled. As we will describe in Section 3.3.1, various existing etching recipes were trialed and found to be unsatisfactory, in that they had inadequate resolution and, in some instances, destroyed the semiconductor nanowires.

It has been found that by using a hard mask (in our case Si_xN_y) in combination with a basic etchant (in our case tetramethyl ammonium hydroxide (TMAH)) Al can be etched in the presense of InSb and the like with good resolution and without destroying the

semiconductor. The metal layer may also be any metal which is compatible with the etchant solution, i.e. alkali-etchable metal (as listed in Ref. [76]). And the hard mask may comprise any hard mask material which will not react with the etchant solution and will adhere to the metal. In particular, Si_xN_y and SiO_x have been proven to function similarly. The Si_xN_y hard mask is patterned using electron beam lithography and lift-off and is deposited with a sputtering technique. The thickness of the Si_xN_y hard mask is in the range of 15 to 25 nm, optionally about 20 nm.

The etchant solution should be a basic etchant solution. The etchant solution may comprise, as an active component, a strong base. Examples of strong bases include alkali metal hydroxides such as NaOH and KOH; alkaline earth metal hydroxides such as $Ba(OH)_2$; and quaternary ammonium hydroxides such as TMAH investigated in our experiments. It has surprisingly been found that the use of a basic etchant solution allows metal such as Al to be etched in the presence of InSb, without excess damage to the InSb. Using a basic etchant in combination with a hard mask further allows for high-resolution etching to be achieved. It has been found that the etchant creeps under the mask only to a small extent, and that the shape of the edge of the remaining Al corresponds well to the shape of the edge of the mask.

The etchant solution is typically an aqueous solution. The concentration of TMAH is not particularly limited and may be selected as appropriate. In our fabrication we often used a TMAH concentration of 25 % by weight. Further experiments were performed using MF321 as the etchant solution, a more dilute solution having a TMAH concentration of about 1.91 % by weight and similar results were obtained. Thus we infer that the TMAH concentration may be in the range 0.2 M (1.91 wt % MF321) to 3 M (25 wt % TMAH).

The reaction time for the etch may be selected as appropriate depending, for example, the concentration of the etchant, the thickness of the metal film to be etched. Typical reaction times are in the range 40 seconds to 5 minutes. Another way to determine the reaction time used in implementations with Al is that the Al needs to remain in contact with the etchant until the silvery color of the Al visibly fades plus about 30 seconds, before terminating the etch.

The etching is performed at the room temperature in the cleanroom, namely 20±2°C. By performing the etch at or below room temperature, diffusion of Al into InSb and/or damage to InSb by the etchant may be reduced. The etchant solution is typically agitated during the etch. The agitation may comprise manual agitation or the use of a magnetic stirrer.

The etching needs to be terminated by rinsing. Rinsing removes residual etchant from the surface of the chip, thereby improving resolution since any residual etchant may continue to etch the metal film and exacerbate creeping under the mask. Examples of solvents useful for rinsing are water and/or isopropanol. Rapid rinsing allows for improved resolution, for example, the chip may be rinsed in a first rinsing bath for about 5 seconds. Multiple sequential rinsing steps are performed, usually three sequential rinsing baths. The solvent in each rinsing bath may be independently selected.

Fig. 3.5 shows two examples of etched devices using this method. The examples show InSb nanowires (network), confirming that the InSb was not removed by the etchant. The dark region corresponds to the Si_xN_y hard mask. As is typical for sputtered thin

films, the hard mask has a bright, rolled edge. The creeping distance, corresponding to the distance from the visible edge of the Al (visible in panel a and indicated by the green false-color in panel b) under the mask to the edge of the mask, is shown by the orange arrows. The creeping distance was only about 100 nm, demonstrating an improvement in resolution, while comparative examples are shown in the next section. Further, the shape of the edge of the Al conformed well to the shape of the edge of the mask, showing that the etch was well-controlled.

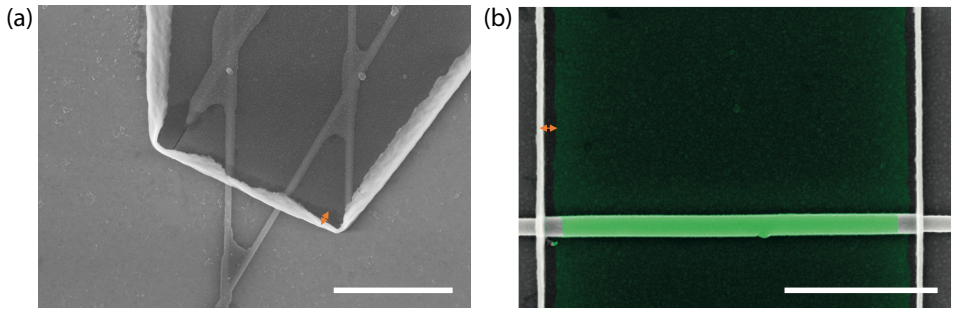

Figure 3.5: **Selective etch of Al on SAG InSb nanowire networks. (a)** An InSb nanowire network covered by a Si_xN_y hard mask (dark region). The hard mask has a bright, rolled edge. Creeping is indicated with the orange arrow. Scale bar is 1 µm. **(b)** An InSb nanowire covered by a Si_xN_y hard mask, whose bright, rolled edge can be seen on two sides. Al is false-colored in green for a clear illustration of the creeping (orange arrow). Scale bar is 1 µm.

Furthermore, Fig. 3.4(f) shows a TEM micrograph of the region where the edge of Al after etching is located, taken through a cross-section of the nanowire (Fig. 3.4(b)). Slight degradation to the exposed surface of the InSb nanowire was observed. The damage did not extend beyond a depth of about 5 nm. We think this is an acceptable degree of damage, and is comparable to the level of damage caused when etching Al on InAs using Transene-D.

The devices used in chapters 6 and 7 are synthesized using this etching method.

3.3.1. COMPARATIVE EXAMPLES

Fig. 3.6 shows several comparative examples involving various combinations of masks and etchants, during our finding of a selective etching recipe for SAG InSb-Al.

Firstly we tried to perform the etching using a buffered solution of hydrogen fluoride as the etchant, which is a commercially available acidic etchant for Al [41, 77]. Buffered HF gave very poor resolution, with a high rate of creep under the mask. Then we considered Transene-D as a natural solution for the Al etching, since Transene-D has been reported to give good yields and resolution in InAs-Al systems [78]. Transene-D is a commercially available acidic etchant which comprises an aqueous solution of phosphoric acid, sodium m-nitrobenzene sulfonate and acetic acid. PMMA was used as a soft polymer mask with the openings defined using e-beam lithography. The etch was performed at a temperature of 48.1°C and the reaction time was 14 seconds. Fig. 3.6(a) shows that the InSb nanowire network was etched away, leaving voids of the SAG growth mask. Further, the edges of the etched region have badly defined, rough edges indicative of uncon-

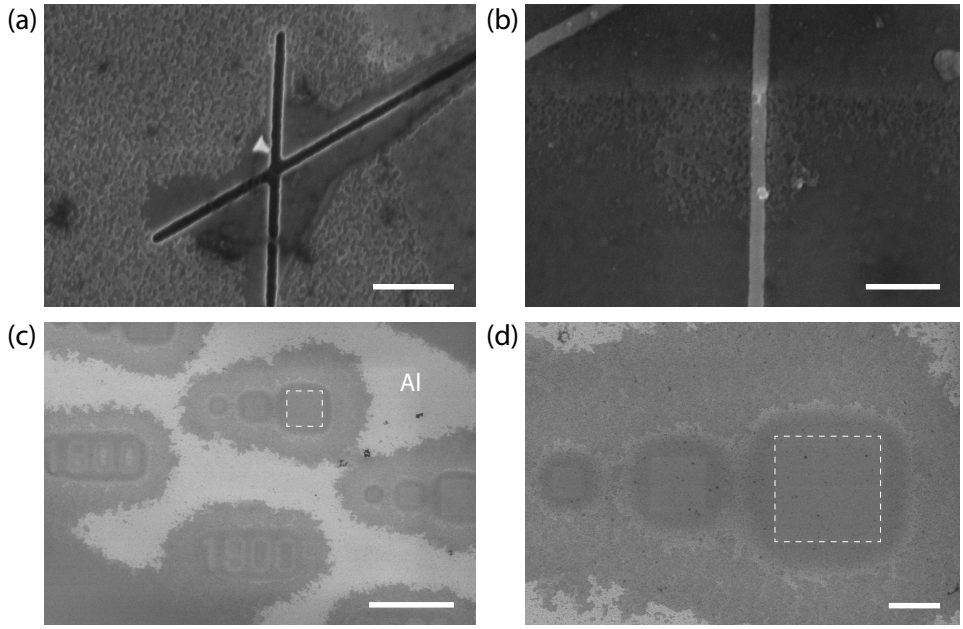

Figure 3.6: **Comparative examples of other combinations of masks and etchants.** **(a)** Transene-D as the etchant with PMMA mask. The nanowire network is etched away, leaving voids of the SAG growth mask. Scale bar is 300 nm. **(b)** MF321 as the etchant with PMMA mask. The edges of the Al are uneven and poorly defined. Scale bar is 200 nm. **(c)** 25 % TMAH aqueous solution as etchant with PMMA mask. White dashed lines show the location of one of the etch windows defined by the mask. A creeping distance of the order of several microns is observed. The edges of the Al have a poorly defined, irregular shape. Scale bar is 5 µm. **(d)** Zoom-in of (c). Scale bar is 1 µm.

trolled creeping of the etchant under the mask.

In the next example, PMMA was still used as the etch mask and MF321 was used as the basic etchant solution. The etch was performed at room temperature and the reaction time was 150 seconds. As illustrated in Fig. 3.6(b), unlike the acidic etchant e.g. Transene-D, MF321 did not remove the InSb nanowire. However, uncontrolled creeping of the etchant under the mask was observed. The extent of the creep was of the order of a few microns. The edges of the Al were uneven and poorly defined.

Having the thought that the reaction time needs to be shortened to reduce the creeping distance by using an etchant with higher concentration, we tested the 25 % TMAH aqueous solution while still using PMMA as the mask. Micrographs of this test are shown in Fig. 3.6(c) and (d). The location of one of the etch windows defined by the mask is shown by dashed lines. Dark regions of the micrographs correspond to regions where Al was removed. Bright regions correspond to regions covered by Al. As can be seen, similar to the previous example, a creeping distance of the order of several microns was observed. The edges of the Al again had a poorly defined, irregular shape. These findings demonstrate that adjusting the concentration of the etchant and the reaction time did not solve the problem of creeping.

3.4. ELECTRICAL MEASUREMENT SET-UP

The electrical measurements presented in this thesis are two-terminal voltage-bias measurements, namely two leads from the device mounted in a dilution refrigerator are connected to the measurement set-up at room temperature. As illustrated in Fig. 3.2, a voltage is applied to the device and the current is measured through the set-up. We use the "IVVI rack" developed by Raymond Schouten and DEMO here in QuTech [79]. The IVVI rack allows the measurement modules to be isolated from noise sources in the power grid since it is powered by batteries and using optical communication.

During the preparation of Chapter 4 in 2020, we conducted a re-calibration of the measurement set-up used in 2016 – 2018. Section 4.4.2 together with Refs. [80] and [81] provides an extensive description of the electrical measurement set-up and it is thus no longer reiterated in this chapter.

4

LARGE ZERO-BIAS PEAKS IN INSB-AL HYBRID SEMICONDUCTOR-SUPERCONDUCTOR NANOWIRE DEVICES

We report electron transport studies on InSb-Al hybrid semiconductor-superconductor nanowire devices. Tunnelling spectroscopy is used to measure the evolution of subgap states while varying magnetic field and voltages applied to various nearby gates. At magnetic fields between 0.7 T and 0.9 T the differential conductance contains large zero bias peaks (ZBPs) whose height reaches values of order $2e^2/h$. We investigate these ZBPs for large ranges of gate voltages in different devices. We discuss possible interpretations in terms of Andreev bound states and Majorana zero modes. [1]

[1] This work has been published as, *Large zero bias peaks in InSb-Al hybrid semiconductor-superconductor nanowire devices*, H. Zhang*, M. W. A. de Moor*, J. D. S. Bommer*, **D. Xu**, G. Wang, N. van Loo, C.-X. Liu, S. Gazibegovic, J. A. Logan, D. Car, R. L. M. Op het Veld, P. J. van Veldhoven, S. Koelling, M. A. Verheijen, M. Pendharkar, D. J. Pennachio, B. Shojaei, J. S. Lee, C. J. Palmstrøm, E. P. A. M. Bakkers, S. Das Sarma, L. P. Kouwenhoven. *arXiv preprint* arXiv:2101.11456 (2021).

* These authors contributed equally to this work.

4.1. INTRODUCTION

Tunnelling spectroscopy in electrical transport is an important tool to measure the presence of states at energies smaller than the gap of bulk superconductors. Such subgap states exist, for instance, near magnetic impurities, inside vortices and at interfaces with other materials [53, 82**?**]. In hybrid combinations of a superconductor with a semiconductor, subgap states can have properties from both materials such as the particle-hole symmetry from the superconductor and the spin-related properties from the semiconductor. In confined regions, this leads to a variety of subgap states generally known as Andreev bound states (ABS) [53, 82**?**]. A magnetic field B lifts the spin degeneracy of the ABS, turning them into non-degenerate, single-fermionic states. Tunnelling spectroscopy allows to measure the energy evolution as a function of B, enabling to identify the underlying quantum properties of individual ABS.

Recent interest has focussed on the possibility to induce a topological phase in a hybrid of a superconductor with a one-dimensional semiconducting nanowire [10, 13, 14, 18]. A bulk-boundary correspondence dictates that the topological phase in the bulk comes together with localized boundary states at zero energy. These states are 'half-fermionic' with the two halves spatially separated at the two ends of the nanowire. Each half, if the two are sufficiently far from each other, is called a Majorana Zero Mode (MZM) and interestingly obeys non-Abelian statistics [83]. In the past decade there has been much theoretical and experimental interest to identify and study MZMs, with tunnelling spectroscopy as the primary tool [23–27, 36, 37].

The difficulty is, however, that interfaces, edges and nanowire-ends are often locations where subgap states arise from all kinds of non-topological origins, including electrostatic accumulation, disorder, and smoothly varying potentials. The challenge is to distinguish MZMs from these other types of localized states. Such a distinction may come from some of the peculiar signatures of MZMs, most prominently the requirement of zero energy independent of parameter values like B or a gate voltage, V_g, that tunes the electron density. In tunnelling spectroscopy this shows up as a zero-bias peak (ZBP), which is called a "robust ZBP" when it remains at zero voltage-bias while varying B or V_g over significant ranges. The topological MZM interpretation also requires this ZBP to be quantized (at zero temperature) at a constant value of $2e^2/h$ with variations in systems parameters, i.e., the ZBP should be robust both in sticking to zero voltage and having a quantized value of $2e^2/h$ as magnetic field and various gate voltages are varied [84–86]. Such robust quantized ZBPs have not yet been observed experimentally. Note that finite temperature, finite tunnelling amplitude, finite wire length, dissipation and disorder could all affect the height of a ZBP [18, 53].

A robust ZBP is, however, only a necessary property of topological MZMs but not sufficient to serve as an unambiguous proof of its existence. Numerical studies have shown that various shapes of electrostatic potentials near the end of a wire can also induce states at zero energy, without the need of a topological phase in the bulk of the nanowire [50, 51, 87]. Such states are denoted as 'trivial' (as opposed to 'topological') and are part of the ABS family. Since an ABS is a single-fermionic state and a MZM is half-fermionic, this gives rise to a distinguishing feature. Assuming zero temperature, then in the generic ABS case the height of the ZBP can reach a maximum value of $4e^2/h$ while for a MZM the ZBP cannot go above half that value, $2e^2/h$ [35, 85, 86].

Numerical studies have also shown that trivial end-states (ABS) can be remarkably fixed to zero energy over extended regions in B and V_g [87]. These zero-energy trivial states can be mathematically decomposed into two half-fermionic states. The difference with MZMs is that in this case, there is no topological phase in the bulk and the two half-fermionic states have strongly overlapping wavefunctions localized near the same wire-end. Depending on parameter values such as temperature and tunnel coupling to the spectroscopy lead, each half-fermionic state can contribute to the height of the ZBP by an amount between 0 and $2e^2/h$, and thus together yield a ZBP height between 0 and $4e^2/h$.

In fact, more detailed numerical studies [52, 77, 88] have shown that for parameter values relevant for the existing devices, one half-fermionic state of the ABS may occasionally couple much stronger to the lead than the other. At zero temperature the maximum contribution of just one half-fermionic state results in a ZBP height of $2e^2/h$, and without detailed knowledge of the system, it is indistinguishable from the signature of a MZM. This seriously complicates the desired, unambiguous distinction between an ABS and a MZM because they both may lead to an apparent ZBP height at $2e^2/h$ for the tunnelling conductance from one end.

The two half-fermionic states created from the decomposition of a trivial ABS have been denoted as 'partially separated ABS' (ps-ABS) to indicate some spatial separation of the two corresponding wavefunctions but only over a partial distance of the full wire length [88]. Alternatively, they have been called 'quasi-Majoranas' emphasizing that, despite the absence of a topological phase, these spatially-overlapping states are self-adjoint and individually obey non-Abelian statistics [52], even though they are not isolated.

An additional complication is that in the presence of a magnetic field, disorder can also induce states at energies smaller than the superconducting gap, including at zero energy [47]. These disorder-induced states may lead to ZBPs with conductance values anywhere between 0 and $4e^2/h$, and thus including $2e^2/h$. Disorder-induced ZBPs have a different dependence to variations in magnetic field and gate voltages [54, 55], but it may require microscopic knowledge of the device for a clear distinction. Thus, ZBPs could arise from topological MZM, ps-ABS (or equivalently quasi-MZM) localized near the ends, or from disorder and are therefore by themselves insufficient to distinguish experimentally the different scenarios. We, moreover, note that each of these scenarios is expected to occur in very small parameter ranges. To find experimental proof for any of these scenarios requires a detailed search including fine tuning of parameters.

The majority of experimental papers [23–27, 36, 37] have reported ZBP heights much lower than $2e^2/h$, predominantly due to finite temperature and other broadening effects such as dissipation [89]. Tunnelling spectroscopy on nanowires defined in a two-dimensional electron gas have shown ZBP heights near $2e^2/h$ [39]. We have previously reported tunnelling spectroscopy on InSb nanowires covered by Al, indicating ZBP heights with values close to $2e^2/h$ despite varying B and V_g parameters [15]. We reported this as an observation of conductance quantization serving as evidence for Majorana states [15]. After several issues were brought to our attention, we re-examined the data set as well as the technical details of our experimental setup. During this process, discrepancies with the original publication arose which led us to conclude that we can no longer claim a

robust quantization, leading to a full retraction of the publication in Ref. [15].

In this manuscript we report the re-analysed data of Ref. [15], together with previously unpublished data from the same set of measurements. We first describe the experiments and present the data. At the end of this manuscript, we discuss the implications in the context of the various signatures for disorder-induced subgap states, ABS, and MZM.

Our work, presented here, along with the recent theoretical developments involving quasi-Majoranas and disorder, should serve as a strong cautionary message for all Majorana experiments in all platforms, clearly emphasizing that the experimental observations of zero-bias conductance peaks, no matter how compelling, should be considered only as necessary and by no means sufficient conditions for the existence of topological MZMs.

4.2. EXPERIMENT

Fig. 4.1 shows a scanning electron micrograph of device A. An InSb nanowire is covered by a thin superconducting Al shell. The nanowire is contacted by normal metal contacts, which are used to apply a bias voltage V and drain a current I to ground. The 'tunnel gates' are used to control the transmission through the uncovered segment between the left electrical contact and the wire section covered with the Al shell. A voltage V_{TG} is applied to both tunnel gates simultaneously. The electron density in the nanowire segment covered by Al can be tuned by applying a voltage V_{SG} to both of the 'super gates'. The doped substrate can be used as a global backgate. Unless otherwise noted, the backgate is grounded, i.e. $V_{\mathrm{BG}} = 0$.

The device is mounted in a dilution refrigerator with a base temperature of about 20 mK, and a three-axis vector magnet which is used to align a magnetic field B along the nanowire axis. We measure the differential conductance, $\mathrm{d}I/\mathrm{d}V$, through the device by applying a small ac excitation voltage and measuring the resulting current response using a lock-in amplifier. An extensive description of the measurement circuit is provided in Appendix 4.4.2.

In Fig. 4.2 we show the differential conductance, $\mathrm{d}I/\mathrm{d}V$, versus V and B for different values of V_{TG} with V_{SG} fixed. At $B = 0$, we resolve the coherence peaks of the superconducting gap at $V = \pm 0.21$ mV (see also green curve in panel (e)). As B increases, two levels detach from the gap edge and cross at zero bias, forming a ZBP. This is illustrated by the orange line cut in Fig. 4.2(e), showing a ZBP which reaches a value of $2e^2/h$ at 0.8 T. The evolution of the zero-bias conductance versus B for different values of V_{TG} is shown in Fig. 4.2(d). While for $V_{\mathrm{TG}} = -7.74$ mV the ZBP reaches a maximum height close to $2e^2/h$, this maximum can be decreased (blue curve) or increased (black curve) by changing V_{TG}. We also note that the dependence on V_{TG} is non-monotonic, which will be further investigated in the next section. Due to uncertainties in some of the parameters of our setup, as well as the calibration procedure detailed in Appendix 4.4.2, the conductance we extract has a typical error margin of a few percent. We illustrate the effect of this in Fig. 4.2(f) by zooming in on the section indicated by the dashed rectangle in Fig. 4.2(d). The extracted conductance is shown as a coloured line, with the error margin shown as a dark (1σ) and light (2σ) shading in the same colour. While a value of $2e^2/h$ for the maximum conductance is consistent with the error margin for $V_{\mathrm{TG}} = -7.74$ mV, it is outside

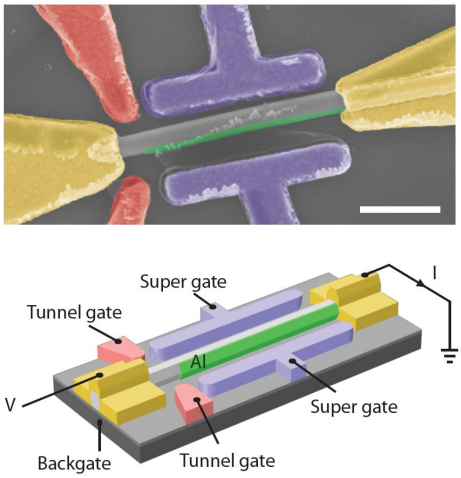

Figure 4.1: False color scanning electron micrograph of device A (upper panel) and its schematics (lower panel). An InSb nanowire (grey) is covered on two of its six facets by a thin superconducting Al shell (green) with a thickness of approximately 10 nm. Side gates and contacts are Cr/Au (10 nm/100 nm). The substrate is p-doped Si, which can be used as a global backgate, covered by 285 nm SiO_2. The two tunnel gates (red) are shorted externally, as are the two super gates (purple). A bias voltage V is applied to the contact (yellow) on the left and a current I is drained from the contact on the right. Scale bar is 500 nm.

the 2σ-margin for $V_{TG} = -7.8,\ -7.92\,\text{mV}$.

Next, we fix $B = 0.8\,\text{T}$ and investigate the evolution of the peak height as a function of V_{TG}, shown in Fig. 4.3(a). The ZBP is present between $V_{TG} = -7.95\,\text{V}$ and $V_{TG} = -7.5\,\text{V}$, while for more negative values the peak splits away from zero energy. Near $V_{TG} = -7.6\,\text{V}$, there may be a sign of peak splitting. We also observe sudden changes in conductance which are likely due to charge rearrangements in the electrostatic environment of the nanowire. These instabilities, referred to as "charge jumps", are commonly observed in our devices. This is most likely due to the constraints placed on the fabrication process by the limited thermal budget [42], as too high temperatures will lead to intermixing between InSb and Al. This restricts our fabrication to room temperature processes which is not sufficient to remove all resist residues (visible in Fig. 4.1) and these can serve as charge traps. While some charge jumps occur stochastically and do not repeat upon remeasuring the same parameter range, other are reproducible. Charge jumps and hysteresis can lead to variation in the measured conductance values at nominally equal parameter settings (measurement history is specified in Appendix 4.4.6). Additional discussion on charge jumps is provided in Appendix 4.4.4.

In some cases, a charge jump seems to reset the electrostatic potential on the tunnel gate, causing conductance features to repeat after the jump. This is, for instance, visible in Fig. 4.3(a) at $V_{TG} = -7.97\,\text{V}$ (indicated by the white arrow, see also Appendix 4.4.4). Such charge jumps make the relation between tunnel barrier height and V_{TG} non-monotonic. We can, however, compare the height of the ZBP to the out-of-gap conductance to investigate the effect of the tunnel barrier height on the ZBP.

In the range $V_{TG} = -7.93\,\text{V}$ to $-7.6\,\text{V}$ (a significant charge jump occurred at $-7.6\,\text{V}$),

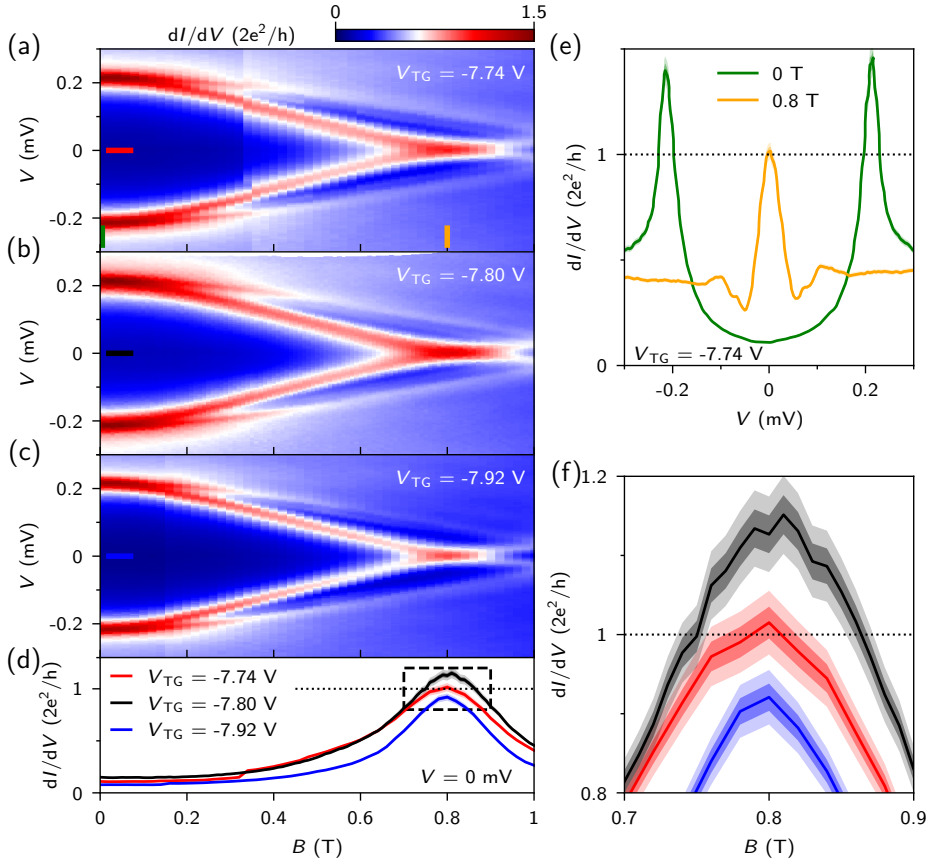

Figure 4.2: (**a**-**c**) $\mathrm{d}I/\mathrm{d}V$ versus V and B at three different settings of V_{TG}. B is aligned with the nanowire axis for all measurements. $V_{\mathrm{SG}} = -6.5\,\mathrm{V}$, $V_{\mathrm{BG}} = 0$. Fridge base temperature is ~20 mK for all measurements unless specified. (**d**) Horizontal linecuts at $V = 0\,\mathrm{mV}$ for panels a-c. (**e**) Vertical linecuts from panel a, at $B = 0\,\mathrm{T}$ (green) and $0.8\,\mathrm{T}$ (orange). (**f**) Close-up of the data in panel d, indicated by the dashed rectangle. Darker shading indicates the 1σ standard error in the conductance measurement, while the lighter shade indicates the 2σ error. Data was obtained from device A.

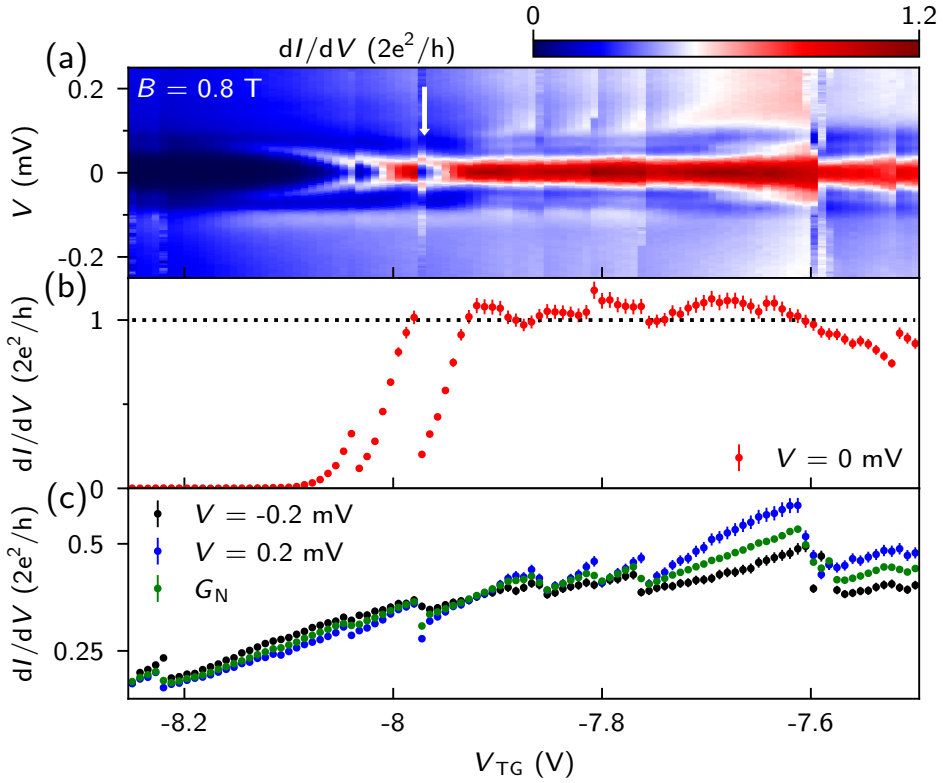

Figure 4.3: (**a**) $\mathrm{d}I/\mathrm{d}V$ versus V_{TG} at $B = 0.8\,\mathrm{T}$, $V_{\mathrm{SG}} = -6.5\,\mathrm{V}$, $V_{\mathrm{BG}} = 0$. White arrow indicates a charge jump with a particularly large effect on the conductance. (**b**) Horizontal linecut from (a) at $V = 0\,\mathrm{mV}$, showing the height of the ZBP remains roughly constant over a range in V_{TG}. (**c**) Horizontal linecuts at finite bias, $\pm 0.2\,\mathrm{mV}$ (black, blue), showing the out-of-gap conductance increasing over the same range in gate voltage. We further characterize the out-of-gap conductance by taking the average value for $|V| \geqslant 0.2\,\mathrm{mV}$, which we label G_{N} (green). Error bars are given at 2σ for clarity. Data was obtained from device A.

the zero-bias conductance fluctuates near $2e^2/h$, with a mean of 1.05 and a standard deviation of 0.05 in the unit of $2e^2/h$. (Fig. 4.3b). We consider this to be an example of "plateau-like" behaviour (see also Appendix 4.4.5). In the same range, the out-of-gap conductance increases significantly, as shown in panel (c) by the line traces taken at $|V| = -0.2\,\mathrm{mV}$ (black) and $|V| = 0.2\,\mathrm{mV}$ (blue). We take the average conductance for $|V| \geqslant 0.2\,\mathrm{mV}$, G_N (shown in green in Fig. 4.3(c)), as a proxy for the transmission to the lead. While the relative fluctuation in the ZBP height is 5%, G_N increases by almost 40% over the same range, and generally increases with gate voltage. This indicates that ZBP-height does not simply scale with the transmission coupling to the lead.

We investigate this further in Fig. 4.4. In panel (a) we show linecuts taken from Fig. 4.3(a), where we have indicated the linecuts with a ZBP height close to $2e^2/h$ in red. We use a Lorentzian function, thermally broadened by 20 mK, to fit the peaks and extract their height and width (see Appendix 4.4.7 for details). Examples of these fits are shown in Fig. 4.4(c)-(e), together with the calculated G_N. This allows to plot the peak height and width as a function of G_N in Fig. 4.4(b). The peak widths increase with G_N and are larger than 50 μeV, indicating that the peak is mainly broadened by the coupling to the lead and not by temperature ($3.5k_\mathrm{B}T = 15\,\mu\mathrm{eV}$ assuming an effective electron temperature of 50 mK). At the same time, there is no straightforward dependency of the peak height on G_N. Note that a small peak splitting may occur at high G_N.

We note that the measurements shown in Figs. 4.3 and 4.4 were selected after fine-tuning parameters in a dedicated search for quantized plateaus (see Appendix 4.4.5 for a discussion of our measurement methodology). We will discuss this dedicated search more in the discussion section.

The plateau behavior of the ZBP is striking but not convincingly present for all B and V_SG values where ZBPs are present. This can be seen in Fig. 4.5, which shows a scan like Fig. 4.3, but at a lower B-field of 0.7 T. Again, a ZBP is present over a sizeable V_TG range, but in this case the peak height deviates from $2e^2/h$ with the maximum ZBP-height reaching $\sim 1.5 \times 2e^2/h$. The variation in the ZBP height is also significantly larger than the G_N variation (Fig. 4.5c), different from the behaviour at 0.8 T in Fig. 4.3 (see Appendix 4.4.5 for quantified plateau criteria). Due to charge jumps and other instabilities, the effective potential can drift over time or change irreversibly after a large voltage swing. When returning to the same gate settings, the electrostatic potential is not necessarily the same. Fig. 4.2 was measured between 36 to 48 hours before Fig. 4.3 which was measured 30 hours before Fig. 4.5. A detailed timeline of the various data sets used in this manuscript can be found in Appendix 4.4.6.

So far, we have discussed the behaviour at a fixed value of V_SG, which sets the electron density in the nanowire. We now turn our attention to the dependence of the ZBP on this gate parameter. Due to the cross-capacitance between the super and tunnel gates, changing V_SG not only changes the density, but also the transmission of the junction. Although the reverse also takes place while changing V_TG, the influence of V_SG affects the entire narrow tunnel junction while the cross-coupling effect of V_TG is confined to only the superconducting segment immediately next to the junction. Therefore, to compensate for the more significant cross-coupling of V_SG, we simultaneously adjust V_TG to keep G_N approximately constant. In Figs. 4.6(a) and 4.6(b) we plot the conductance as a function of V at 0.8 and 0.9 T, respectively, along the trajectory in V_SG-V_TG space indicated by

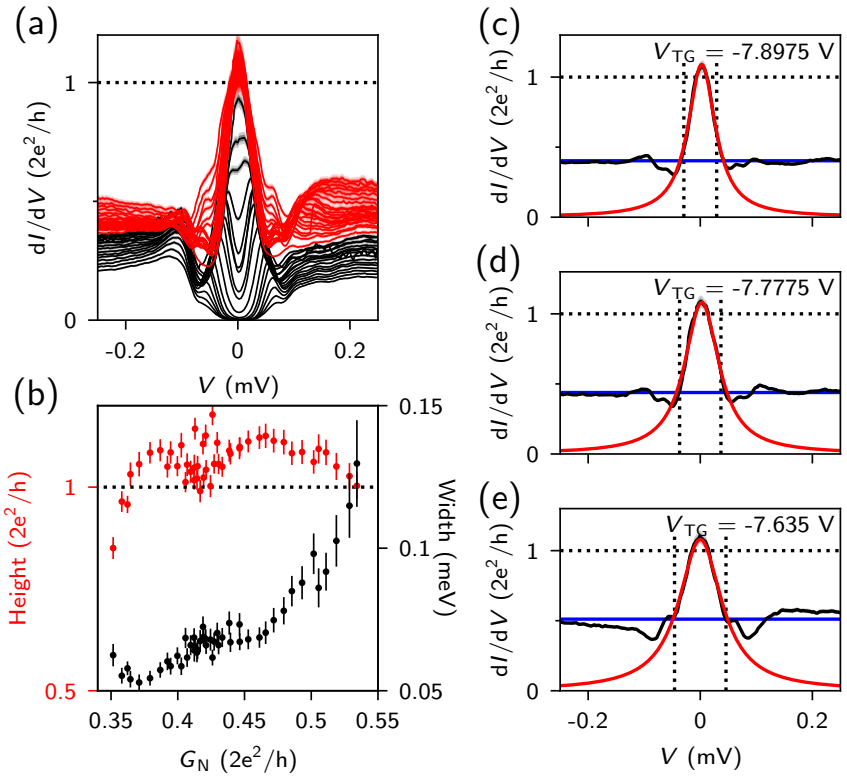

Figure 4.4: (**a**) dI/dV versus V traces corresponding to linecuts in Fig. 4.3(a), showing the ZBP curves for V_{TG} ranging from -7.9275 V to -7.6125 V (red curves, ZBP height $> 0.95 \times 2e^2/h$). Due to peak splitting, the ZBP height drops lower for more negative V_{TG} (black curves). To avoid crowding, every other linecut is plotted. (**b**) ZBP height (red circles) and ZBP width (black circles) extracted from all linecuts of Fig. 4.3(a) for -7.9275 V $< V_{\mathrm{TG}} <$ -7.61 V, as a function of above-gap conductance (G_{N}). The ZBP height and width are determined by fitting a Lorentzian shape to the data, several examples of which are shown in panels (**c**-**e**) (red lines). The blue lines indicate the extracted value of G_{N} for the same gate voltage. Error bars in panel (b) are given at 2σ.

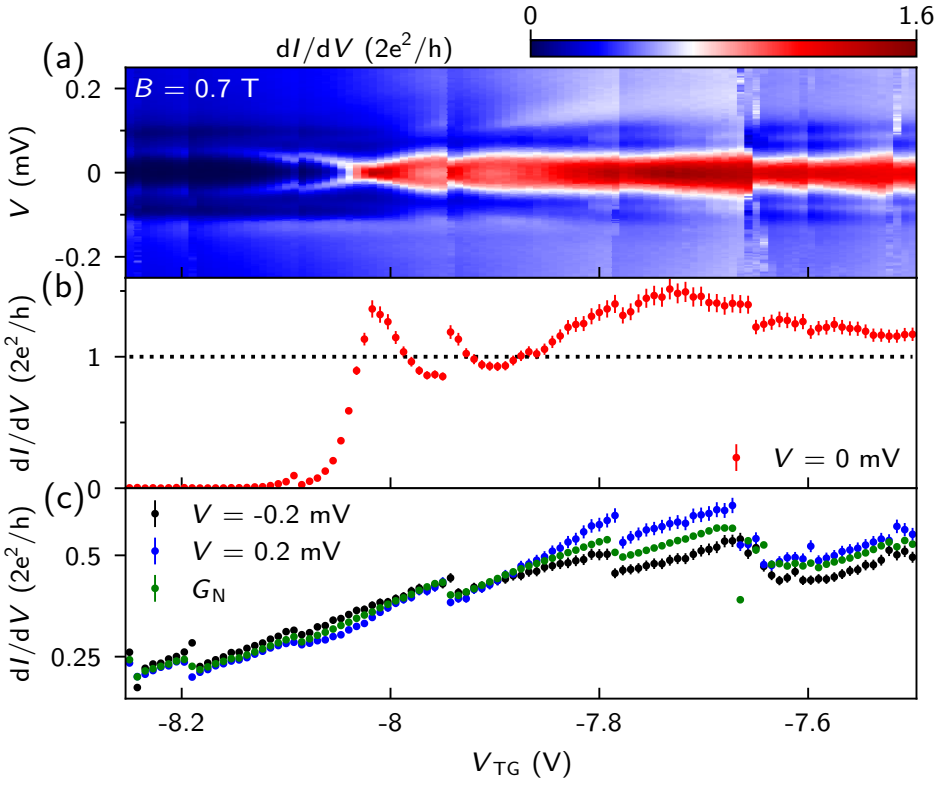

Figure 4.5: (**a**) $\mathrm{d}I/\mathrm{d}V$ versus V_{TG} at $B = 0.7\,\mathrm{T}$, $V_{\mathrm{SG}} = -6.5\,\mathrm{V}$, $V_{\mathrm{BG}} = 0$. (**b**-**c**) Horizontal linecuts from (a), showing ZBP height and above-gap conductance, respectively. The ZBP height exceeds $2e^2/h$ considerably at this field value. Data was obtained from device A.

the dashed line in Fig. 4.6c. For both values of B, the ZBP persists over a sizable range in V_{SG}. At 0.8 T, the peak height first fluctuates around $2e^2/h$ with an amplitude of about $0.2 \times 2e^2/h$ (see also the line cuts in panel (d), left column). The decreasing conductance at $V = 0$ for $V_{SG} > -5.1$ V can mostly be attributed to the finite splitting of the ZBP. Similar splitting behaviour is observed at 0.9 T (see also the line cuts in panel (d), right column).

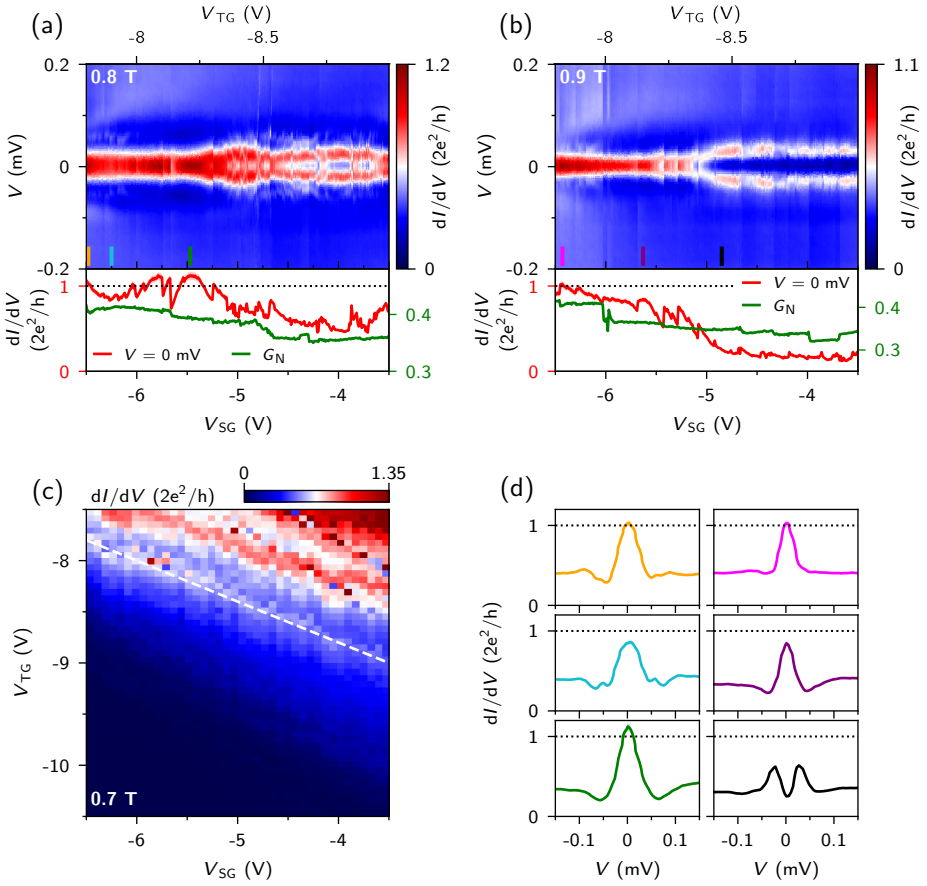

Figure 4.6: (**a**-**b**) dI/dV versus V_{SG} at $B = 0.8$ T and 0.9 T, respectively. Lower panels show the ZBP height (red curve) and G_N (average conductance for $|V| \geq 0.2$ mV, green curve), with the (almost invisible) shaded region representing the error bar. V_{TG} is adjusted while sweeping V_{SG}, as shown on the top axis, to keep the above-gap conductance roughly constant. (**c**) Conductance at $V = -0.5$ mV as a function of V_{TG} and V_{SG} at 0.7 T. The gate voltage scans in panels a and b follow the white dashed line. (**d**) Several vertical linecuts from panes a and b showing ZBPs and split peaks at gate voltages and magnetic fields indicated by the correspondingly colored bars. Data was obtained from device A.

A similar scan at $B = 0.7$ T is plotted in Fig. 4.7(a). A ZBP is present for most of the measured range, but with a height which significantly exceeds $2e^2/h$ (see also the line

cuts in panel (d), left column). The number of charge jumps is also notably increased, causing G_N to fluctuate and vary more strongly than in the previous figure. These instabilities make it difficult to get a consistent data set, which is demonstrated by the fact that the conductance at $V_{SG} = -6$V and $B = 0.7$T measured 16 hours later is lower by about $0.4 \times 2e^2/h$ (Fig. 4.7(b)).

Several detailed features can be observed inside the gap at finite energy, which appear to be interacting with the ZBP. In Fig. 4.7(c) we zoom in on the dashed rectangle in panel (a), showing an irregular behaviour of the ZBP with the peak height around $2e^2/h$ when the peak is at $V = 0$ but dropping below this value when the peak is split (see also the line cuts in panel (d), right column). We speculate that this ZBP behaviour is due to several subgap states in the junction region [90].

We observe similar behaviour in device B, of which a scanning electron micrograph is shown in Fig. 4.8(a). This device is more stable, with less frequent charge jumps. The length of the proximitized section in this device is 0.9µm, which is 0.3µm shorter than in device A. Due to non-ideal device fabrication, the lower tunnel-gate was shorted to the left contact and thus kept at the potential of this lead during measurements. The upper tunnel-gate was shorted to the global back-gate and thus the same voltage was applied to both simultaneously. In Fig. 4.8(b) we plot the conductance as a function of V and B, showing a ZBP with a maximum height slightly exceeding $2e^2/h$ at 0.83 T. In Figs. 4.8(c) and 4.8(d) we show the dependence on V_{SG} and $V_{TG,BG}$, respectively, giving very similar results. The ZBP is present for a sizable gate range for both scans. In addition, both gates tune G_N significantly, indicating a substantial capacitive coupling to the junction. The green dashed lines illustrate the region where G_N is increasing while the ZBP height remains roughly constant, indicating a plateau-like behaviour. In this measurement, the peak height starts to increase further when the gate voltage is changed to more positive values. In a scenario with quasi-Majoranas, this increase could be due to an increased coupling to the second, more remote state [52]. Alternatively, in a scenario with MZMs this could indicate the opening of a second sub-band in the junction.

In Figs. 4.3, 4.4 and 4.8 we zoomed in on ZBPs taken at particular settings where the peak height has a tendency to stick to $2e^2/h$. We emphasize that, for different parameter settings, we can find ZBPs which have no tendency at all to stick to $2e^2/h$. As an example, we show a data set taken on device C in Fig. 4.9. The B dependence (Fig. 4.9a) looks similar to the ones shown for devices A and B, with a ZBP-height close to $2e^2/h$ at 0.74 T. The ZBP persists over a sizable range in V_{BG} (Fig. 9d). We also observe ZBPs for lower B-fields when V_{BG} is changed (Fig. 4.9b). The ZBP-height increases monotonically in this case, and the value $2e^2/h$ does not appear to have a particular significance. The peak shape can be fitted with a Lorentzian line shape of varying height (Fig. 4.9f), with the peak height and width sharing a markedly different relation from the one shown in Fig. 4.4, see Appendix 4.4.7. When V_{TG} is changed, we also see that this peak is highly unstable, only appearing at $V = 0$ for very specific values (Fig. 4.9c). This type of level-crossing is similar to the typical Andreev bound state peaks reported in literature [48]. While we show these different types of behaviours in different devices, we expect that all of these behaviours could be measured in a single device if the parameter space is exhaustively searched. We note that the behaviour shown in Fig. 4.5 may be an intermediate case between a monotonically increasing peak height and the formation of a

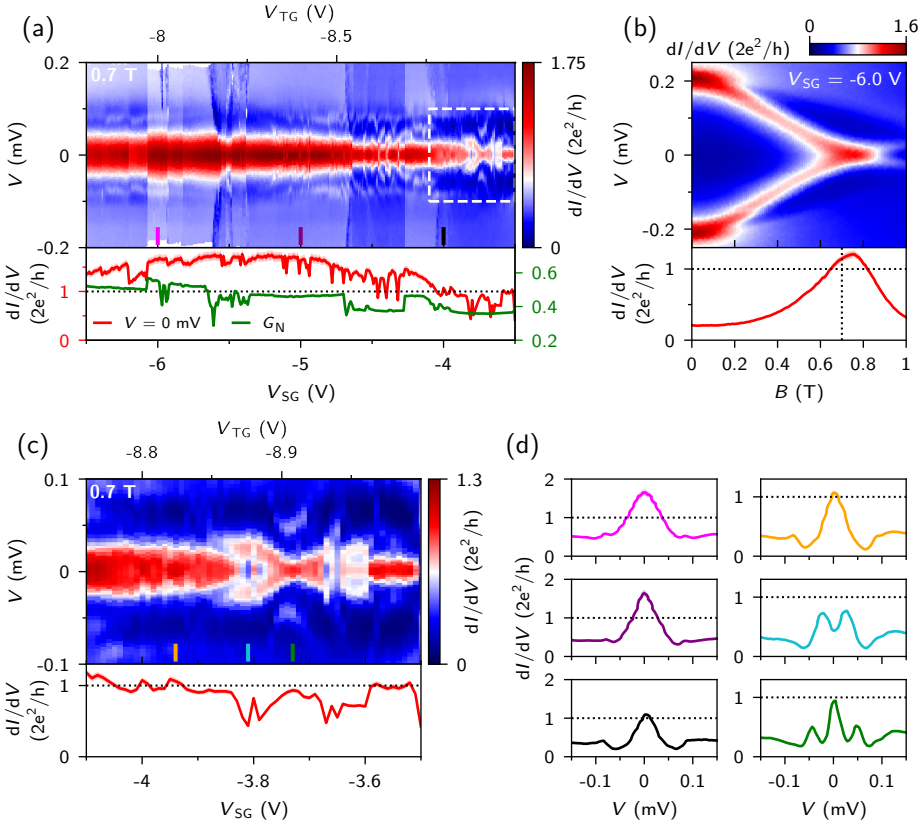

Figure 4.7: (**a**) $\mathrm{d}I/\mathrm{d}V$ versus V_{SG} at $B = 0.7\,\mathrm{T}$, with V_{TG} compensation following the white dashed line in Fig. 6c. Lower panel shows the ZBP height (red curve) and G_N (average conductance for $|V| \geqslant 0.18\,\mathrm{mV}$, green curve), respectively. The ZBP height significantly exceeds $2e^2/h$, consistent with the peak height measured in Fig. 4.5. (**b**) Top panel shows B dependence of a ZBP whose height significantly exceeds $2e^2/h$, at $V_{SG} = -6.0\,\mathrm{V}$, $V_{TG} = -8.0\,\mathrm{V}$. Bottom panel shows horizontal linecuts at $V = 0\,\mathrm{mV}$, showing the B dependence of ZBP height. (**c**) Zoom-in of the white dashed rectangle in panel a, where the peak height is close to $2e^2/h$. The ZBP in this gate range shows oscillatory (peak vs split peak) behavior. (**d**) Several vertical linecuts from a-c at gate voltages indicated by the correspondingly-colored bars. Data was obtained from device A.

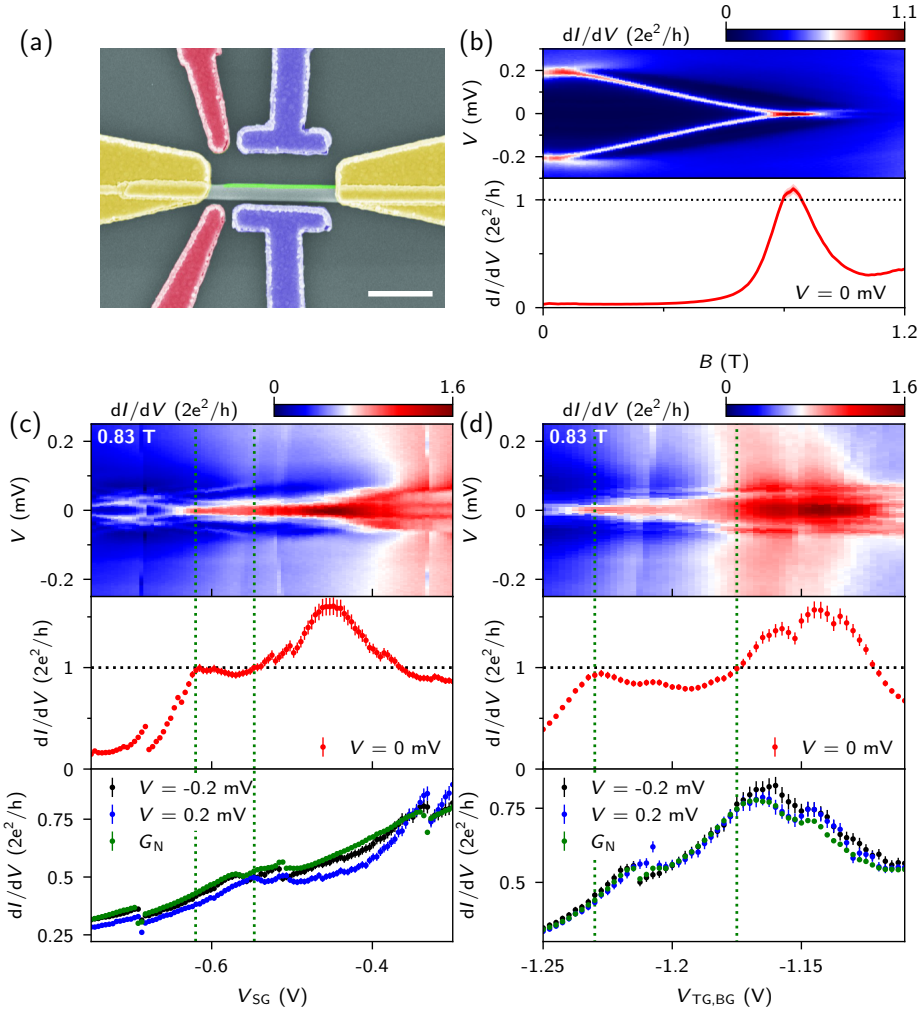

Figure 4.8: (**a**) False color scanning electron micrograph of device B. In this device, the lower tunnel gate is shorted to the left lead and thus follows its potential during the measurement. The upper tunnel gate is shorted to the backgate, and thus follows the potential of the backgate, $V_{TG} = V_{BG}$. Scale bar is 500 nm. (**b**) dI/dV vs V and B. Bottom panel shows the horizontal linecut at $V = 0$ mV, showing behavior similar to device A with the maximum of the peak height slightly exceeding $2e^2/h$. (**c**) dI/dV versus V_{SG} at 0.83 T. The two lower panels are the horizontal linecuts at $V = 0$ mV (red line), and ± 0.2 mV (blue and black lines), as well as the average normal state conductance G_N. The two dashed green lines indicate a plateau region of the zero-bias conductance. $V_{TG,BG} = -1.23$ V. (**d**) dI/dV vs $V_{TG,BG}$ at 0.83 T. The two lower panels show the zero-bias and normal state conductance, similar to panel c. The two dashed green lines indicate the plateau region of the zero-bias conductance. $V_{SG} = -0.615$ V. Error bars are given at the 2σ level. Data was obtained from device B.

plateau-like peak height.

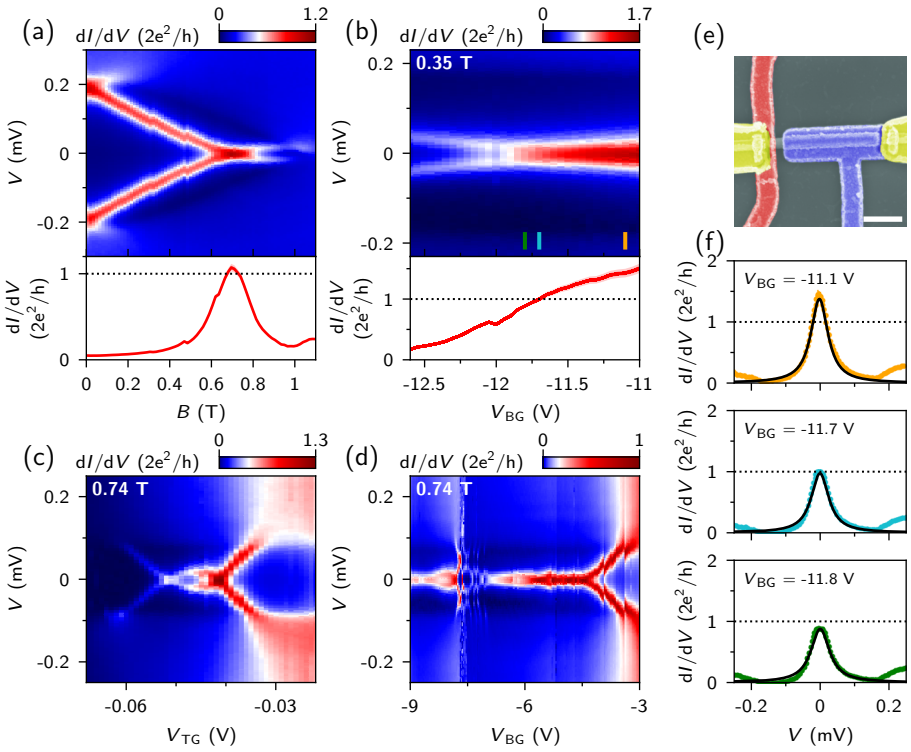

Figure 4.9: (**a**) dI/dV versus V and B. Bottom panel shows the horizontal linecut at $V = 0$ mV. $V_{BG} = -5.58$ V, $V_{TG} = -0.045$ V, $V_{SG} = 0.045$ VVSG = 0.045 V. (**b**) dI/dV versus V and V_{BG} (with more negative gate voltage values compared to (a)) at a lower field of 0.35 T. $V_{TG} = -0.01$ V, $V_{SG} = 0$ V. The lower panel shows a zero-bias linecut where the ZBP height monotonically increases and crosses $2e^2/h$ without any particular feature. (**c**) dI/dV versus V and V_{TG} at 0.74 T, showing the peak as a result of a level crossing. $V_{BG} = -5.58$ V, $V_{SG} = 0$ V. (**d**) dI/dV versus V and V_{BG} at 0.74 T, showing the peak remains unsplit over a sizable gate voltage range with the presence of several charge jumps. $V_{TG} = -0.03$ V, VSG = 0 V. (**e**) False color scanning electron micrograph of device C. The top gates, separated from the nanowire by 30 nm thick SiN dielectric, serve as the tunnel gate (red) and super gate (purple). Scale bar is 500 nm. (**f**) Vertical linecuts from panel b, at the gate voltages indicated by the colored lines. Lorentzian fits are shown in black. Error bars are given at the 2σ level. Data was obtained from device C.

4.3. DISCUSSION

Between the early reports on ZBPs in 2012, improvements in materials and fabrication [37, 41, 72, 91, 92] have yielded much cleaner tunneling spectroscopy results. The induced gap has become 'hard' in the sense that no subgap states are visible at 0 T [42, 91]. Andreev enhancement in QPCs has indicated interface transparencies exceeding 0.95 [92]. In these cleaner devices, the ZBPs reach heights of order $2e^2/h$ relative to a low background conductance [39, 93, 94]. These observations strongly suggest that in clean de-

vices tunnel spectroscopy can resolve individual quantum states. Moreover, unintentional (Coulomb blockaded) quantum dots can be excluded [37, 92], which if hybridized with a superconductor, can also give rise to anomalies at zero bias [48].

Other forms of unintentional potentials, that could result in ZBPs, cannot easily be dismissed. One of us reported simulations assuming a random disorder potential (without Coulomb blockade) that resemble our experimental results [55]. Pan and Das Sarma dubbed this regime as the ugly one in the sequence "good, bad and ugly" ZBPs arising, respectively, from topological MZMs, quasi-MZMs, and disorder. Our experiments cannot exclude the ugly regime of random disorder. We do note that open questions remain. For instance, our ZBPs are very persistent in gate voltage, whereas random disorder may result in mesoscopic fluctuations in both peak height and splitting [47]. The scale in disorder, gate voltage, or chemical potential, for the occurrence of mesoscopic fluctuations is presently unknown, and whether disorder should induce mesoscopic fluctuations in these systems for the experimental parameter values is a relevant open question.

The 'bad regime' in Pan and Das Sarma is characterized by a smooth potential inducing quasi-Majorana (or ps-ABS) states in a magnetic field. In principle, quasi-Majoranas develop into topological MZMs when further increasing magnetic field. Signatures of such a transition, such as a closing and re-opening of the induced gap, have not yet been reported in the literature. Note that when the bulk Al gap closes before a topological transition occurs, then the quasi-Majoranas cannot transform to topological MZMs.

Numerical simulations show that quasi-Majoranas stick to zero energy over strikingly large ranges in the parameter space of (B, V_{TG}, V_{SG}) [52, 77, 88]. It is fairly easy to find parameter values for a smooth potential to simulate our experimental results with a high degree of resemblance, including the presence of plateau regions near $2e^2/h$. However, with fine tuning one can also generate plateau regions near $2e^2/h$ in the ugly regime [55]. This makes it hard to distinguish the ugly from the bad regime as long as we do not know our device parameters in sufficient detail. Tunnelling spectroscopy by itself thus appears to be unable to distinguish between disorder and quasi-MZMs as the origin of the observed ZBPs.

The "good regime" in Pan and Das Sarma contains a topological phase in the bulk and MZMs at the two opposite ends of the one-dimensional system. An experimental demonstration of this topological phase requires simultaneous spectroscopy on both the ends as well as the bulk. Preliminary results have been reported in a multi-probe device [95–97] but has the complication of possible unintentional potentials at each probe. A non-local scheme in a three-terminal geometry has been proposed [98] that would allow bulk and end spectroscopy for the same parameter settings.

In conclusion, we have reported large ZBPs with heights on the order of $2e^2/h$. Robust ZBPs sticking to zero energy has been reported earlier [23–27, 36, 37]. These studies, however, all reported limited peak heights, an order of magnitude less than $2e^2/h$. ZBPs with a height of order $2e^2/h$ were first reported from devices based on InAs 2DEGs [39]. Our large ZBPs are measured on InSb nanowires partially covered with Al. We frequently observe ZBPs with heights of order $2e^2/h$. In two devices we have found evidence for plateau behaviour where the peak height remains close to $2e^2/h$ while changing gate voltages over ranges where the normal conductance changes significantly. We note, however, that these plateaus are the result of a dedicated search motivated by proposals

that such plateau behaviour would be indicative for MZMs [35, 85, 86]. Although, for a local spectroscopy experiment, we cannot think of another method, such a dedicated search has the potential to lead to confirmation bias and effectively yield false-positive evidence for MZMs. New numerical studies have shown that disorder-induced states and local, quasi-Majoranas can also yield plateau behaviour. Our data sets, nor any other data set reported in the literature that we know of, can make a distinction between the different possible origins dubbed as the "good, bad and ugly" in Ref. [55] since it would require knowledge of the microscopic potential landscape in the device. Our local measurements should be complemented with non-local conductance in order to be able to claim a correlation between a gap in the bulk of the nanowire while measuring ZBPs at the two ends [98].

4.4. APPENDICES

4.4.1. ADDITIONAL DEVICES

Over 60 devices were fabricated and tested over the course of the project. Out of these, we selected 11 devices, which showed good transport characteristics and had functional electrostatic gates, for extensive measurements. Although most of these devices show ZBPs after fine tuning gate voltages and magnetic field, some even with peak heights close to $2e^2/h$, only 2 devices (Device A and B) show behavior consistent with a plateau in the ZBP height in a specific parameter range. The other devices show behavior similar to what is shown in Fig. 4.9 (data taken from device C). Scanning electron micrographs of devices A, B and C are shown in Fig. 4.1, Fig. 4.8a and Fig. 4.9e, respectively. In Fig. 4.10 we show the scanning electron micrographs and device schematics of the other 8 devices.

Devices 1 and 2 are side-gated devices, similar in design to devices A and B. Device 3 is covered by 30 nm of SiN dielectric and has a local tunnel gate as well as a global backgate separated from the nanowire by 20 nm thick LPCVD Si_3N_4. For all other devices, the global backgate is covered by 285 nm of SiO_2. Devices 4 and 5 have a similar design to device C, with a tunnel gate and super gate on top, separated from the nanowire by 30 nm of SiN dielectric. Devices 6 to 8 have two layers of gates and dielectric. The nanowire is first covered by 30 nm of SiN and the local tunnel gate, which are subsequently covered by another layer of 30 nm SiN and the super gate.

Since this work was first conducted, several works have been published investigating the role of device geometry and gate design on the topological phase diagram through Schrödinger-Poisson simulations, see e.g. ref [99, 100]. The device geometry can also play a role in generating Andreev bound states due to potential inhomogeneities, see e.g. ref [53, 87].

4.4.2. MEASUREMENT CIRCUIT AND CONDUCTANCE CALCULATION

The experiments described in this work consist of two-terminal voltage-biased conductance measurements. A schematic representation of the measurement circuit is shown in Fig. 4.11. The device is mounted onto a PCB with integrated RC filters (orange dashed box). This PCB is mounted to the mixing chamber plate of a dilution refrigerator, with additional RC filters (blue dashed box). In addition to the RC filters, pi filters and copper

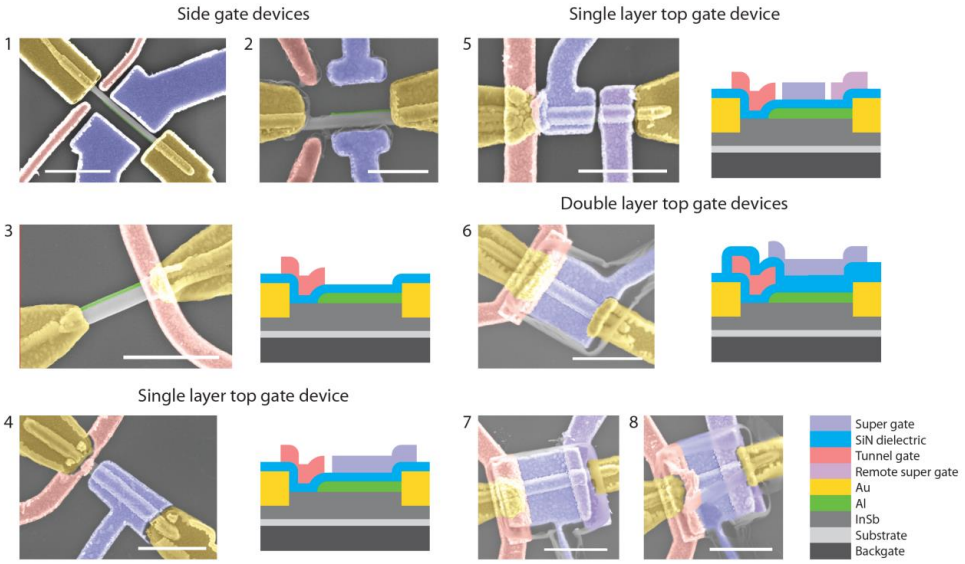

Figure 4.10: Scanning electron micrographs and design schematics of 8 additional devices studied during this project. The scale bar is 1 µm for all panels except for device 2, where it is 500 nm.

powder filters are installed to filter high frequency noise. We apply both a DC and AC voltage to the sample through an in-house built S3b voltage amplifier [101]. The resulting current is amplified by an in-house built M1b current-to-voltage converter [102]. The DC component of the voltage output of the current-to-voltage converter is measured with a Keithley 2000 multimeter, while the AC component, consisting of an in-phase (X) and quadrature (Y) signal, is detected using an SR830 lock-in amplifier.

Because of the additional series resistances in the circuit, the actual voltage across the device, V, is less than the applied voltage V_{dc}:

$$V = V_{\mathrm{dc}} - I_{\mathrm{dc}} R_{\mathrm{series}} \tag{4.1}$$

where R_{series} is the sum of the filter resistances in the circuit, as well as the input impedance of the current-to-voltage converter and the output impedance of the voltage source. We have independently calibrated this series resistance. This resistance also needs to be accounted for when calculating the differential conductance, $\mathrm{d}I/\mathrm{d}V$, giving

$$\frac{\mathrm{d}I}{\mathrm{d}V} = \frac{I_{\mathrm{ac}}}{V_{\mathrm{ac}} - I_{\mathrm{ac}} R_{\mathrm{series}}} \tag{4.2}$$

As we are interested in the response in the dc limit, ideally one would take only the in-phase component of the ac current, $I_{\mathrm{ac}} = I_{\mathrm{X,ac}}$, to calculate the differential conductance. However, due to the limited bandwidth of the current-to-voltage converter, a phase shift is introduced which means the quadrature component $I_{\mathrm{Y,ac}}$ cannot be neglected. Additionally, the gain of the converter is reduced, resulting in an underestimation of the total AC current. Due to additional reactive elements in the circuit, such as the RC-filters,

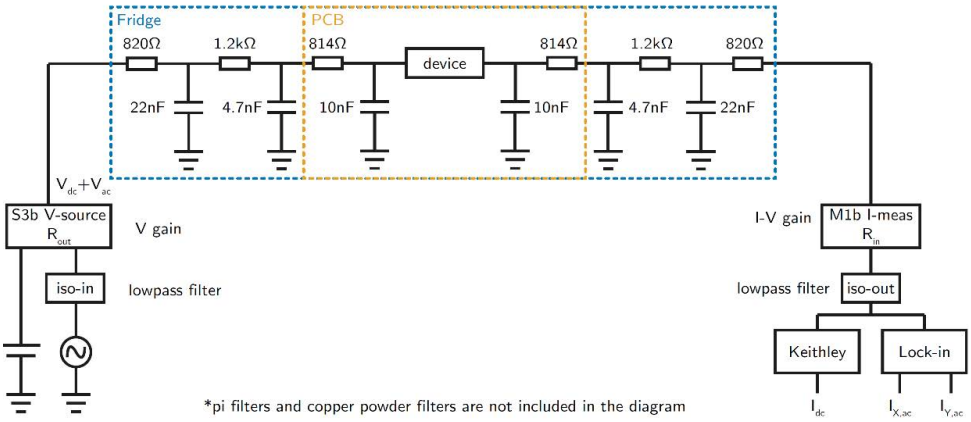

Figure 4.11: Schematic representation of the measurement circuit. Note that each fridge line includes additional pi filters and copper powder filters which are not shown (cutoff frequencies >10 MHz and negligible resistance).

the amount by which the current is underestimated also depends on the device conductance, making it very complicated to extract this quantity directly from the measured signals. To remedy these effects, we have used a bootstrapping method to calibrate the measured ac conductance to the numerical derivative of the dc signal. This method is explained in detail in ref. [80] with access via the online data repository [**?**]. For additional information regarding the measurement of differential conductance using a lock-in amplifier, see ref. [81]. The uncertainties introduced by this procedure, as well as the uncertainties in the independently measured values of the series resistance in the circuit and the gain of the current-to-voltage converter, have been included in the error bars for the presented conductance data.

4.4.3. DISCUSSION ON CONTACT RESISTANCE

As discussed in Appendix 4.4.2, because we conduct our experiments in the two-terminal configuration, we need to account for additional series resistances in the circuit when calculating the conductance through our devices. The resistances in the measurement circuit are known, but it is possible that there is an additional barrier at the interface between the metal leads and the semiconductor nanowire, generally called “contact resistance”. Depending on the materials and fabrication procedures used, this interface can go from a highly-resistive Schottky-type contact, to a moderately transparent Ohmic contact, to fully transparent. As long as the applied bias voltage is small, it is generally assumed that the contact resistance is independent of the voltage, i.e., Ohmic. While ideally one would use a four terminal configuration to circumvent this problem, the nanowires used in this work are too short to allow for four independent contacts, which means that at best a quasi-four terminal configuration can be used where a single contact on the wire is split into two separate lines on the PCB. While this eliminates the

effect of the known series resistances in the circuit, it leaves the contact resistance undetermined.

A typical method to estimate the contact resistance is by matching the conductance plateaus in a quantum point contact (QPC) to their quantized values. However, this requires at least two plateaus to be present. Alternatively, in an Andreev QPC the role of the second plateau can be taken by the enhanced conductance at $V = 0$. For a single channel Andreev QPC with a transmission T, these two quantities are related by the Beenakker formula [29] (assuming $\mu \gg \Delta$ [103])

$$G(V = 0) = G_S = \frac{2e^2}{h} \frac{2T^2}{(2-T)^2} \tag{4.3}$$

As T can be deduced from the value of the conductance plateau outside the superconducting gap, in principle one could use this formula to determine the series resistance as a fitting parameter. As an alternative approach, one can use the DC signal and the size of the superconducting gap as an independent estimate. The measured superconducting gap is not expected to change with V_{TG}. If, however, the wrong series resistance is subtracted, the superconducting gap will appear to change with V_{TG} as the bias axis becomes distorted.

In Fig. 4.12 we present an Andreev QPC measured in device C. In panel a, we show the extracted differential conductance before any series resistances in the circuit are accounted for. The edge of the superconducting gap appears to move to higher bias as the gate voltage is increased, because the effective voltage drop over the junction decreases when the device conductance increases. When we correct for the independently calibrated series resistance (for this measurement, $17.152 \pm 0.089\,\mathrm{k\Omega}$), this effect disappears. In Fig. 4.12c, we see that for low transmission the system shows a hard gap (bottom), while on the plateau the conductance is strongly enhanced inside the gap (top). Using the BTK model [33], we can fit the conductance as a function of V to extract the superconducting gap, as well as the transmission T, which is related to the BTK Z parameter via $T = 1/(1+Z)^2$. We plot the extracted transmission in Fig. 4.12d (red dashed line), in addition to the out-of-gap conductance G_N (green) and the conductance at $V = 0$, G_S (purple). The expected conductance G_S based on the extracted transmission and the Beenakker formula is plotted as the blue dashed line. In Fig. 4.12d we plot the values of G_S as a function of the transmission (black dots), showing excellent agreement with the Beenakker formula (red line), demonstrating that this data set can be described accurately by a single ballistic channel connecting a normal and a superconducting reservoir without subtracting a contact resistance. As the transmission on the plateau already closely approaches the value of 1, it is unlikely that a significant additional series resistance remains unaccounted for in the circuit.

Alternatively, using the methods of minimizing the variation of the superconducting gap with V_{TG}, as well as matching the plateau values of the Andreev QPC, we find that an optimal series resistance between 17 and 17.7 kΩ, depending on the specifics of the fitting procedure. Based on these results, as well as results obtained from other devices, we consider it likely that the total contact resistance is in the range of a few hundred Ohms, possibly up to 1 kΩ. We have not corrected for this, as the described procedures contain several assumptions (e.g. whether or not the contact barrier is Ohmic). It should be noted that this means the reported conductance values could be underestimated.

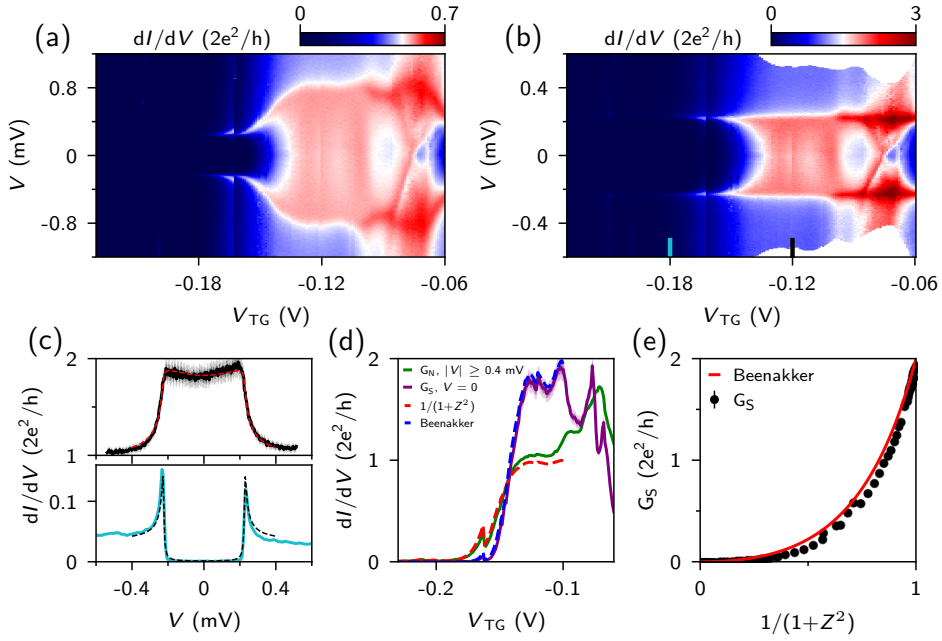

Figure 4.12: Ballistic Andreev transport. (**a**) $\mathrm{d}I/\mathrm{d}V$ versus V and V_{TG} before correcting for a series resistance in the circuit. (**b**) $\mathrm{d}I/\mathrm{d}V$ versus V and V_{TG} after correcting for the known series resistances. (**c**) Line trace at $V_{\mathrm{TG}} = -0.18\,\mathrm{V}$ (bottom) and $V_{\mathrm{TG}} = -0.12\,\mathrm{V}$ (top), showing a hard gap and enhanced conductance due to Andreev transport, respectively. Dashed lines are fits to the BTK model. (**d**) Out-of-gap conductance G_{N} (averaged for $|V| \geqslant 0.4\,\mathrm{mV}$, green) and conductance at $V = 0$, G_{S}. Dashed lines indicate the transmission $1/(1+Z)^2$ as extracted from the BTK fit (red), and the predicted zero-bias conductance from the Beenakker formula (blue). (**e**) G_{S} plotted versus the transmission $1/(1+Z)^2$ (black dots), showing excellent agreement with the Beenakker prediction (red line). Data was obtained from device C.

4.4.4. DISCUSSION ON CHARGE JUMPS

In addition to designed elements such as the metal gates, the electrostatic environment of a mesoscopic device can be affected by the presence of local charge traps. These traps can be located e.g. in the dielectric materials or in residues left over from the fabrication process. As gate voltages are changed during the experiment, these traps can be charged or discharged. When there are many traps present, this will generally result in changing electric fields which are visible in the experiment as effective gate drifts and hysteresis. When a single trap suddenly charges or discharges itself in such a way that the effective gate potential is suddenly shifted, we speak of a "charge jump". These charge jumps can occur stochastically, or in a reproducible fashion where the charging and discharging process is triggered by the application of a specific gate voltage. Such charge rearrangements are well-known properties of semiconductor electronic devices in general, not just the specific devices studied in this work.

In Fig. 4.13, we show an example of a non-reproducible, stochastic charge jump. In panel a, the gate voltage is slowly decreased until $V_{TG} = -0.163$ V, indicated by the white arrow. At this point, a charge jump occurs, which shifts the gate potential by about 0.007 V. When the same measurement is conducted again, the charge jump is no longer present, as shown in Fig. 4.13b. In this panel, we see other features also seen in panel a.

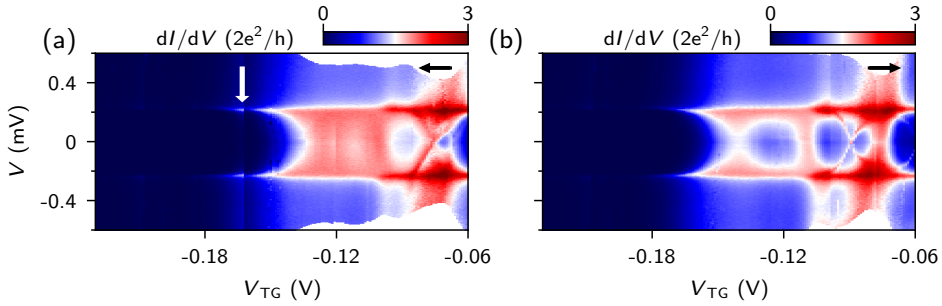

Figure 4.13: (**a**) Same as Fig. 4.12b. The white arrow indicates a charge jump which causes a shift in V_{TG}. (**b**) The same measurement taken consecutively, where the charge jump is now absent. Black arrows indicate the direction in which the gate voltage is changed over the course of the measurement. Data was obtained from device C.

Another difference is the change in Andreev enhancement on the plateau, which is very sensitive to precise details of the gate potential and therefore the most likely feature to be affected by a jump. In general, a charge jump will not exactly correspond to a change in the gate potential, but instead constitute a more complex (and unknown) shift in the local electric field. However, when the measured conductance is almost exactly repeated for every bias voltage, it stands to reason that the particular charge jump in question approximates a shift in the applied gate voltage. We illustrate this situation in Fig. 4.14a. In black, we plot the seven traces at fixed V_{TG} to the left of the charge jump, while in red we plot the seven traces to the right. Every trace to the left of the charge jump is almost identical to one shifted by 0.007 V to the right. We can see this more clearly in Fig. 4.14b, where we have plotted the conductance as a function of V_{TG} for several values

of the bias voltage V (black lines). If we shift these traces by 0.007 V (dashed red lines), we see almost an exact match in the overlapping region. This indicates that this particular charge jump indeed approximates a shift in the applied gate voltage.

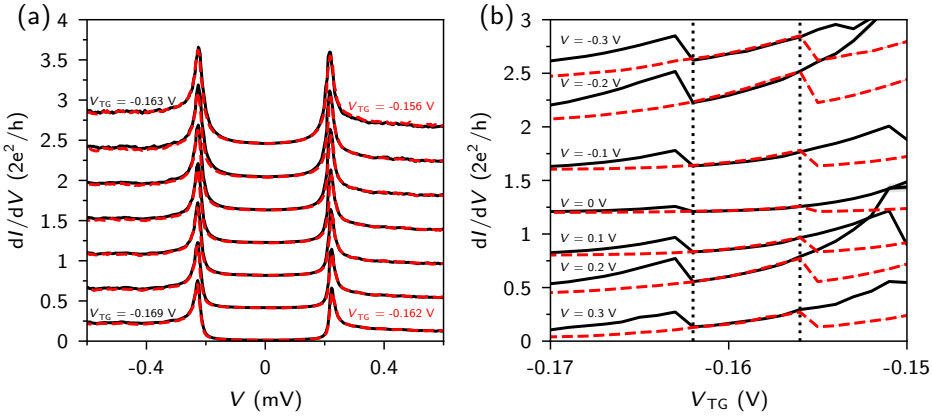

Figure 4.14: (**a**) Line traces at fixed V_{TG} from Fig. 4.13a, showing the data just to the left of the charge jump (black) and to the right (red). Traces are offset by 0.8 e^2/h for clarity. (**b**) Line traces at fixed V from Fig. 4.13a (black), and the same line traces shifted by 0.007 V (red). In the overlapping region (indicated by the vertical dotted lines), the two traces match for every bias voltage.

A similar analysis can be used to show that the charge jump indicated by the white arrow in Fig. 4.3 corresponds to an effective shift in the tunnel gate voltage, shown in Fig. 4.15. In contrast, the jumps in the conductance which can be observed at $V_{\mathrm{TG}} = -7.86$, -7.81, and -7.76 V do not cause the conductance values to repeat, suggesting that these jumps do not correspond to effective shifts in the tunnel gate potential. They could instead be caused by single charged impurities or resonances near the NS-junction. The fact that similar jumps are observed in Fig. 4.5, albeit at slightly different gate voltages, suggests that these are reproducible resonances in a certain part of the parameter space, the energy levels of which can be altered by magnetic field or gate voltage sweeps.

4.4.5. DISCUSSION ON PLATEAU-LIKE FEATURES

Previous studies of zero-bias peaks have mainly focused on the presence of a peak at zero bias voltage. The next step is to consider the height of the peak. If the height of a ZBP remains constant while changing parameters, it is referred to as a "plateau". If the plateau value is close to $2e^2/h$, it is called a "quantized plateau". We emphasize that both a robust ZBP and a stable quantization are signatures of MZMs although not sufficient for an unambiguous proof of their existence.

A plateau is generally considered to be a region of parameter space in which the value of some quantity remains constant to within some acceptable tolerance. In the context of Majorana zero modes, the constant quantity is the height of the zero-bias conductance peak, with the region of parameter space being a subset of the parameter space of the topological phase, with the exact extent depending on additional details such as the relevance of finite size or temperature. Additionally, in the case of a sufficiently long,

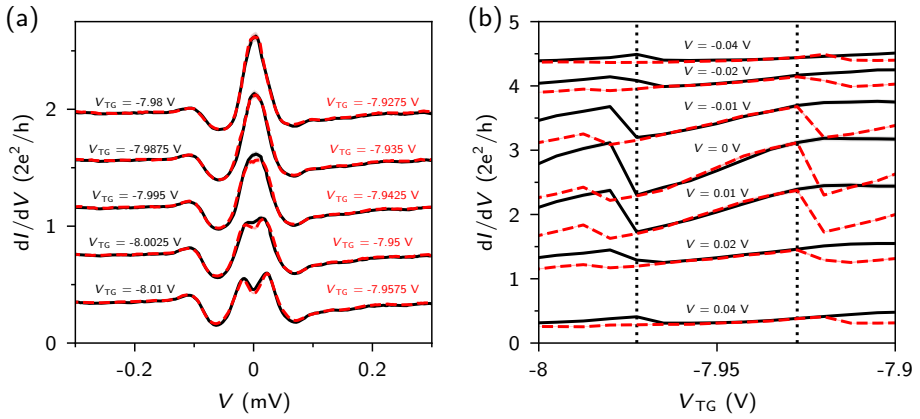

Figure 4.15: (**a**) Line traces at fixed V_{TG} from Fig. 4.3a, showing the data just to the left of the charge jump marked by the white arrow (black) and to the right (red). Traces are offset by 0.8 e^2/h for clarity. (**b**) Line traces at fixed V from Fig. 4.14a (black), and the same line traces shifted by 0.0525 V (red). In the overlapping region (indicated by the vertical dotted lines), the two traces match for every bias voltage.

ideal 1D single subband Majorana wire and for temperatures smaller than the lifetime broadening (i.e. FWHM of ZBP) [104], the value of the conductance plateau should be quantized to the universal value of $2e^2/h$ to within experimental accuracy.

The total parameter space in our experiments is far too large to search exhaustively. It is clear that given the number of experimental tuning parameters, some well-defined protocol must be followed in order to collect enough data in a timely manner to form a conclusion. Therefore, a heuristic has to be developed to guide the search for possible stable zero-bias peaks with a quantized height. In the experiments described in this manuscript, the procedure generally consists of the following steps. First, a fairly coarse search is conducted across gate voltages and magnetic field to locate possible zero-bias peaks. Once a candidate is found, its stability with respect to the control parameters, such as gate voltages and magnetic field, is checked. If a feature is deemed sufficiently stable, we determine whether the peak height approaches the quantized value for some parameter settings. If this is the case, further parameter sweeps are performed in an attempt to establish the extent of the parameter space over which the peak height remains close to $2e^2/h$. It should be noted that the same experimental tuning procedure could in principle be applied to search for plateaus at other conductance values, which would serve as an important cross-check of the assumption that a zero-bias peak with a constant height can only be achieved at $2e^2/h$. In practice, given time constraints, however, this cross-check was not performed systematically for conductance values other than $2e^2/h$.

Based on our experience with this experimental tuning heuristic, we propose a few conditions which, although perhaps not entirely sufficient, seem necessary before a feature can credibly be labeled as a plateau.

The first condition relates to the robustness of the zero-bias peak. The conductance spectroscopy signal must show a peak at zero bias for the entire range of the plateau-like

region. This is in order to ensure that variations in the zero-bias conductance reflect a change in the peak height, rather than e.g. changes in the peak energy splitting while a parameter such as a gate voltage changes.

The second condition regards the stability of the peak height. The fluctuation of the peak height over the plateau-like region must not exceed 5% of the mean value. This 5% limit on the fluctuation allows to account for small variations due to experimental noise.

The third condition concerns the conductance behavior away from zero bias. The average derivative of the above-gap conductance with respect to the control parameter exceeds the average derivative of the zero-bias conductance by at least a factor 3 over the range of the plateau-like region. This to ensure that the peak height remains constant, while the control parameter (V_{TG}) is in fact changing the sample in a meaningful way (by changing the tunnel barrier height). In principle, this should apply simultaneously to all control parameters to some degree, although depending on the theoretical model, the expected stability with respect to e.g. the super gate voltage (i.e. chemical potential) can be much worse than the expected stability with respect to e.g. the tunnel gate voltage (i.e. coupling to the lead). Also, the precise quantitative relationships between the experimental tuning parameters (e.g. super gate voltage and tunnel gate voltage) and the theoretical parameters (e.g. chemical potential and tunneling amplitude) are at best known only qualitatively through numerical simulations since the precise electrostatic boundary conditions applying to the actual sample are never exactly known.

With these conditions in hand, we zoom in on the plateau-like region in Fig. 3, shown in Fig. 4.16. Based on the first condition, we can bound the plateau-like region on the left side at $V_{TG} = -7.93$V. On the right side, we bound the region by the significant charge jump at $V_{TG} = -7.6$V. Taking the average over this range for both the zero-bias conductance and G_N, we can compare the relative changes between the two, as well as the fluctuations. We see that while the zero-bias conductance generally stays within 5% of the average value, G_N changes by almost 40% over the entire range. Additionally, while the zero-bias conductance fluctuates around the average with a small average derivative, G_N follows an increasing trend. We could therefore state that our conditions have been met, and in this respect this feature can be considered as a plateau with reasonable stability.

In contrast, we take another look at the feature present in Fig. 5, with the plateau analysis shown in Fig. 4.17. In this case, we again use the first condition to bound the region on the left at $V_{TG} = -7.88$V, and a charge jump to bound the region on the right at $V_{TG} = -7.67$V. We see that in this case, the zero-bias conductance varies considerably more than 5% of the average value. Additionally, the average derivative of the zero-bias conductance actually exceeds the average derivative of G_N. Based on these considerations this feature does not qualify as a plateau according to our protocol.

The conditions we have set here are somewhat subjective. For example, if one widens or narrows the accepted range of the conductance fluctuations, varies the extent of the tuning parameter range, or demands a larger difference between the derivatives at zero bias and the above-gap conductance, one could reach different conclusions regarding specific data sets. As an example, using the plateau range defined by the vertical dotted green lines in Fig. 4.8c we would conclude that a plateau is present based on the conditions we have set. In Fig. 4.8d, the conductance varies too much to qualify the se-

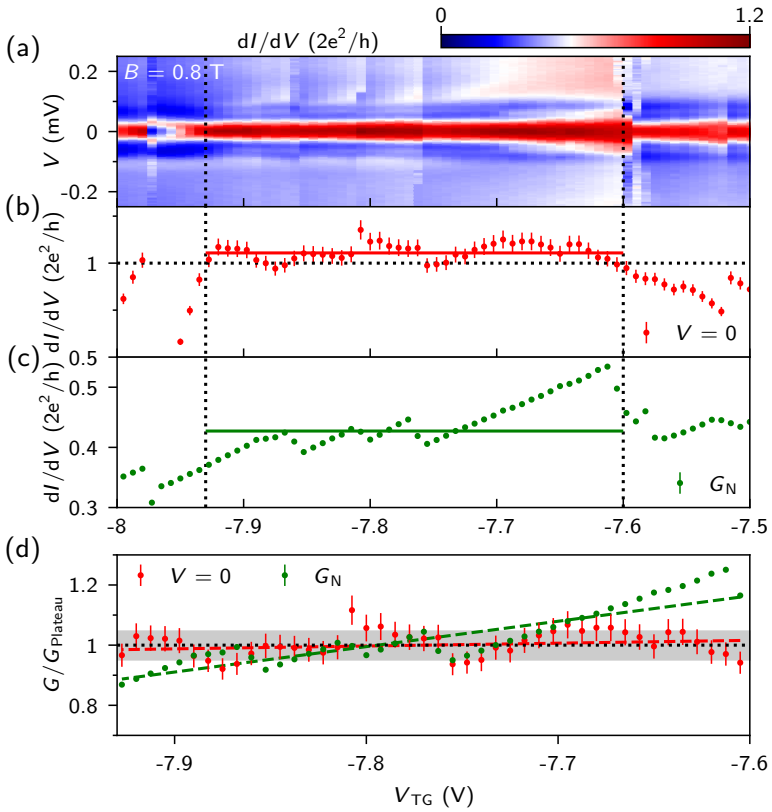

Figure 4.16: (**a**-**c**) Zoom in of Fig. 4.3a-c. The vertical black dotted lines indicate the candidate plateau-like region, i.e. the region under consideration for the test outlined in the text. The red and green horizontal lines in panels b and c indicate the average conductance in this region, which we call G_{Plateau}. (**d**) The relative conductance as a fraction of G_{Plateau}. The dashed lines are linear fits over the plateau region, indicating the average derivative for the zero-bias conductance (red) and G_N (green). The gray shaded area shows a 5% window around the value of G_{Plateau}.

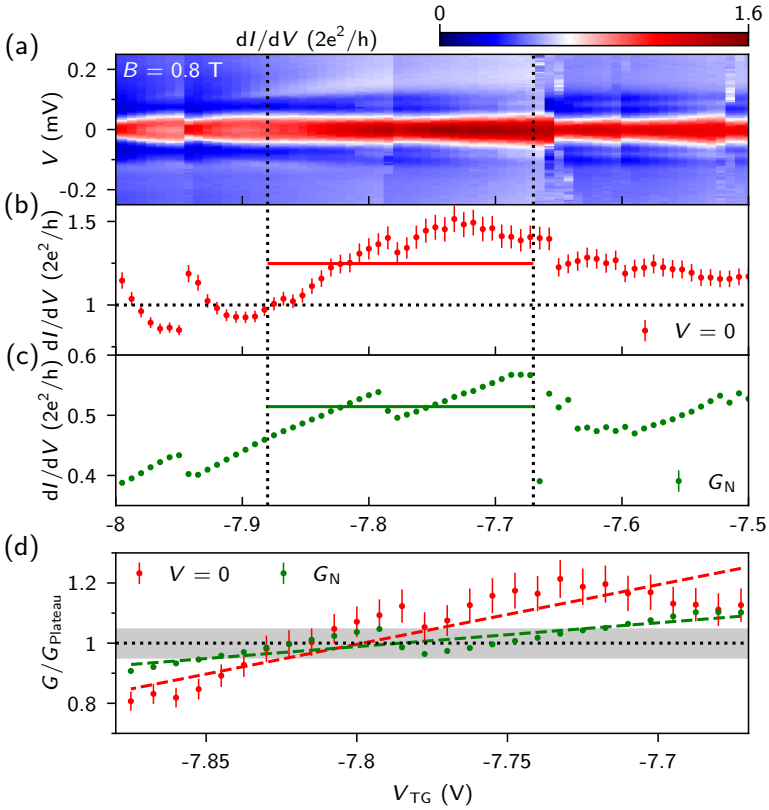

Figure 4.17: (**a**-**c**) Zoom in of Fig. 4.5a-c. The vertical black dotted lines indicate a candidate plateau-like region, which does not meet the stability condition. The red and green horizontal lines in panels b and c indicate the average conductance in this region, which we call G_{Plateau}. (**d**) The relative conductance as a fraction of G_{Plateau}. The dashed lines are linear fits over the plateau region, indicating the average derivative for the zero-bias conductance (red) and G_N (green). The gray shaded area shows a 5% window around the value of G_{Plateau}.

lected range as a plateau. However, one could choose to extend the selected range to the right until the second and third conditions are violated for Fig. 4.8c, or to crop the range slightly such that they are satisfied for Fig. 4.8d.

To give another example, if one cuts the considered region in Fig. 4.17 in half and only uses the data between $V_{\mathrm{TG}} = -7.78\,\mathrm{V}$ and $V_{\mathrm{TG}} = -7.67\,\mathrm{V}$, we can find a "plateau" at $2.8\ e^2/h$ which satisfies our first and second conditions, but not the third, as the ratio of the derivatives is only 1.6. However, if the third condition is applied less strictly, and we only demand that the average derivative of the above-gap conductance exceeds that of the zero-bias conductance, this feature would pass the test.

It is not unlikely that given a sufficiently large data set, regions of parameter space can generically be found which satisfy the types of conditions we have set out. It is also apparent that the described tuning heuristic and our assignment protocol can influence whether or not a plateau can be found at a specific value. This analysis is therefore not intended to draw sharp distinctions, but rather to illustrate the uncertainties when it comes to a definition of a plateau in an experimental context. Such ambiguities exist in defining stability of conductance quantization in all topological systems, particularly in the early days of the experimental developments. Examples include the quantum spin Hall effect [105], the quantum anomalous Hall effect [106] and the 5/2 fractional quantum Hall plateau [107, 108]. A continued effort is needed to understand and improve the microscopic conditions for a quantized plateau with an acceptable experimental accuracy as well as the ramifications for the theoretical interpretation.

4.4.6. MEASUREMENT TIMELINE

As mentioned, our devices tend to be relatively unstable, making it difficult to maintain consistent measurement conditions over time. Charging and discharging charge traps in the environment, either due to sudden jumps or from actively sweeping the gate voltage, combined with gate drifts on the scale of hours complicate the comparison of different data sets if they were measured sufficiently far apart. This distance can be measured either in time or in the amount of parameter space which was explored in between different measurements. In Table 4.1, we list the date and time each data set was taken, as well as the range over which various parameters had been explored since the previous entry in the table. When data sets are taken consecutively (labeled 'CS'), we expect the results to generally be consistent between them. However, if sufficiently time and/or parameter distance separates two data sets, we expect the settings cannot be compared directly.

4.4.7. COMPARISON OF LORENTZIAN FITS WITH FWHM ANALYSIS

In Fig. 4.4, we show the peak height and width as extracted from the data in Fig. 4.3 via a fit to a Lorentzian line shape thermally broadened by 20 mK:

$$\begin{aligned} G(V, T = 20\,\mathrm{mK}) &= \int \mathrm{d}\epsilon G(\epsilon, 0) \frac{\mathrm{d}}{\mathrm{d}\epsilon} f(eV - \epsilon, T = 20\,\mathrm{mK}), \\ G(E, 0) &= G_0 \frac{\Gamma^2}{\Gamma^2 + E^2} \end{aligned} \tag{4.4}$$

Data set	Device	Date	Time started	Time finished	Parameter range since previous entry			
					V_{TG} (V)	V_{SG} (V)	V_{BG} (V)	B (T)
Fig. 8b	B	3-3	14:45	18:40	-	-	-	-
Fig. 8c	B	8-3	19:41	21:54	-2.0 – -0.75	-2.1 – 1.5	-2.0 – -0.75	0 – 1.2
Fig. 8d	B	8-3	23:00	23:45	CS	CS	CS	CS
Fig. H1	B	14-3	14:50	00:35	-2.5 – -1.11	-0.9 – 5.25	-2.5 – -1.11	0 – 1.3
Fig. 6c	A	27-3	11:52	18:04	-	-	-	-
Fig. 7a	A	27-3	23:09	03:12	CS	CS	Fixed	CS
Fig. 6a	A	28-3	03:14	07:16	CS	CS	Fixed	CS
Fig. 6b	A	28-3	07:19	11:21	CS	CS	Fixed	CS
Fig. 2b	A	28-3	12:27	15:34	-6.5 – -3.5	-9.0 – -7.8	Fixed	0.6 – 0.9
Fig. 7b	A	28-3	15:35	18:29	CS	CS	Fixed	CS
Fig. 2a	A	29-3	01:03	02:45	-9.0 – -6.0	-6.5 – -5.5	Fixed	0 – 1.0
Fig. 2c	A	29-3	04:26	06:08	-7.92 – -7.74	Fixed	Fixed	0 – 1.0
Fig. 3	A	30-3	13:46	15:45	-9.21 – -6.75	-7.5 – -4.5	Fixed	0 – 1.0
Fig. 5	A	31-3	20:07	22:36	-8.25 – -7.5	Fixed	Fixed	0 – 1.0
Fig. C1	C	7-4	14:48	23:20	-	-	-	-
Fig. D1b	C	7-4	23:21	08:38	CS	CS	CS	CS
Fig. 9d	C	18-4	15:23	18:52	-	-	-	-
Fig. 9c	C	18-4	19:13	20:43	CS	CS	CS	CS
Fig. 9a	C	18-4	23:47	02:11	-0.1 – -0.03	-1.5 – 1.5	Fixed	Fixed
Fig. 9b	C	23-4	19:23	20:18	-0.1 – 0.1	-1.5 – 1.5	-22.5 – 0	-0.1 – 1.1

Table 4.1: Measurement timeline of all the data sets included in this manuscript. For the parameter changes, we describe the range over which these parameters were since the previous entry. We indicate consecutive measurements by 'CS'. If the parameter remains unaltered until the measurement is initiated it is labeled 'Fixed'. All data sets were taken in 2017.

Here, the peak height is given by G_0, and the peak width is 2Γ. An alternative way to determine these parameters is to take the conductance value at $V = 0$ as the height and take the full width at half maximum (FWHM) for the width. This method is less dependent on the exact peak shape, which can be advantageous when analyzing peaks which are broadened beyond the Lorentzian regime [104].

Fig. 4.18a shows an example of this procedure, with the results for the full data set used in Fig. 4.4 shown in Fig. 4.18b. Comparing the results for the height (Fig. 4.18c) and width (Fig. 4.18d), we see that although the methods show some quantitative differences, especially for the broader peaks, they produce the same qualitative trends. The peak width has a positive correlation with G_N, while the peak height shows no clear correlation with either the peak width or G_N (as shown in more detail Fig. 4.20a).

In Fig. 4.19 we show the same analysis performed on the data set reported in Fig. 4.9b. Again, we see that the Lorentzian and FWHM analysis give qualitatively similar results. However, in this case the peak height has a positive correlation with G_N, and a negative correlation with the peak width, indicating that this peak is most likely due to a level crossing (see Fig. 4.20b).

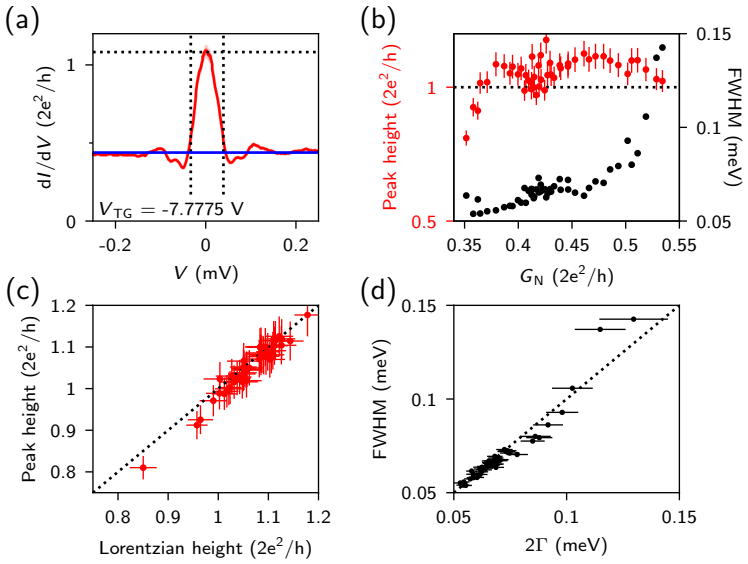

Figure 4.18: (**a**) Example of the peak height and width analysis used in panel (b). The height is determined by $\mathrm{d}I/\mathrm{d}V$ at $V = 0$ (dotted horizontal line). The FWHM is then determined by finding the values of **V** where the conductance equals half the peak conductance (vertical dotted lines). The extracted value of G_N is shown by the blue line. (**b**) Peak height (red circles) and FWHM (black circles) as a function of G_N. (**c**) Comparison of the peak height found by taking the conductance value at $V = 0$ with the height extracted from the Lorentzian fit. The dotted line indicates the points where the two values are equal. (**d**) Comparison of the FWHM with the peak width extracted from the Lorentzian fit (2Γ). The dotted line indicates the points where the two values are equal.

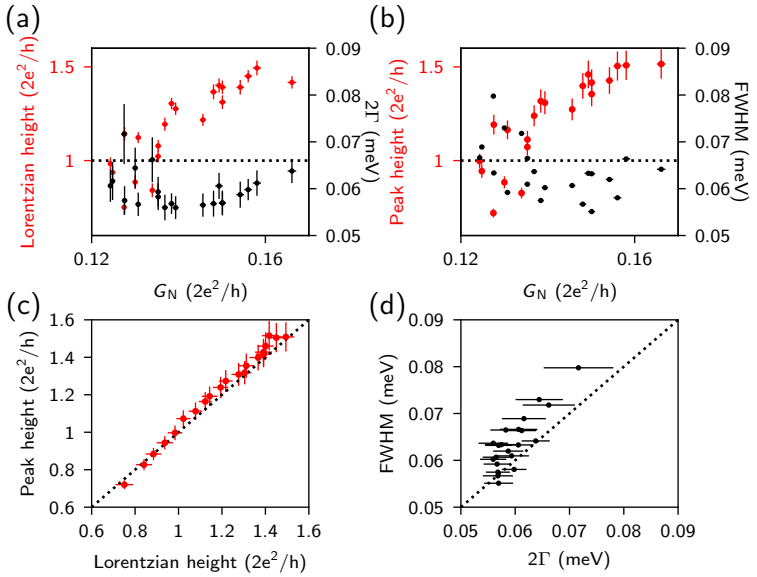

Figure 4.19: (**a**) Results of the Lorentzian fit of the peaks in Fig. 4.9b in the range $V_{BG} = -11.9\,V$ to $V_{BG} = -10.9\,V$. (**b**) Results of the FWHM analysis on the same data set. (**c**) Comparison of the peak height found by taking the conductance value at $V = 0$ with the height extracted from the Lorentzian fit. The dotted line indicates the points where the two values are equal. (**d**) Comparison of the FWHM with the peak width extracted from the Lorentzian fit (2Γ). The dotted line indicates the points where the two values are equal.

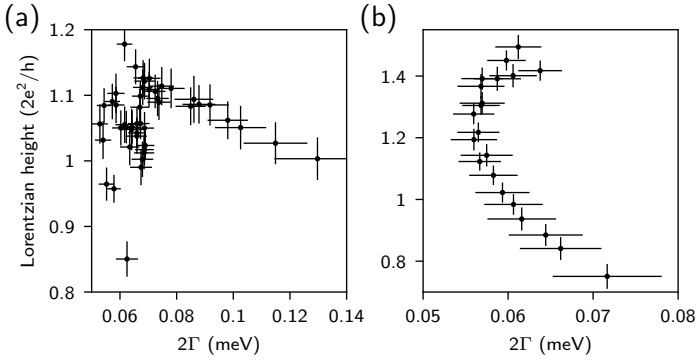

Figure 4.20: (**a**) Peak height as obtained by Lorentzian fit as a function of the peak width 2Γ for the data presented in Fig. 4.3. The Pearson's correlation coefficient is 0.009, indicating there is little to no linear correlation between the two variables. The decreasing trend in the peak height for the widest peaks could be indicative of the onset of peak splitting. (**b**) Peak height as a function of peak width for the data presented in Fig. 4.9b. The correlation coefficient is -0.562, indicating a negative correlation between the peak height and the peak width.

4.4.8. TEMPERATURE DEPENDENCE OF THE ZBP HEIGHT

At $T = 0$, the conductance through a Majorana zero mode should be quantized at $2e^2/h$ independent of the tunnel coupling to the lead. While the peak height is constant, the peak width is determined by this tunnel coupling. At finite temperature, thermal broadening of the Fermi edge in the metallic lead gives rise to an increase in the peak width as well as a decrease in the peak height, with the effect size depending on the ratio of the tunnel and thermal broadening [104]. In Fig. 4.21a, we show the temperature dependence of the ZBP reported in Fig. 4.8 of the main text. From the line traces in Fig. 4.21b, we see that as the temperature is increased, the peak height decreases while the peak width increases.

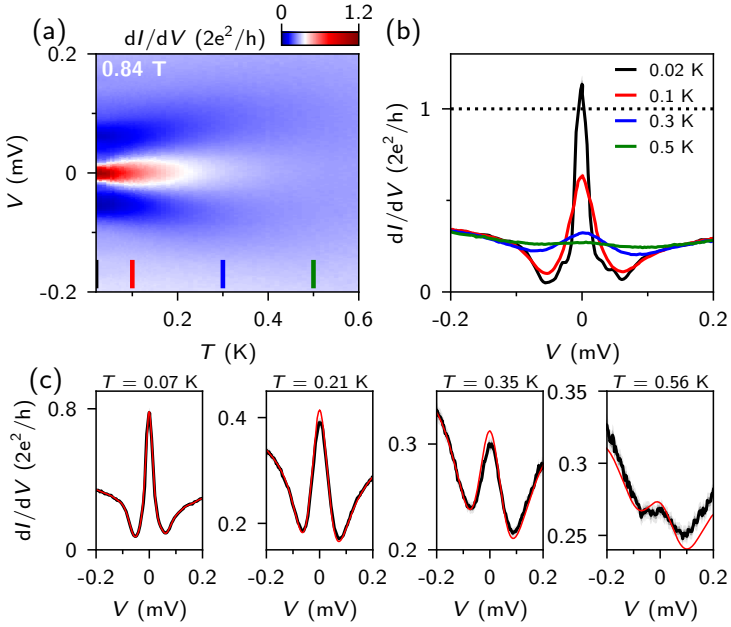

Figure 4.21: Temperature dependence of the ZBP height. (**a**) Differential conductance $\mathrm{d}I/\mathrm{d}V$ as a function of voltage V and temperature T at $B = 0.84\,\mathrm{T}$. $V_{\mathrm{SG}} = -0.39\,\mathrm{V}$, $V_{\mathrm{TG}} = V_{\mathrm{BG}} = -1.255\,\mathrm{V}$. (**b**) Line traces from panel (a), illustrating the decrease in the peak height as the temperature is increased. (**c**) Examples of the zero-bias peak height for different temperatures. Experimental data is shown as the black curves, while the red curves are obtained by taking the conductance at base temperature (20 mK) and performing a convolution with the derivative of the Fermi distribution at the given temperature. Data was obtained from device B.

For any discrete resonance coupled to a reservoir, the conductance at temperature T can be calculated from the conductance at $T = 0$ via a convolution with the derivative of the Fermi-Dirac distribution f:

$$G(V,T) = \int \mathrm{d}\epsilon G(\epsilon,0)\frac{\mathrm{d}}{\mathrm{d}\epsilon}f(eV-\epsilon,T) \tag{4.5}$$

For a given peak shape, this can be converted to a universal scaling function which only depends on the ratio of the tunnel coupling and the temperature [39].

To simulate the effect of the increasing temperature, we use the data at base temperature ($T = 20\,\mathrm{mK}$) to approximate $G(V,0)$, and calculate the expected conductance at higher temperatures. Fig. 4.21c shows the measured conductance at a few selected temperatures in black, with the simulated trace shown in red. We see that there is a good agreement between the two, indicating that the decrease in peak height can be attributed to the increase in temperature through the increase of the thermal broadening. This is further demonstrated in Fig. 4.22. For low temperatures, the peak width is mostly determined by the tunnel broadening, and the peak height approaches a saturation of 2.3 e^2/h as the temperature is decreased towards 0. When the temperature is increased, the relative importance of the thermal broadening mechanism increases, leading to a decrease in the peak height.

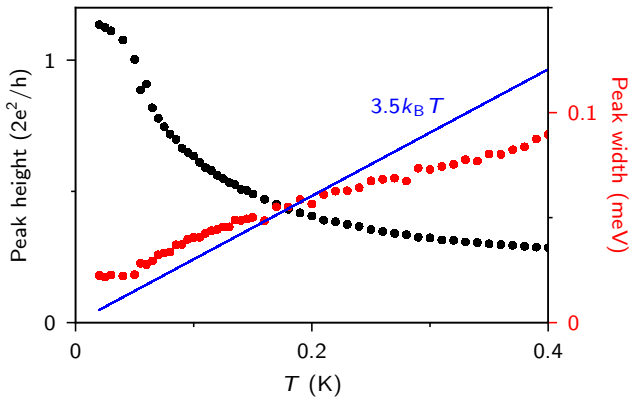

Figure 4.22: Extracted ZBP height (black) and width (red) as a function of temperature. As the temperature increases, thermal broadening starts to dominate over tunnel broadening in determining the peak width, causing the ZBP height to decrease. The blue line indicates the energy scale associated with the thermal broadening, $3.5k_B T$.

5

ELECTRIC FIELD TUNABLE SUPERCONDUCTOR-SEMICONDUCTOR COUPLING IN MAJORANA NANOWIRES

We study the effect of external electric fields on superconductor-semiconductor coupling by measuring the electron transport in InSb semiconductor nanowires coupled to an epitaxially grown Al superconductor. We find that the gate voltage induced electric fields can greatly modify the coupling strength, which has consequences for the proximity induced superconducting gap, effective g-factor, and spin-orbit coupling, which all play a key role in understanding Majorana physics. We further show that level repulsion due to spin-orbit coupling in a finite size system can lead to seemingly stable zero bias conductance peaks, which mimic the behavior of Majorana zero modes. Our results improve the understanding of realistic Majorana nanowire systems.

This chapter has been published as, *Electric field tunable superconductor-semiconductor coupling in Majorana nanowires*, M. W. A. de Moor*, J. D. S. Bommer*, **D. Xu***, G. W. Winkler, A. E. Antipov, A. Bargerbos, G. Wang, N. van Loo, R. L. M. Op het Veld, S. Gazibegovic, D. Car, J. A. Logan, M. Pendharkar, J. S. Lee, E. P. A. M. Bakkers, C. J. Palmstrøm, R. M. Lutchyn, L. P. Kouwenhoven, and H. Zhang in New Journal of Physics **20**, 103049 (2018).
* These authors contributed equally to this work.

5.1. INTRODUCTION

The hybrid superconductor-semiconductor nanowire system is the prime candidate to realize, control, and manipulate Majorana zero modes (MZMs) for topological quantum information processing [61, 62, 109]. Majorana zero modes can be engineered in these hybrid nanowire systems by combining the one dimensional nature of the nanowire, strong spin-orbit coupling, superconductivity, and appropriate external electric (to control the chemical potential) and magnetic fields (to control the Zeeman energy) to drive the system into a topologically non-trivial phase [13, 14]. To induce superconductivity in the semiconductor nanowire, it needs to be coupled to a superconductor. The electronic coupling between the two systems turns the nanowire superconducting [20], known as the proximity effect. Following this scheme, the first signatures of MZMs were observed in these hybrid systems, characterized by a zero bias peak (ZBP) in the tunneling conductance spectrum [23–26]. Since then, significant progress has been made in Majorana experiments [15, 18, 36, 37], enabled by more uniform coupling between the superconductor and semiconductor nanowire. This has been achieved by improved interface engineering: through careful ex situ processing [72, 92, 110], by depositing the superconductor on the nanowires in situ [41, 91], and a combination of *in situ* and *ex situ* techniques [42], finally leading to the quantization of the Majorana conductance [15].

However, the treatment of the superconductor-semiconductor coupling in the interpretation of experiments is often oversimplified. This coupling has recently been predicted to depend substantially on the confinement induced by external electric fields [111]. In this work, we experimentally show that the superconductor-semiconductor coupling, as parameterized by the induced superconducting gap, is affected by gate induced electric fields. Due to the change in coupling, the renormalization of material parameters is altered, as evidenced by a change in the effective g-factor of the hybrid system. Furthermore, the electric field is shown to affect the spin-orbit interaction, revealed by a change in the level repulsion between Andreev states. Our experimental findings are corroborated by numerical simulations.

5.2. EXPERIMENTAL SET-UP

We have performed tunneling spectroscopy experiments on four InSb–Al hybrid nanowire devices, labeled A–D, all showing consistent behavior. The nanowire growth procedure is described in [42]. A scanning electron micrograph (SEM) of device A is shown in Fig. 5.1(a). Fig. 5.1(b) shows a schematic of this device and the measurement set-up. For clarity, the wrap-around tunnel gate, tunnel gate dielectric and contacts have been removed on one side. A normal-superconductor (NS) junction is formed between the part of the nanowire covered by a thin shell of aluminum (10 nm thick, indicated in green, S), and the Cr/Au contact (yellow, N). The transmission of the junction is controlled by applying a voltage V_{Tunnel} to the tunnel gate (red), galvanically isolated from the nanowire by 35 nm of sputtered SiN_x dielectric. The electric field is induced by a global back gate voltage V_{BG}, except in the case of device B, where this role is played by the side gate voltage V_{SG} . Further details on device fabrication and design are included in sections 5.9.1 and 5.9.2. To obtain information about the density of states (DOS) in the proximitized nanowire, we measure the differential conductance $\mathrm{d}I/\mathrm{d}V_{\text{Bias}}$ as a function of applied

bias voltage V_{Bias}. In the following, we will label this quantity as $\mathrm{d}I/\mathrm{d}V$ for brevity. A magnetic field is applied along the nanowire direction (x-axis in figures 5.1(b),(c)). All measurements are performed in a dilution refrigerator with a base temperature of 20 mK.

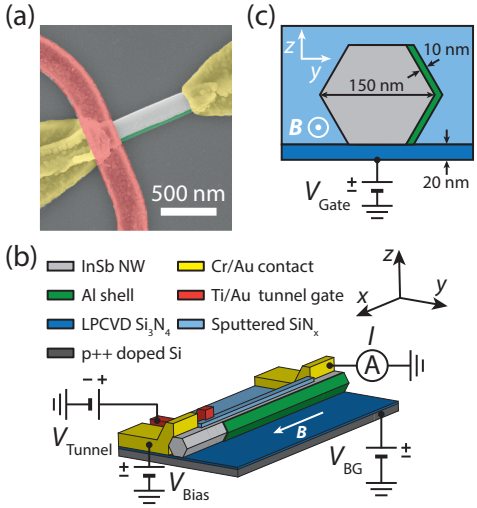

Figure 5.1: **Device schematics.** (**a**) SEM of device A, with InSb nanowire in gray, superconducting aluminum shell in green, Cr/Au contacts in yellow, and local tunnel gate in red. Scale bar is 500 nm. (**b**) Schematic of experimental set-up. The substrate acts as a global back gate. The magnetic field is applied along the nanowire direction (x-axis). (**c**) Geometry used in the numerical simulations. A uniform potential V_{Gate} is applied as a boundary condition at the interface between substrate and dielectric. The superconductor (green) is kept at a fixed potential, which is set by the work function difference at the superconductor-semiconductor interface.

5.3. THEORETICAL MODEL

The device geometry used in the simulation is shown in Fig. 5.1(c). We consider a nanowire oriented along the x-direction, with a hexagonal cross-section in the yz-plane. The hybrid superconductor-nanowire system is described by the Bogoliubov–de Gennes (BdG) Hamiltonian

$$\begin{aligned} H = &\left[\frac{\hbar^2\mathbf{k}^2}{2m^*} - \mu - e\phi\right]\tau_z + \alpha_y(k_z\sigma_x - k_x\sigma_z)\tau_z \\ &+ \alpha_z(k_x\sigma_y - k_y\sigma_x)\tau_z + \frac{1}{2}g\mu_{\text{B}}B\sigma_x + \Delta\tau_x. \end{aligned} \tag{5.1}$$

The first term contains contributions from the kinetic energy and the chemical potential, as well as the electrostatic potential ϕ. The second and third terms describe the Rashba spin–orbit coupling, with the coupling strength α_y (α_z) depending on the y-component (z-component) of the electric field. The Zeeman energy contribution, proportional to g, the Landé g-factor, is given by the fourth term. Finally, the superconducting pairing Δ is included as the fifth term. All material parameters are position dependent, taking different values in the InSb nanowire and the Al superconductor. For additional details

about the simulation, see sections 5.9.3 and 5.9.4.

If the coupling between the superconductor and semiconductor is small (compared to the bulk gap of the superconductor Δ, known as weak coupling), superconductivity can be treated as a constant pairing potential term in the nanowire Hamiltonian, with the induced superconducting gap being proportional to the coupling strength [112]. However, if the coupling becomes strong, the wave functions of the two materials hybridize, and the superconductor and semiconductor have to be considered on equal footing [113]. We achieve this by solving the Schrödinger equation in both materials simultaneously. When desired, the orbital effect of the magnetic field is added via Peierls substitution [114]. The simulations are performed using the `kwant` package [115].

The electrostatic potential in the nanowire cross-section is calculated from the Poisson equation, assuming an infinitely long wire. We use a fixed potential V_{Gate} as a boundary condition at the dielectric-substrate interface. The superconductor enters as the second boundary condition, with a fixed potential to account for the work function difference between superconductor and semiconductor [116]. We approximate the mobile charges in the nanowire by a 3D electron gas (Thomas–Fermi approximation). It has been demonstrated that the potentials calculated using this approximation give good agreement with results obtained by self-consistent Schrödinger–Poisson simulations [117]. The calculated potential for a given V_{Gate} is then inserted into the Hamiltonian 5.1.

By solving the Schrödinger equation for a given electrostatic environment, we can see how the gate potential alters the electronic states in the nanowire, how they are coupled to the superconductor, and how this coupling affects parameters such as the induced gap, effective g-factor, and spin–orbit energy.

5.4. GATE VOLTAGE DEPENDENCE OF THE INDUCED SUPERCONDUCTING GAP

When the transmission of the NS-junction is sufficiently low (i.e., in the tunneling regime), the differential conductance $\mathrm{d}I/\mathrm{d}V$ is a direct measure of the DOS in the proximitized nanowire [118]. In Fig. 5.2(a), we plot $\mathrm{d}I/\mathrm{d}V$ measured in device A as a function of applied bias voltage V_{Bias} and tunnel gate voltage V_{Tunnel}, for $V_{\text{BG}} = -0.6\,\text{V}$. In the low transmission regime, we resolve the superconducting gap Δ around $250\,\mu\text{eV}$, indicated by the position of the coherence peaks. The ratio of sub-gap to above-gap conductance (proportional to the normal state transmission of the junction, T) follows the behavior expected from BTK theory [29, 33], indicating the sub-gap conductance is dominated by Andreev reflection processes (proportional to T^2). This is generally referred to as a hard gap. However, for more positive back gate voltages, the sub-gap conductance is larger and shows more resonances, as is illustrated in Fig. 5.2(b) for $V_{\text{BG}} = -0.3\,\text{V}$. Fig. 5.2(c) shows line traces taken at a similar transmission (above-gap conductance) for both cases. The sub-gap conductance for $V_{\text{BG}} = -0.3\,\text{V}$ (black line) exceeds that of the hard gap case (red line) by an order of magnitude. This is indicative of a surplus of quasi-particle states inside the gap, referred to as a soft gap.

The gate voltage induced transition from soft to hard gap is generically observed in multiple devices. To understand this phenomenology, we calculate the electron density in the nanowire cross-section for different values of V_{Gate}. Because the charge neutral-

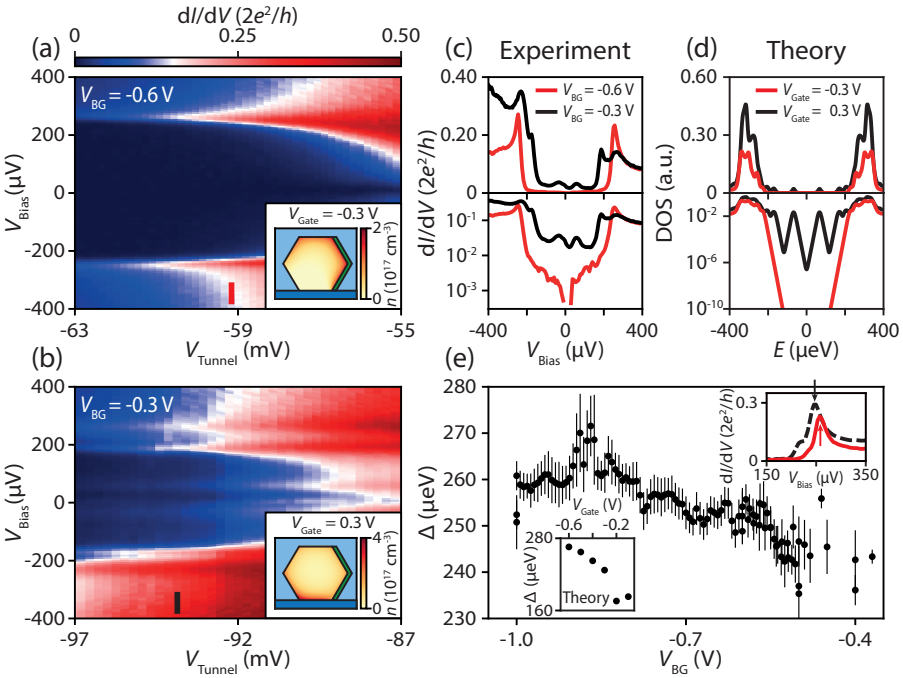

Figure 5.2: **Gate dependence of the induced superconducting gap.** (**a**), (**b**) Differential conductance dI/dV measured in device A as a function of V_{Bias} and V_{Tunnel} for $V_{\mathrm{BG}} = -0.6\,\mathrm{V}$ (**a**) and $V_{\mathrm{BG}} = -0.3\,\mathrm{V}$ (**b**). Insets show the calculated electron density in the wire for $V_{\mathrm{Gate}} = -0.3\,\mathrm{V}$ and $V_{\mathrm{Gate}} = 0.3\,\mathrm{V}$, respectively. (**c**) Line-cuts from (a) and (b), indicated by the colored bars, in linear (top) and logarithmic (bottom) scale. (**d**) Calculated DOS for the density profiles shown in the insets of (a) and (b), shown in red and black, respectively. (**e**) Induced gap magnitude Δ as a function of V_{BG}, showing a decrease for more positive gate voltages. Top right inset: line traces showing the coherence peak position (indicated by the arrow) for $V_{\mathrm{BG}} = -0.6\,\mathrm{V}$ (solid red line) and $V_{\mathrm{BG}} = -0.4\,\mathrm{V}$ (dashed black line). Bottom left inset: induced gap from the calculated DOS as a function of V_{Gate}, consistent with the experimental observation.

ity point in our devices is unknown, there is a difference between the gate voltages used in the experiment and the values of V Gate used in the simulation. By comparing the transition point between hard and soft gaps in the experiment and the simulation, we estimate that the experimental gate voltage range $-0.6\,\mathrm{V} < V_{\mathrm{BG}} < -0.4\,\mathrm{V}$ roughly corresponds to the simulated gate voltage rang $-0.4\,\mathrm{V} < V_{\mathrm{BG}} < -0.2\,\mathrm{V}$.

For more negative V_{Gate} , the electric field from the gate pushes the electrons towards interface with the superconductor (inset of Fig. 5.2(a)). We solve the Schrödinger equation for the calculated electrostatic potential and find that this stronger confinement near the interface leads to a stronger coupling. This results in a hard gap, as illustrated by the calculated energy spectrum (Fig. 5.2(d), red line). However, for more positive voltages, the electrons are attracted to the back gate, creating a high density pocket far away from the superconductor (inset of Fig. 5.2(b)). These states are weakly coupled to the superconductor, as demonstrated by a soft gap structure (Fig. 5.2(d), black line, see also section 5.9.5). We can therefore conclude that the electron tunneling between the semi-

conductor and the superconductor is strongly affected by the gate potential.

The change in superconductor-semiconductor coupling does not just affect the hardness, but also the size of the gap. For each back gate voltage, we fit the BCS-Dynes expression [119] for the DOS in order to extract the position of the coherence peaks, giving the gap size Δ. The results are shown in Fig. 5.2(e). Further details on the fitting procedure are given in section 5.9.6. As V_{BG} becomes more positive, the superconductor-semiconductor coupling becomes weaker, reducing the size of the gap. From $V_{\mathrm{BG}} > -0.4\,\mathrm{V}$ onward it becomes difficult to accurately determine the gap, as it tends to become too soft and the coherence peaks are not always clearly distinguishable. The top right inset shows the shift of the coherence peak (indicated by the arrows) to lower bias voltage as V_{BG} is increased. The lower left inset shows the extracted coherence peak position from the numerical simulations, showing the same trend with gate voltage. However, the theoretically calculated induced gap is generally smaller than the experimentally observed gap. It has been demonstrated that disorder at the outer surface of the superconductor (e.g., due to oxidation) leads to an increase in the induced gap due to breaking of momentum conservation, which increases the superconductor-semiconductor hybridization [111]. Additionally, the gap decreases more slowly when the gate voltage is more positive. As this kind of disorder is present in our devices, but was not included in the simulation, this is a likely cause for the discrepancy between theory and experiment.

5.5. EFFECTIVE g-FACTOR

As the electric field induced by the back gate clearly has an important effect on the hybridization between the nanowire and the superconductor, we now look at the effect this has on the Zeeman term in the Hamiltonian. This term affects the energy dispersion of spinful states in a magnetic field. We study the dispersion of the states in the nanowire by measuring $\mathrm{d}I/\mathrm{d}V$ in device A as a function of applied bias voltage and magnetic field, as shown in figures 5.3(a) and (b). We define the effective g-factor as $g_{\mathrm{eff}} = \frac{2}{\mu_B}\left|\frac{\Delta E}{\Delta B}\right|$, with $\left|\frac{\Delta E}{\Delta B}\right|$ the absolute value of the average slope of the observed peak in the differential conductance as it disperses in magnetic field. This effective g-factor is different from the pure spin g-factor g_{spin}, as the dispersion used to estimate g_{eff} is generally not purely linear in magnetic field, and has additional contributions from the spin-orbit coupling, magnetic field induced changes in chemical potential, and orbital effects [111, 116, 120]. The effective g-factor is the parameter which determines the critical magnetic field required to drive the system through the topological phase transition [121]. We obtain the slope $\left|\frac{\Delta E}{\Delta B}\right|$ from a linear fit (shown as black dashed lines in figures 5.3(a), (b), see section 5.9.7 for details) of the observed peak position. Fig. 5.3(c) shows the extracted g_{eff} for device A, with more positive back gate voltages leading to larger g_{eff} (visible as a steeper slope). A similar result has recently been reported in hybrid InAs–Al nanowires [122].

We use our numerical model to calculate the DOS in the nanowire as a function of applied magnetic field, shown in figures 5.3(d) and (e). From the calculated spectrum, we apply the same procedure used to fit the experimental data to extract g_{eff} (white dashed lines). The results for different values of g_{Gate} are given in Fig. 5.3(f) as black circles. The applied back gate voltage changes the hybridization of the states in the InSb ($\left|g_{\mathrm{spin}}\right| = 40$ [74]) and the Al ($\left|g_{\mathrm{spin}}\right| = 2$). As a more positive gate voltage increases the

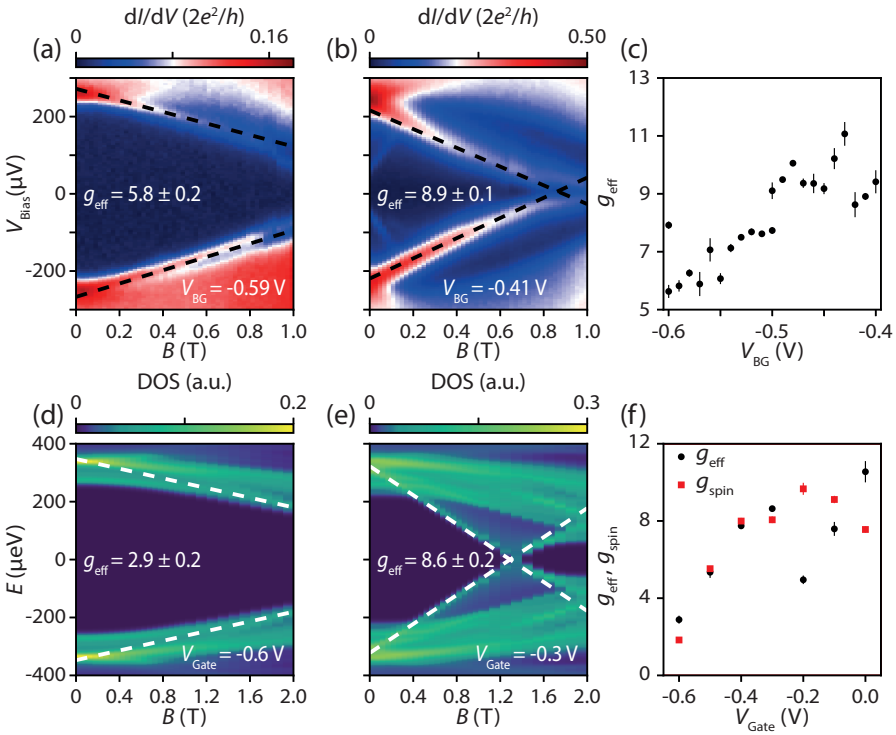

Figure 5.3: **Effective g-factor.** (**a**),(**b**) dI/dV measured in device A as a function of applied bias voltage V_{Bias} and magnetic field B for $V_{\text{BG}} = -0.59\,\text{V}$ and $V_{\text{BG}} = -0.41\,\text{V}$, respectively. The effective g-factor is extracted from a linear fit of the lowest energy state dispersion (dashed lines). (**c**) g_{eff} as a function of V_{BG}, showing an increase as the gate voltage becomes more positive. Data from device A. (**d**),(**e**) Simulated DOS in the nanowire as a function of magnetic field for $V_{\text{Gate}} = -0.6\,\text{V}$ and $V_{\text{Gate}} = -0.3\,\text{V}$, respectively. (**f**) Extracted g_{eff} (based on lowest energy state in the spectrum, black circles) and g_{spin} (based on the spectrum at $k = 0$, red squares) from the simulation.

weight of the wave function in the InSb, we expect the renormalized g-factor to increase as the gate voltage is increased, consistent with the results of figures 5.3(c) and (f).

To see how well g_{eff} describes the Zeeman term in the Hamiltonian, we turn our attention to the energy spectrum at $k = 0$. At this point, the effect of spin-orbit coupling vanishes. If orbital effects are excluded, we can then define the absolute value of the pure spin g-factor as $g_{\text{spin}} = \frac{2}{\mu_B}\left|\frac{\Delta E(k=0)}{\Delta B}\right|$. The resulting values for g_{spin} are shown as red squares in Fig. 5.3(f). By comparing the results for g_{eff} and g_{spin}, we can conclude that when the lowest energy state has a momentum near $k = 0$ (as is the case for $V_{\text{Gate}} > -0.2\,\text{V}$), the effect of spin-orbit coupling is negligible, and g_{eff} is a good proxy for the pure spin g-factor. However, when this is no longer the case, deviations can be observed, as is the case for $V_{\text{Gate}} \geqslant -0.2\,\text{V}$. As we expect the experimental gate voltage range of Fig. 5.3(c) to be comparable to values of $V_{\text{Gate}} < -0.2\,\text{V}$, we conclude that the experimentally obtained g_{eff} is a reasonable approximation of g_{spin} in this parameter regime.

However, we stress once more that in general, one needs to be careful when interpreting the g_{eff} extracted from experimental data as the g-factor entering the Hamiltonian in the Zeeman term.

The increasing trend of g_{eff} does not change when the orbital effect of magnetic field is considered (see section 5.9.7, Fig. 5.16). However, there is a significant increase in the predicted values, in agreement with previous findings for InAs nanowires [120]. The values in Fig. 5.16 are larger than the ones generally observed in our experiment (see Fig. 5.3(c)), suggesting that the orbital effect is not a dominant mechanism in determining the effective g-factor in these devices. We note that the data from device A used to make these plots was taken solely in the hard gap regime, where one expects a strong confinement near the superconductor. This suppresses the orbital contribution of the magnetic field. Another possible explanation for the discrepancy between the results of the simulation and the experimental data is an overestimation of the density in the nanowire, as higher sub-bands have a stronger contribution from the orbital effect. Minimizing the orbital effect is desirable for Majorana physics, as the orbital contributions of the magnetic field are detrimental to the topological gap [114].

5.6. LEVEL REPULSION DUE TO SPIN-ORBIT COUPLING

The term in the Hamiltonian that remains to be explored describes the Rashba spin–orbit coupling. The strength of the spin-orbit coupling is determined by the parameter α, which depends on the material (and thus, on the superconductor-semiconductor coupling), and the electric field [123–125]. Therefore, we expect that this term will be affected by the gate potential as well. In finite systems, the spin-orbit interaction can couple states with different orbitals and spins [126]. These states are thus no longer orthogonal to each other, and the spin-orbit mediated overlap between them causes energy splitting, leading to level repulsion [48, 127, 128]. This level repulsion, which is generic in class D systems in the presence of superconductivity, magnetic field and spin–orbit coupling [47, 129], can be extracted from the low energy nanowire spectrum as measured by tunneling spectroscopy [130].

In figures 5.4(a)–(c), we show the evolution of the level repulsion between the two lowest energy sub-gap states (labeled L_1 and L_2, as indicated by the white dashed lines in panel (c)) in device B. For these measurements, the global back gate is grounded, with the electric field being induced by applying a voltage to the side gate (side gate shown in section 5.9.2).

We parameterize the level repulsion by two quantities: the coupling strength δ_{SO}, and the splitting A, defined as the maximum deviation of L_1 from zero energy after the first zero crossing. This splitting has previously been linked to the overlap between two MZM in a finite system [43]. In Fig. 5.4(e), we zoom in on the anti-crossing feature in panel Fig. 5.4(b), showing the minimum energy difference between L_1 and L_2 (given by $2\delta_{\text{SO}}$) and the splitting A. We extract these parameters by a fit of the anti-crossing (solid green lines, with the uncoupled states shown by the dashed black lines, details of the fitting procedure are in section 5.9.8).

Because we expect finite size effects to be relevant, we cannot use our previous theoretical model, as it is based on an infinitely long nanowire. Therefore, we modify the model to take into account the finite size of the nanowire system, and calculate the low

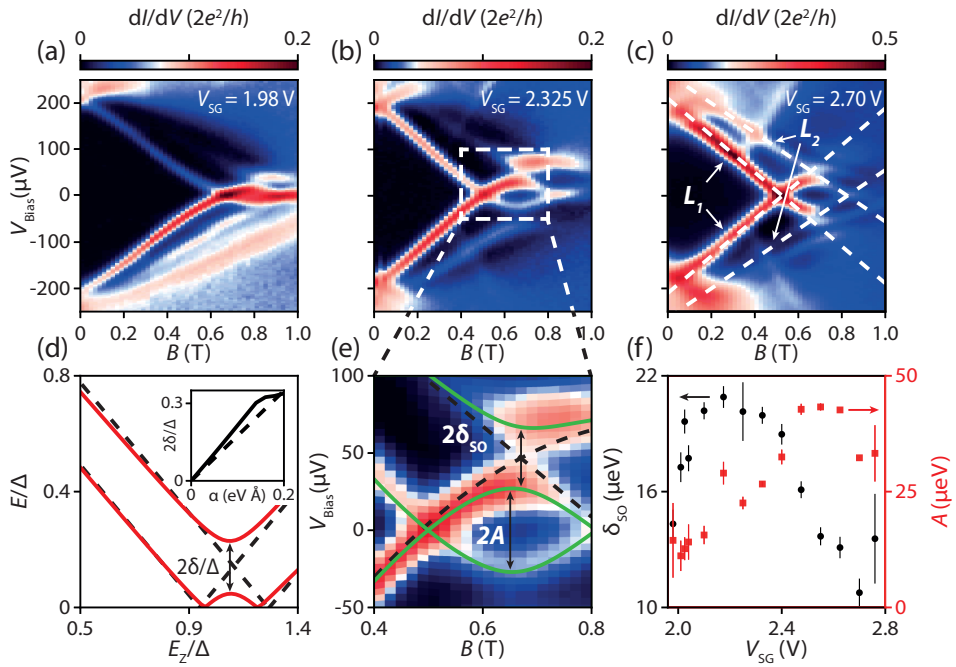

Figure 5.4: **Spin-orbit coupling induced level repulsion.** (**a**-**c**) $\mathrm{d}I/\mathrm{d}V$ as a function of V_{Bias} for device B, showing the dispersion of sub-gap states in magnetic field, for V_{SG} = 1.98 V, 2.325 V, and 2.70 V, respectively. The two lowest energy states L_1, L_2, and their particle-hole symmetric partners are indicated by the white dashed lines. (**d**) Calculated low energy spectrum of the finite nanowire system as a function of the Zeeman energy E_Z for α = 0 eV Å(dashed black lines) and α = 0.1 eV Å(solid red lines), showing the opening of an energy gap 2δ due to spin-orbit coupling. Inset: the energy gap 2δ as a function of the Rashba α parameter (solid line), and the estimate $2\delta = \alpha\pi/l$ (dashed line), with l the nanowire length. All energy scales are in units of the superconducting gap Δ. (**e**) Zoom-in of the anti-crossing in (**b**), showing the splitting A and the coupling strength δ_{SO}. Green solid lines indicate a fit of the anti-crossing, with the dashed black lines showing the uncoupled energy levels. (**f**) Coupling δ_{SO} (black circles) and splitting A (red squares) as a function of V_{SG}, showing opposite trends for these parameters.

energy spectrum for different values of the Rashba spin-orbit strength (see section 5.9.9). In Fig. 5.4(d), we plot the two lowest energy states in the nanowire as a function of the Zeeman energy ($E_Z = \frac{1}{2} g \mu_B B$), in units of the superconducting gap Δ. If $\alpha = 0$ (no spin-orbit coupling, dashed black lines), there is no coupling between the states, and no level repulsion occurs. However, if spin-orbit coupling is included (e.g., $\alpha = 0.1$ eV Å, solid red lines), the levels repel each other, with the magnitude of the anti-crossing given by 2δ. The level repulsion strength scales with α (inset of Fig. 5.4(d)), providing a way to estimate α based on the low energy spectrum using $2\delta \sim \alpha\pi/l$, where l is the length of the nanowire.

In Fig. 5.4(f), we plot δ_{SO} (black circles) and A (red squares) as a function of the applied side gate voltage. The two parameters follow opposite trends, with A being maximal when δ_{SO} is minimal. When δ_{SO} is larger, the levels repel each other more, leading to L_1 being pushed closer to zero energy, reducing the splitting A. When $V_{\mathrm{SG}} < 2.0$ V, both

parameters become smaller with decreasing V_{SG}. At this point, other states at higher energies become relevant for the lowest energy dispersion (a situation demonstrated in Fig. 5.4(a)), and our method to extract these parameters breaks down. We expect this method to be reliable when the energetically lowest two states can be clearly separated from the rest.

Because δ_{SO} depends not only on α, but also on the details of the confinement potential, as well as the coupling to the superconductor, a precise estimate goes beyond the current approximations in our model. That being said, based on the observed magnitude of δ_{SO} and our simulations of the finite nanowire system, we can estimate the Rashba parameter α to be around 0.1 eVÅ in this gate voltage range. This value is comparable to the values reported in InSb nanowire based quantum dots [131], and smaller than the values measured in weak anti-localization experiments [124]. A large value of α is beneficial for Majorana physics, as it determines the maximum size of the topological gap [132].

5.7. ZBP IN EXTENDED MAGNETIC FIELD RANGE

In the previous sections, we have described the effect of the gate induced electric field on the various terms in the Hamiltonian (1). As this Hamiltonian is known to describe Majorana physics, we now turn our attention to possible signatures of MZMs in this system. In particular, when $2\delta_{SO}$ becomes comparable to the energy of L_2, we find that L_1 can become pinned close to zero bias over an extended range in magnetic field, as demonstrated in Fig. 5.5(b) (data from device A). Fig. 5.5(d) shows that the state stays pinned to zero energy over a range of over 0.2 T, corresponding to a Zeeman energy of over 300 μeV, which is larger than the induced gap. The stability of the ZBP in terms of the ratio of Zeeman energy to induced gap is comparable to the most stable ZBPs reported in literature [36, 37]. When we fix the magnetic field to $B = 0.26$ T and change the back gate voltage (Fig. 5.5(e)), it appears that there is a stable ZBP over a few mV as well.

We might be tempted to conclude that this stability implies this is a MZM. However, if we change either the gate voltage (Fig. 5.5(a),(c)) or the magnetic field (Fig. 5.5(f)) a little bit, we observe that this stability applies only to very particular combinations of gate voltage and magnetic field. One should keep in mind that in a finite system, MZMs are not expected to be stable with respect to local perturbations if the system size is comparable to the Majorana coherence length, which is likely the case in our devices. This further complicates the determination of the origin of the observed peaks. As we find no extended region of stability, we conclude that it is unlikely that this state pinned to zero energy is caused by a topological phase transition. Rather, this seems to be due to a fine-tuned coincidence in which the repulsion between two states combined with particle-hole symmetry leads to one of the states being pinned to $E = 0$. We reiterate that simply having a stable zero energy state over an extended range in magnetic field is not sufficient to make claims about robust Majorana modes [50, 51, 87]. Further experimental checks, such as stability of the ZBP in an extended region of the parameter space spanned by the relevant gate voltages [37], as well as magnetic field, are required in order to assign a possible Majorana origin.

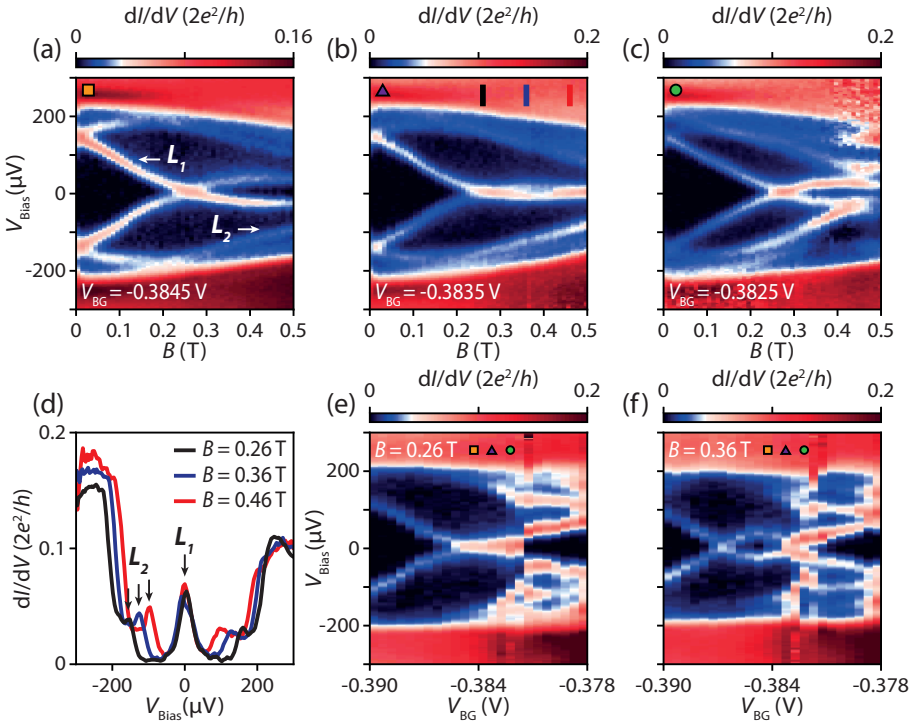

Figure 5.5: **Zero bias pinning due to strong level repulsion.** (**a**-**c**) dI/dV as a function of V_{Bias} for device A, showing the dispersion of L_1 and L_2 as a function of magnetic field for V_{BG} = -0.3845 V, -0.3835 V, and -0.3825 V, respectively. (**d**) Line traces at magnetic fields indicated by the colored bars in (b), showing the stable pinning of L_1 to zero bias voltage. (**e**,**f**) dI/dV measured as a function of V_{BG} at fixed magnetic field B = 0.26 T and 0.36 T, respectively. Gate voltages from (a), (b), and (c) are indicated by orange square, purple triangle, and green circle, respectively.

5.8. CONCLUSION AND OUTLOOK

We have used InSb nanowires with epitaxial Al superconductor to investigate the effect of the gate voltage induced electric field on the superconductor-semiconductor coupling. This coupling is determined by the distribution of the wave function over the superconductor and semiconductor, and controls essential parameters of the Majorana Hamiltonian: the proximity induced superconducting gap, the effective g-factor, and spin–orbit coupling. Our observations show that the induced superconductivity, as parameterized by the hardness and size of the induced gap, is stronger when the electrons are confined to a region close to the superconductor. The stronger coupling leads to a lower effective g-factor. We also determine that the gate voltage dependence of the effective g-factor is dominated by the change in coupling to the superconductor, rather than by orbital effects of the magnetic field. Finally, we study the effect of level repulsion due to spin-orbit coupling. Appropriate tuning of the repulsion leads to level pinning to zero energy over extended parameter ranges, mimicking the behavior expected from MZMs. Our result deepens the understanding of a more realistic Majorana nanowire system. More impor-

tantly, it is relevant for the design and optimization of future advanced nanowire systems for topological quantum information applications.

AUTHOR CONTRIBUTIONS

M.W.A.d.M., J.D.S.B., **D.X.**, and H.Z. fabricated the devices, performed the measurements, and analyzed the data. G.W.W., A.B., A.E.A., and R.M.L. performed the numerical simulations. N.v.L. and G.W. contributed to the device fabrication. R.L.M.O.h.V., S.G., and D.C. grew the InSb nanowires under the supervision of E.P.A.M.B.. J.A.L., M.P., and J.S.L. deposited the aluminum shell on the nanowires under the supervision of C.J.P.. L.P.K. and H.Z. supervised the project. M.W.A.d.M. and H.Z. wrote the manuscript with comments from all authors. M.W.A.d.M., J.D.S.B., and **D.X.** contributed equally to this work.

5.9. METHODS AND ADDITIONAL DATA

5.9.1. FABRICATION PROCEDURE

1. **Nanowire deposition**: a SEM-based nanomanipulator is used to deterministically place the InSb-Al nanowires unto a degenerately p-doped Si substrate covered by 20 nm of LPCVD Si_3N_4 (devices A, C, and D) or 285 nm of thermal SiO_2 (device B).

2. **Mask preparation & lithography**: for every fabrication step, we use standard electron beam lithography techniques to create the mask. The mask consists of a layer of PMMA 950KA6 spun at 4000 rpm. After writing, the mask is developed in a solution of MIBK:IPA (1:3 ratio) for 60 s, followed by a IPA rinse for 60 s. After each deposition step, liftoff is done using acetone.

3. **Contact preparation & deposition**: before depositing the contact material, the Al and AlO_x are locally removed by Ar plasma etch. The contacts are deposited by electron beam evaporation of Cr/Au (10/100-200 nm). For device B, the side gates are also evaporated in this step.

4. **Dielectric deposition**: as a top gate dielectric we sputter 35 nm of SiN_x (devices A, C, and D).

5. **Top gate deposition**: the top gates are deposited by electron beam evaporation of Ti/Au (10/200 nm) (devices A, C, and D).

5.9.2. DEVICE INFORMATION AND SCHEMATICS

See Fig. 5.6.

5.9.3. SIMULATION OF ELECTROSTATICS AND NANOWIRE SPECTRUM

For the electrostatics simulations we use the geometry of device A (as shown in Fig.1(c) of the main text). We describe the device as an infinite wire oriented along the x-direction, with a hexagonal cross-section in the yz-plane. The electrostatics are described by the Poisson equation

$$\nabla \cdot \left(\epsilon_r(\mathbf{r})\nabla\phi(\mathbf{r})\right) = \frac{\rho_{\text{tot}}[\phi(\mathbf{r})]}{\epsilon_0}, \tag{5.2}$$

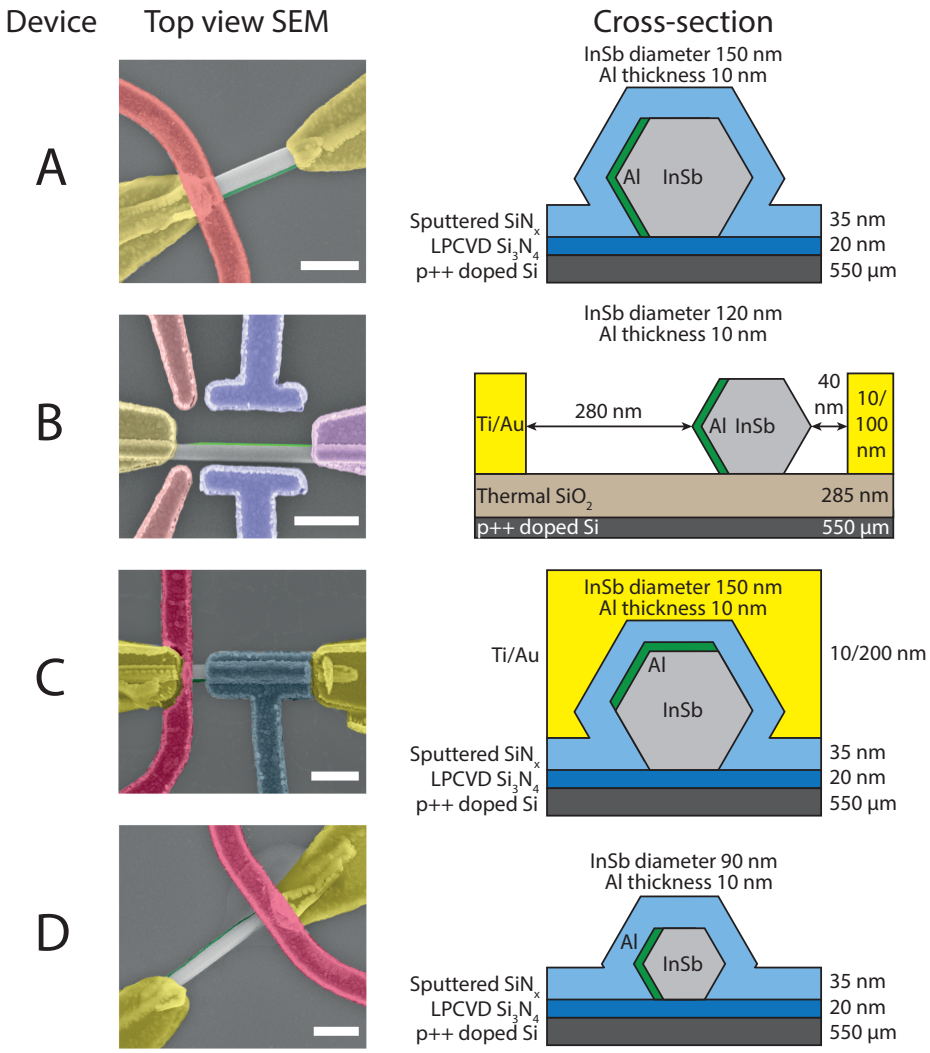

Figure 5.6: SEM images and schematic cross-sectional views of the devices used as part of this research. Data from devices A and B is presented in the main text. Data from devices C and D is presented in the supplement for completeness. Note that the data for device B is obtained by changing the voltage on the side gate (V_{SG}), shown in blue in the SEM image. Scale bar is 500 nm.

Table 5.1: Material parameters for InSb and Al.

Parameter	InSb	Al
m^*	0.0139 [21]	1
g	-40 [74]	2
Δ	0 meV	0.34 meV [134]
E_F	0 eV	10 eV [135]

where $\rho_{tot}[\phi(\mathbf{r})]$ is a functional of the potential $\phi(\mathbf{r})$. We include four contributions to ρ_{tot},

$$\rho_{tot} = \rho_e + \rho_{hh} + \rho_{lh} + \rho_{fixed}, \tag{5.3}$$

where ρ_e, ρ_{hh} and ρ_{lh} are the mobile charges of the conduction band, heavy hole band and light hole band of the InSb nanowire and ρ_{fixed} are the fixed charges in the system. For the mobile electron charges we assume a 3D electron gas density (Thomas-Fermi approximation)

$$\rho_e(\phi) = -\frac{e}{3\pi^2}\left(\frac{2m_e|\phi|\theta(-\phi)}{\hbar^2}\right)^{3/2}, \tag{5.4}$$

with θ the Heaviside step function, and for the holes

$$\rho_i(\phi) = \frac{e}{3\pi^2}\left(\frac{2m_i|\phi - E_G|\theta(\phi - E_G)}{\hbar^2}\right)^{3/2}, \tag{5.5}$$

with E_G the band gap and i corresponding to the heavy hole (hh) and light hole (lh) band respectively. For the effective masses, we take the bulk InSb values [21]. We include hole bands to describe the additional screening when the electrochemical potential is in the valence band, which can become relevant for very negative gate voltages due to the narrow band gap of InSb. To model the influence of the sputtered dielectric on the nanowire surface, the wire is wrapped in a 1 nm surface layer of 2.5×10^{18} cm^{-3} positive charge density. In the absence of other charges and gates this charge pins the conduction band of InSb at about -0.069 eV below the Fermi level at the surface. For the InSb-Al interface we assume the conduction band of InSb is pinned -0.08 eV below the Fermi level due to the work function difference between the two materials. A negative band offset of the semiconductor to the superconductor is required for a hard induced gap in the InAs-Al system [111], and we assume a similar situation in InSb-Al hybrid devices. While the precise numbers for the surface accumulation and band-offset at the InSb-Al interface are unknown, it is known that InSb wires have about a 10 times smaller density than InAs wires [91, 133], and the parameters were adjusted from the InAs ones accordingly. The Al layer is assumed to be grounded, and enters as a Dirichlet boundary condition which is set to +0.08 V. The boundary condition at the substrate-dielectric interface is set to the applied gate voltage, V_{Gate}. On the remaining three boundaries of the system we use Neumann conditions. For the dielectric constant of InSb, the sputtered SiN_x, and the LPCVD Si_3N_4 we take take 15.15, 7.5, and 8 respectively.

After the electrostatic potential has been calculated for a given V_{Gate}, we plug it into the Schrödinger equation and solve it for the cross-section of the device. We use a Rashba Hamiltonian with a Bogoliubov-de Gennes (BdG) superconducting term [30]

$$\begin{aligned} H = &\frac{\hbar^2}{2m^*(y,z)}(k_x^2+k_y^2+k_z^2)\tau_z - (E_{\text{F}}(y,z)+e\phi(y,z))\tau_z + \alpha_y(y,z)(k_z\sigma_x - k_x\sigma_z)\tau_z \\ &+ \alpha_z(y,z)(k_x\sigma_y - k_y\sigma_x)\tau_z + \frac{1}{2}g(y,z)\mu_{\text{B}}B\sigma_x + \Delta(y,z)\tau_x, \end{aligned} \tag{5.6}$$

where the effective mass m^*, the Fermi level E_{F}, the electrostatic potential ϕ, the Rashba parameters α_i, the g-factor and the superconducting pairing Δ are functions of the (y,z)-coordinates and depend on the material. Since ϕ is not solved in Al it is correspondingly set to zero there. The material parameters for InSb and Al are summarized in Tab. 5.1. If desired, the orbital effect is added to Eq. (5.6) by the Peierls substitution $k_z \to k_z - \frac{\pi}{\phi_0}B(y-y_0)$, with ϕ_0 the magnetic flux quantum. y_0 is chosen such that the average vector potential in Al is zero, resulting in a vanishing supercurrent [114]. The Hamiltonian is discretised on a quadratic mesh and constructed using the `kwant` package [115]. To accommodate the small Fermi wavelength of Al a discretisation length of 0.1 nm is used.

5.9.4. ELECTRIC FIELD DEPENDENCE OF SPIN-ORBIT COUPLING

The Rashba couplings α_y and α_z, which are nonzero only in the semiconductor region, result from the symmetry breaking by the electrostatic potential and are obtained from [21]

$$\alpha_i = \frac{eP^2}{3}\left[\frac{1}{E_0} - \frac{1}{(E_0+\Delta_0)^2}\right]\bar{\mathscr{E}}_i, \tag{5.7}$$

where the average electric field in direction i is obtained by averaging $\mathscr{E}_i$ over the whole semiconductor region. Parameters for bulk InSb are used [21]: the Kane matrix element $P = 0.9641$ eV nm, the bandgap $E_0 = 0.237$ eV, and the spin-orbit gap $\Delta_0 = 0.810$ eV. The resulting Rashba parameters α_i are plotted in Fig. 5.7(a).

We define the spin-orbit energy $E_{\text{SO}} = \frac{m^*(\alpha_y^2+\alpha_z^2)}{2\hbar^2}$. The spin-orbit energy is plotted as a function of V_{Gate} in Fig. 5.7(b). The average electric field in the nanowire increases as the applied gate voltage becomes more negative, leading to an enhancement of the spin-orbit coupling. At $V_{\text{Gate}} = 0.08$ V, the average electric field in the nanowire becomes equal to 0 due to symmetry, eliminating the influence of spin-orbit coupling on the nanowire spectrum.

5.9.5. SIMULATED BAND STRUCTURE

The band structure of the superconductor-semiconductor nanowire system for different values of V_{Gate} is shown in Fig. 5.8. To quantify the coupling of a given state to the superconductor, we calculate the weight of the state in the semiconducting region SM (see Fig. 5.1(c)) as $W_{\text{SM}} = \iint_{\text{SM}} |\Psi(k_{\text{F}})|^2 \, dy\, dz$.

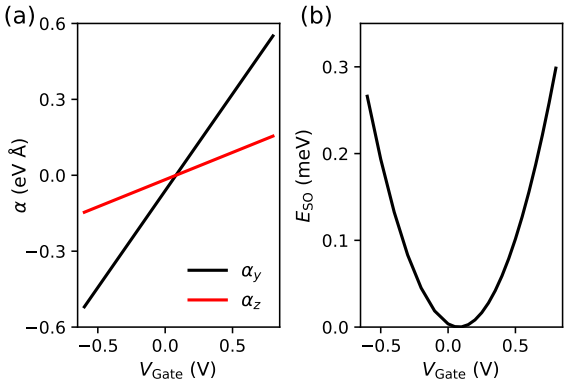

Figure 5.7: (**a**) Rashba coefficients α_y and α_z as a function of V_{Gate}. At V_{Gate} = 0.08 V, the average electric field in the wire goes to zero due to symmetry, leading to vanishing spin-orbit coupling. (**b**) Calculated E_{SO} as a function of V_{Gate}.

5

5.9.6. GAP FITTING & ADDITIONAL DATA

To extract the gap, we measure the differential conductance $\mathrm{d}I/\mathrm{d}V$ as a function of V_{Bias} and tunnel gate voltage V_{Tunnel} for different back gate voltages V_{BG}. In the tunneling limit, $\mathrm{d}I/\mathrm{d}V$ is approximately proportional to the density of states. To ensure we are in this limit, we take only the traces where the conductance at high bias ($\sim 500\,\mu$V) is between 0.03 and $0.08{\cdot}2e^2/h$. We use the BCS-Dynes expression for a dissipation broadened superconducting density of states [119] to arrive at the following expression for the conductance:

$$\frac{\mathrm{d}I}{\mathrm{d}V} = G_{\text{N}}\mathrm{Re}\left\{\frac{V_{\text{Bias}} - i\Gamma}{\sqrt{(V_{\text{Bias}} - i\Gamma)^2 - \Delta^2}}\right\}. \tag{5.8}$$

This equation is fitted to the data (separately for positive and negative bias), as shown in Fig. 5.9 for V_{BG} = -0.6 V. We take the average of the extracted gap values for different values of V_{Tunnel}, with the errorbar given by the standard deviation (results plotted in Fig. 5.2(e)).

Device B shows similar behavior to device A: as the side gate voltage is increased, the observed gap becomes smaller (as illustrated in Fig. 5.10).

In Fig. 5.11, we show differential conductance traces as a function of V_{Bias} in device D for different values of the back gate voltage. The voltage on the tunnel gate is chosen such that the transmission through the junction (parameterized by G_{N}) is constant.

Although the sub-gap conductance is similar for all three gate voltages, there is a strong broadening of the coherence peak as the gate voltage becomes more positive. This broadening is associated with dissipation due to an increase in the number of quasiparticles, caused by pair breaking in the superconductor. We plot the extracted gap Δ and dissipation broadening Γ in Fig. 5.12.

As in the other devices, the gap decreases for more positive gate voltages, although in this case the effect is minor. The size of the gap is quite stable over an extended range in

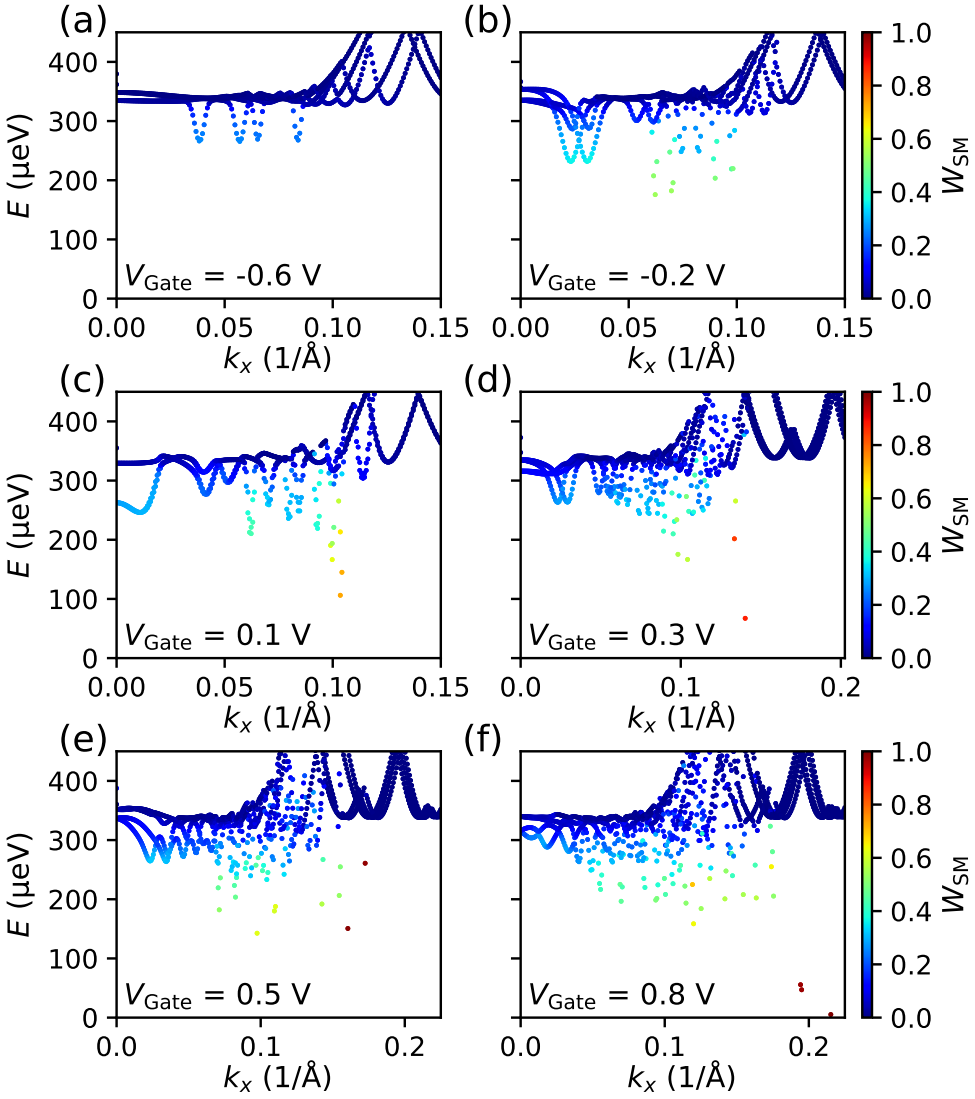

Figure 5.8: Band structure of the hybrid system calculated at $B = 0$ T for different values of V_{Gate}. The color indicates the weight of a given state in the semiconducting region. As the gate voltage is increased, the population of states with higher W_{SM} leads to a soft gap.

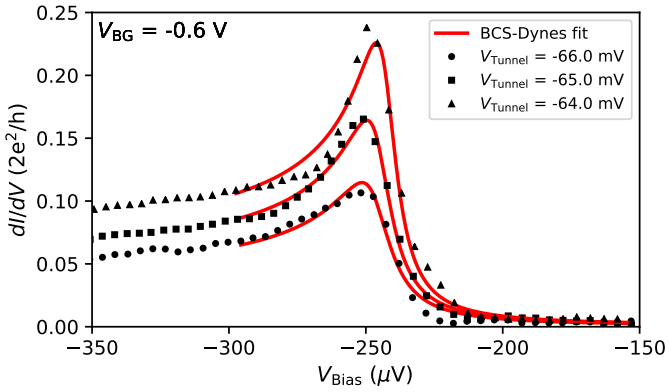

Figure 5.9: Fit (red line) of Equation (5.8) to conductance data from device A (black circles, squares and triangles) for different values of the tunnel gate voltage.

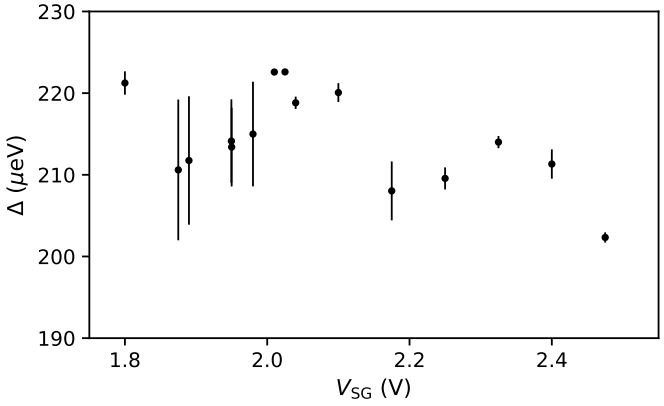

Figure 5.10: Extracted gap Δ as a function of V_{SG} for device B.

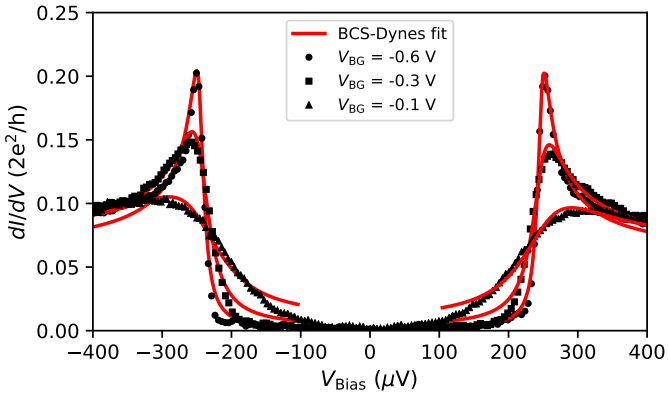

Figure 5.11: Fit (red line) of Equation 5.8 to conductance data from device D (black circles, squares and triangles) for different V_{BG} at similar junction transparencies. The dissipation broadening sharply decreases for more negative gate voltages.

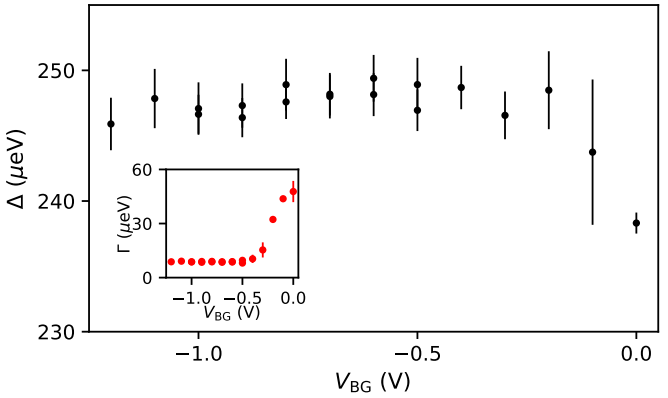

Figure 5.12: Extracted gap Δ as a function of V_{BG} for device D. Inset: dissipation broadening Γ as a function of V_{BG}. A decrease in the gap is accompanied by an increase in broadening, signalling the emergence of a soft gap.

gate voltage. We speculate that this is related to the diameter of the wire, which is smaller than in the other devices. The reduced thickness means the superconductor can screen the gate voltage more effectively throughout the wire diameter, reducing the effect of the gate on the superconductor-semiconductor coupling.

5.9.7. g-FACTOR FITTING & ADDITIONAL DATA

For each back gate voltage, we measure the $\mathrm{d}I/\mathrm{d}V$ as a function of V_{Bias} and the magnetic field B. We then identify the lowest energy peak in the spectrum. The position of this peak at a given field is obtained by a peak finding algorithm, the results of which are shown as the green circles in Fig. 5.13. The slope $|\frac{\Delta E}{\Delta B}|$ is determined by a linear fit (dashed black line in Fig. 5.13). From the slope, we get g_{eff} by using the relation $|\Delta E| = \frac{1}{2} g_{\mathrm{eff}} \mu_{\mathrm{B}} |\Delta B|$ for a spin-$\frac{1}{2}$ particle, with μ_{B} the Bohr magneton. This procedure is performed separately for positive and negative bias. The reported g_{eff} is then calculated as a weighted average of the absolute value of the positive and negative bias results (weights determined by the variance of the fit parameters).

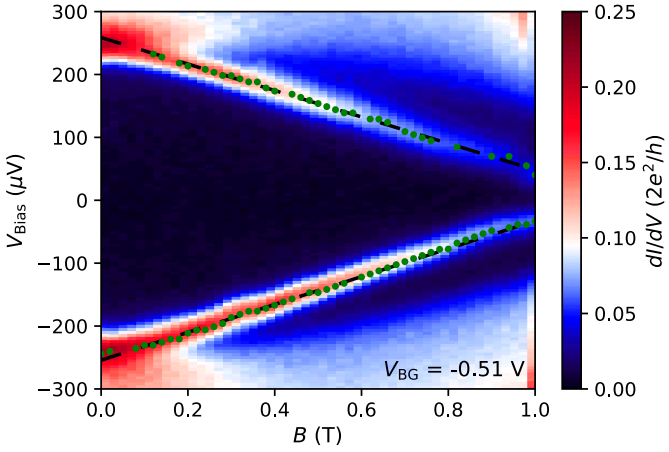

Figure 5.13: Differential conductance as a function of V_{Bias} and magnetic field. We apply a linear fit (dashed black lines) to the extracted peak positions (green circles) to obtain the average slope $\frac{\Delta E}{\Delta B}$.

The effective g-factor for device A is reported in the main text (Fig. 5.3(c) and Fig. 5.4(d), respectively). In Fig. 5.14, we plot the extracted g-factors of both L_1 and L_2 in device B. For completeness, data from device C is shown in Fig. 5.15.

The effective g-factor of L_1 (black circles) changes appreciatively when the side gate voltage is changed, with the effect comparable to the one observed in device A. In contrast, g_{eff} of L_2 (red squares) is almost unaffected by the gate and has a lower value. This may be due to L_2 being closely confined near the superconductor, leading to a decreased g-factor due to stronger hybridization, and a weaker gate response due to enhanced screening.

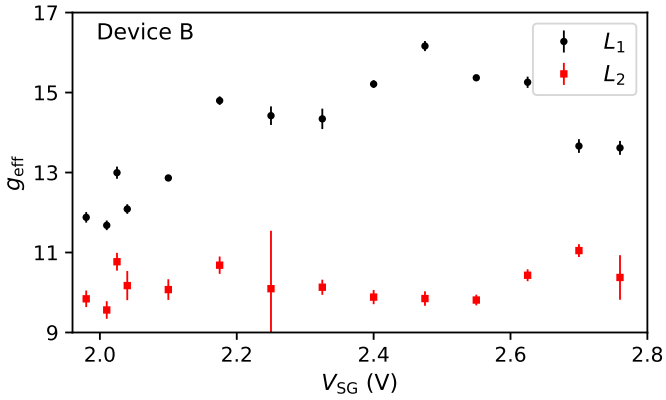

Figure 5.14: Extracted values of g_{eff} as a function of V_{SG} for L_1 (black circles) and L_2 (red squares) in Device B.

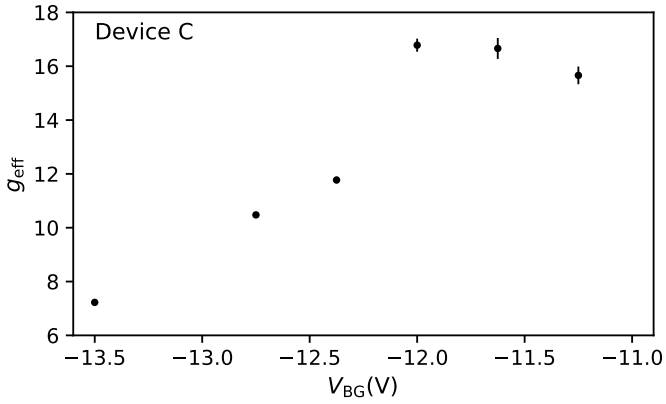

Figure 5.15: Extracted values of g_{eff} for Device C.

To determine the importance of orbital effects, we calculate the nanowire spectrum as a function of magnetic field including this effect (figures 5.16(a),(b)). The orbital effect leads to an increase of the extracted values of g_{eff} and g_{spin} (Fig. 5.16(c)). Note that the definition of g_{spin} used in the main text is no longer valid when the orbital effect is included. Nevertheless, for consistency we apply the same procedure. As we do not observe these high g-factors in any of our devices, we conclude that the orbital effect does not give a significant contribution to the observed changes of g_{eff} with the gate voltage.

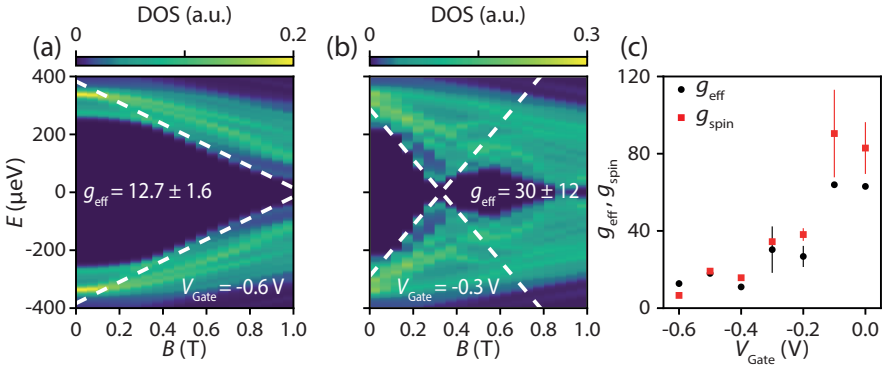

Figure 5.16: (**a**,**b**) Simulated nanowire spectrum as a function of magnetic field including orbital effects. (**c**) Extracted g_{eff} (black circles) and g_{spin} (red squares) as a function of V_{Gate}.

5.9.8. ANTICROSSING FITTING

Near the anticrossing, we approximate the energy of the lowest sub-gap state L_1 as $E_1 + \frac{1}{2}g_1\mu_B B + aB^2$. The linear term represents the Zeeman contribution to the energy, while the quadratic term is a correction to account for the curvature at high fields. This is possibly due to the presence of additional levels interacting with L_1 in this field range. As the dispersion of L_2 is mostly linear in the field range of interest, we approximate it as $E_2 - \frac{1}{2}g_2\mu_B B$. Adding the coupling parameter δ_{SO}, we find the energy levels of the coupled system from the eigenvalues of the matrix

$$\begin{bmatrix} E_1 + \frac{1}{2}g_1\mu_B B + aB^2 & \delta_{\text{SO}} \\ \delta_{\text{SO}} & E_2 - \frac{1}{2}g_2\mu_B B \end{bmatrix}.$$

By fitting the expression for the eigenvalues to the data, we extract the parameters $E_{1,2}$, $g_{1,2}$, a, and δ_{SO}. To prevent overfitting, we use estimates for the uncoupled asymptotes to constrain the fit parameters. From the obtained parameters we also calculate the splitting A, defined as the maximum deviation from zero energy of the lowest energy state L_1, after the first zero energy crossing has occurred.

5.9.9. SIMULATION OF FINITE SIZE NANOWIRE SYSTEM

To simulate the finite nanowire system, we solve the Hamiltonian (5.1) in a simplified setup. We consider a rectangular cross-section in the yz-plane similar to the one used

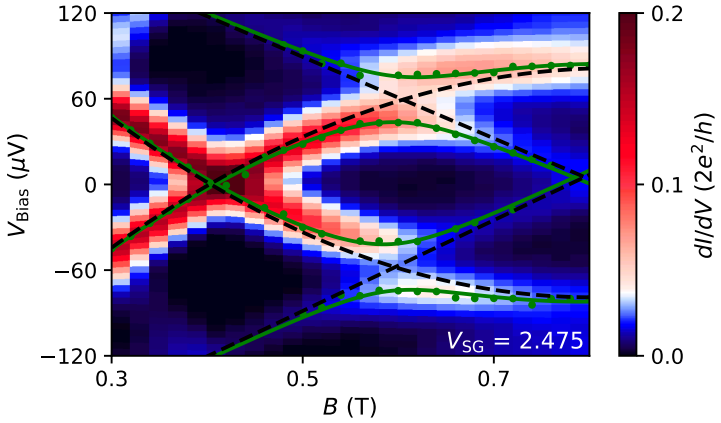

Figure 5.17: Data from device B, showing the differential conductance $\mathrm{d}I/\mathrm{d}V$ as a function of V_{Bias} and B for $V_{\text{BG}} = 2.475$ V. Green dots indicate the peak positions found using a peak finding algorithm. The fit to the data is shown in green, with the uncoupled asymptotes as the black dashed lines.

in reference [111], where the top facet of the rectangle is covered by the superconductor, and a uniform gate voltage V_{Gate} is applied to the bottom facet, as illustrated in Fig. 5.18. First, we assume an infinitely long nanowire oriented in the x-direction, and calculate the electrostatic potential in the Thomas-Fermi approximation, similar to the procedure described in 5.9.3. The fermi level in the nanowire is tuned such that it supports the same number of transverse modes at $V_{\text{Gate}} = 0$ as the hexagonal nanowire studied previously. We use the same material parameters as in the previous simulation, which can be found in table 5.1.

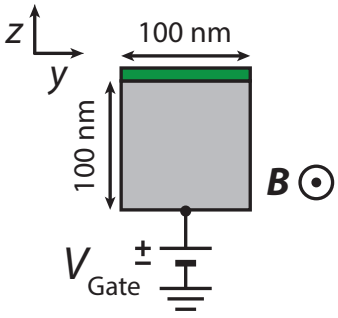

Figure 5.18: Schematic cross-section of the geometry used to simulate the finite nanowire system. A potential V_{Gate} is applied to the bottom facet, while the potential at the top facet is fixed by the work function difference between the two materials. The magnetic field is applied in the x-direction, along length of the nanowire.

We then plug the resulting electrostatic potential into 5.1 and solve the Schrödinger equation to find the low energy spectrum of the finite nanowire. We take a length of 750 nm, similar to the studied devices. We calculate only the modes in the semiconductor,

assuming a superconducting gap of $\Delta = 250\ \mu$eV. We find that the origin of the level repulsion between states is indeed spin-orbit coupling, which couples different longitudinal (along the x-direction) states within the same transverse (y- and z-directions) subband.

The result is illustrated in Fig. 5.19, where we plot the low energy spectrum as a function of Zeeman energy E_Z for a fixed value of V_{Gate} and different values of α. An increase in the spin-orbit coupling strength leads to an increase in the level repulsion.

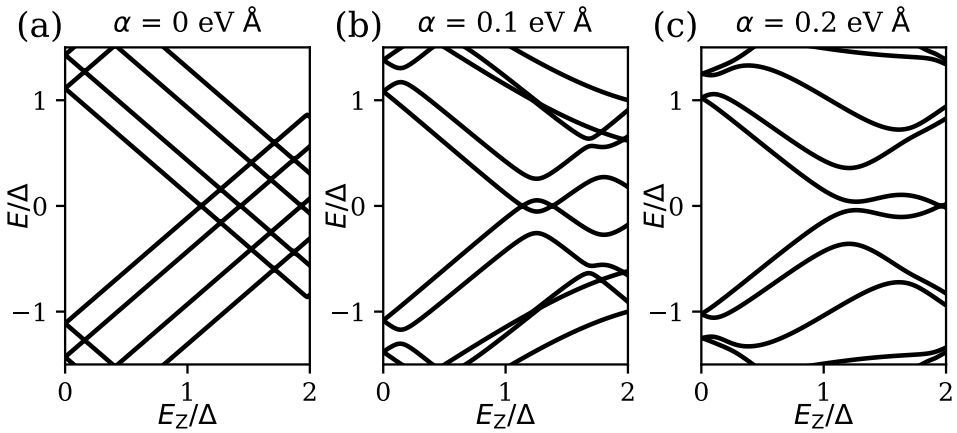

Figure 5.19: Calculated low energy spectrum of the finite size nanowire as a function of Zeeman energy for different values of α. Values calculated for V_{Gate} = -0.536 V, which is also used in main text Fig.4(d). All energy scales are in units of the superconducting gap Δ.

However, even if α is fixed, the magnitude of the level repulsion can be changed by changing the confinement potential, as demonstrated in Fig. 5.20.

When the gate voltage is changed, it alters the confinement potential. This affects the energy of the levels coupled by the spin-orbit coupling, and as such directly influences the magnitude of δ, even though the spin-orbit coupling strength itself is not changed appreciatively. In Fig. 5.21 we plot the calculated energy gap due to level repulsion, 2δ, and the maximum splitting from zero energy of the lowest energy state after the first zero crossing, A, as a function of V_{Gate}. The two parameters follow opposite trends, consistent with the experimental observation in Fig. 5.4(f).

However, the trend with gate voltage is opposite: δ increases with more positive gate voltage, whereas in the experiment it decreases. We note that the geometry used in this simulation is a simplified version of the one used in the experiment. The dependence of the confinement energy on gate voltage is strongly dependent on the geometry, which differs between the simulation and the experiment. It is therefore expected that the trend of δ with gate voltage is not universal, and requires the details of the systems to be very similar before comparisons can be made.

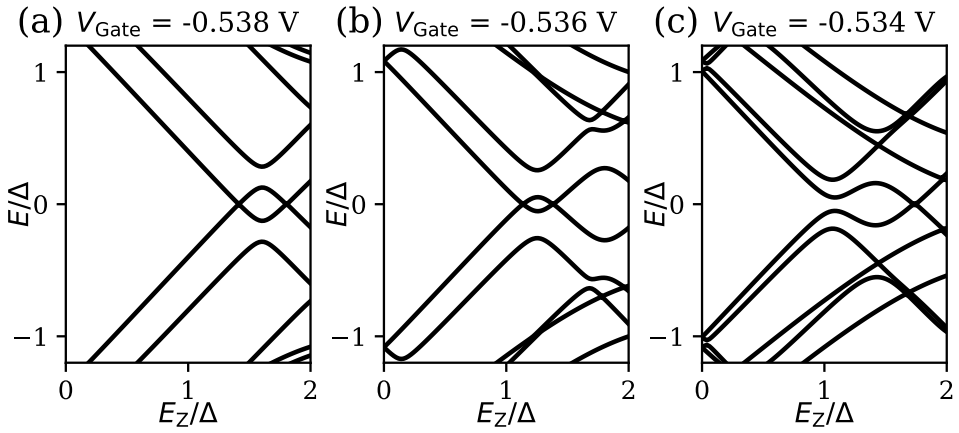

Figure 5.20: Calculated low energy spectrum of the finite size nanowire as a function of Zeeman energy for different values of V_{Gate}. Values calculated $\alpha = 0.1$ eV Å, energy scales in units of Δ.

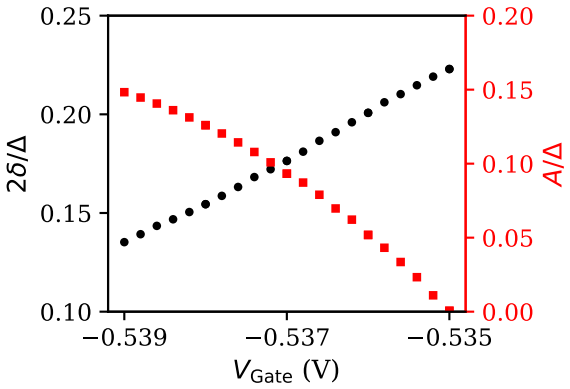

Figure 5.21: Dependence of the energy gap 2δ and the splitting A, in units of Δ, on the gate voltage V_{Gate}.

5.9.10. ADDITIONAL ZBP DATA

Fig. 5.22(a) shows the differential conductance measured in device A as a function of V_{Bias} and V_{Tunnel}, for B = 0.35 T and V_{BG} = -0.37 V. The low energy spectrum in this parameter regime does not depend on the transmission of the NS-junction. In Fig. 5.22(b), we show line traces for different values of V_{Tunnel}. Even though the transmission of the junction is changed by a factor of two, the peak position of the low energy states are not affected. Data from main text Fig. 5.5 was obtained for V_{Tunnel} = -87 mV.

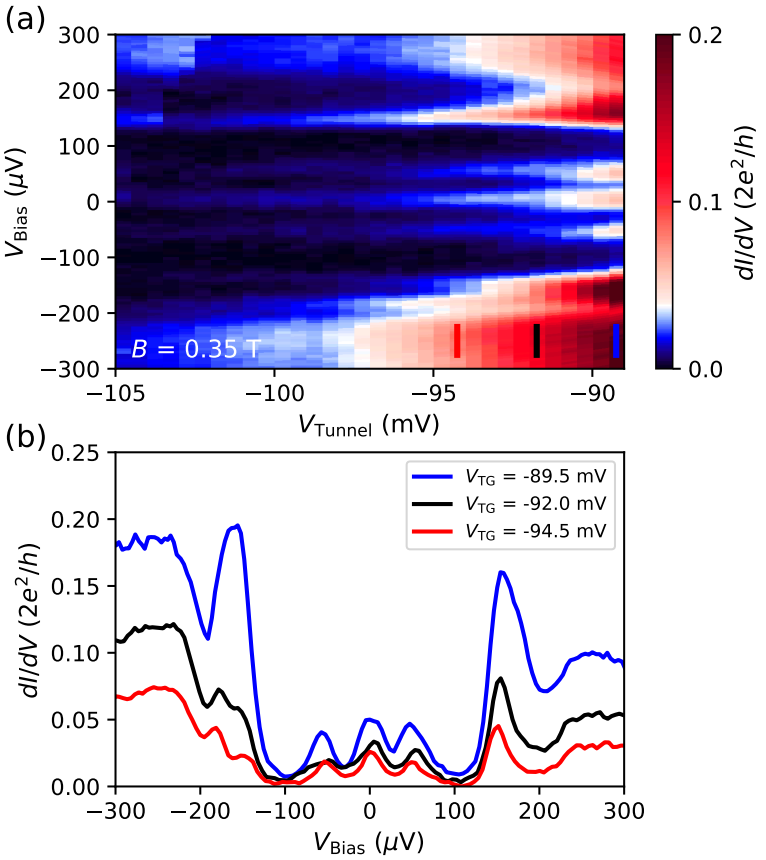

Figure 5.22: (**a**) dI/dV measured in device A as a function of V_{Bias} and V_{Tunnel} for B = 0.35 T and V_{BG} = -0.37 V. (**b**) Line traces at the values of V_{Tunnel} indicated by the colored lines in panel (a).

Fig. 5.23 shows additional data on the evolution of the level repulsion between L_1 and L_2 in device A (supplementing the data presented in main text figures 5.5(a-c)) as the back gate voltage is increased. As discussed in the main text, we do not find an extended region in parameter space with a stable zero bias conductance peak.

In Fig. 5.24 we show the low energy spectrum of device A as a function of V_{Bias} and

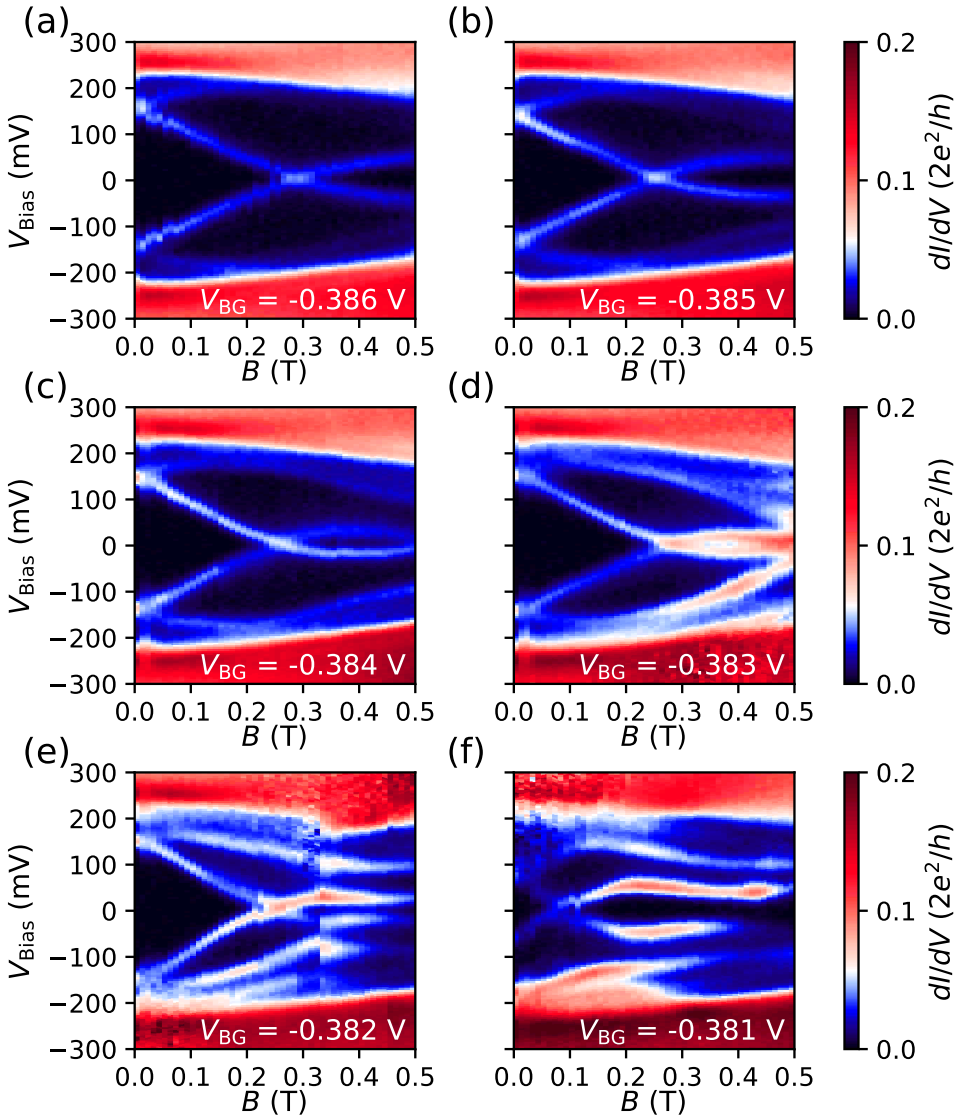

Figure 5.23: Differential conductance as a function of V_{Bias} and magnetic field. Although the lowest energy state stays near zero over an extended magnetic field range for some gate voltages, this behavior is not robust.

V_{BG} for different magnetic fields (supplementing the data presented in main text figures 5.5(e,f)). For specific combinations of magnetic field and gate voltage, we can find a zero energy state. However, as we do not find an extended region in parameter space, it is unlikely that a topological phase transition is responsible for this observation.

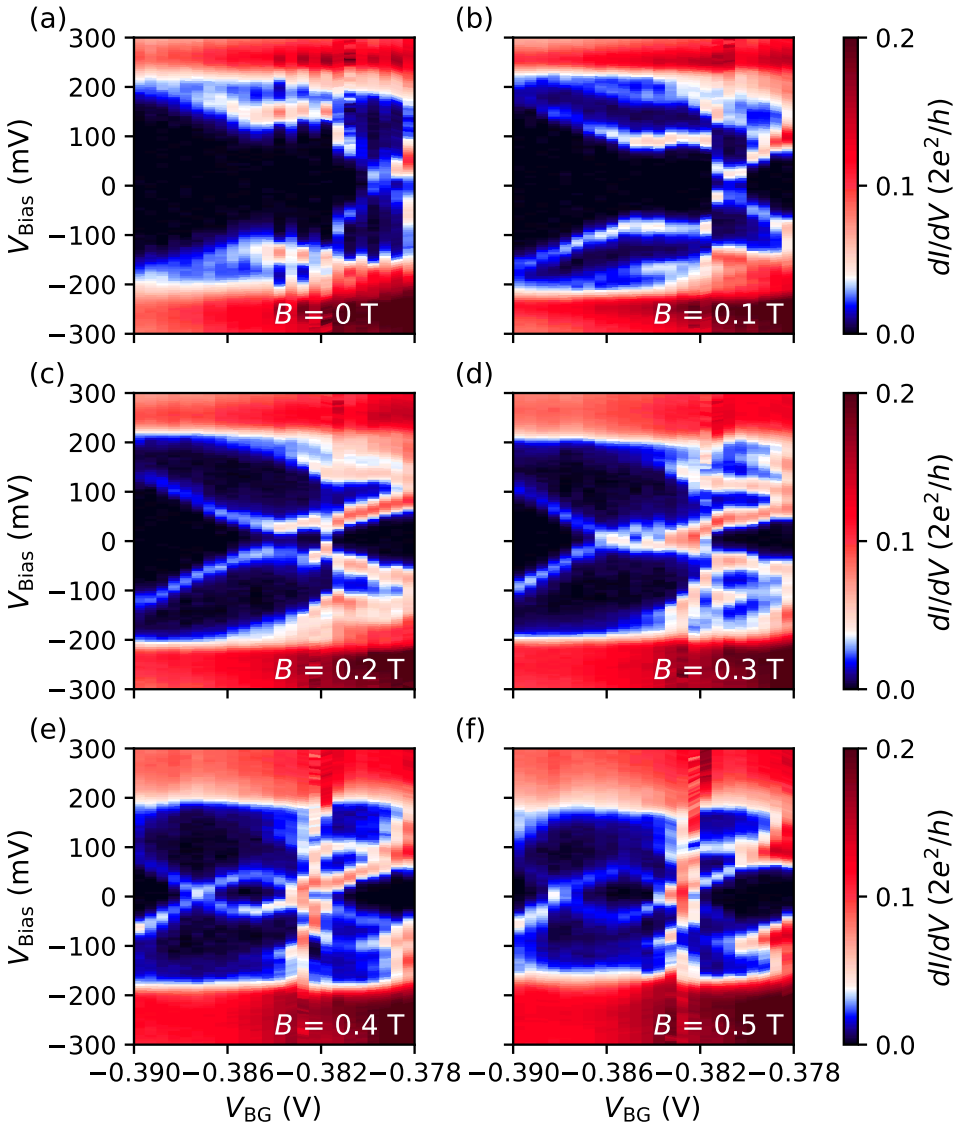

Figure 5.24: Differential conductance as a function of V_{Bias} and V_{BG}. We find some stable ZBPs for certain ranges in back gate voltage at specific fields, but this is only true for fine tuned parameters.

6

IN-PLANE SELECTIVE AREA INSB-AL NANOWIRE QUANTUM NETWORKS

Strong spin-orbit semiconductor nanowires coupled to a superconductor are predicted to host Majorana zero modes. Exchange (braiding) operations of Majorana modes form the logical gates of a topological quantum computer and require a network of nanowires. Here, we utilize an in-plane selective area growth technique for InSb-Al semiconductor-superconductor nanowire networks. Transport channels, free from extended defects, in InSb nanowire networks are realized on insulating, but heavily mismatched InP (111)B substrates by full relaxation of the lattice mismatch at the nanowire/substrate interface and nucleation of a complete network from a single nucleation site by optimizing the surface diffusion length of the adatoms. Essential quantum transport phenomena for topological quantum computing are demonstrated in these structures including phase-coherence lengths exceeding several micrometers with Aharonov-Bohm oscillations up to five harmonics and a hard superconducting gap accompanied by $2e$-periodic Coulomb oscillations with an Al-based Cooper pair island integrated in the nanowire network.

This chapter has been published as, *In-plane selective area InSb-Al nanowire quantum networks*, Roy L. M. Op het Veld*, **Di Xu***, Vanessa Schaller, Marcel A. Verheijen, Stan M. E. Peters, Jason Jung, Chuyao Tong, Qingzhen Wang, Michiel W. A. de Moor, Bart Hesselmann, Kiefer Vermeulen, Jouri D. S. Bommer, Joon Sue Lee, Andrey Sarikov, Mihir Pendharkar, Anna Marzegalli, Sebastian Koelling, Leo P. Kouwenhoven, Leo Miglio, Chris J. Palmstrøm, Hao Zhang and Erik P. A. M. Bakkers in Commun Phys **3**, 59 (2020).
* These authors contributed equally to this work.

6.1. INTRODUCTION

Indium-antimonide (InSb) and Indium-arsenide (InAs) nanowires are promising candidates for realizing Majorana-based topological quantum computers [18]. InSb, in particular, is interesting for its high electron mobility, strong spin-orbit coupling and large Landé g-factor [124, 136, 137]. Over the past years, extensive efforts have been made to improve the quality of InSb nanowires, grown by the vapor-liquid-solid (VLS) mechanism [38, 73]. A major achievement is the clean and epitaxial semiconductor-superconductor interface relying on in situ metal evaporation and complex substrate processing [42, 91]. This has been critical for showing high quality Majorana zero-modes, a milestone toward braiding experiments [15]. To braid these Majorana states, scalable nanowire networks with a high degree of interconnectivity are required [62]. Recently, out-of-plane growth of InSb nanowire networks has been demonstrated by merging multiple wires during VLS growth. Phase-coherent and ballistic transport have been observed, demonstrating the high quality of these network structures [42, 138]. This technique, however, requires predefined positioning of the nanowires with nanometer accuracy in order to form networks, leading to a drastic decrease in yield with increasing network complexity. Moreover, merging of VLS nanowires inevitably forms a widening of the nanowire diameter at and around the junction with a 75% chance of a defect forming at the junction, which negatively affects the one-dimensionality of the system [42].

A more scalable approach, would be to use an in-plane selective area growth (SAG) technique (i.e., parallel to the substrate surface), that relies on a template or mask to selectively grow one semiconductor material on top of another [139–145]. This technique has several advantages over out-of-plane growth. First, the flexibility of network designs is significantly enhanced, as the preferred design can be written and etched directly into a mask, enabling complex structures. Second, the growth can be confined within the mask, keeping the entire structure one-dimensional with an easily controllable and constant cross-section size. Finally, the technique excels in scalability, readily allowing for the growth of complex structures suggested for Majorana braiding experiments in a variety of theoretical proposals [59, 61, 62]. The large lattice mismatch between InSb and any other III-V semiconductor substrate material [146], however, poses an important challenge making it difficult to grow defect-free InSb nanowires on large-bandgap or insulating substrates. Furthermore, the disorder created by the lattice mismatch can be detrimental to the topological protection of Majorana states [37]. Most of the previous SAG studies have focused on an InAs-based material system for nanowire networks [140–144], which has a smaller lattice mismatch with InP or GaAs substrates. InSb nanowires have been grown by SAG using molecular beam epitaxy (MBE) [145, 147]. Here, we demonstrate an in-plane SAG technique for scalable and high-quality InSb nanowire networks, which shows all the relevant quantum transport properties (e.g., long coherence length and excellent-induced superconducting properties) necessary for topological qubits.

6.2. RESULTS

6.2.1. GROWTH OF IN-PLANE SELECTIVE AREA INSB NETWORKS

In this study, we use InP as a substrate because it has a type I band alignment with InSb and becomes semi-insulating at low temperatures. The large bandgap of 1.34 eV compared to 0.17 eV of InSb ensures good confinement [148]. The lattice mismatch between these materials is 10.4%, making large-scale defect-free growth of InSb a challenge [149]. It is important to have defect-free single crystalline material to obtain a high carrier mobility by reducing electron scattering [150]. On a (100) substrate, many stacking faults are expected to form inclined to the substrate (along the {111} planes) to relax the lattice strain [139]. To avoid the formation of these inclined defects, we use InP (111)B as the growth substrate. We will show that strain from the lattice mismatch is relieved directly at the substrate/nanowire interface. Moreover, atomically flat twin planes can form parallel to the substrate, above which the nanowires grow without extended defects, separating the mismatch-induced disorder from the nanowire top part. On a (111)B substrate, growth nuclei with an odd and even number of horizontal twins will have a 180°-rotated crystallographic orientation, with respect to each other. When these nuclei merge by lateral growth, an inclined defect is formed at the interface; details of the atomic structure of such a defect can be found in Supplementary Fig. 6.6. These defects may act as scattering sites for electrons and can be found in many reported SAG studies [139, 143, 144, 150]. Therefore, it is important to enable growth of a complete, in-plane network structure from a single nucleation site, which is difficult to achieve for MBE-grown InSb [145, 147]. For this, a large surface diffusion length of the precursor material is required, as well as a low nucleation probability. Here, we show that metalorganic vapor-phase epitaxy (MOVPE)-grown InSb in-plane selective area networks (InSANe) can indeed generate complicated 1D networks from a single nucleation site.

First, the desired structures are etched into a 20-nm-thick Si_xN_y mask (Supplementary Fig. 6.7), aligned to four different crystal directions, the [−211], [−101], [−1 − 12], and [0 − 11], on an InP (111)B substrate (Fig. 6.1a). These four orientations are all threefold symmetric, such that networks can be grown with angles of 30, 60, and 90 degrees between two nanowires (Supplementary Fig. 6.8). The growth starts by forming a nucleus in one of the lines, which develops into an InSb island over time (Fig. 6.1b, Supplementary Fig. 6.9). All nuclei are terminated with a {111}B top facet and {110} side facets (Fig. 6.1b), regardless of the line orientation, implying that surface growth kinetics and lateral growth rates are identical for all <110> and <112> growth directions. For longer growth times, the growth continues, starting from this single nucleus, in the lateral direction following the mask opening by growing {110} facets, as evidenced by atomic force microscopy and transmission electron microscopy (TEM). When the structure is fully grown in the in-plane direction, the growth continues in the vertical <111>B direction. The height of the InSb network can be precisely tuned by the growth time (Supplementary Fig. 6.10). Under ideal conditions, a yield of up to 80% can be achieved for structures several microns in length (Supplementary Fig. 6.11). When the InSb grows higher than the mask, it also starts to expand in the lateral direction, especially at acute corners of the structure (Supplementary Fig. 6.12), which is not ideal for transport measurements as the one-dimensional confinement is lost. An example of a network is shown in Fig. 6.1c (and Supplementary Fig. 6.13), whose structure corresponds to the proposed geometry

of a four-topological-qubit device [61]. The {110} planes of the original growth fronts are visible on the convex corners of this structure (Fig. 6.1d). These facets do not form on the concave corners due to the connection with another branch of the network (Supplementary Fig. 6.12). Our platform provides freedom of design and scalability for a plethora of device structures (Supplementary Fig. 6.14).

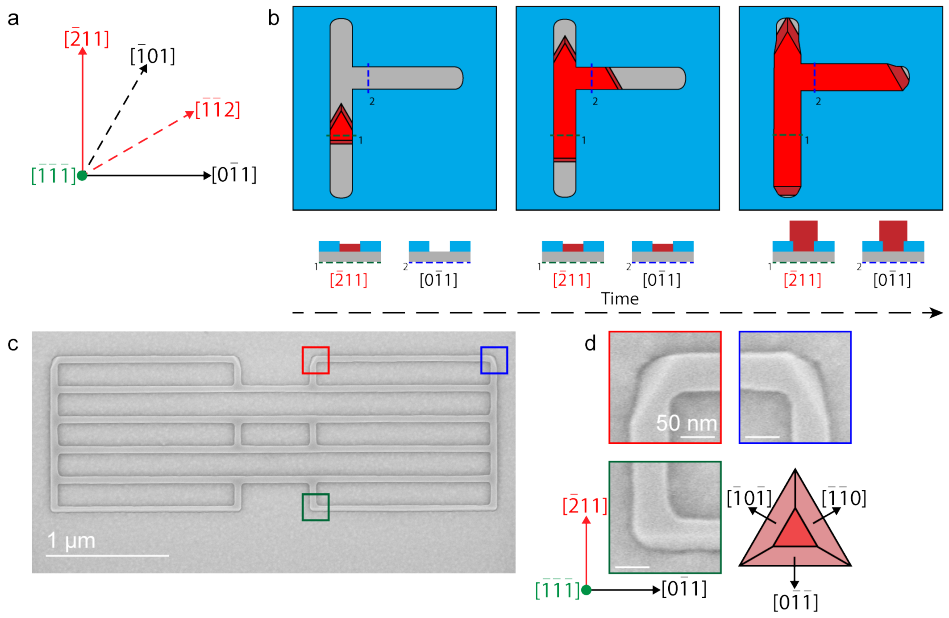

Figure 6.1: **Controlled growth of in-plane selective area InSb networks.** **a** The four growth directions on a (111)B substrate suitable for in-plane nanowire growth. **b** Time evolution for growth of an in-plane InSb (red) nanowire network on an InP (111)B substrate (gray) with a 20 nm thick Si_xN_y mask (light blue) for selectivity. The growth fronts remain the same during the growth of the network. Schematics of the cross-sections below show the relative height of the InSb compared to the height of the mask. The network grows much faster in the in-plane direction than the out-of-plane direction (Supplementary Fig. 6.10). **c** The in-plane InSb nanowires controllably grow in the <112> and the <110> families of crystal directions. Scale bar is 1µm. **d** Zoom-in on the corners of the structure in **c**. Scale bar is 50 nm. The {110} facets that form the growth fronts are still visible at these edges.

In order to minimize the formation of inclined defects, the number of nucleation sites in the mask openings per unit length (n) is investigated as a function of the input V/III ratio of the tri-methyl-indium (TMIn) and tri-methyl-antimony (TMSb) precursors. For this purpose, InSb is grown for a short time (1 min) to observe the early stages of nucleation and understand the nucleation probability as a function of V/III ratio. n is determined for growth in the <112> and <110> oriented trenches for different V/III ratios (Fig. 6.2). Datapoints are averages of ten 40 nm wide and 50µm long lines on each sample. The results show a clear decrease of n, and thus an increase of the diffusion length of the adatoms on the InP surface, with increasing V/III ratio. At the highest TMSb pressures, the nucleation of InSb islands is completely inhibited. The inset in Fig. 6.2a is a logarithmic plot of the same data up to a V/III ratio of 20,000, showing a decrease

of n with increasing V/III ratio. We note that there is no parasitic growth on the mask under any of these conditions. The red circle and black square (blue and green triangle) datapoints are all taken with the same TMIn (TMSb) partial pressure and varying TMSb (TMIn) partial pressure, respectively. Fig. 6.2a shows that these datapoints all follow the same trend, indicating that not the total flow but the V/III ratio is important in the studied range. Fig. 6.2b shows a scanning electron microscopy (SEM) image of nuclei grown using a low V/III ratio. The InSb islands are only tens of nanometers long and 20 nm thick. Fig. 6.2c shows an SEM image of a representative nucleus grown with a very high V/III ratio. Here, the InSb island is much longer (300 nm) and <20 nm high. The time series in Supplementary Fig. 6.10 shows that the InSb structures nucleate from a single site and over time, during growth under the same growth conditions, no new nucleation sites appear as all grown segments in a single structure are connected at all times. From these results, we conclude that Sb changes the surface energy on the InP substrate and enhances the surface diffusion of the In precursor material [151]. For the growth of large networks, a high V/III ratio is thus beneficial to have a minimum number of nucleation events. By integrating over the total volume of all nuclei in a 50µm long line structure, we find that the lateral growth rate is determined by the TMIn flux (with higher flux giving faster growth rates) and the V/III ratio (with higher V/III ratio giving slower growth rates). The largest single crystalline networks we have fabricated with our method have a wire diameter of 60 nm with lengths of up to 11µm (Supplementary Fig. 6.14d).

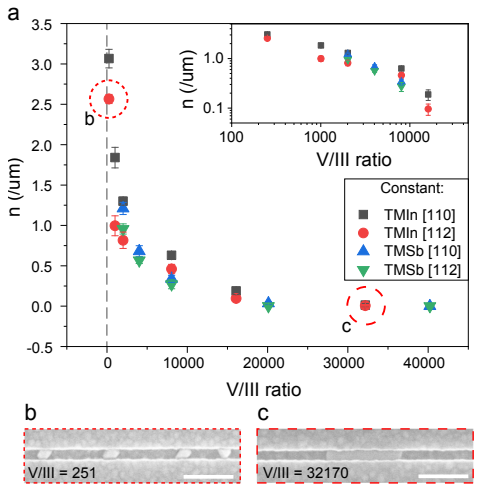

Figure 6.2: **Effect of V/III ratio on nucleation of InSb on InP. a** The average number of nucleation points n per micrometer trench length as a function of the V/III ratio during the growth for different crystal directions of the mask openings ([110] and [112]). The datapoint averages are gathered by analyzing 500µm length of mask opening (ten lines, each 50µm long) and error bars represent the standard deviation. Varying the TMSb (TMIn) flow with constant TMIn (TMSb) flow leads to the same value for n as a function of V/III, showing that the total flow does not influence the nucleation of the InSb on the InP. At a ratio of 40,000, the nucleation of InSb is completely inhibited by Sb adatoms on the InP surface. Inset: logarithmic plot of the data up to a V/III ratio of 20,000. **b**, **c** Top-view SEM image showing the different morphologies of, and distance between, InSb islands for low **b** and high **c** V/III ratios. Scale bar in **b**, **c** is 200 nm.

6.2.2. PHYSICAL CHARACTERIZATION

The structural quality of the in-plane wires has been investigated by TEM. Focused ion beam (FIB) sample preparation was used to cut out cross-sections parallel and perpendicular to the long axis of in-plane [−211] and [0−11] oriented nanowires. Fig. 6.3a shows a cross-sectional view of a nanowire grown along the [−211] direction. The energy-dispersive X-ray spectroscopy (EDX) elemental mapping (Fig. 6.3b) shows the InP substrate (green) with the InSb nanowire (red) grown slightly higher than the Si_xN_y mask (blue, top indicated by a white dash on the right). An inverse fast Fourier transform (IFFT) of a zoom-in on the InSb/InP interface (Fig. 6.3c) shows misfit dislocations (Supplementary Note 6.4.1.1) and their confinement to the interface between the two materials. This real space image was constructed by filtering for the (110) periodicity in the fast Fourier transform (FFT) pattern of a high-resolution scanning TEM (STEM) image and subsequently creating an IFFT image. In this image, the ratio of the number of InP/InSb atomic columns is 96/87 = 1.1034. The 10.34% decrease in vertical lattice planes is in good agreement with the reported value of a 10.4% lattice mismatch between InSb and InP [137], indicating that the heterostructure is fully relaxed (inelastically) at the interface in the lateral direction. Here, it should be mentioned that when imaging orthogonally to this crystal direction the InP/InSb interface cannot be imaged accurately due to the slight recess of the wire into the substrate. Most likely, along the long axis, misfit dislocation planes will also be present with the dislocation lines located at the interface, as we do not see vertically extending defects orthogonal to the long axis of the wires in TEM studies. An FFT of the InSb, the InSb/InP interface, and the InP regions of the high-resolution STEM image (Fig. 6.3d in green, blue, and purple box, respectively) show that the InSb and the InP are both single crystalline, while the FFT pattern of the interface region displays a combination of two single crystalline patterns with a different lattice constant, indicating that the materials are fully relaxed. To visualize the presence of horizontal twin planes (Supplementary Note 6.4.1.4) in the InSb structures, we investigate a cross-section of a nanowire grown along the <110> direction (Fig. 6.3e). A zoom-in on the bottom part (Fig. 6.3f) reveals a set of two twin boundaries a few nanometers above the InP/InSb interface (Fig. 6.3g). Horizontal twin planes have in total been observed in 12 out of 17 TEM samples (six in perpendicular cuts of <110> grown wires and six in parallel cuts of <112> grown wires, the other five TEM samples did not show horizontal twin planes). The twin planes are always located within a few nanometers above the InSb/InP interface and a single crystalline InSb transport channel always forms above the horizontal twin. Once a twin plane is formed in a nucleus it will be extended into the rest of the network by lateral growth. We note that antiphase boundaries (Supplementary Note 6.4.1.2) and inclined twin planes (Supplementary Note 6.4.1.3) are absent in these structures. The complete relaxation of lattice strain at the nanowire/substrate interface (bottom part) followed by horizontal twin planes helps to separate the electron wavefunctions in the active region of the device from the interface disorder [152]. This effect allows us to fabricate in-plane InSb nanowires on InP that have quantum transport properties comparable to free-standing structures, as demonstrated by the high-quality quantum transport in the next section.

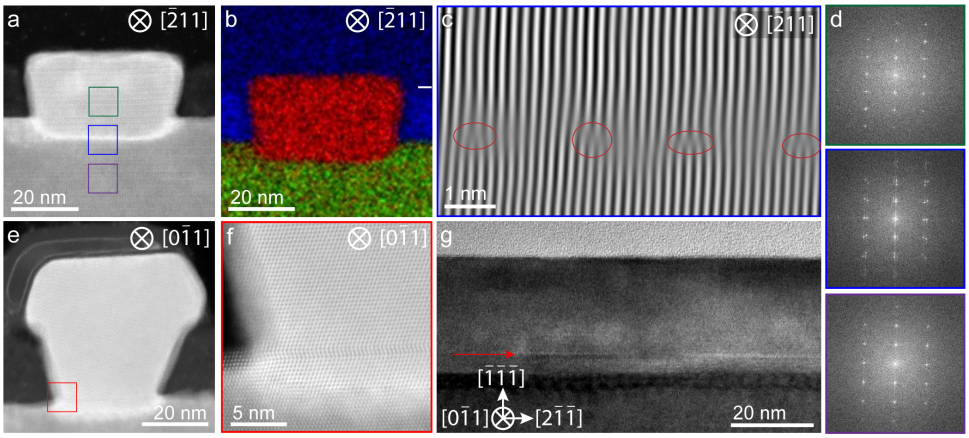

Figure 6.3: **Crystal quality analysis of InSb nanowires and the InSb/InP interface. a** Cross-section transmission electron microscope (TEM) image of an in-plane selective area (InSANe) InSb nanowire grown and imaged along the [−211] direction. Scale bar is 20 nm. **b** EDX map of a with P (green), Sb (red), and Si (blue) depicted showing the InSb nanowire, the InP substrate, and the Si_xN_y mask. The top of the mask is indicated by a white dash on the right; note that SiO_x has been deposited on top of the sample to protect it during focused ion beam sample preparation. Scale bar is 20 nm. **c** Zoom-in on the InSb/InP interface in a (blue square) focusing on the atomic columns using an inverse fast Fourier transform (FFT) procedure filtered for the (110) periodicity. Scale bar is 1 nm. The vertical lines represent the columns of atoms which, at the interface of InSb/InP, show misfit dislocations, encircled in red. Counting the ratio of InSb columns and InP columns gives a lattice mismatch of 10.34%. **d** Fast Fourier transform of the InSb nanowire (**a**, green), the InSb/InP interface (**a**, blue), and the InP substrate (**a**, purple), demonstrating that the InSb and InP regions are both single crystalline. The FFT of the InSb/InP interface region shows double spots indicating two different lattice parameters. **e** Cross-section TEM image of an InSANe InSb nanowire grown and imaged along the [0 − 11] direction. Scale bar is 20 nm. **f** Zoom-in of **e** where a pair of horizontal twin planes can be observed a few nanometers above the InP/InSb interface. Scale bar is 5 nm. **g** Cut along a <112> direction grown wire, looking in the perpendicular <110> zone axis. A few nanometers above the InP/InSb interface, a horizontal twin plane can be observed along the entire observed length of the wire, indicated here by a red arrow. Scale bar is 20 nm.

6.2.3. QUANTUM TRANSPORT

We now turn to the quantum transport properties of our InSb InSANe system to demonstrate its feasibility for topological quantum information processing. The key ingredient in the measurement-based gate operation and topological qubit readout is the phase coherence, which can be revealed by the Aharonov-Bohm (AB) effect [61, 62]. The magneto-conductance in Fig. 6.4a reveals the AB oscillations in a fabricated InSANe device shown in the inset of Fig. 6.4b. The oscillation amplitude is 20% of e^2/h at 20 mK, about an order of magnitude larger than for previously reported InSb VLS nanowire network structures [42]. Therefore, higher harmonics (up to the third) in the FFT are observed (Fig. 6.4b). This means that the electron's interference due to phase coherence remains measurable after circulating through the loop 1.5 times, translating to 9 microns in this device. We note that the precise value of the phase-coherence length is not crucial, and that a large AB amplitude, especially higher orders of AB oscillations, presents the qualitative advancement in this work compared to previous studies. A second device shows an even larger AB amplitude (~ 60% of e^2/h in Fig. 6.4c) and up to five harmonics in the FFT spectrum (Fig. 6.4d), with the SEM image of the device shown in the inset of

Fig. 6.4d. The measured AB period matches the loop area in all measured devices, i.e., their periods equal h/ne (for the nth harmonic). This result corroborates that the lattice mismatch-induced disorder at the nanowire-substrate interface has negligible effect on the phase-coherent transport. Finally, we observe a sharp weak anti-localization (WAL) peak in the magneto-conductance of this device around zero-magnetic field (Fig. 6.4e), indicating the strong spin-orbit nature of the InSb nanowire. Fitting this WAL curve requires a new theoretical model applicable for nanowire networks, which will be developed in future studies.

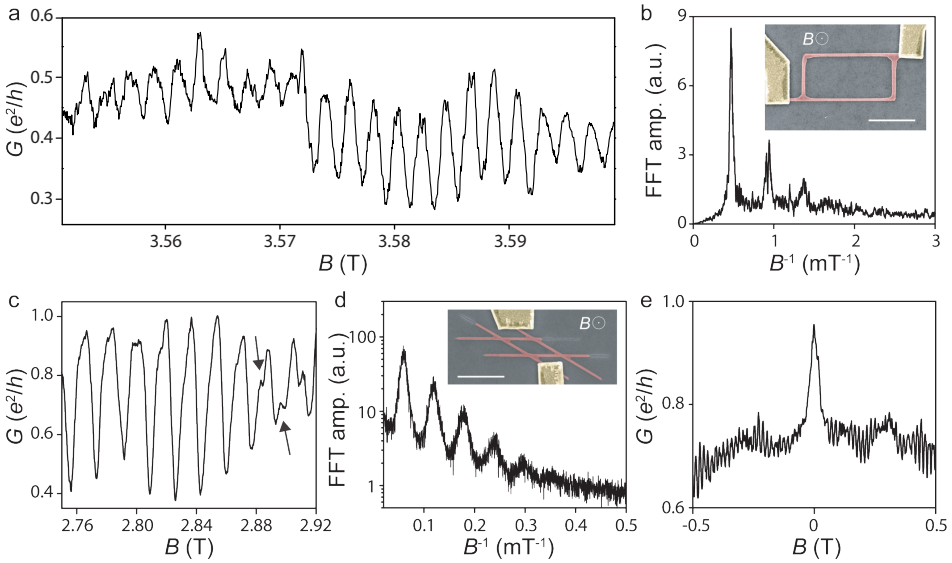

Figure 6.4: **Aharonov–Bohm and WAL effects in InSANe nanowire loops. a** Magneto-conductance of device A shows Aharonov–Bohm (AB) oscillations with a period of ~2 mT. **b** Fast Fourier transform (FFT) spectrum of the AB oscillations from device A, indicating the frequency peaks up to the third-order harmonic. Inset, false-color scanning electron microscopy (SEM) image of the device. An InSb nanowire loop (red) is in contact with normal metal electrodes Cr/Au (yellow) with an out-of-plane magnetic field and a fridge temperature of 20 mK. The device has a global top gate that is not shown in the SEM image. Scale bar is 1 µm. The measured AB period matches the loop area of ~2 µm^2. **c** Magneto-conductance of device B shows a larger AB period and oscillation amplitude (~ 0.6 e^2/h), due to its smaller loop area compared to device A. The arrows indicate oscillations due to higher AB harmonics. **d** FFT spectrum of device B (SEM in inset with scale bar 1 µm) showing up to five harmonic peaks. **e** Magneto-conductance of device B (ensemble averaged) shows a sharp WAL peak at $B = 0$ T.

The next important step is to introduce superconductivity in the InSb InSANe system. In order to form superconducting contacts for the creation of Majorana zero modes, the InSANe InSb samples, after growth, are transferred from an MOVPE to an MBE system. Here, the surface oxides are removed using atomic hydrogen cleaning under (ultra-high vacuum) UHV conditions followed by 7 nm aluminum deposition at a sample temperature of 120 K, leading to a clean and smooth InSb-Al interface (Supplementary Fig. 6.15) [42].

Since in situ shadowing methods to selectively grow superconductors on these InSb in-plane structures are not yet developed, we exploit a reliable selective etching recipe to selectively etch Al on InSb. This novel fabrication recipe enables us to define the posi-

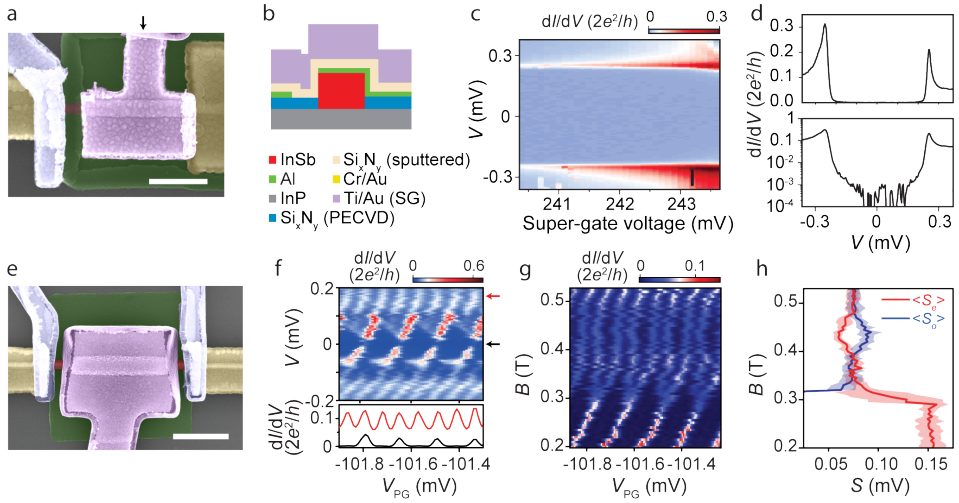

Figure 6.5: **Hard gap and 2e-periodic Coulomb blockade in InSANe InSb–Al hybrid nanowire devices. a** False-color scanning electron microscopy (SEM) of a typical normal–nanowire–superconductor (N–NW–S) device for illustration purpose, with a schematic of the device cross-section **b** at the position indicated by the black arrow in **a**. The InSb nanowire (red) is covered by a 7 nm thick Al layer (green, covered by the etch mask). Part of the Al film on the nanowire is selectively etched before normal metal electrodes deposition (yellow, Cr/Au), and gate-tuneable tunnel barrier. The tunnel- and super-gates are Ti/Au (blue and purple, respectively), deposited on top and separated from the wire by a Si_xN_y dielectric layer as seen in the cross-section schematic on the right. Scale bar is 500 nm. Fridge temperature is 20 mK. **c** Differential conductance (dI/dV) as a function of bias voltage (V) and super-gate voltage in the tunneling regime, resolving a hard superconducting gap ($\Delta \sim 250\mu$eV) with the line-cuts (both linear and logarithmic scale) shown in **d** at gate voltage indicated by black bar in **c**. The sub-gap/above-gap conductance suppression reaches two orders of magnitude. **e** False-color SEM of the superconducting island device. The Al island on the nanowire is ~1µm long, with a top plunger gate (purple) to tune the electron density, and two tunnel-gates (blue) to control the tunnel coupling to the two leads. Scale bar is 500 nm. **f** Differential conductance of the island device as a function of bias and plunger-gate voltage resolving the Coulomb blockade diamonds. The horizontal line-cut at zero bias (black curve) shows 2e-periodic Coulomb oscillations where each peak corresponds to adding/removing two electrons (one Cooper pair), suggesting negligible quasi-particle poisoning. At higher bias voltage where quasiparticle can be excited, the Coulomb oscillations become 1e-periodic. **g** Magnetic field dependence of the Coulomb oscillations at zero bias voltage with the field direction along the wire. The 2e-peaks split into 1e-peaks at ~1µm, indicating a sub-gap state crosses zero energy. **h** Even (S_e red) and odd (S_o blue) peak spacing extracted from **g**, with error bars indicated with shaded areas, showing possible Majorana or Andreev oscillations.

tions of tunnel barriers and the Al film by lithography, facilitating flexible device designs. Fig. 6.5a shows such a device where part of the Al is selectively etched away, and a tunnel gate electrode is added to deplete the InSb wire locally. A super-gate is deposited on the superconducting region of the nanowire whose cross-section is shown in Fig. 6.5b. The differential conductance on this normal-nanowire-superconductor (N-NW-S) device reflects the quasi-particle density-of-states in the proximitized nanowire segment, i.e., the induced superconducting gap as shown in Fig. 6.5c with a line-cut in Fig. 6.5d. The sub-gap conductance reaches zero, indicating a hard gap, a necessary condition for topological protection. Magnetic field dependence of accidental quantum dot levels reveals an effective g-factor of 18.6 (Supplementary Fig. 6.16), smaller than the bare InSb g-factor of 50 (Supplementary Fig. 6.17), but significantly larger than that of Al ($|g| = 2$), indicating the wavefunction hybridizes between InSb and Al [122, 152]. The measured hard gap with a gap size close to Al bulk, together with the effective g-factor defined by the coupling between Al and InSb, suggest that the electron wavefunction is mainly distributed near the top of the wire (close to Al) where the wire is single crystalline with no noticeable disorder [111, 117, 153]. This again supports that disorder at the InP/InSb interface has a negligible effect (see Supplementary Fig. 6.18, a cross-section TEM of a typical device).

Finally, we explore the transport of a hybrid InSb/Al island device (Fig. 6.5e), with a finite charging energy. The charging energy of the hybrid island can mediate the coupling between the two Majorana states for qubit operations and readout [60–62]. If the charging energy is less than the superconducting gap, the system ground state energetically "favors" even number of electrons, i.e., all electrons on the island form Cooper pairs in the superconducting condensate [43]. In transport, each Coulomb blockade diamond then corresponds to two electrons (one Cooper pair), as shown in Fig. 6.5f, as well as in Supplementary Fig. 6.19. The 2e-periodic Coulomb oscillation at zero bias (black curve) indicates negligible quasi-particle poisoning. A higher bias voltage can excite quasi-particles, resulting in the regular 1e-periodic Coulomb oscillations (red curve). Applying a magnetic field along the nanowire splits the 2e-peaks into 1e-peaks (Fig. 6.5g), with oscillating even/odd peak spacing (Fig. 6.5h). This 2e-1e transition might be interpreted as the appearance of two Majorana states, which allows the coherent "teleportation" of a single electron [43]. The oscillating peak spacing could be attributed to overlapping Majorana wavefunctions [22]. We note that a trivial explanation for the 2e-1e transition based on Andreev bound states cannot be ruled out at this point [44, 154, 155].

6.3. DISCUSSION

We have studied the growth dynamics of in-plane InSb nanowires on InP (111)B substrates. Despite the large mismatch between the wires and the substrate, single crystalline transport channels, free from extended defects, are formed due to immediate strain relaxation at the nanowire-substrate interface. Correspondingly, these in-plane InSb-based devices show high-quality quantum transport, with long phase-coherence length, a hard superconducting gap, 2e-Coulomb blockade peaks, and possible Majorana/Andreev signatures. The next step is to establish Majorana zero modes in these structures by performing key experiments like correlation and Majorana braiding [156].

DATA AVAILABILITY

The raw data and the data analysis codes that support the findings of this chapter are available at `https://doi.org/10.5281/zenodo.4589484`.

AUTHOR CONTRIBUTIONS

R.L.M.O.H.V., S.M.E.P., J.J., C.T., and E.P.A.M.B. carried out the substrate processing and the InSb synthesis. **D.X.**, V.S., Q.W., M.W.A.d.M., B.H., K.V., J.D.S.B., L.P.K., and H.Z. fabricated the devices and performed the transport measurements. J.S.L., M.P., and C.J.P. have deposited the superconductor. S.K. and J.J. have performed the FIB cuts for the TEM lamella and M.A.V. is responsible for the TEM analysis. A.S., A.M., and L.M. performed the theoretical modeling of defect formations. R.L.M.O.H.V., **D.X.**, M.A.V., H.Z., and E.P.A.M.B. have authored the paper, with contributions from all authors.

6.4. SUPPLEMENTARY INFORMATION

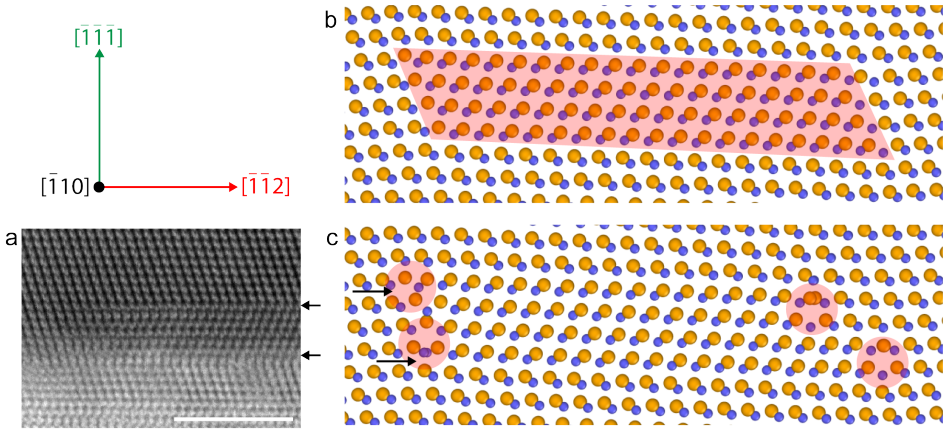

Figure 6.6: **Molecular Dynamics simulation on crystal relaxation between two twinned regions. a**: cross section transmission electron microscopy (TEM) image looking along the <110> zone axis, with a twinned region on the right, indicated by the black arrows. Scale bar is 5 nm. The twinned region is not present on the left side of the image. In order to understand how the twins are connected to the original crystal orientation at their lateral boundaries, atomic simulations are performed using the semi-empirical Vashishta energy potentials for InP, which takes the first- and second-nearest neighbours into account. There is no potential available for InSb, but there is no general limitation, since we are looking for crystallographic ordering, which is the same for both semiconductors. **b**: Crystal cell containing a twinned region (marked in red, starting at the black arrows, with the same orientation as the TEM image) with lateral boundaries parallel to the <110> direction prior to molecular dynamics (MD) annealing and energy minimization. **c**: crystal cell after MD annealing and energy minimization. 90° extrinsic stacking fault dislocation lines are formed parallel to the <1-10> direction (highlighted by red circles in the schematic cross-section), each composed by two 30° Shockley partial dislocations located in consecutive lattice planes. This is the only way a (111) oriented twin in the InSb lattice can be terminated and connected to the original crystal orientation, without forming amorphous regions at their boundary. It should be noted that raising the annealing temperature to 1000 K did not change the final structure of the InP cell in **b**. In conclusion, twins are always accompanied by dislocation lines running along all the <110> directions in the basic (111) plane, providing additional relieve of the residual misfit stain. This enables the InSb crystal above the twin plane to be completely free of any strain-induced defects.

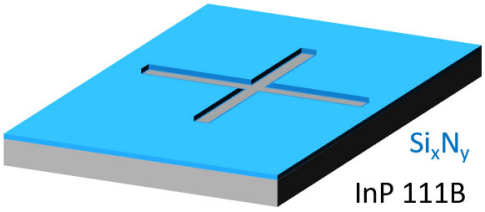

Figure 6.7: **Substrate after processing.** An InP (111)B undoped 2-inch wafer is used as the growth substrate for In-plane Selective Area Network (InSANe) InSb nanowires. First, the native surface oxides are removed by dipping the wafer in H_2O:H_3PO_4 10:1 for 3 minutes. Next, a 20 nm Si_xN_y layer is deposited using plasma enhanced chemical vapor deposition (PeCVD). Resist (ZEP520A + C60) is spun at 2000 RPM for 60 sec and then baked at 150L' for 15 min. Electron beam lithography is used to define the structures. The wafer is developed using n-amyl acetate for 60 sec, followed by an methyl-iso-butylketon: isopropanol (MIBK:IPA 89:11) mixture for 45 seconds and finally an IPA rinse. Next, the Si_xN_y is locally removed using reactive ion etching with CHF_3, an anisotropic dry etching technique. The resist is stripped, and the wafer is cleaned by oxygen plasma exposure. A final H_2O:H_3PO_4 10:1 clean is performed for 3 minutes, in order to remove the surface oxide on the InP substrate prior to growth.

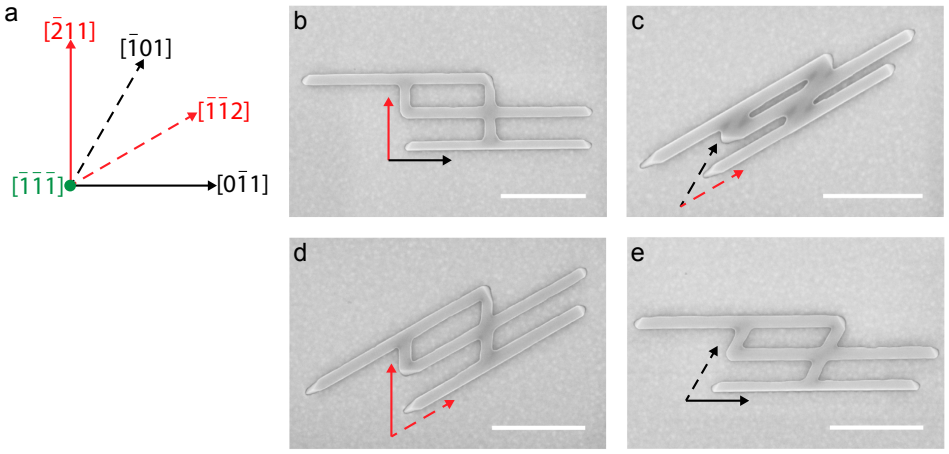

Figure 6.8: **Sensitivity to crystal directions.** In-plane InSb nanowires can be grown in specific crystal directions, namely the <112> and the <110> families of directions. In order to create in-plane networks, mask openings must be in any combination of these directions. **a**: Crystal directions on a (111)B substrate showing the first quadrant of <112> and <110> directions. Combinations can be made with <112> and <110> directions in either 90 degrees (**b**) or 30 degrees (**c**). Under 60 degrees angles combinations of <112> directions (**d**) or <110> directions (**e**) can be defined. Scale bars are 500 nm.

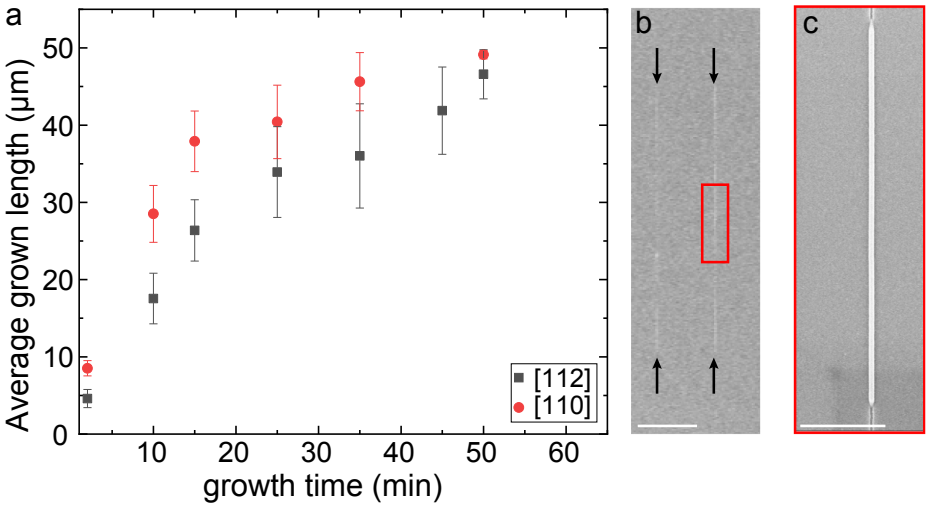

Figure 6.9: **Crystal direction dependent grown length as a function of growth time.** **a**: Average grown length of 50µm long openings in the mask in the <112> (black squares) and <110> (red circles) crystal directions as a function of growth time. In all cases the same temperature of 470Ľ and V/III ratio of ~ 8000 is used during growth in the metalorganic vapour-phase epitaxy (MOVPE). The error bars are the standard deviation of the average, taken over ten lines per datapoint. **b**: scanning electron microscopy (SEM) image showing two 50µm lines (indicated with black arrows) in the <112> direction after 35 minutes of growth. Scale bar is 10 µm. A zoom-in is shown in (**c**), clearly showing a grown segment on InSb nanowire (bright white), with at the top and bottom of the image a small segment of line in the mask that is not yet grown. Scale bar is 1µm.

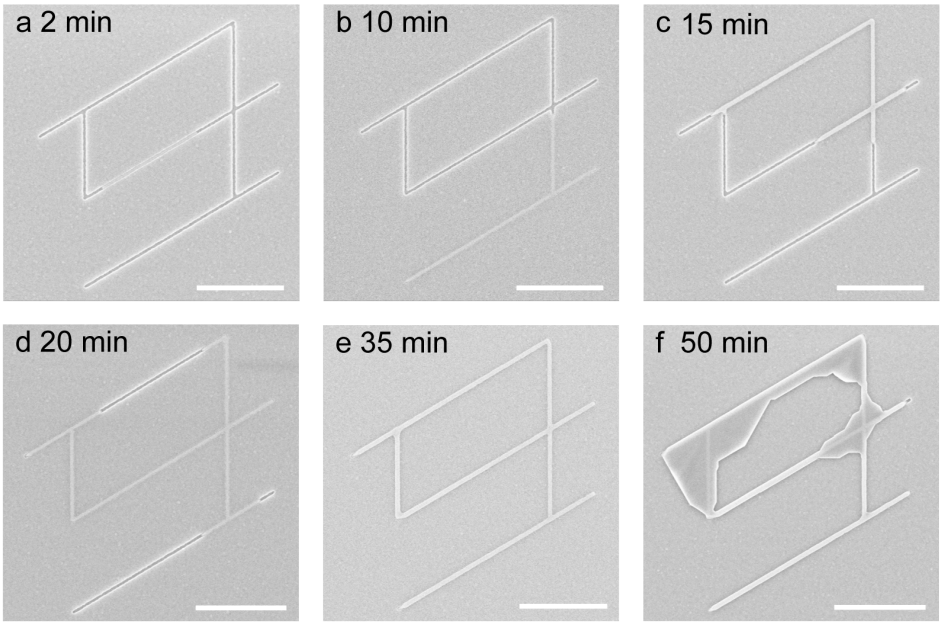

Figure 6.10: **Network growth as a function of growth time. a-f**: scanning electron microscopy (SEM) image of a representative structure (out of hundreds of similar structures on the same sample) at different growth times under the same growth conditions. Scale bars are 1 µm. The growth starts with one nucleation site (**a**) and starts growing outwards, following the openings in the mask (**b-d**). Note that no new nucleation sites are formed. Once the structure is fully filled, it starts to grow only in the vertical direction (**e**). When growth is not stopped in time, the structure starts growing out of and over the mask (**f**).

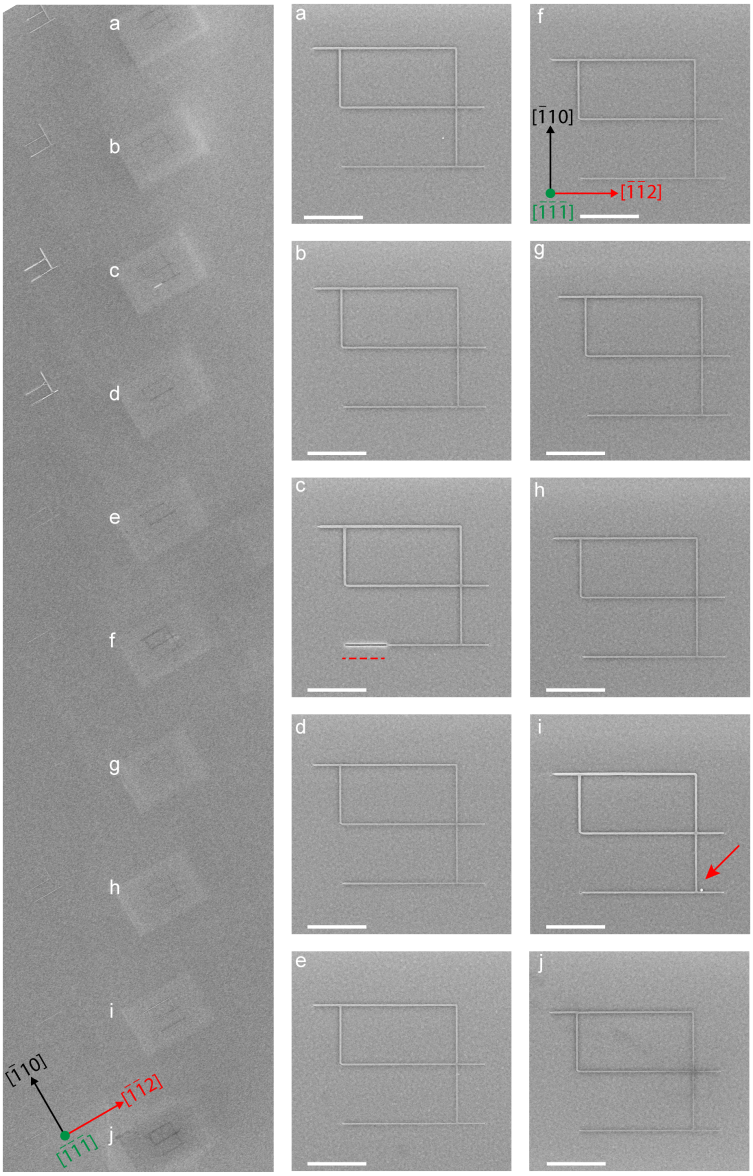

Figure 6.11: **Yield demonstration of well grown structures.** Overview SEM image of a region on the sample containing 10 repetitions of the same design, in this case a single qubit structure, labelled (**a-j**). Scale bars are 1µm. As evidenced in (**a-j**), a yield of up to 80% can be achieved under ideal growth conditions. (**c**) shows a structure where the last part of the bottom arm is not fully grown (red dashed line). **i**: scanning electron microscopy (SEM) image of a fully-grown structure with a small particle close to the bottom arm, indicated by the red arrow.

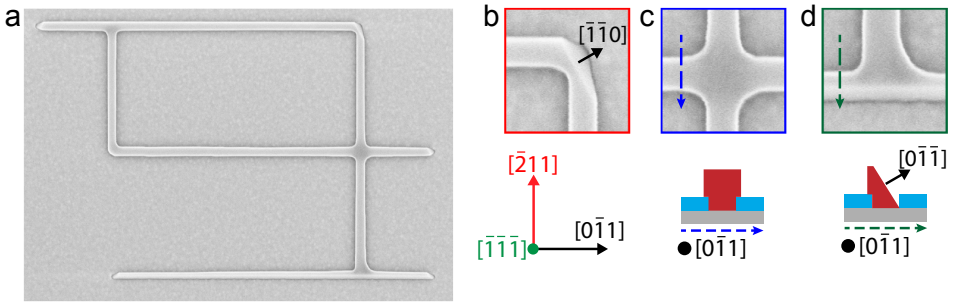

Figure 6.12: **Influence of extended arms on terminating side facets. a**: Scanning electron microscope image of an InSb nanowire network in a single qubit design structure. Scale bar is 1 µm. The terminating <110> side facets shown in main figure 1 are visible in (**b**) (red square) and (**d**) (green square). **b**: The top-right corner of the structure shows the [-1-10] terminating facet. **c**: The cross-junction is missing the [0-1-1] terminating side facet, which is present in (**d**). The extra arm extending down, changes the preferred terminating side facet here. A sketch is shown for both (**c**) and (**d**) to illustrate the difference in geometry.

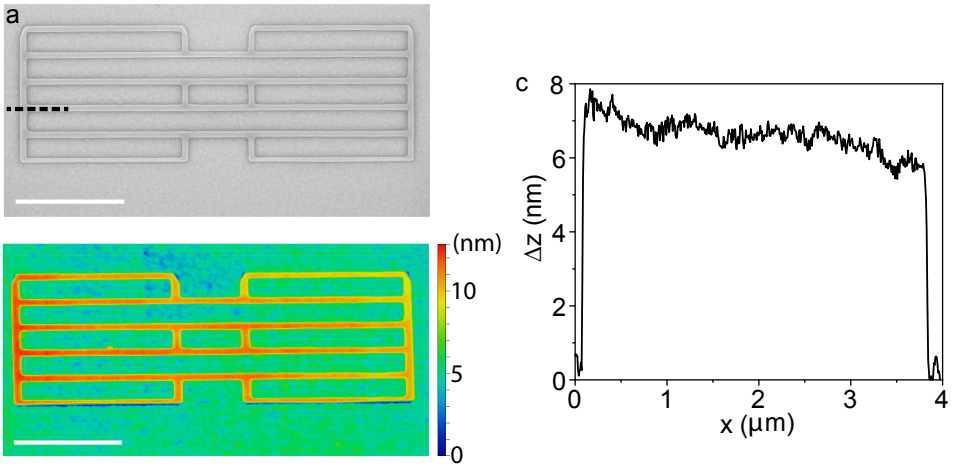

Figure 6.13: **Atomic force microscopy analysis of in-plane selective-area InSb network. a**: scanning electron microscopy (SEM) image of a 4-qubit design. **b**: atomic force microscopy (AFM) height color map of the same structure as in (**a**) showing the uniform height of the InSb structure. **c**: Line cut taken through the 4th line in the [110] direction showing the height relative to the top surface of the Si_xN_y mask. The height changes ~1.5 nm over a length of 4 µm, or 1 atomic step per 2 µm indicating a layer by layer growth on the top (111)B surface of the structure. Scale bars are 1 µm.

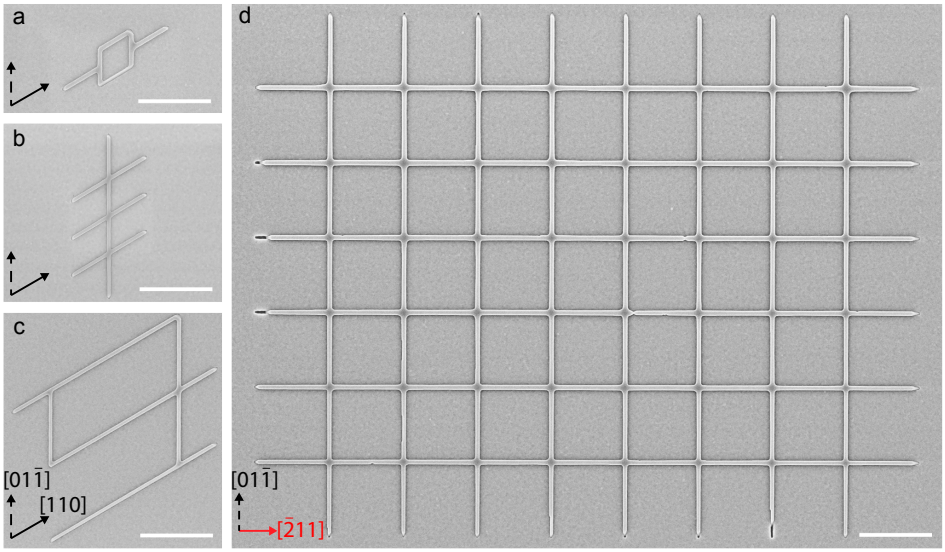

Figure 6.14: **Scalability of In-plane Selective Area Networks of InSb nanowires. a-d**: To demonstrate the scalability of this growth technique, different network designs in different sizes have been grown on the same substrate in the same growth run. All scalebars are the same size and represent 1 µm, showing that the growth of 200 nm by 200 nm loops (**a**), up to 11 µm by 11 µm hashtag networks (**d**) can be grown at the same time, independent of crystal direction, given that the mask is opened in <112> and/or <110> crystal directions.

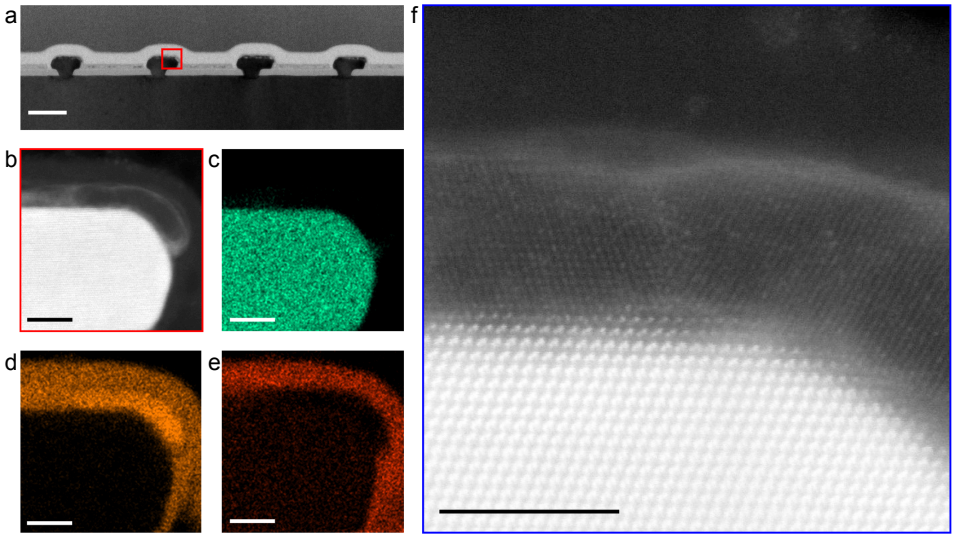

Figure 6.15: **Al interface in the InSANe InSb-Al hybrid system.** **a**: cross-section transmission electron microscopy (TEM) view of four InSANe InSb nanowires grown on top of an InP (111)B substrate. Scale bar is 100 nm. **b**: Zoom-in of the red area in (**a**), showing the InSb nanowire top edge with a 5 nm Al layer deposited on the wire. Energy-Dispersive X-Ray spectroscopy (EDX) analysis of the area in (**b**) shows the Sb (**c**, green), Al (**d**, orange) and O (**e**, red) in the InSb-Al hybrid network, depicting an oxide free InSb-Al interface. Scale bar is 10 nm. **f**: A zoom-in on the interface in (**b**) shows the clean and smooth interface between the InSb wire and the Al. The crystal lattice of two separate Al grains can be identified in the image, showing the high quality of the Al layer. Scale bar is 5 nm.

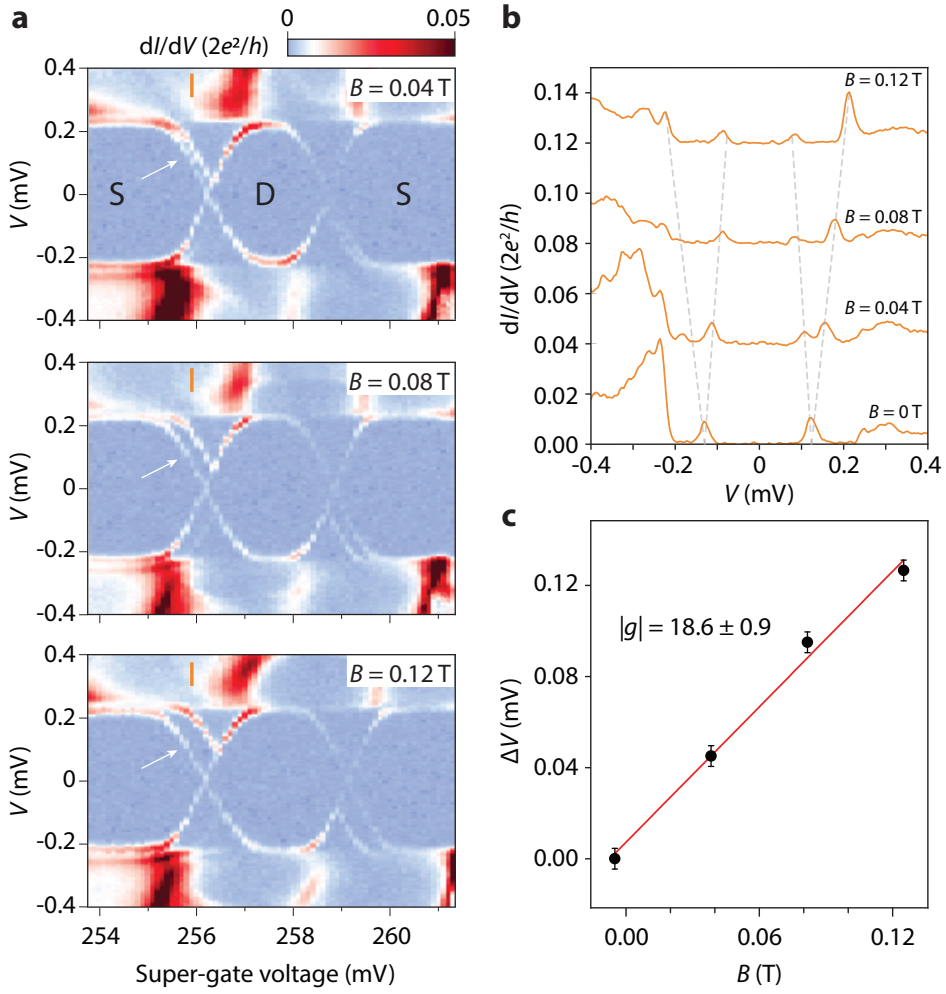

Figure 6.16: **Extraction of the g-factor in the N-NW-S device. a** Differential conductance of the N-NW-S device measured as a function of bias voltage V and supergate voltage at different magnetic fields (0.04 T, 0.08 T and 0.12 T from top to bottom) along the nanowire. Andreev levels corresponding to the transitions between the singlet and doublet states (indicated with S/D respectively) are observed. [48] Note that the Andreev levels corresponding to singlet ground states have Zeeman splitting (white arrows). **b**: Line traces from panel **a** at the super-gate voltage of 255.9 mV (at orange lines in **a**), plus the line trace at the same super-gate voltage at zero magnetic field. Offset between lines is $0.04 \times 2e^2/h$. Zeeman splitting is indicated by the dashed lines. **c** The spacing between the split peaks (black dots) or **b** (positive side) as a function of B. The slope of the linear fit (red line) is used to extract the g-factor. The error bars are given by the uncertainty of peak-finding, simply taking the interval of data.

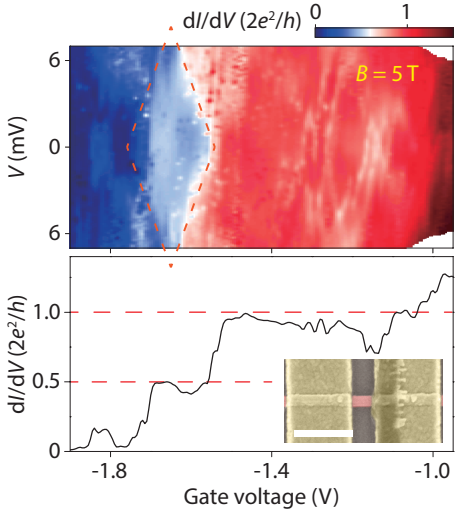

Figure 6.17: **Quantized conductance of an in-plane InSb nanowire.** Upper panel: differential conductance measured as a function of bias voltage V and gate voltage at a magnetic field of 5 T perpendicular to the substrate. Conductance plateaus are visible, and the plateau of e^2/h is indicated with red dashed lines. A g-factor of around 57 can be roughly extracted. Lower panel: horizontal line cut of the upper panel at $V = 0$. Conductance at e^2/h and $2e^2/h$ is marked with red dashed lines. We note the plateau quality is expected to be worse than VLS InSb nanowires [74], probably due to the facts that 1) the nanowire was heavily etched by Argon plasma before contact deposition; 2) near the pinch-off region, the top gate pushes the electron wavefunction towards the nanowire bottom (substrate with large lattice mismatch). Both introduce extra disorders which degrade the plateau quality. Inset: SEM image of the quantum point contact device. A nanowire segment (red) is contacted by Au (yellow) with 200 nm spacing. Global dielectric and top gate are not shown in this image. Scale bar is 500 nm. A minimum smoothing was applied together with a series resistance of 2.5 kΩ subtracted following the method in Ref [74].

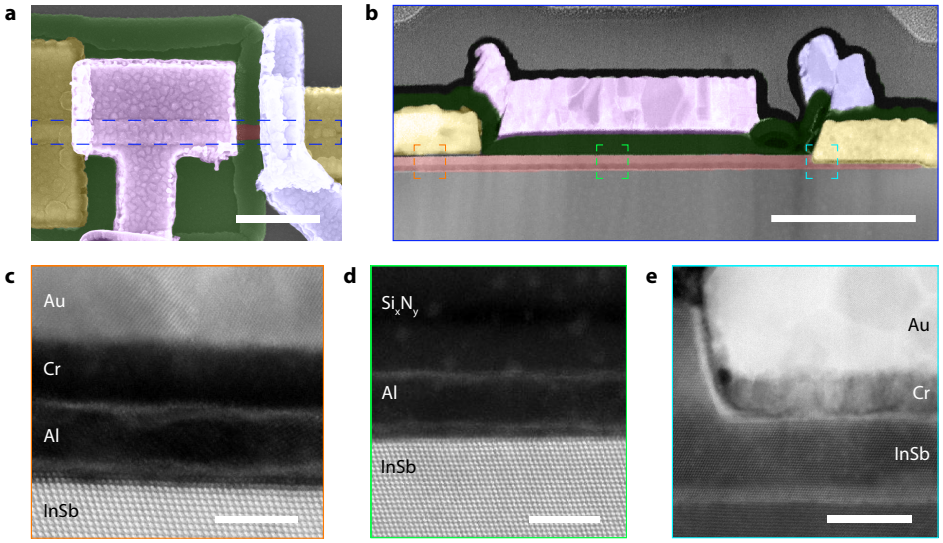

Figure 6.18: **Cross-section TEM of a N-NW-S device. a** scanning electron microscopy (SEM) image of a normal-nanowire-superconductor (N-NW-S) device. The InSb nanowire (red) is covered by an Al layer (green, covered by the etch mask). Contacts are Cr/Au (yellow). The tunnel- (blue) and super-gates are Ti/Au, deposited on top and separated from the wire by a Si_xN_y dielectric layer. Scale bar is 500 nm. The area indicated with blue dashed lines shows where the TEM specimen is made. **b** Cross-section transmission electron microscopy (TEM) image of the device. The structures have the same colors as those of the corresponding structures in **a**, except for the Si_xN_y dielectric colored in green together with Al. Scale bar is 500 nm. **c** High resolution TEM image of the orange region in **b**, showing the structure of the super contact. Note that the Ti/Au can contact the nanowire from the facet not covered by Al even though the AlO_x layer on top of Al is not sufficiently removed by a milling process. Scale bar is 5 nm. **d** High resolution scanning TEM (STEM) image of the green region in **b**, showing the structure of the InSb-Al-Si_xN_y dielectric stack. Scale bar is 5 nm. **e** High resolution STEM image of the cyan region in **b**, showing the structure of the normal contact. Note that the milling process before depositing Cr/Au has etched into the InSb sufficiently to form an oxygen-free contact interface. Scale bar is 20 nm.

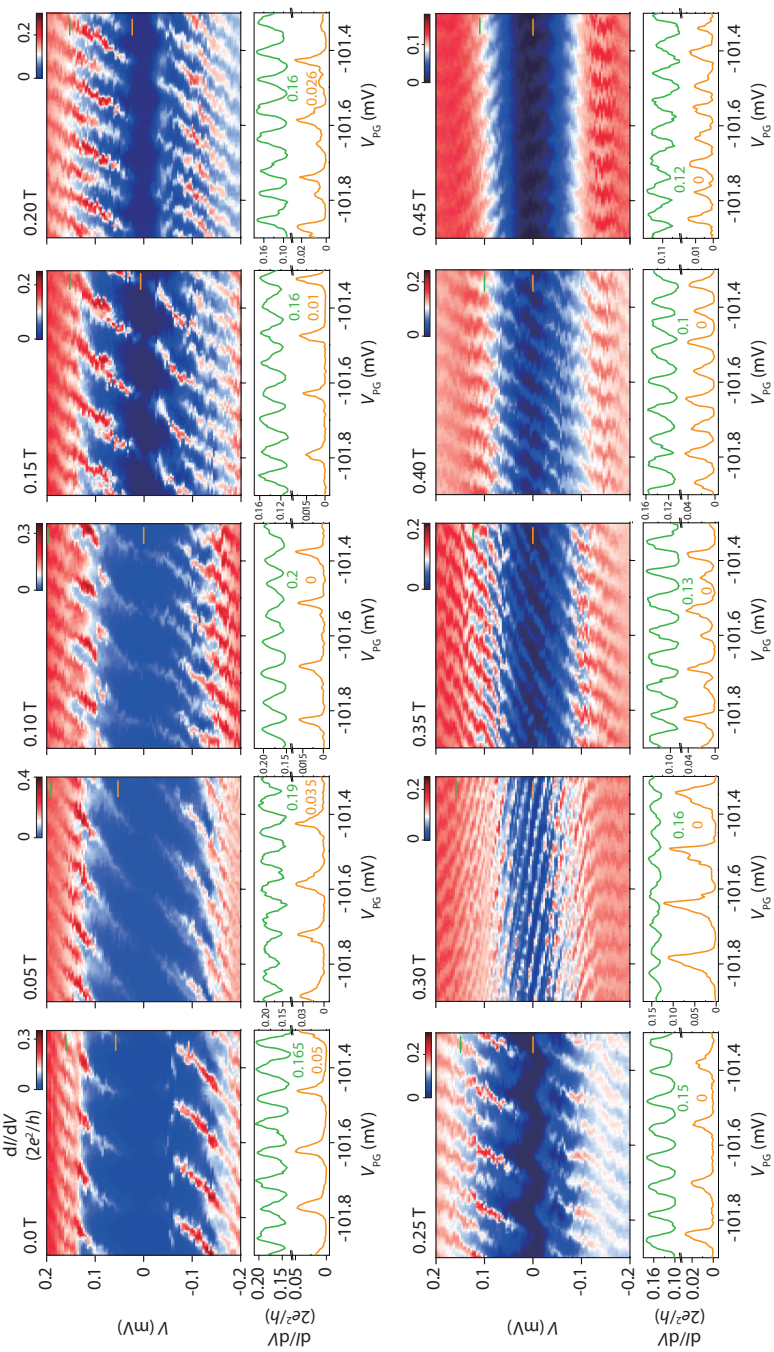

Figure 6.19: **Coulomb diamond of InSb-Al island device: transition from 2*e*-periodic to 1*e*-periodic.** Differential conductance as a function of plunger gate V_{PG} and bias voltage V at different fixed parallel magnetic fields (from 0 T to 0.45 T, with 0.05 T step). The Coulomb diamond is not symmetric due to the asymmetric tunnelling strength of the two barriers. The panels below show line cuts at low bias (orange lines) and high bias (green lines) with the bias voltage indicated (in units of mV). The transition from 2*e*-periodic to 1*e*-periodic oscillations can be observed at low bias voltages.

6.4.1. TYPES OF POSSIBLE DEFECTS THAT CAN BE DISTINGUISHED IN SELECTIVE AREA GROWN STRUCTURES

1. Misfit dislocations at the interface between the substrate and the wire. These arise due to a mismatch in lattice constant of the two materials. Their location is confined to the interface.

2. An antiphase boundary, which is formed if two nuclei, in which one of them has a twinned orientation with respect to the (111)B growth substrate, merge. This results in a charged plane between the two nuclei, leading to detrimental effects on the transport in the channel. (The orientation of a possible anti-phase boundary is vertical or inclined to the substrate.)

3. Inclined twin planes (being introduced during growth of a single nucleus rather than by the merging of two nuclei). These have been shown to increase the resistance of the channel [157], and have been observed in literature [139, 144].

4. Horizontal twin planes, as observed in our structures, a few nm above the substrate/wire interface.

In our structures, we observe misfit dislocations at the interface (**1**), which is unavoidable due to the large lattice mismatch of 10.4% in our material system. Just above the plane with misfits we observe a horizontal twin plane (**4**) in most of our structures. This twin plane is parallel to the electronic transport direction and therefore does not negatively affect the transport properties — as a matter of fact, the horizontal twin electrically isolates the transport channel from the misfits. The electron wavefunction is located near the InSb/Al interface at the top of the wire. This transport channel is free of defects, since we do not observe defects (**2**) and (**3**) in our structures. The detrimental effects on electronic transport reported in [141] were not observed in our structures. The conductance could be effectively pinched off and the charge carrier density fully depleted.

6.5. POST-PUBLICATION REMARK ON THE HARD-GAP DATA

When we prepared the data repository in 2021 for this publication as shown above, I realized that it is necessary to make a remark on the hard-gap data, as the awareness of scientific rigor has been enhanced and the importance of publishing raw data has become more recognized in the past two years in the community.

Fig. 6.5c was made as a crop of the data shown in Fig. 6.20a. In the full data range several accidental quantum dot levels are visible. I would like to point out that this data still illustrates a hard gap, as the coherence peaks at $V \sim \pm 250\,\mu$eV are clearly visible throughout the gate range, and the sub-gap conductance is highly suppressed unless the accidental quantum dot creates sub-gap resonances. Note that the dot resonances are not hidden but studied in Fig. 6.16 whose gate range is around 255 meV, and mentioned in Section 6.2.3. However, readers may have the impression of a monotonic above-gap conductance change in Fig. 6.5c and I would like to clarify the existence of dot levels to the readers of this thesis.

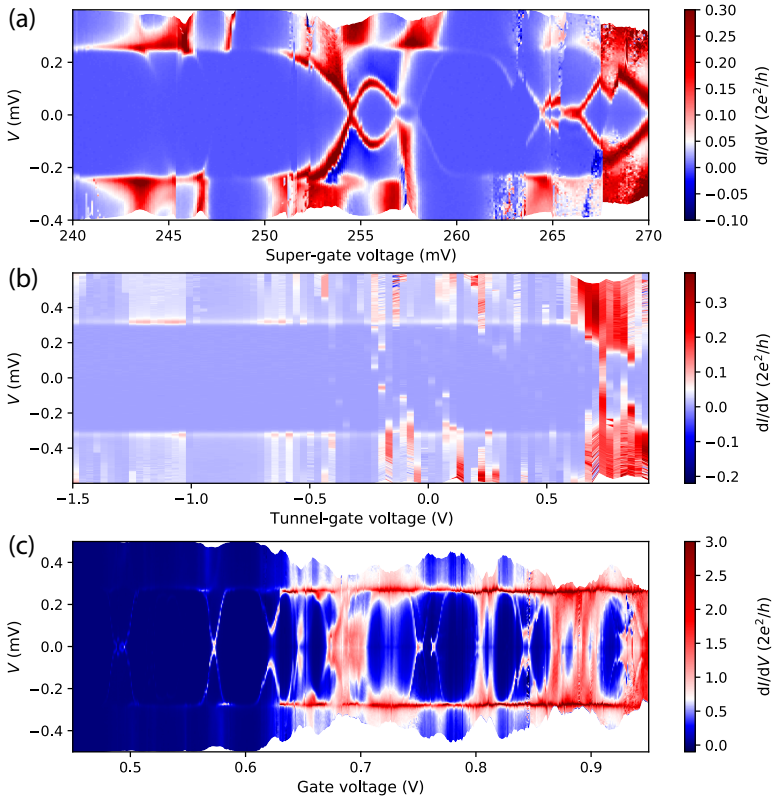

Figure 6.20: **Raw data of hard gaps. a** Differential conductance ($\mathrm{d}I/\mathrm{d}V$) as a function of bias voltage (V) and super-gate voltage, an illustration of the full data range of Fig. 6.5c. **b&c** $\mathrm{d}I/\mathrm{d}V$ as a function of V and tunnel-gate voltage (**b**) or global gate voltage (**c**) on other two devices on different growth wafers.

As an expansion of this topic, hard gaps have been reproduced multiple times on the

SAG InSb-Al in question. To be specific, from 2018 to 2020, among the 12 N-nanowire-S SAG devices that had gate tunabilities, we observed consistent hard gaps in 11 devices. Here I illustrate measurements on other two devices on different growth wafers in Fig. 6.5b and c. As the gates tune the devices from the tunneling regime to open regime, accidental quantum dot levels emerge and become pronounced in the high conductance regime. Hard gaps persist throughout the gate ranges with Δ varying from $\sim 250\,\mu$eV to $\sim 300\,\mu$eV, probably depending on the thickness of Al. In general, data cleanliness on these SAG devices may be concluded as being inferior to the best results in VLS InSb-Al nanowires.

7

MAGNETIC FIELD INDUCED ANDREEV BOUND STATE OSCILLATIONS IN HYBRID SAG NANOWIRES

In this chapter we present a further study of the transport properties of SAG InSb nanowires with epitaxial Al superconductor. We observe oscillating Andreev bound states in two SAG N-nanowire-S devices, which have not yet been observed in VLS wires. We investigate possible explanations for the oscillating Andreev bound states. Numerical simulations on hybrid SAG nanowires are performed to examine the assumption of a magnetic flux induced interference acting on a ringlike electron distribution in hybrid SAG nanowires.

7.1. INTRODUCTION

Among researchers' efforts towards Majorana zero modes in hybrid nanowire systems, various systems have been investigated. After we studied hexagonal VLS InSb nanowires with Al covering two or three facets in chapters 4 and 5, we focus on in-plane SAG InSb-Al nanowires (starting from Chapter 6).

In this chapter we report several measurements in which we observe signatures of oscillatory Andreev bound states in two SAG N-nanowire-S devices. These oscillations arouse our interest because we never observed similar behaviors in VLS nanowire systems. Inspired by experiments in full-shell nanowires [158, 159] as well as related theoretical works [99, 160], we examine the assumption of a magnetic flux induced interference in SAG nanowires via numirical simulations.

7.2. EXPERIMENTS

Fig. 7.1(a) illustrates a N-nanowire-S device fabricated on an in-plane SAG InSb network (device A). The Al film is etched away outside the Si_xN_y mask (green), thus the upper and lower contacts (yellow) serve as the super and the normal contacts, respectively. Note that the normal contact has an overlap with the Si_xN_y mask, so it forms an functional contact on the segment of nanowire that is not covered by the Si_xN_y mask, and a creeping segment (~200 nm) of the nanowire after the chemical etching acts as a nanowire junction situated between the normal contact and the region with Al. Note that there are two parallel nanowire junctions on the two sides of the hashtag-like in-plane network. We fix the left gate at 0 V during the experiments, at which the left channel keeps depleted. Therefore, the property of the right channel (red) is probed via standard tunelling spectroscopy using AC lock-in measurements in a dilution refrigerator with a base temperature of 20 mK. A DC bias voltage V_{Bias} is applied between the normal and the super contacts and a voltage V_{TG} is applied to the tunnel gate (light blue) to tune the tunnel barrier height. Since the underlying nanowire network is complex, the black dashed line is added in Fig. 7.1(a) to indicate the junction being measured. As one of a batch of devices for characterization study, no gate is designed for tuning the electron density in the nanowire segment. An in-plane magnetic field B is applied along the nanowire junction.

Fig. 7.1(b) shows the differential conductance, $\mathrm{d}I/\mathrm{d}V$, versus V_{Bias} and B for different fixed values of V_{TG}. At $B = 0$, we observe a superconducting gap with the size of $\Delta \sim 250\,\mu\text{eV}$. When $V_{\text{TG}} = 1.625\,\text{V}$, as B increases, two subgap states move towards zero energy. After they cross each other at zero energy, they continue to evolve towards the gap edge. After reaching the gap edge, the subgap states repeat their previous behaviors and cross at zero energy again. Between the states and the superconducting gap edge, finite differential conductance indicate that other subgap states fill this energy range, as Fig. 7.3(b) shows. This oscillating behavior of subgap states has not yet been observed in VLS nanowires.

As V_{TG} increases from 1.625 V to 1.670 V, we observe similar oscillating behaviors, and the positions where subgap states cross at zero energy move towards higher B values. Line traces in Fig. 7.1(c) show zero-bias line cuts from Fig. 7.1(b), in which two peaks in each plot indicate the positions where the subgap states reach zero energy. These line traces demonstrate an increasing oscillating period as the gate voltage increases,

although in this case a period can not be strictly defined as the oscillations do not show enough periods and the oscillations seem irregular.

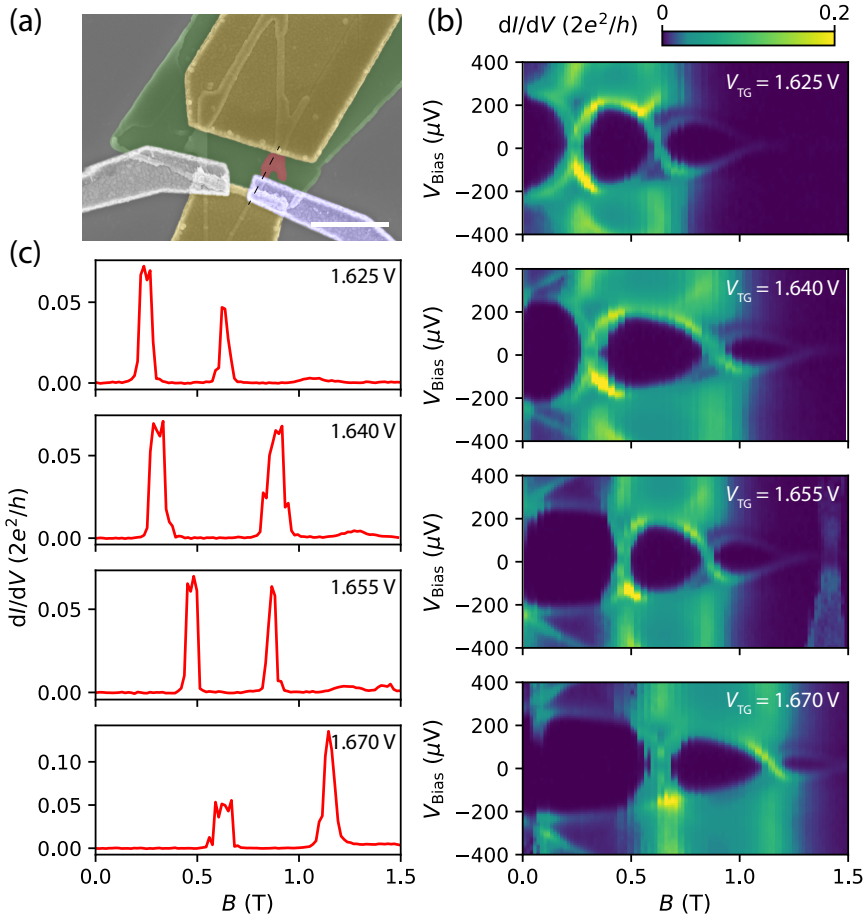

Figure 7.1: **Andreev bound state oscillation in device A. (a)** False color SEM micrograph of device A. Al is selectively etched on the nanowire (red) outside the Si_xN_y mask (green). A super contact (upper yellow) and a normal contact (lower yellow) are deposited on the nanowire. A top tunnel gate (light blue) is deposited on a dielectric. Scale bar is 1 µm. The black dashed line indicates the nanowire section being measured. **(b)** Differential conductance as functions of bias voltage and magnetic field. From top to bottom the tunnel-gate voltage is increased. **(c)** Zero-bias line cuts in (b).

Based on the distance of the two visible peaks in Fig. 7.1(c) and assuming it represents the period of the oscillation, we can try to estimate what the size of the superconducting ring would be if the oscillatory behavior is induced by the Little-Parks effect. When $V_{TG} = 1.625\,V$, we take $\Delta B \approx 0.4\,T$ and estimate the radius of the assumed ring to be $\sim 40\,nm$ according to Eq.
refeq:ABSoscillation; when $V_{TG} = 1.670\,V$, $\Delta B \approx 0.6\,T$ and the radius is $\sim 32\,nm$. A typical cross section of a SAG nanowire has the dimensions $100\,nm \times 40\,nm$ based on Fig. 6.18.

Without cross-section TEM, we do not know the exact sectional area of the nanowire in device A. The estimated size of the ring is in the order of the radius of a typical SAG nanowire.

In another N-nanowire-S device (device B), we observe similar oscillating behavior. A SEM image of device B is shown in Fig. 7.2(a). Device B was originally designed as a correlation-type device with two normal contacts (yellow on both sides) and two superconducting drains (upper and lower grey) expecting to connect to the Al shell from the substrate from either side. But the two superconducting drains are both not connected to the nanowire (red). Further, the right tunnel gate (bottom right yellow) is shorted to the right contact, serving then together as the super contact. The etch mask for selectively etching Al is shown in green. Another dielectric layer is then deposited (covering all parts in this image and not false-colored) and the tunnel-gate (light blue) and the super-gate (purple) are deposited on top of the dielectric.

In Fig. 7.2(b), oscillating subgap states are visible when $B < 0.92\,\mathrm{T}$. Compared to device A, it is clear that only one Andreev bound state is oscillating. Taking the magnetic period estimated to be 0.5 T, the radius of the assumed ring is $\sim 36\,\mathrm{nm}$, again in the order of the radius of a typical SAG nanowire. When B is above 0.92 T, the device seems to enter a different regime and the oscillatory period of the Andreev bound state becomes larger and interacts with other Andreev bound states between 1.5 T and 2 T. If increasing the super-gate voltage V_{SG}, the influence on the oscillatory period below 0.92 T is hardly visible as the change of V_{SG} is very tiny, but the states between 0.92 T and 2 T is tunable by V_{SG}. Note that gate voltages are tuned along the trajectory in the V_{SG}-V_{TG} space as shown in supplementary Fig. 7.6. Fig. 7.2(c) shows line cuts at several B fields at $V_{\mathrm{SG}} = 8\,\mathrm{V}$. The Andreev bound states that are tunable between 0.92 T and 2 T show a typical crossing as a function of V_{SG} at $B = 1.2\,\mathrm{T}$, as shown in Fig. 7.2(d). Since there is a cross point at zero energy, a zero-bias peak can be measured if we tune V_{SG} to that specific point (supplementary Fig. 7.7), but is nothing but a trivial Andreev bound state crossing.

7.3. SIMULATIONS OF HYBRID SAG NANOWIRE

There have been studies on full-shell nanowires where a full superconducting shell surrounds a semiconductor nanowire core, and tunneling spectroscopy measurements have been performed [158–160]. A symbolic feature in full-shell wires is a sequence of lobes given by the Little-Parks effect, and each lobe is associated with a quantized number of twists of the superconducting phase [30]. The Little-Parks effect originally refers to a periodicity of the superconducting critical temperature T_c as a function of magnetic flux if the superconductor has a cylinder-shape [161]. Since the superconducting gap in BCS theory is associated to T_c proportionally [162], the Little-Parks effect also manifests itself as an oscillatory behavior of the superconducting gap, as observed in full-shell wires. The period of the sequential lobes in full-shell wires is given by

$$\Delta B = \frac{\Phi_0}{A} = \frac{h/2e}{A} \tag{7.1}$$

where A is the cross sectional area of the superconducting shell.

We have shown in Chapter 4 that gate voltages on a hybrid nanowire can push the electrons in the nanowire towards the interface with the superconductor, or attract the

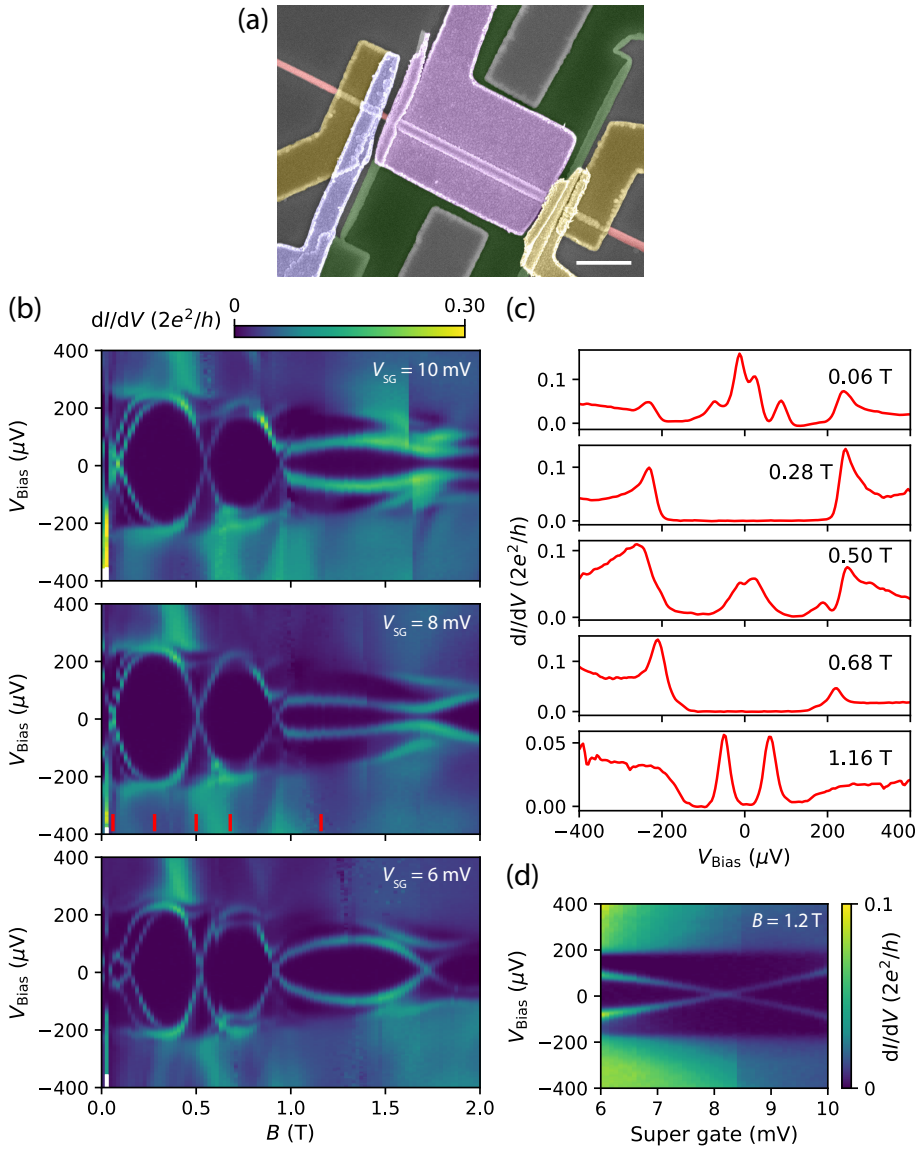

Figure 7.2: **Andreev bound state oscillation in device B. (a)** False-colored SEM image of Device B. The left contact (left yellow) is used as the normal contact, while the right tunnel gate (bottom right yellow) is shorted to the right contact (right yellow), serving then together as the super contact. The etch mask for selectively etching Al is shown in green. Another dielectric layer is then deposited (covering all parts in this image and not false-colored) and the tunnel-gate (light blue) and the super-gate (purple) are deposited on top of the dielectric. **(b)** Differential conductance as functions of bias voltage and magnetic field. From top to bottom the super-gate voltage is decreased. The magnetic field in each measurement is swept from 0 to 2 T. **(c)** Vertical line cuts at the positions with red labels in the middle panel of (b). **(d)** Differential conductance as a function of V_{SG} at $B = 1.2$ T.

electrons towards the gate. Depending on different situations, the electron wavefunction can either have a higher weight of semiconducting properties or a higher weight of superconducting properties [111, 152].

When the electrons are pulled away from the interface with the superconductor, they are weakly coupled to the superconductor. We infer that if this situation happens in a nanowire with a small cross sectional area, even if the superconductor is not a full-shell, the electron wavefunction carrying superconducting properties may form a ring, thus reveal Little-Parks-like properties. Ref. [99] performed such a simulation shown in Fig. 7.3. When the density of electrons forms a ring together with the superconductor (on two facets) and the density of states show oscillatory behavior as a function of in-plane magnetic field along with bulk-gap closing. The oscillating minima correspond to half-integer magnetic flux quanta, while the maxima correspond to integer flux quanta. SAG hybrid nanowires have a smaller cross section (Fig. 6.3 and 6.18) compared to VLS nanowires and can thus be a good candidate to realize this oscillatory behavior.

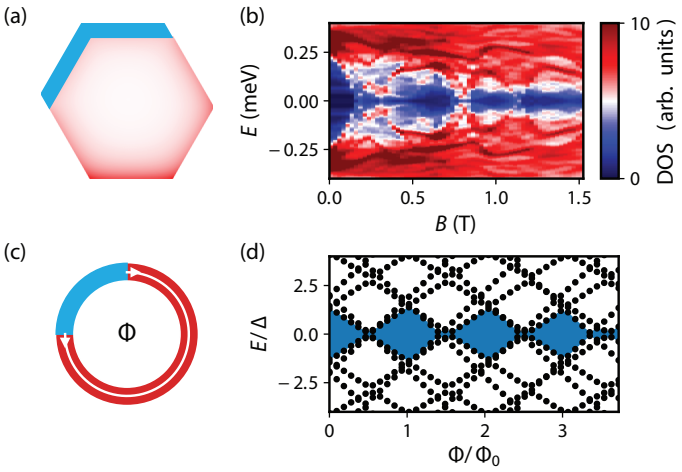

Figure 7.3: **(a)** Simulated density in a hexagonal nanowire cross-section with two facets covered by Al. **(b)** Simulated density of states as a function of energy and magnetic field. **(c)** Toy model of such a simulation, showing oscillatory behavior. Red circle denotes the ring of electron wave function in the nanowire and blue region is the superconductor. **(d)** Energy levels in the toy model as a function of magnetic flux. Adapted from [99].

It is worth notifying that Ref. [99] considers InAs nanowires, in which the conduction band bends below the Fermi level at the InAs surface, leading to an accumulation layer of electrons. There has not been simulations proving that a ring-like distribution of electrons can form in InSb nanowires.

In order to study whether we expect Little-Parks-like oscillations in InSb nanowires and in particular geometry of the SAG, we performed numerical simulations on the system with the cross sectional geometry shown in Fig. 7.4(a)-(c), while the system is set to be infinite in the x direction. Because we do not have the exact geometry of the SAG devices from TEM study, the geometry in the simulations is based on an estimation according to the typical size of SAG nanowires (e.g. in figures 6.3 and 6.18) and parameters used in the fabrication process. On the interface of InSb and Si_xN_y, the density of in-

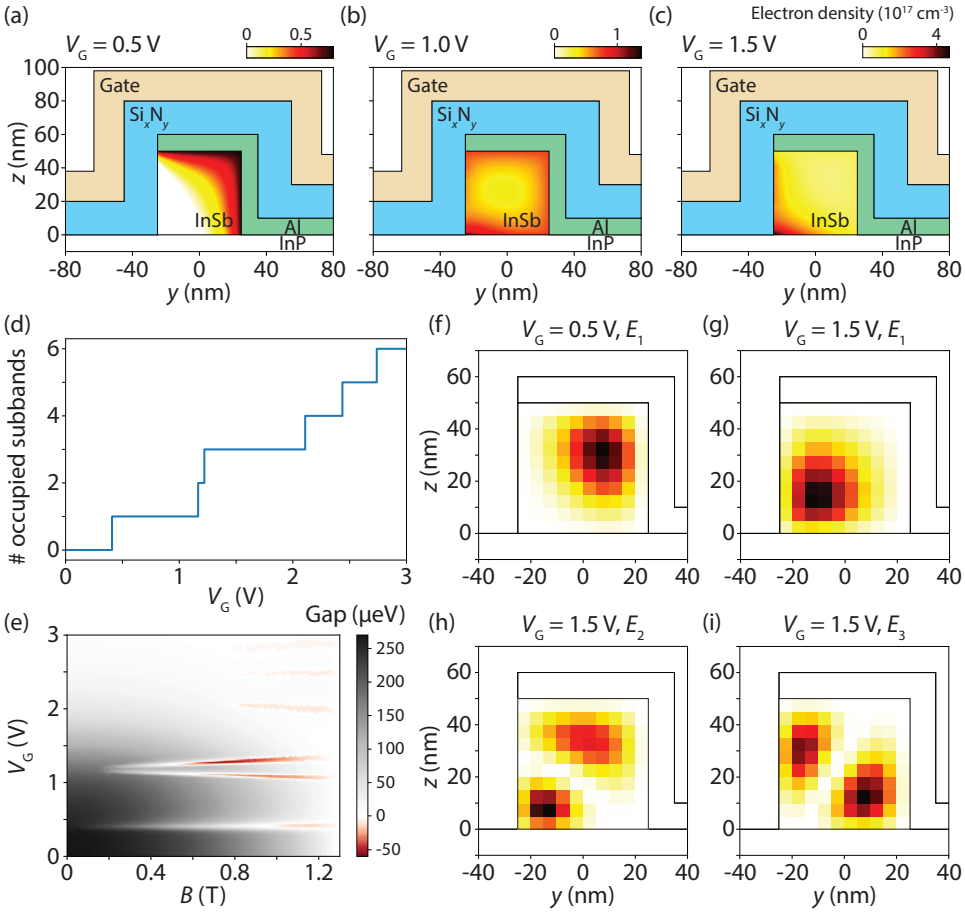

Figure 7.4: **Simulations of hybrid SAG nanowire. (a)-(c)** Cross sectional geometry used in the simulations. The color plots in the InSb area show calculated electron density in the SAG nanowire at $V_G = 0.5$ V, $V_G = 1.0$ V and $V_G = 1.5$ V, respectively. **(d)** Simulated numbers of occupied subbands at the density of interface trap of electrons $D_{it} = 1 \times 10^{13}\,\mathrm{cm}^{-2}\mathrm{eV}^{-1}$ as a function of the gate voltage V_G. The subbands are populated while increasing V_G. The critical field $B_c = 1.5$ T, the induced gap $\Delta = 250\,\mu$eV, the band offset between Al and InSb 50 meV (electron accumulation), and the Rashba spin-orbit coupling $\alpha_R = 0.05$ eV nm. **(e)** Gap as a function of the gate voltage V_G and the magnetic field B. **(f)** Probability density of the first subband at $V_G = 0.5$ V in the square cross section of the nanowire. **(g)-(i)** Probablity density of the first 3 subbands at a higher gate voltage $V_G = 1.5$ V. Color scales in (f)-(i) are in arbitrary unit.

terface trap of electrons is set to $D_{\text{it}} = 1 \times 10^{13}\,\text{cm}^{-2}\text{eV}^{-1}$ in the simulations, which is a typical value in InSb hybrid devices [163, 164]; the InP substrate is treated as a dielectric without D_{it}. Similar to Ref. [165], the simulation solves the electrostatic potential within the Thomas-Fermi approximation in a Bogoliubov-de Gennes equation discretized on a finite-difference grid.

We note that the simulation in Fig. 7.3(a) is given by a bottom gate configuration, while in SAG devices, the electric field generated by the top gate only acts from one side facet of the nanowire, due to the screening effect of the Al film on the other two facets. A more positive voltage pulls the electrons closer to the top gate and thus increases the effective area of the closed loop, as depicted by electron density under Thomas-Fermi approximation in Fig. 7.4(a)-(c). The superconductor Al is treated as a self-energy, meaning that the superconductor is integrated out as a boundary condition to each site of InSb at boundary with Al, where a self-energy term is applied. The treatment of Al is different from Ref. [99] where Al is discretized in very small steps, being computationally very expensive. We do not expect the difference of the two numerical methods affect the simulation results.

The orbital effect is included by Peierls substitution. And the gap closing is given by $\Delta(B) = \Delta\sqrt{1 - \frac{B^2}{B_c^2}}$, where Δ and B_c are the induced gap and the critical field, respectively. Fig. 7.4(d) shows the numbers of occupied subbands when ramping the gate voltage V_{G}. The subbands becomes populated when increasing the gate voltage. In Fig. 7.4(b), the calculated gap size is plotted as a function of V_{G} and B. We observe the appearance of gap closing and even gap inversion, but we do not observe any oscillatory behavior of the gap along the horizontal direction. At $V_{\text{G}} > 2\,\text{V}$, we do not even expect a well-defined superconducting gap. Therefore, we then choose a lower gate voltage ($V_{\text{G}} = 0.5\,\text{V}$ in Fig. 7.4(f)) and a higher gate voltage ($V_{\text{G}} = 1.5\,\text{V}$, which may represent the regime of our measurements, to plot the probability density of the occupied subbands in Fig. 7.4(g)-(i)). Unfortunately we do not observe a ring-shaped distribution of the electron wave function together with the Al shell, no matter in which region the wave function is located.

Nevertheless, we indeed obtain a ringlike electron density in Fig. 7.4(b), seemingly contradicting that there is no region in Fig. 7.4(e) showing magnetic field dependent oscillations. On the one hand the distribution is rather an occupation of the whole cross section of the nanowire. On the other hand this happens when there is only one occupied subband as shown in Fig. 7.4(d), and the first subband does not form a ringlike distribution with the Al film. Even if we assume that the electron density shown in Fig. 7.4(a)-(c) would demonstrate a magnetic flux dependence, the period of magnetic field in the resulting oscillations would decrease as the gate voltage increases, being the opposite of the measurements in Fig. 7.1.

7.4. DISCUSSION

Via the simulation study we feel it not conclusive to claim that the oscillatory behavior is due to the Little-Parks-like interference. We acknowledge that device A and device B are not specifically designed for such a study of Little-Parks-like oscillations in SAG nanowires, since device A is just a test device and device B has a much more compli-

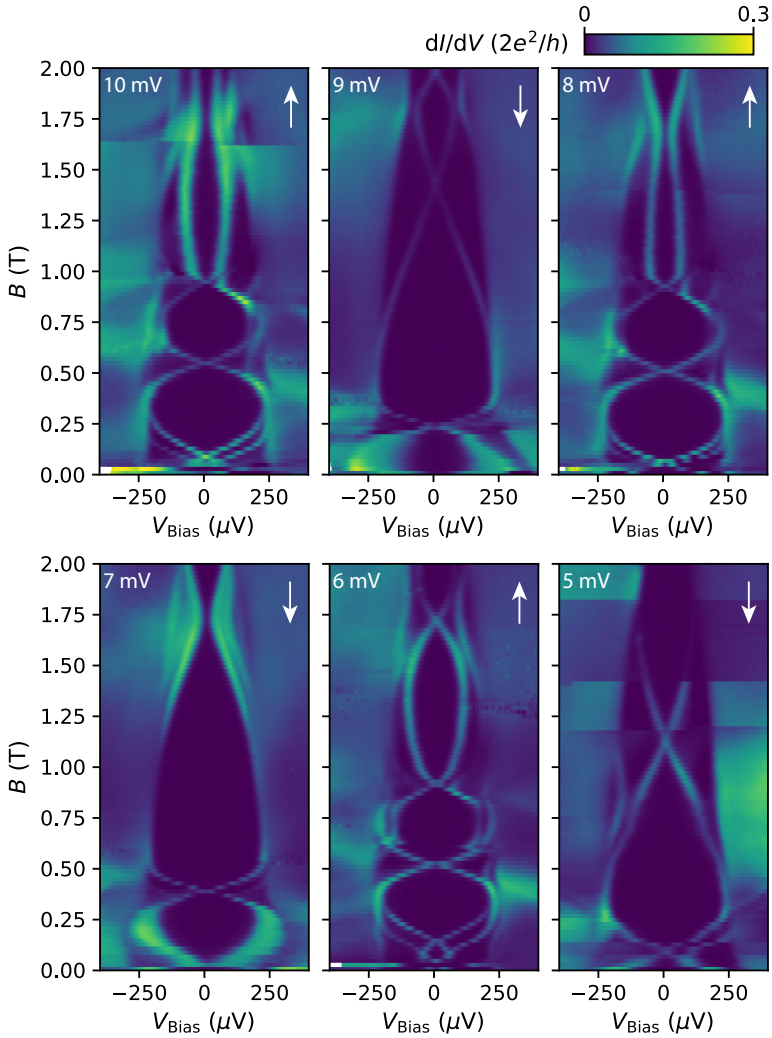

Figure 7.5: **Ramping direction dependence of the magnetic field in device B.** Differential conductance as functions of bias voltage vs magnetic field. From top left to bottom right the super-gate voltage is decreased. The super-gate voltage is labeled at the top left corner of each panel. The ramping direction of the magnetic field is labeled with the white arrow in each panel. The plots at V_{SG} = 10 mV, 8 mV and 6 mV are identical to those in Fig. 7.2(b).

cated design than a device that is needed for this study. Apart from a bulk effect like the Little-Parks effect, it is likely to be a behavior of junction states. Indeed we see that the oscillatory Andreev bound states have a very large g-factor that is likely from the semiconductor and there is often an above-gap quantum dot resonance visible when the subgap state oscillation happens. The magnetic field induced energy change of such states is due to Zeeman effect, which can be a manifestation of the behavior in Ref. [48] where gate voltage tunable Andreev bound states are investigated.

This oscillatory behavior only exists in a very small gate range as device B shows, and can be very fragile. Fig. 7.5 shows a group of measurements in device B with decreasing V_{SG}. The oscillations happens only when ramping the magnetic field from 0 to 2 T, while a decreasing magnetic field no longer reveals the oscillation. We find no explanation yet for this dependence of ramping direction.

We would like to only treat these measurements as a precursor for the study of this type of phenomena. It would be a good opportunity to study Little-Parks-like effect in SAG nanowires if the oscillatory behavior is reproduced in a clean and simple N-nanowire-S device.

DATA AVAILABILITY

The raw data and the data analysis codes that support the findings of this chapter are available at `https://doi.org/10.5281/zenodo.6390952` (not including those of Section 7.3).

CONTRIBUTIONS TO THE PROJECT

D. Xu, Q. Wang, B. Hesselmann and V. Schaller fabricated the devices. **D. Xu**, Q. Wang, J. D. S. Bommer, B. Hesselmann, M. W. A. de Moor, V. Schaller and H. Zhang performed the transport measurements. **D. Xu** performed data analysis presented in this chapter. L. Bourdet performed the simulations, and made contribution to the discussion of the results. R. L. M. Op het Veld and J. Jung carried out the growth of SAG InSb networks under the supervision of E. P. A. M. Bakkers at Eindhoven University of Technology. The project was supervised by H. Zhang and L. P. Kouwenhoven.

7.5. SUPPLEMENTARY INFORMATION

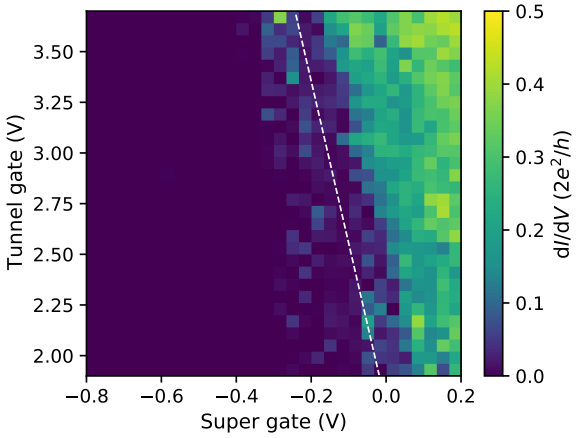

Figure 7.6: **Gate compensation.** Conductance at $V_{\mathrm{Bias}} = 0.3\,\mathrm{mV}$ as a function of V_{TG} and V_{SG} at zero magnetic field. The gate voltage scans in device B follow the white dashed line.

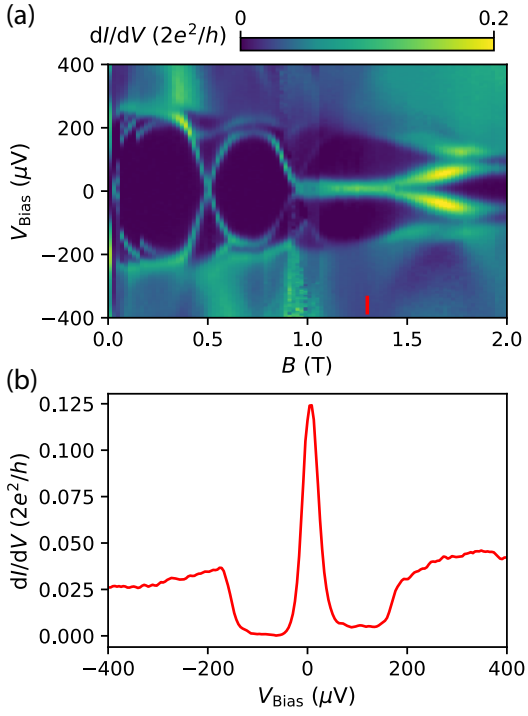

Figure 7.7: **Occasional zero-bias peak in device B. (a)** Differential conductance as functions of bias voltage and magnetic field. **(b)** Vertical line cut at the position with red label in (a).

8

AHARONOV-BOHM EFFECT IN SAG NANOWIRE NETWORKS

In the previous works, we have demonstrated that nanowire networks grown by the in-plane SAG technique [75] shows phase-coherent transport, one of the requirements for measurement-based gate operation and topological qubit readout. The SAG technique makes it possible to perform phase-coherent experiments on more complex networks, thus a tool to study phase-coherent phenomena in nanowire structures is needed. In this chapter, we report an extensive study on phase-coherent experiments on nanowire networks and develop a model to demonstrate their phase-coherent properties. This chapter can be read as a direct comparison with Chapter 5 in Ref. [77].

8.1. PHASE COHERENCE IN AN AHARONOV-BOHM RING

In a ring-shaped semiconductor nanostructure, an Aharonov-Bohm (AB) experiment can be realized with an external magnetic field applied vertical to the plane of the ring structure [68, 166]. An incoming electron splits at the entrance of the ring into two partial waves in different branches and they propagate in different directions along the ring. The two partial waves interfere at the exit of the ring, resulting in constructive or destructive interference.

Fig. 8.1(a) depicts an AB ring, which consists of an upper and a lower arm, connecting to the left and right leads. We define that an electron wave acquires a dynamical phase χ_1 when propagating in the upper arm and χ_2 in the lower arm. More importantly, a magnetic phase $(-)\phi_1$ is collected by an electron traveling (counter)clockwise along the upper arm, while the magnetic phase $(-)\phi_2$ is collected (counter)clockwise along the lower arm. Therefore, the phases that an electron wave collects when propagating in the AB ring are given by the forms written in Fig. 8.1(a). The sum of the phases $\phi_{1,2}$ is determined by the magnetic field penetrating the ring:

$$\phi_1 + \phi_2 = \frac{e}{\hbar}\oint_L \mathbf{A}\cdot \mathrm{d}\mathbf{l} = \frac{e}{\hbar}\iint_S \mathbf{B}\cdot \mathrm{d}\mathbf{S} = \frac{2\pi\Phi}{\Phi_0} \equiv \phi_{\mathrm{AB}} \tag{8.1}$$

where L is the closed trajectory along the ring, $\mathbf{A}$ is the electromagnetic vector potential, $\mathbf{S}$ is the area of the ring, $\mathbf{B}$ is the magnetic field, $\Phi_0 = \frac{h}{e}$ is the magnetic flux quantum[1], and ϕ_{AB} is the phase collected by the trajectory encircling the ring.

Following Ref. [167], we decompose the AB ring into two beam splitters, formed by the left(right) lead and the upper and lower arms, sketched in Fig. 8.1(b). An incident electron to a beam splitter can either be reflected back, or propagate in the upper or the lower emergent branch. Thus we note that the number of possible trajectories that an electron can take from the left lead and right lead are vast and scales exponentially with respect to the attempts that it arrives at a beam splitter. The number of attempts m ($m \geqslant 2$ because a path of an electron has to go through at least two beam splitters) can yield 2^{m-1} possible trajectories. We consider the possible trajectories (where the electron reaches the beam splitters up to 4 times and can generate up to 3 harmonics of the AB oscillation) and list them in Fig. 8.1(c).

Before we calculate the oscillation amplitudes given by the interference among these trajectories, a scattering matrix of the beam splitter needs to be defined. We assume that an incident electron upon the beam splitter has a probability $|r|^2$ to be reflected back. We then assume that the upper and the lower emergent paths of the beam splitter are symmetric. Thus, we write the scattering matrix s in the form given by [77]

$$s = \begin{bmatrix} -\frac{1-r}{2} & \frac{1+r}{2} & \sqrt{\frac{1-r^2}{2}} \\ \frac{1+r}{2} & -\frac{1-r}{2} & \sqrt{\frac{1-r^2}{2}} \\ \sqrt{\frac{1-r^2}{2}} & \sqrt{\frac{1-r^2}{2}} & -r \end{bmatrix} \tag{8.2}$$

Note that s is given in a form for a time-reversal symmetric system, whereas a magnetic

[1] Note that the flux quantum here is different from when people normally use this term, which is the superconducting flux quantum $h/2e$.

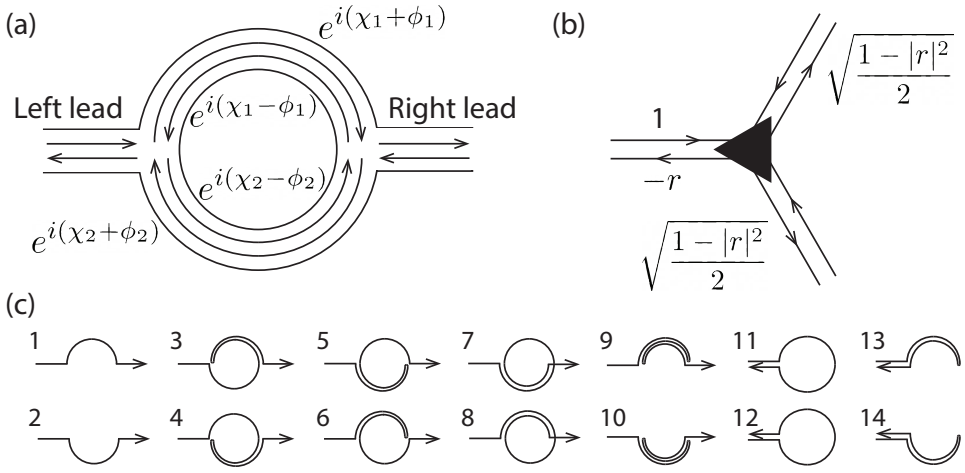

Figure 8.1: **Schematic illustrations of process happening in an Aharanov-Bohm ring. (a)** An AB ring connected to two leads. When an electron propagates through the ring, it picks up a dynamical phase $\chi_{1,2}$ and a magnetic phase $\phi_{1,2}$, along the upper and lower arm, respectively. **(b)** A 3-channel beam splitter, with the scattering amplitudes of an incoming electron wave with a reflection probability of $|r|^2$. **(c)** Possible trajectories of an electron through the AB ring, where the electron reaches the beam splitters up to 4 times and can generate up to 3 harmonics of the AB oscillation.

field is required in an AB experiment, but we assume the magnetic field is weak enough to preserve time-reversal symmetry approximately.

To calculate the conductance through the ring, we need to consider the contributions of each trajectory individually. The conductance through a trajectory is given by the Landauer formula $G = \frac{2e^2}{h} P$ [168], in which $P = |t|^2$ is the interference contribution of 2 trajectories with the transmission amplitude t of a certain trajectory. As an example, let us consider trajectory 1 (in Fig. 8.1(c)). An electron enters the ring and picks up the factor $\sqrt{\frac{1-r^2}{2}}$ to propagate into the upper arm, inside which it acquires the factor $e^{i(\chi_1+\phi_1)}$, and at the exit it picks up the factor $\sqrt{\frac{1-r^2}{2}}$ to the right lead, so that

$$t_1 = \sqrt{\frac{1-r^2}{2}} e^{i(\chi_1+\phi_1)} \sqrt{\frac{1-r^2}{2}} = \frac{1-r^2}{2} e^{i(\chi_1+\phi_1)} \tag{8.3}$$

Similarly, for trajectory 2, we get

$$t_2 = \sqrt{\frac{1-r^2}{2}} e^{i(\chi_2-\phi_2)} \sqrt{\frac{1-r^2}{2}} = \frac{1-r^2}{2} e^{i(\chi_2-\phi_2)} \tag{8.4}$$

Let us now look at the interference contribution of trajectories 1 and 2:

$$P_{12} = 2\mathrm{Re}\, t_1 t_2^* = \frac{(r^2-1)^2}{2} \cos\left(\chi_1 - \chi_2 + \phi_1 + \phi_2\right) \propto \cos\left(\chi_1 - \chi_2 + \phi_{\mathrm{AB}}\right) \tag{8.5}$$

which already gives the AB effect with an oscillation period of Φ_0.

As another example, the transmission amplitude of trajectory 7 is

$$t_7 = \frac{(1-r^2)(r+1)^2}{8} e^{i(\chi_1-\phi_1)} e^{2i(\chi_2-\phi_2)} \tag{8.6}$$

Thus the interference contribution of trajectories 1 and 7 gives

$$P_{17} = 2\mathrm{Re}\, t_1 t_7^* = \frac{(r^2-1)^2(r+1)^2}{8} \cos\left(-2\chi_2 + 2\phi_1 + 2\phi_2\right) \propto \cos\left(-2\chi_2 + 2\phi_{AB}\right) \tag{8.7}$$

indicating the AB effect with a period of $\Phi_0/2$ which contributes to the second harmonic.

The listed 12 possible trajectories in Fig. 8.1(c) cover all possible trajectories where the electron reaches the beam splitters up to 4 times and can generate up to the 3rd harmonic. We examine all pairs of the trajectories and list those pairs which contributes to different orders of the AB effect in Table 8.1.

1st order				2nd order		3rd order
1-2	1-3	1-6	1-8	1-7	2-8	7-8
1-10	2-4	2-5	2-7	3-8	4-7	
2-9	3-4	3-5	3-7	5-7	6-8	
3-8	4-6	4-8	4-10	7-9	8-10	
5-6	5-8	5-10	6-7	11-12[2]		
6-9	7-10	8-9	9-10			
11-13	11-14	12-13	12-14[1]			

Table 8.1: Contributions of pairs of trajectories in Fig. 8.1(c) to each order of the interference.

Before summing up, we need to consider the decoherence of electron waves that in reality leads to a phase uncertainty between partial electron waves, meaning a disappearance of interference. The phase uncertainty $\langle\delta\phi^2\rangle$ is described as [170]

$$\langle\delta\phi^2\rangle \approx \frac{1}{\hbar^2}\int_0^{t_0} \mathrm{d}t \int_0^{t_0} \mathrm{d}t' \langle V(t)V(t')\rangle \tag{8.8}$$

where $V(t)$ describes a potential experienced by an electron which spends the time t_0 from being splitted into the ring until interference. At low temperatures the phase uncertainty increases exponentially with temperature and linearly with time. Following Ref. [170], we can write the phase uncertainty after the electron travels over a distance l as

$$\langle\delta\phi^2\rangle = \frac{t_0}{\tau_\phi(T)} = \frac{l}{L_\phi(T)} \tag{8.9}$$

where $\tau_\phi(T)$ is the dephasing time and $L_\phi(T)$ is the phase coherence length. Because of these magnitude relations, we can write the decreasing factor of the amplitude of the

[1] The pairs involving trajectories from 11 to 14 give negative contributions to the interference amplitude because the electrons exit the ring at the incident lead.

[2] This pair is the interference of time-reversed paths which propagate clockwise and counterclockwise along the ring and results in the so-called Altshuler-Aronov-Spivak (AAS) oscillation [169]. It gives negative contribution to the conductance when interfering constructively.

nth harmonic as $e^{-\frac{nL}{L_\phi(T)}}$, where L is the semi-perimeter of the AB ring, if the AB ring is geometrically symmetric as depicted in Fig. 8.1(a), which is the case in our experiments.

The temperature-dependent phase coherence length can be described by

$$L_\phi(T) = \frac{L}{\alpha} T^{-k} \tag{8.10}$$

where α is a dephasing factor which is dependent on the length of the path that the electron travels. In a ballistic scenario, $k = 1$ [171], and in a diffusive scenario, $k = 1/2$ [172].

Finally, we add the factor $e^{-\frac{nL}{2L_\phi(T)}}$ to the transmissions amplitude (of the form e.g. Eq. 8.3) of each trajectory (trajectories 1,2: $n = 1$; trajectories 3-10: $n = 3$; trajectories 11,12: $n = 2$). The factor of 2 is added in the denominator so that L stays consistent in representing the semi-perimeter of the AB ring in the following formulas. Summing up all pairs listed in Table 8.1 for each order, assuming the dynamical phases $\chi_1 = \chi_2 = \chi$, we have

$$\begin{aligned} P_{\mathrm{AB},n=1} =& \frac{(r^2-1)^2}{2} e^{-\frac{L}{L_\phi(T)}} \cos\phi_{\mathrm{AB}} + \frac{(r^2-1)^2}{2} \left[2r^2\cos(2\chi) - r^2 + 1\right] e^{-\frac{2L}{L_\phi(T)}} \cos\phi_{\mathrm{AB}} \\ &+ \frac{(r^2-1)^2}{32} \left(15r^4 - 4r^3 - 6r^2 - 4r - 1\right) e^{-\frac{3L}{L_\phi(T)}} \cos\phi_{\mathrm{AB}} \end{aligned} \tag{8.11}$$

$$\begin{aligned} P_{\mathrm{AB},n=2} =& \frac{(r+1)^2(r^2-1)^2}{8} \left[2\cos(2\chi) - 1\right] e^{-\frac{2L}{L_\phi(T)}} \cos(2\phi_{\mathrm{AB}}) \\ &+ \frac{(r+1)^2(r^2-1)^2(3r^2-2r+1)}{16} e^{-\frac{3L}{L_\phi(T)}} \cos(2\phi_{\mathrm{AB}}) \end{aligned} \tag{8.12}$$

$$P_{\mathrm{AB},n=3} = \frac{(r+1)^4(r^2-1)^2}{32} e^{-\frac{3L}{L_\phi(T)}} \cos(3\phi_{\mathrm{AB}}) \tag{8.13}$$

Note that the term having the form $\cos(2\chi)\cos\phi_{\mathrm{AB}}$ represents terms shaped like $\frac{1}{2}\left[\cos(\phi_{\mathrm{AB}} - 2\chi) + \cos(\phi_{\mathrm{AB}} + 2\chi)\right]$. These contributions depend on dynamical phases and correspond to a shift of the oscillating pattern with respect to the B-axis, and would disappear if one does Fourier transform to the oscillation and averages over the phase shifts. Further, we neglect higher order contributions in each term due to an exponential decay. Then the conductance due to each harmonic is described as

$$G_{\mathrm{AB},n=1}(T) = \tilde{C} \cdot \frac{1}{2}(r^2-1)^2 e^{(-\alpha+\beta)T^k} \tag{8.14}$$

$$G_{\mathrm{AB},n=2}(T) = \tilde{C} \cdot \frac{1}{8}(r+1)^2(r^2-1)^2 e^{(-2\alpha+\beta)T^k} \tag{8.15}$$

$$G_{\mathrm{AB},n=3}(T) = \tilde{C} \cdot \frac{1}{32}(r+1)^4(r^2-1)^2 e^{(-3\alpha+\beta)T^k} \tag{8.16}$$

in which we use $\tilde{C}$ to absorb constant prefactors as well as the conductance quantum. In the temperature scaling, we use the factors α and β as the time (order) dependent and independent dephasing terms, respectively. The phase coherence length only depends on the coefficient α as shown in Eq. 8.10. The coefficient β indicates additional dephasing mechanisms such as thermal averaging [173] and gate-induced charge fluctuation [171].

Further, let $t = \frac{1}{2}(1-r)$, thus we have a unified form

$$G_{\mathrm{AB},n}(T) = Ct^2(1-t)^{n+1}e^{(-n\alpha+\beta)T^k} \tag{8.17}$$

in which C absorbs all constant prefactors.

In the following sections, we will use Eq. 8.17 to fit the temperature dependence of the amplitudes of AB oscillations obtained in experiments.

As a comparison, Ref. [77] uses $G'_{\mathrm{AB},n}(T) = C't'^2(1-t')^{n-1}e^{(-n\alpha'+\beta')T^k}$ as the fitting formula to the same data set that we will fit[1]. This formula looks similar to Eq. 8.17 in format, although it was not derived using the beam splitter model, and the meanings of t and t' are different. Instead of considering the entrance and the exit of the loop as beam splitters, this model treats the ring as a 1D Fabry-Perot etalon: t' is defined as the transmission from the loop to the leads, and $(1-t')$ thus accounts for that the electron stays in the loop and not exits from the lead. This means that the model does not distinguish between the electrons propagating in the loop and being reflected at a node. We think that the beam splitter model used in this chapter represents the loop better.

Note that the difference between the two approaches is in the relative prefactors of the different orders (C and t), not in the temperature scaling (the exponential function involving α, β and k). Since we will only use the fitting parameter α to extract the phase coherence length, we do not expect much different results compared to Ref. [77].

8.2. MAGNETOCONDUCTANCE OSCILLATIONS IN SAG NETWORKS AND DATA PROCESSING

The magnetoconductance in a SAG nanowire hashtag device A (Fig. 8.2(a) inset) is measured to investigate its phase coherence properties. A magnetic field is applied in the out-of-plane direction. The magnetoconductance is obtained in the field range of 1 to 5 T for 16 top gate voltages in the range of 0 to 0.15 V. An example of such a measurement is shown in Fig. 6.4(c). We observe clear AB oscillations with amplitudes reaching up to $0.2 \cdot e^2/h$. To extract the periodicity as well as the amplitude of these oscillations, we use a Hann window and apply a discrete Fourier transform (DFT), and the resulting spectrum are further ensemble averaged over the 16 gate voltages (Fig. 8.2(a), black line). The universal conductance fluctuations (UCF) result in a power law background with a high peak at low frequencies close to 0 [174, 175]. We observe up to the 5th harmonics of the AB oscillation in the spectrum. We can measure the size of the nanowire loop based on the SEM image and estimate the 1st order (h/e periodic) AB oscillation has a period of $\Delta B = 17\,\mathrm{mT}$. Fig. 8.2(b) shows the extracted peak frequencies against peak number, showing that they nicely follow the estimations based on the geometry of the nanowire loop for all the orders.

To illustrate our data processing to the Fourier spectrum, we plot the averaged Fourier spectrum in logarithmic scale in Fig. 8.2(c) (black line). To avoid the UCF background influencing the extraction of oscillation amplitudes, we fit the low frequency ($B^{-1} < 40\,\mathrm{T}^{-1}$)

[1] Primes are added to the parameters to distinguish them from those in Eq. 8.17.

part of the spectrum with a power law (blue line), and it is then subtracted from the spectrum (corrected spectrum shown in red).

To proceed with extracting the amplitudes of each harmonic, we need to select the frequency ranges over which the Fourier spectra can be integrated, following the analysis process in Ref. [77]. The integration range is determined by applying Gaussian fits to each peak based on the measurement at 20 mK, as shown in Fig. 8.2(d) by the colored solid lines. The integration ranges are set to $\left[f_n - 2\sigma_n, f_n + 2\sigma_n\right]$, with f_n the mean of the Gaussian fit to the nth peak, and σ_n the corresponding standard deviation, shown as the colored dashed lines in Fig. 8.2(d). We note that these windows visibly cover the regions one would expect the integrations to apply and do not overlap among themselves, making it plausible to proceed with the integrations and extracting the amplitudes described in the following sections. Because we observe undoubtably clear spectra for multiple-order oscillations, we feel it acceptable to use the maximum found for each peak, or the peak value of the Gaussian fit itself as the amplitude of a harmonic. Nevertheless, integrating the spectra in a certain frequency range for each harmonic instead of taking the values at specific frequencies helps avoid fluctuations in the extracted amplitudes due to small shifts in frequency among different spectra [166].

8.3. TEMPERATURE DEPENDENCE

To extract the phase coherence length in device A, we can fit the decay of the AB peak amplitude as a function of temperature for multiple orders as indicated by Eq. 8.17. At each temperature, we measure the magnetoconductance in the range from -1.4 T to -0.4 T, at 6 top gate voltages between 0.130 V and 0.135 V for an ensemble average of the Fourier spectra. The averaged Fourier spectra at different temperatures are shown in Fig. 8.3(a). As we expect, the amplitude of each harmonic decreases with increasing temperature. The UCF background are also expected to decrease with higher temperature, as shown in Fig. 8.3(b), indicating a decrease of the phase coherence length [170]. The extracted amplitudes of each harmonic at a given temperature $G_{\mathrm{AB},n}(T)$ are plotted in Fig. 8.4.

Results of fits to Eq. 8.17 are shown in Fig. 8.4(a) and b for the diffusive case ($k = 1/2$) and the ballistic case ($k = 1$), respectively. To more clearly demonstrate the exponential decay of the amplitudes with temperature, plots in logarithmic scale are shown in Fig. 8.4(c) and (d). To fit the data, we use a least square optimization with the data points weighted by their relative error.

Table 8.2 shows the parameters obtained from the fits shown in Fig. 8.4. The first order can be better fitted by the diffusive fit, while higher orders are better fitted by the ballistic fit. This is due to the fact that the diffusive assumption better represents the behavior of electrons at higher temperatures, where only the first harmonic gives a measurable signal. The diffusive behavior in this particular case of SAG nanowire is likely due to dislocations at the nanowire-substrate interface. The ballistic model gives better fits at lower temperatures. A possible reason for this is that the temperatures used in the fits are measured on the mixing chamber plate in this set-up, while the electron temperature could deviate from the mixing chamber temperature below 100 mK and is expected to be higher than the measured temperature.

According to Table 8.2, both models predict a t close to 0.5, which gives a reflection r close to 0, meaning an electron is barely reflected back at a beam splitter. We need

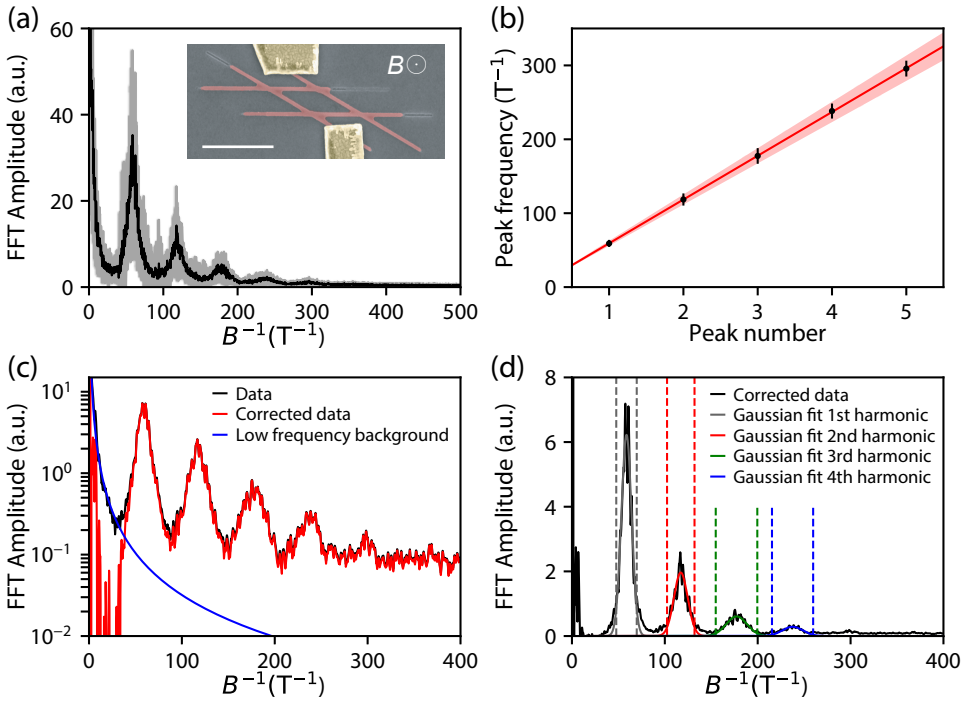

Figure 8.2: **AB effect in device A and data processing. (a)** Fourier transform of the magnetoconductance, averaged over 16 gate voltages. The black line shows the average value, while the gray shading indicates the spread as measured by the standard deviation. Up to 5 harmonics are visible. Inset: false-color scanning electron microscopy (SEM) image of the device. An InSb nanowire loop (red) is in contact with normal metal electrodes Cr/Au (yellow) with an out-of-plane magnetic field and a fridge temperature of 20 mK. The device has a global top gate that is not shown in the SEM image. Scale bar is 1 µm. **(b)** Peak frequency as a function of peak number (black circles), matching the values expected based on the loop size as measured by SEM (red line), with the red shaded region indicating the estimated uncertainty. **(c)** Fourier spectrum of the magnetoconductance in device A (black line) at 20 mK. The low frequency background due to UCF is fitted with a power law (blue line), and subtracted from the data (corrected data shown by the red line). **(d)** Gaussian fits to the first four peaks (solid gray, red, green, and blue lines, respectively). The integration windows, determined by the width of the Gaussians, are indicated by the dashed lines.

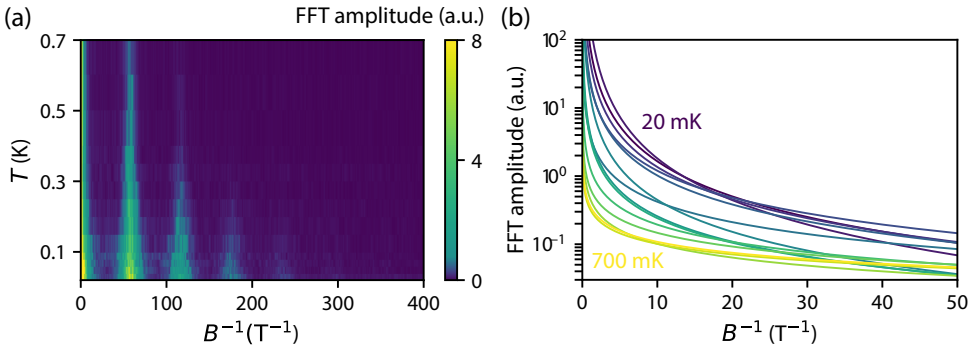

Figure 8.3: **Temperature dependence of the Fourier spectra. (a)** Fourier spectra (horizontal line traces) of the AB oscillation as a function of temperature (vertical direction) in device A. The color shows the amplitude of the FFT. **(b)** The low frequency background obtained in the data analysis due to UCF plotted for the temperatures from 20 mK to 700 mK.

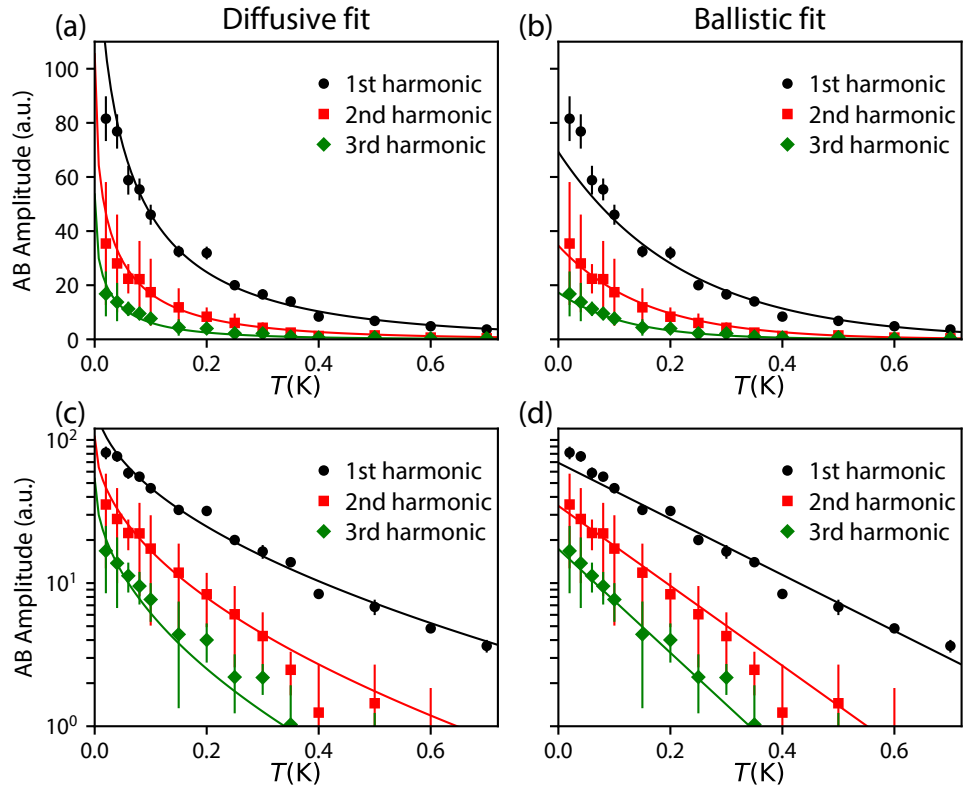

Figure 8.4: **Temperature dependence of the AB amplitude in device A.** Extracted amplitudes for the first three harmonics (black circles, red squares and green diamonds, respectively) as a function of temperature. Solid lines indicate fits to Eq. 8.17. (**a**) Linear scale, $k = 1/2$ (diffusive). (**b**) Linear scale, $k = 1$ (ballistic). The same data are plotted in logarithmic scale in (**c**) (diffusive), and (**d**) (ballistic) for clearer demonstration of the exponential decay.

to limit the range of t in the fitting process from 0 to 0.5, and especially in the ballistic case t hits the boundary of 0.5, indicating no reflection ($r = 0$). We notice that the fit does not give a better result if we lift this restriction. Since R_n^2 of the ballistic fit already indicate good fitting result, we believe either the electrons get barely reflected or the ballistic scenario does not represent the actual situation in the device. For these reasons, we consider the diffusive scenario a more likely model, and we also consider that the phase coherence length at 20 mK $L_\phi(20\,\text{mK}) = 9.47 \pm 2.53\,\mu\text{m}$ a more realistic result.

For both models a considerable β can be obtained, suggesting dephasing mechanisms that are not dependent on the loop trajectory. We speculate that the main contribution to this type of dephasing comes from the additional sections of InSb nanowire extending from the corners of the loop. These "dephasing stubs" have been extensively studied in the context quantum dots, and have been shown to significantly affect the phase coherence properties of mesoscopic systems [176, 177].

Fit to Eq. 8.17		Ballistic fit ($k = 1$)		Diffusive fit ($k = 1/2$)	
Parameter	Unit	Value	Standard deviation	Value	Standard deviation
t	-	0.50	0.04	0.49	0.07
C	a.u.	1108	92	3320	394
α	K^{-1}	1.92	0.33	1.04	0.28
β	K^{-1}	-2.59	0.48	-3.70	0.44
R_1^2	-	0.91	-	0.95	-
R_2^2	-	0.98	-	0.96	-
R_3^2	-	0.98	-	0.93	-
$L_\phi(1\,\text{K})$	μm	0.73	0.12	1.34	0.36
$L_\phi(20\,\text{mK})$	μm	36	6	9.47	2.53

Table 8.2: **Parameters corresponding to the fits shown in Fig. 8.4**. The parameters R_n^2 refer to the coefficient of determination of the fit of the nth harmonic. Phase coherence lengths are calculated based on Eq. 8.10, with $L = 1.4\,\mu\text{m}$.

8.4. AHARONOV-BOHM RING WITHOUT DEPHASING STUBS

To make a comparison between Aharonov-Bohm loops with and without dephasing stubs, we later modified the growth mask design to create SAG nanowire loop without extra dephasing stubs except sections allowing source and drain contacts. Such a device (device B) is shown in the inset Fig. 8.5(a). Different from device A where two pairs of parallel nanowires form a 30° angle, device B has a rectangular shape. Similar to the data processing of device A in Section 8.2, the Fourier spectrum of the AB oscillation averaged over 6 gate voltages is shown in Fig. 8.5(a). Two harmonics are visible, which is not necessary to indicate a shorter phase coherence length but is likely because the loop circumference ($5.92 \pm 0.20\,\mu\text{m}$) is significantly larger than that of device A ($2.80 \pm 0.16\,\mu\text{m}$). The period of the first order is 2.1 mT, corresponding to the expected h/e periodic oscillation according to the dimensions of this loop.

Shown in Fig. 8.5(c), similar to device A, the UCF background is fitted at the low fre-

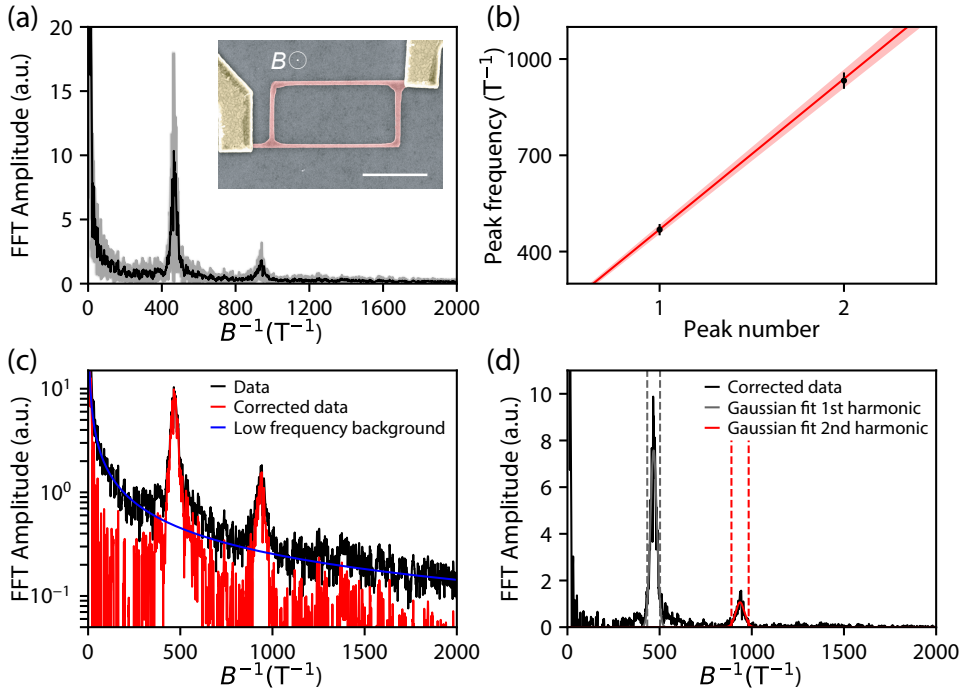

Figure 8.5: **AB effect in device B and data processing. (a)** Fourier transform of the magnetoconductance, averaged over 6 gate voltages. The black line shows the average value, while the gray shading indicates the spread as measured by the standard deviation. Up to 2 harmonics are visible. Inset: false-color scanning electron microscopy (SEM) image of the device. An InSb nanowire loop (red) is in contact with normal metal electrodes Cr/Au (yellow) with an out-of-plane magnetic field and a fridge temperature of 20 mK. The device has a global top gate that is not shown in the SEM image. Scale bar is 1 µm. **(b)** Peak frequency as a function of peak number (black circles), matching the values expected based on the loop size as measured by SEM (red line), with the red shaded region indicating the estimated uncertainty. **(c)** Fourier spectrum of the magnetoconductance in device B (black line) at 20 mK. The low frequency background due to UCF is fitted with a power law (blue line), and subtracted from the data (corrected data shown by the red line). **(d)** Gaussian fits to the two peaks (solid gray and red, respectively). The integration windows, determined by the width of the Gaussians, are indicated by the dashed lines.

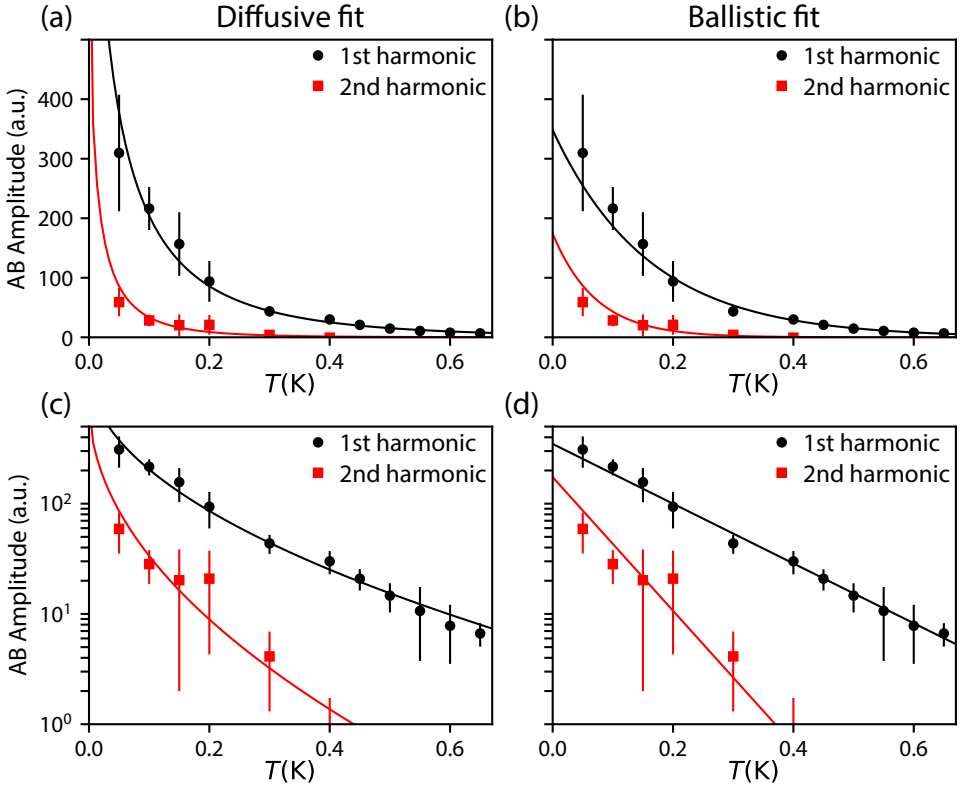

Figure 8.6: **Temperature dependence of the AB amplitude in device B.** Extracted amplitudes for the first two harmonics (black circles and red squares, respectively) as a function of temperature. Solid lines indicate fits to Eq. 8.17. (**a**) Linear scale, $k = 1/2$ (diffusive). (**b**) Linear scale, $k = 1$ (ballistic). The same data are plotted in logarithmic scale in (**c**) (diffusive), and (**d**) (ballistic) for clearer demonstration of the exponential decay.

quency part ($120\,\mathrm{T}^{-1} < B^{-1} < 320\,\mathrm{T}^{-1}$) with a power law (blue line) and subtracted from the Fourier spectrum (black line). The resulted red line is then used to extract the amplitudes of different harmonics. Fig. 8.5(d) shows the Gaussian fits (colored solid lines) to each Fourier peak and the corresponding integration windows (colored dashed lines).

Fig. 8.6 shows the extracted amplitudes of each harmonic (scatter plots) as well as diffusive (a,c) and ballistic (b,d) fits. The amplitudes of the second harmonic drops below noise level for temperatures above 250 mK, which should be avoided in the fitting process, thus we set a lower threshold of 1.3 (a.u.) for the extracted amplitudes to apply the fits.

The fitting results are shown in Table 8.3. Similar to device A, we notice that $t = 0.5$ for both the ballistic and the diffusive scenarios, indicating that an electron is barely reflected back at a beam splitter. It is worth notifying that Ref. [77] obtains similar t values with similar functional form of the fit although the meaning of t is different. We need to point out that artifacts due to the fitting procedure or the form of the fit function can not be excluded to cause the value of t. The values of β is slightly reduced compared to those obtained from device A, suggesting that dephasing is suppressed by removing dephasing stubs from the AB ring. We obtain a phase coherence length of $5.96 \pm 2.46\,\mu\mathrm{m}$ at 20 mK, in the same order of magnitude but shorter compared to device A.

It is worth noting that a set of two harmonics is the bare minimum to perform the fit based on Eq. 8.17, which separates the exponential term to an order-dependent dephasing contribution and an order-independent one, namely α and β, as it essentially constitutes a linear fit of two points. Given the poor fits of the second harmonic in both scenarios indicated by R_2^2, we would like to mention that it is hard to draw conclusions on the results of the dephasing terms. Ref. [172] points out that the contribution to the AB oscillation amplitude by the phase coherence length can depend on the size of the loop. Therefore, to make a better comparison and to obtain higher harmonics to make the fits more significant, we propose to fabricate devices with the same loop size, with and without dephasing stubs. However, we have not yet managed to measure a loop with a similar size as device A and without dephasing stubs, due to an ubiquitous low fabrication yield on SAG chips.

8.5. BIAS DEPENDENCE

In Section 8.1 we have demonstrated that the phase of the AB oscillation is dependent on dynamical phases. Equations 8.5 and 8.7 both give examples in such a manner. In a two-terminal measurement, the time reversibility manifests itself as the relation $G(B) = G(-B)$, indicating the magnetoconductance must be even in magnetic field with a phase restricted to 0 or π. This is called the Onsager-Büttiker symmetry relation and holds at a relatively small bias voltage [28]. This relation indicates that when the dynamical phase changes, e.g. induced by applying a small bias voltage, π phase shift is expected to be observed instead of a smooth phase change [178].

To investigate the bias dependence of the AB oscillation, we apply a DC bias voltage to the source-drain on device A. Fig. 8.7(a) shows the measured magnetoconductance versus bias in a magnetic field range of 0.1 T showing ~ 6 periods. A π phase shift is observed at $\sim \pm 150\,\mu\mathrm{V}$. Two line traces at bias voltages of $80\,\mu\mathrm{V}$ and $230\,\mu\mathrm{V}$ in Fig. 8.7(b) demonstrate 0 and π phase oscillations.

Fit to Eq. 8.17		Ballistic fit ($k=1$)		Diffusive fit ($k=1/2$)	
Parameter	Unit	Value	Standard deviation	Value	Standard deviation
t	-	0.50	0.16	0.50	0.26
C	a.u.	5569	617	26462	4091
α	K^{-1}	7.71	2.16	3.51	1.45
β	K^{-1}	1.47	2.22	-3.10	1.53
R_1^2	-	0.96	-	0.95	-
R_2^2	-	0.51	-	0.59	-
$L_\phi(1\,\mathrm{K})$	µm	0.38	0.11	0.84	0.35
$L_\phi(20\,\mathrm{mK})$	µm	19.2	5.4	5.96	2.46

Table 8.3: **Parameters corresponding to the fits shown in Fig. 8.6**. The parameter R_n^2 refers to the coefficient of determination of the fit of the nth harmonic. Phase coherence lengths are calculated based on Eq. 8.10, with $L = 2.96\,\mu\mathrm{m}$.

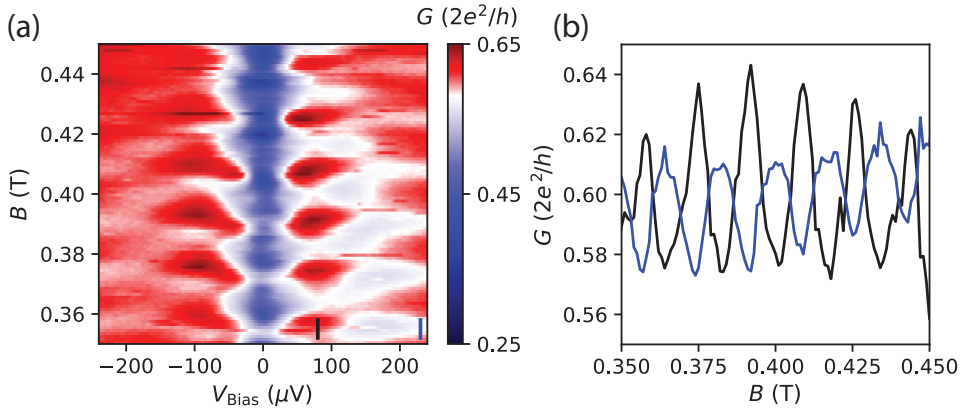

Figure 8.7: **Bias dependence of the AB oscillations. (a)** Magnetoconductance of device A plotted versus B and V_{Bias}. **(b)** Vertical line cuts at the positions indicated by the black and blue labels in (a).

8.6. CONCLUSION

The SAG platform provides a relatively easy method to implement nanowire networks, allowing us to perform an extensive study on the phase coherence properties of nanowire networks, one of the key ingredient needed for measurement-based gate operation and topological qubit readout [75]. Compared to the VLS platform shown in Section 3.1, the SAG platform is much more practical for AB measurements and indeed demonstrated good phase coherence properties. We note that this is the first time that higher order harmonics of AB oscillation are demonstrated for InSb nanowire networks.

After investigating the temperature dependence of the AB oscillations for multiple orders, we extrated the phase coherence length of $L_\phi(20\,\mathrm{mK}) = 9.47 \pm 2.53\,\mu\mathrm{m}$. We also tried to study if reducing dephasing stubs makes contribution to longer phase coherence length but did not obtain conclusive evidences. Thus we propose that devices with the

same loop size, with and without dephasing stubs, should be studied in the future. If our assumption on the dephasing stubs is true, this proposal is worth investigating and would be beneficial to meet the requirements of topological qubits [61, 62].

It is also worth pointing out that we only studied heterogeneous nanowire loops, i.e. containing nanowire sections in different growth directions. We note that both devices consist of two pairs of parallel wires intersecting at 30° or 90° angle, meaning one parallel pair is grown along the ⟨110⟩ direction while the other is grown along the ⟨112⟩ direction, given the six-fold symmetry of the InP substrate. Therefore, loops that only contain ⟨110⟩ or ⟨112⟩ nanowires can be studied for comparison.

DATA AVAILABILITY

The raw data and the data analysis codes that support the findings of this chapter are available at `https://doi.org/10.5281/zenodo.6390952`.

CONTRIBUTIONS TO THE PROJECT

D. Xu, K. Vermeulen, Q. Wang and B. Hesselmann fabricated the devices. **D. Xu**, M. W. A. de Moor, K. Vermeulen, and B. Hesselmann performed the transport measurements. The fitting model was developed by **D. Xu** in discussions with M. W. A. de Moor. The analysis presented in this chapter was performed by **D. Xu** on the basis of analysis codes written by M. W. A. de Moor. R. L. M. Op het Veld and J. Jung carried out the growth of SAG InSb networks under the supervision of E. P. A. M. Bakkers at Eindhoven University of Technology. The project was supervised by H. Zhang and L. P. Kouwenhoven.

9

CONCLUSIONS AND OUTLOOKS

Als je ergens niet bent, ben je óf te vroeg óf te laat.

Johan Cruijff

9.1. CONCLUSIONS

In this section we summarize important results in each chapter of this thesis. This thesis demonstrates research along two venations: the VLS InSb nanowire platform and the SAG platform with epitaxial Al. On VLS hybrid nanowires, we performed tunneling spectroscopy studies on various phenomena due to the induced superconductivity, especially on ZBPs. On the SAG platform, we have shown preliminary results on the induced superconductivity and studied its phase coherent properties benefited from its network nature.

CHAPTER 4

In the VLS InSb nanowires with epitaxial Al emerging from 2017, We report large ZBPs with heights on the order of $2e^2/h$. This chapter is a rewritten work of Ref. [15]. The ZBP height reachs the order of $2e^2/h$ after hard superconducting gap and ballistic transport in hybrid QPCs have been achieved. We further investigate the behavior of the zero-bias conductance as functions of various parameters, such as the tunnel gate voltage and the super gate voltage. Plateau-like ZBP height close to $2e^2/h$ is observed in certain tunnel gate ranges.

Besides the original Majorana interpretation of these ZBPs that could be due to confirmation bias in 2017-2018, we discussed other possibilities giving rise to zero-bias anomalies, namely the "good, bad and ugly" ZBPs [55] resulted from a topological phase, quasi-Majoranas due to a smooth potential and random disorder potential, respectively. We note that the large ZBPs are a milestone in hybrid nanowire systems in 2017, though subsequent numerical studies have shown that we cannot identify conclusive explanations on these ZBPs. Therefore, non-local experiments has to be complemented in order to help distinguish possible origins of the ZBPs.

CHAPTER 5

After we observed large ZBPs in VLS InSb-Al nanowires in Chapter 4, we conducted more detailed studies on this system, here namely how the electric fields affects the coupling between the semiconductor and the superconductor.

We find that the induced superconducting gap, the effective Landé g-factor and the spin-orbit coupling strength in hybrid nanowires can be tuned by the electrostatic environment, i.e. applied gate voltage. The change of these quantities is dominated by the coupling between the semiconductor and the superconductor. These effects are corroborated by Schrödinger-Poisson simulations on the device geometry. We also notice that the tunability of spin-orbit coupling induces level repulsion and leads to accidental zero-bias anomalies, thus understanding the effect of the electrostatic environment is essential for interpreting zero-bias anomalies. The detailed understanding of the interplay of gate voltage and electronic properties will help advance the design and operation of even more complex devices based on hybrid semiconductor-superconductor heterostructures.

CHAPTER 6

The novel platform of "SAG" in-plane nanowires of InSb on InP substrate has been successfully developed. We studied the growth dynamics and achieved single crystalline nanowires despite the large lattice mismatch between the wires and the substrate. Transport results on these nanowires have shown high-quality phase-coherence. Based on a hard-mask selective etching method, hybrid devices demonstrated hard superconducting gap and $2e$-Coulomb blockaded transport. The SAG platform will allow scalable experiments for more complicated quantum transport, paving the way towards Majorana braiding.

CHAPTER 7

We have demonstrated oscillatory behaviors of Andreev bound states as a function of magnetic field in two SAG hybrid nanowire devices. We explored the possible mechanism where a flux dependent Little-Parks-like effect could induced these oscillations. Numerical study shows that this is unlikely in the SAG devices.

CHAPTER 8

The high-quality Aharonov-Bohm (AB) effect in SAG networks shown in Chapter 6 stimulated an extensive study on its phase coherent properties. Compared to the VLS platform, SAG makes it relatively easy to implement nanowire networks for this research. We demonstrated for the first time higher order harmonics of AB in InSb nanowire networks. We described the data processing to extract the AB amplitudes for each harmonic and developed the fitting model on their temperature dependence in order to extract the phase coherence length. We obtained a phase coherence length at 20 mK of $9.47 \pm 2.53\,\mu$m. Note that the values of the phase coherence length cannot be simply compared among similar works due to wide difference in fitting models.

In future studies, we may use devices with the same loop size, with and without dephasing stubs, to compare the phase coherence length. And loops that only contain $\langle 110 \rangle$ or $\langle 112 \rangle$ nanowires can be studied to avoid the influences due to different growth directions.

9.2. OUTLOOKS

In this section we discuss the improvements and possible future projects proceeding the findings of this thesis. These will be discussed separately for the SAG platform and for the VLS nanowires.

9.2.1. IMPROVEMENTS ON SAG

Because SAG has been shown to have relatively good phase coherent properties and $2e$-transport and the motivation of SAG is to build a scalable nanowire network, a natural follow-up project is the "teleportation" as described in Section 2.3.3.

A schematic of this type of device has been shown in Fig. 2.9a, and we have already implemented such a device that meets the requirements on a SAG InSb-Al nanowire loop, as shown in Fig. 9.1. The profile of the nanowire loop with two extra arms can be

seen under the layers of dielectric and gates in the image. The two Cr/Au leads contact the arms of the loop, forming an interferometer. A superconducting island is fabricated on one interference arm by the hard-mask etching method, with gates controlling the tunnel barriers and the chemical potential, while another cutter gate controls the other interference arm.

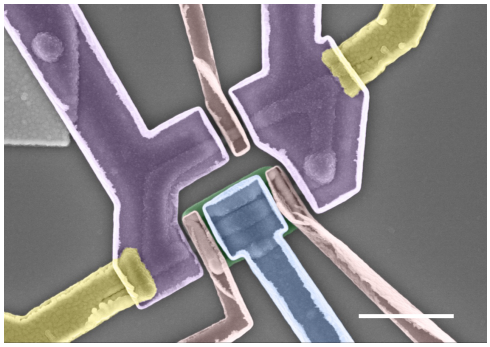

Figure 9.1: **A SEM image hybrid SAG loop device.** The SAG InSb loop has a parallelogram shape (profile visible) with two extra arms available for Cr/Au leads (yellow). A Si_xN_y layer (green) is deposited on top of the contacts and the SAG loop, serving as an etch mask for Al to create a hybrid island. Then another Si_xN_y layer is deposited globally on the chip (not colored) as a dielectric. Three tunnel gates (red) are deposited to control the tunnel barriers on both side of the island as well as a cutter of the reference arm, and global gates (purple) are used to tune the conductance of the interference loop. Scale bar is 1 µm.

Late 2019 to 2020, we have achieved individual control of all gates and measured signatures of $2e$-Coulomb blockade while depleting the reference arm. However, experiments showed that the gates are not stable enough to reproduce the experimental signatures, and gate drifting and jumping happened too much to stabilize the device in a certain regime. The reasons can include that the double layers of dielectric involving standing edges of the hard mask together with the wet etching process and many lithography steps induce too many charge traps that destabilize the gates, or that Al diffuses with InSb over time during the fabrication steps, especially heat producing steps, or even the crystal quality itself.

Therefore, a growth technique that can avoid the superconducting film being selectively etched, namely selective deposition, is needed to overcome the problems. Before we come to the selective deposition technique, I would like to point out the predicament which makes people doubting the significance of this type of measurement. For any experiments involving a hybrid island with a charging energy, the only way to confirm the existence of Majorana zero modes according to an h/e-period interference, not to speak of the π-phase shift, is to make sure the superconducting section has a hard gap and is free from any trivial subgap states. Otherwise, many alternative interpretations of the phenomena can arise and a convincing method to distinguish them from Majorana zero modes has not yet been proposed.

A technique of the selective deposition of the superconductor has been developed by our collaborators in Eindhoven. The selective deposition requires shadowing walls, which is conducted with a similar concept as the selective area growth. Similar to the

SAG growth, openings on the mask are designed for the shadowing walls and high InP walls are selective-area grown on the InP substrate. An illustration of this concept is shown in Fig. 9.2(a) by the green wall.

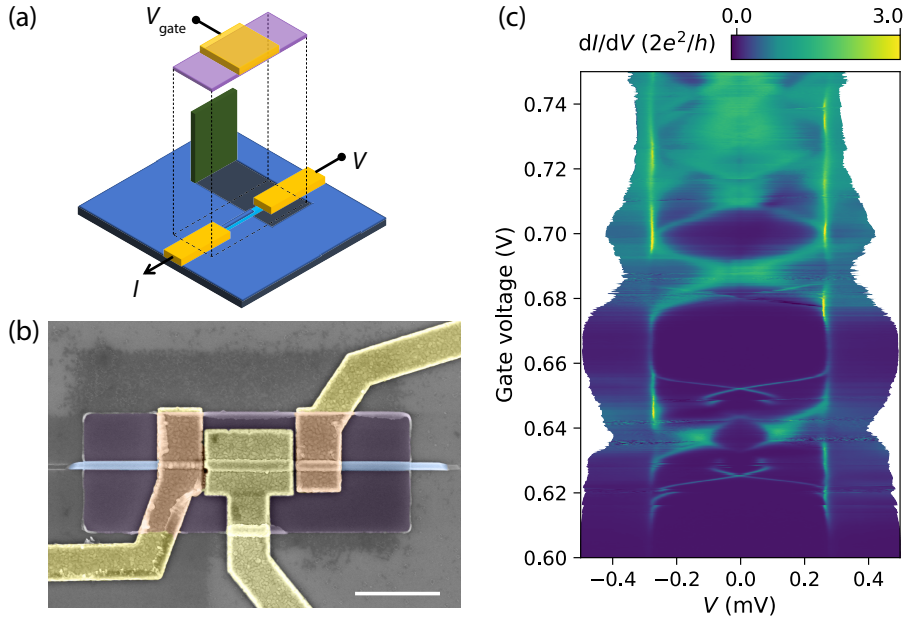

Figure 9.2: **A SAG InSb-Al device with InP shadow wall.** **(a)** Schematic illustration of a SAG N-nanowire-S device with the shadow wall technique. The InP wall (dark green) shadows the Al (dark blue) deposited from the rear left and thus create a shadowed region on the substrate. The InSb nanowire (light blue) is contacted by two Cr/Au leads in the normal region (left, yellow) and the superconducting region (right, yellow). A Si_xN_y layer (purple) is deposited on top of the contacts and the nanowire, serving as an etch mask for Al as well as a dielectric. A top gate (middle, yellow) is deposited on the dielectric. **(b)** SEM image of the device illustrated in (a). Scale bar is 1µm. **(c)** Differential conductance (dI/dV) as a function of gate voltage and bias voltage (V) showing a hard gap, measured in the device in (b).

We have developed a successful fabrication process on this type of growth chips described in Section 3.2, resulting in a N-nanowire-S device with a global top gate (Fig. 9.2(b)) for characterization. Differential conductance dI/dV measured in this device demonstrates hard superconducting gap while sweeping the gate voltage (Fig. 9.2(c)).

Another potential development of the SAG platform is to take local back gates into account. So far all SAG devices rely on top gates which require a dielectric layer directly deposited on the nanowire to separate them. However, the top dielectric layer can be an origin of poor transport results. Back gates on SAG chips not only get over the necessity of top gates, but also allow precise control on the electrostatic environment in the vicinity of the nanowires. Back gates can be integrated into the growth process again with the concept of selective area growth, thus it requires a buffer layer to serve as not only the dielectric that covers the gates, but also the substrate for the growth of semiconductor nanowires. This technique is still under development.

9.2.2. ADVANCES IN VLS HYBRID NANOWIRES

Now let us focus back on the VLS nanowire system. After the era of local tunneling spectroscopy, such as Chapter 4 and 5, researchers have been always trying to explore the nonlocal properties of hybrid nanowire systems. These efforts include local tunneling spectroscopy with nonlocal electrostatic gating in Ref. [93].

A natural design of a nonlocal measurement is a "three-terminal" device, in which the superconducting film that proximitized the nanowire also serves as a drain, while two normal leads contact the nanowires on both sides of the hybrid section. Nevertheless, figuring out the correct measurement scheme and interpreting the nonlocal signals in this type of experiments are not as simple as one may naïvely imagine. The first trials of three-terminal InAs or InSb hybrid nanowire devices have become successful not so long ago, including efforts on tunneling spectroscopy in SAG [179–182], VLS [183–185] and theory [186, 187] from 2019 onwards.

In Delft, the three-terminal devices on VLS nanowires were made possible by *ex situ* depositing superconductors after hydrogen cleaning [165, 183, 184] in our lab. However, drawbacks of tunneling spectroscopy on these devices still exist [185], where not all experimental observations can be explained and many still rely on speculations, while numerical simulations of these devices only provide assessment of consistency but not the very mechanism behind the experimental results.

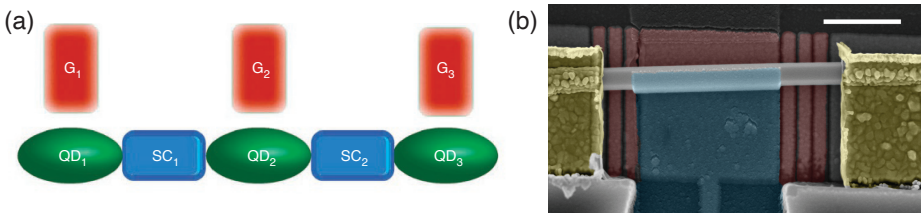

Figure 9.3: **(a)** Conceptional illustration of a chain of quantum dots and superconductors. The chemical potential of each quantum dot can be individually tuned by the gate G_n. Adapted from Ref. [188]. **(b)** SEM image of a device consisting of 2 quantum dots and 1 superconducting region. The nanowire is contacted with Cr/Au leads (yellow) on both sides, while the middle section is proximitized by an Al superconducting film (blue) and at the same time used as a drain. Bottom gates (red) are used to define quantum dots and to tune the chemical potentials of the dots as well as the hybrid nanowire. A thin Al_2O_3 film separates the bottom gates from the nanowire. Scale bar is 500 nm. Taken from Ref. [189].

Researchers in Delft turned to Ref. [188] to get an inspiration to build the next generation of three-terminal devices. A conceptional illustration of this proposal is shown in Fig. 9.3(a). A quantum dot-superconductor array is proposed to hold a Majorana chain and Majorana modes occur at the end quantum dots of the array, realizing an effective Kitaev-chain in an experimental system. A minimal version of this array is realized as shown in Fig. 9.3(b), in which the superconductor film (Al) is deposited using the technique mentioned above. Groups of finger gates create two quantum dots on both ends. Researchers found immediately that integrating quantum dots into the three-terminal setup provides powerful tools to probe the quasiparticle distribution in the hybrid section because quantum dots act as charge filters on the quasiparticles flowing into or out of the superconductor [189].

Theoretical work [190] and experiments have shown that crossed Andreev reflection

(CAR) and elastic co-tunneling (ECT) are the key elements in the measurements, which refer to that an injecting electron is drained as a Cooper pair with transferring a hole to the other lead, or co-tunnels as an electron to the other lead, respectively. These processes should be mediated via an ABS, thus the strengths of CAR and ECT will show their individual dependences on the parameters which tune the ABS. With applying a magnetic field, quantum dots can even further serve as spin filters to probe superconducting paring. This sequence of research opens up a new era of condensed matter research on hybrid semiconductor-superconductor nanowire systems [191–194].

BIBLIOGRAPHY

[1] E. Majorana. Teoria simmetrica dell'elettrone e del positrone. *Il Nuovo Cimento (1924-1942)*, 14:171, September 2008.

[2] P. Drude. Zur Elektronentheorie der Metalle. *Annalen der Physik*, 306:566–613, 1900.

[3] R. P. Feynman. There's plenty of room at the bottom. *Resonance*, 16:890, October 2011.

[4] P. W. Anderson. More Is Different. *Science*, 177:393–396, August 1972.

[5] J. E. Avron, D. Osadchy, and R. Seiler. A Topological Look at the Quantum Hall Effect. *Physics Today*, 56:38–42, August 2003.

[6] M. A. Paalanen, D. C. Tsui, and A. C. Gossard. Quantized Hall effect at low temperatures. *Physical Review B*, 25:5566–5569, April 1982.

[7] B. J. van Wees, H. van Houten, C. W. J. Beenakker, J. G. Williamson, L. P. Kouwenhoven, D. van der Marel, and C. T. Foxon. Quantized conductance of point contacts in a two-dimensional electron gas. *Physical Review Letters*, 60:848–850, February 1988.

[8] K. von Klitzing, G. Dorda, and M. Pepper. New Method for High-Accuracy Determination of the Fine-Structure Constant Based on Quantized Hall Resistance. *Physical Review Letters*, 45:494–497, August 1980.

[9] I. van Weperen, S. R. Plissard, E. P. A. M. Bakkers, S. M. Frolov, and L. P. Kouwenhoven. Quantized Conductance in an InSb Nanowire. *Nano Letters*, 13:387–391, February 2013.

[10] A. Yu. Kitaev. Unpaired Majorana fermions in quantum wires. *Physics-Uspekhi*, 44:131–136, October 2001.

[11] A. Yu. Kitaev. Fault-tolerant quantum computation by anyons. *Annals of Physics*, 303:2–30, January 2003.

[12] L. Fu and C. L. Kane. Superconducting Proximity Effect and Majorana Fermions at the Surface of a Topological Insulator. *Physical Review Letters*, 100:096407, March 2008.

[13] R. M. Lutchyn, J. D. Sau, and S. Das Sarma. Majorana Fermions and a Topological Phase Transition in Semiconductor-Superconductor Heterostructures. *Physical Review Letters*, 105:077001, August 2010.

[14] Y. Oreg, G. Refael, and F. von Oppen. Helical Liquids and Majorana Bound States in Quantum Wires. *Physical Review Letters*, 105:177002, October 2010.

[15] H. Zhang, C.-X. Liu, S. Gazibegovic, D. Xu, J. A. Logan, G. Wang, N. van Loo, J. D. S. Bommer, M. W. A. de Moor, D. Car, R. L. M. Op het Veld, P. J. van Veldhoven, S. Koelling, M. A. Verheijen, M. Pendharkar, D. J. Pennachio, B. Shojaei, J. S. Lee, C. J. Palmström, E. P. A. M. Bakkers, S. Das Sarma, and L. P. Kouwenhoven. Quantized Majorana conductance. *Nature*, 556:74–79, April 2018.

[16] P. Brouwer, K. Ensslin, D. Goldhaber-Gordon, and P. Lee. Nature paper "Quantized Majorana conductance", report from independent experts. March 2021.

[17] M. Leijnse and K. Flensberg. Introduction to topological superconductivity and Majorana fermions. *Semiconductor Science and Technology*, 27:124003, November 2012.

[18] R. M. Lutchyn, E. P. A. M. Bakkers, L. P. Kouwenhoven, P. Krogstrup, C. M. Marcus, and Y. Oreg. Majorana zero modes in superconductor–semiconductor heterostructures. *Nature Reviews Materials*, 3:52–68, May 2018.

[19] C. W. J. Beenakker. Search for Majorana fermions in superconductors. *Annual Review of Condensed Matter Physics*, 4:113–136, April 2013.

[20] P. G. de Gennes. Boundary Effects in Superconductors. *Reviews of Modern Physics*, 36:225–237, January 1964.

[21] R. Winkler. *Spin-Orbit Coupling Effects in Two-Dimensional Electron and Hole Systems*. Springer Tracts in Modern Physics. Springer-Verlag, Berlin Heidelberg, 2003.

[22] S. Das Sarma, J. D. Sau, and T. D. Stanescu. Splitting of the zero-bias conductance peak as smoking gun evidence for the existence of the Majorana mode in a superconductor-semiconductor nanowire. *Physical Review B*, 86:220506, December 2012.

[23] V. Mourik, K. Zuo, S. M. Frolov, S. R. Plissard, E. P. A. M. Bakkers, and L. P. Kouwenhoven. Signatures of Majorana Fermions in Hybrid Superconductor-Semiconductor Nanowire Devices. *Science*, 336:1003–1007, May 2012.

[24] M. T. Deng, C. L. Yu, G. Y. Huang, M. Larsson, P. Caroff, and H. Q. Xu. Anomalous Zero-Bias Conductance Peak in a Nb–InSb Nanowire–Nb Hybrid Device. *Nano Letters*, 12:6414–6419, December 2012.

[25] A. Das, Y. Ronen, Y. Most, Y. Oreg, M. Heiblum, and H. Shtrikman. Zero-bias peaks and splitting in an Al–InAs nanowire topological superconductor as a signature of Majorana fermions. *Nature Physics*, 8:887–895, December 2012.

[26] H. O. H. Churchill, V. Fatemi, K. Grove-Rasmussen, M. T. Deng, P. Caroff, H. Q. Xu, and C. M. Marcus. Superconductor-nanowire devices from tunneling to the multichannel regime: Zero-bias oscillations and magnetoconductance crossover. *Physical Review B*, 87:241401, June 2013.

[27] A. D. K. Finck, D. J. Van Harlingen, P. K. Mohseni, K. Jung, and X. Li. Anomalous Modulation of a Zero-Bias Peak in a Hybrid Nanowire-Superconductor Device. *Physical Review Letters*, 110:126406, March 2013.

[28] M. Buttiker. Symmetry of electrical conduction. *IBM Journal of Research and Development*, 32:317–334, May 1988.

[29] C. W. J. Beenakker. Quantum transport in semiconductor-superconductor microjunctions. *Physical Review B*, 46:12841–12844, November 1992.

[30] M. Tinkham. *Introduction to Superconductivity*. Courier Corporation, January 2004.

[31] N. N. Bogoljubov, V. V. Tolmachov, and D. V. Širkov. A New Method in the Theory of Superconductivity. *Fortschritte der Physik*, 6:605–682, 1958.

[32] R. Landauer. Electrical resistance of disordered one-dimensional lattices. *The Philosophical Magazine: A Journal of Theoretical Experimental and Applied Physics*, 21:863–867, April 1970.

[33] G. E. Blonder, M. Tinkham, and T. M. Klapwijk. Transition from metallic to tunneling regimes in superconducting microconstrictions: Excess current, charge imbalance, and supercurrent conversion. *Physical Review B*, 25:4515–4532, April 1982.

[34] J. H. Davies. *The Physics of Low-dimensional Semiconductors: An Introduction*. Cambridge University Press, Cambridge, 1997.

[35] M. Wimmer, A. R. Akhmerov, J. P. Dahlhaus, and C. W. J. Beenakker. Quantum point contact as a probe of a topological superconductor. *New Journal of Physics*, 13:053016, May 2011.

[36] M. T. Deng, S. Vaitiekėnas, E. B. Hansen, J. Danon, M. Leijnse, K. Flensberg, J. Nygård, P. Krogstrup, and C. M. Marcus. Majorana bound state in a coupled quantum-dot hybrid-nanowire system. *Science*, 354:1557–1562, December 2016.

[37] Ö. Gül, H. Zhang, J. D. S. Bommer, M. W. A. de Moor, D. Car, S. R. Plissard, E. P. A. M. Bakkers, A. Geresdi, K. Watanabe, T. Taniguchi, and L. P. Kouwenhoven. Ballistic Majorana nanowire devices. *Nature Nanotechnology*, 13:192–197, March 2018.

[38] S. R. Plissard, D. R. Slapak, M. A. Verheijen, M. Hocevar, G. W. G. Immink, I. van Weperen, S. Nadj-Perge, S. M. Frolov, L. P. Kouwenhoven, and E. P. A. M. Bakkers. From InSb Nanowires to Nanocubes: Looking for the Sweet Spot. *Nano Letters*, 12:1794–1798, April 2012.

[39] F. Nichele, A. C. C. Drachmann, A. M. Whiticar, E. C. T. O'Farrell, H. J. Suominen, A. Fornieri, T. Wang, G. C. Gardner, C. Thomas, A. T. Hatke, P. Krogstrup, M. J. Manfra, K. Flensberg, and C. M. Marcus. Scaling of Majorana Zero-Bias Conductance Peaks. *Physical Review Letters*, 119:136803, September 2017.

[40] H. Zhang, M. W. A. de Moor, J. D. S. Bommer, D. Xu, G. Wang, N. van Loo, C.-X. Liu, S. Gazibegovic, J. A. Logan, D. Car, R. L. M. Op het Veld, P. J. van Veldhoven, S. Koelling, M. A. Verheijen, M. Pendharkar, D. J. Pennachio, B. Shojaei, J. S. Lee, C. J. Palmström, E. P. A. M. Bakkers, S. Das Sarma, and L. P. Kouwenhoven. Large zero-bias peaks in InSb-Al hybrid semiconductor-superconductor nanowire devices. *arXiv:2101.11456 [cond-mat]*, January 2021.

[41] P. Krogstrup, N. L. B. Ziino, W. Chang, S. M. Albrecht, M. H. Madsen, E. Johnson, J. Nygård, C. M. Marcus, and T. S. Jespersen. Epitaxy of semiconductor-superconductor nanowires. *Nature Materials*, 14:400–406, April 2015.

[42] S. Gazibegovic, D. Car, H. Zhang, S. C. Balk, J. A. Logan, M. W. A. de Moor, M. C. Cassidy, R. Schmits, D. Xu, G. Wang, P. Krogstrup, R. L. M. Op het Veld, K. Zuo, Y. Vos, J. Shen, D. Bouman, B. Shojaei, D. Pennachio, J. S. Lee, P. J. van Veldhoven, S. Koelling, M. A. Verheijen, L. P. Kouwenhoven, C. J. Palmström, and E. P. A. M. Bakkers. Epitaxy of advanced nanowire quantum devices. *Nature*, 548:434–438, August 2017.

[43] S. M. Albrecht, A. P. Higginbotham, M. Madsen, F. Kuemmeth, T. S. Jespersen, J. Nygård, P. Krogstrup, and C. M. Marcus. Exponential protection of zero modes in Majorana islands. *Nature*, 531:206–209, March 2016.

[44] J. Shen, S. Heedt, F. Borsoi, B. van Heck, S. Gazibegovic, R. L. M. Op het Veld, D. Car, J. A. Logan, M. Pendharkar, S. J. J. Ramakers, G. Wang, D. Xu, D. Bouman, A. Geresdi, C. J. Palmström, E. P. A. M. Bakkers, and L. P. Kouwenhoven. Parity transitions in the superconducting ground state of hybrid InSb–Al Coulomb islands. *Nature Communications*, 9:4801, November 2018.

[45] J. Liu, A. C. Potter, K. T. Law, and P. A. Lee. Zero-Bias Peaks in the Tunneling Conductance of Spin-Orbit-Coupled Superconducting Wires with and without Majorana End-States. *Physical Review Letters*, 109:267002, December 2012.

[46] D. Bagrets and A. Altland. Class *D* Spectral Peak in Majorana Quantum Wires. *Physical Review Letters*, 109:227005, November 2012.

[47] D. I. Pikulin, J. P. Dahlhaus, M. Wimmer, H. Schomerus, and C. W. J. Beenakker. A zero-voltage conductance peak from weak antilocalization in a Majorana nanowire. *New Journal of Physics*, 14:125011, December 2012.

[48] E. J. H. Lee, X. Jiang, M. Houzet, R. Aguado, C. M. Lieber, and S. de Franceschi. Spin-resolved Andreev levels and parity crossings in hybrid superconductor–semiconductor nanostructures. *Nature Nanotechnology*, 9:79–84, January 2014.

[49] E. J. H. Lee, X. Jiang, R. Aguado, G. Katsaros, C. M. Lieber, and S. de Franceschi. Zero-Bias Anomaly in a Nanowire Quantum Dot Coupled to Superconductors. *Physical Review Letters*, 109:186802, October 2012.

[50] E. Prada, P. San-Jose, and R. Aguado. Transport spectroscopy of *NS* nanowire junctions with Majorana fermions. *Physical Review B*, 86:180503, November 2012.

[51] G. Kells, D. Meidan, and P. W. Brouwer. Near-zero-energy end states in topologically trivial spin-orbit coupled superconducting nanowires with a smooth confinement. *Physical Review B*, 86:100503, September 2012.

[52] A. Vuik, B. Nijholt, A. Akhmerov, and M. Wimmer. Reproducing topological properties with quasi-Majorana states. *SciPost Physics*, 7:061, November 2019.

[53] E. Prada, P. San-Jose, M. W. A. de Moor, A. Geresdi, E. J. H. Lee, J. Klinovaja, D. Loss, J. Nygård, R. Aguado, and L. P. Kouwenhoven. From Andreev to Majorana bound states in hybrid superconductor–semiconductor nanowires. *Nature Reviews Physics*, 2:575–594, October 2020.

[54] H. Pan, W. S. Cole, J. D. Sau, and S. Das Sarma. Generic quantized zero-bias conductance peaks in superconductor-semiconductor hybrid structures. *Physical Review B*, 101:024506, January 2020.

[55] H. Pan and S. Das Sarma. Physical mechanisms for zero-bias conductance peaks in Majorana nanowires. *Physical Review Research*, 2:013377, March 2020.

[56] H. Pan, C.-X. Liu, M. Wimmer, and S. Das Sarma. Quantized and unquantized zero-bias tunneling conductance peaks in Majorana nanowires: Conductance below and above $2e^2/h$. *arXiv:2102.02218 [cond-mat]*, February 2021.

[57] H. Pan and S. Das Sarma. On-demand large-conductance in trivial zero-bias tunneling peaks in Majorana nanowires. *arXiv:2110.07536 [cond-mat]*, October 2021.

[58] T. Hyart, B. van Heck, I. C. Fulga, M. Burrello, A. R. Akhmerov, and C. W. J. Beenakker. Flux-controlled quantum computation with Majorana fermions. *Physical Review B*, 88:035121, July 2013.

[59] D. Aasen, M. Hell, R. V. Mishmash, A. Higginbotham, J. Danon, M. Leijnse, T. S. Jespersen, J. A. Folk, C. M. Marcus, K. Flensberg, and J. Alicea. Milestones Toward Majorana-Based Quantum Computing. *Physical Review X*, 6:031016, August 2016.

[60] S. Vijay and L. Fu. Teleportation-based quantum information processing with Majorana zero modes. *Physical Review B*, 94:235446, December 2016.

[61] S. Plugge, A. Rasmussen, R. Egger, and K. Flensberg. Majorana box qubits. *New Journal of Physics*, 19:012001, January 2017.

[62] T. Karzig, C. Knapp, R. M. Lutchyn, P. Bonderson, M. B. Hastings, C. Nayak, J. Alicea, K. Flensberg, S. Plugge, Y. Oreg, C. M. Marcus, and M. H. Freedman. Scalable designs for quasiparticle-poisoning-protected topological quantum computation with Majorana zero modes. *Physical Review B*, 95:235305, June 2017.

[63] J. Alicea, Y. Oreg, G. Refael, F. von Oppen, and M. P. A. Fisher. Non-Abelian statistics and topological quantum information processing in 1D wire networks. *Nature Physics*, 7:412–417, May 2011.

[64] B. Béri and N. R. Cooper. Topological Kondo Effect with Majorana Fermions. *Physical Review Letters*, 109:156803, October 2012.

[65] A. Altland and R. Egger. Multiterminal Coulomb-Majorana Junction. *Physical Review Letters*, 110:196401, May 2013.

[66] L. A. Landau, S. Plugge, E. Sela, A. Altland, S. M. Albrecht, and R. Egger. Towards Realistic Implementations of a Majorana Surface Code. *Physical Review Letters*, 116:050501, February 2016.

[67] S. Plugge, L. A. Landau, E. Sela, A. Altland, K. Flensberg, and R. Egger. Roadmap to Majorana surface codes. *Physical Review B*, 94:174514, November 2016.

[68] Y. Aharonov and D. Bohm. Significance of Electromagnetic Potentials in the Quantum Theory. *Physical Review*, 115:485–491, August 1959.

[69] P. Bonderson, M. Freedman, and C. Nayak. Measurement-Only Topological Quantum Computation. *Physical Review Letters*, 101:010501, June 2008.

[70] P. Bonderson, M. Freedman, and C. Nayak. Measurement-only topological quantum computation via anyonic interferometry. *Annals of Physics*, 324:787–826, April 2009.

[71] L. Fu. Electron Teleportation via Majorana Bound States in a Mesoscopic Superconductor. *Physical Review Letters*, 104:056402, February 2010.

[72] Ö. Gül, H. Zhang, F. K. de Vries, J. van Veen, K. Zuo, V. Mourik, S. Conesa-Boj, M. P. Nowak, D. J. van Woerkom, M. Quintero-Pérez, M. C. Cassidy, A. Geresdi, S. Koelling, D. Car, S. R. Plissard, E. P. A. M. Bakkers, and L. P. Kouwenhoven. Hard Superconducting Gap in InSb Nanowires. *Nano Letters*, 17:2690–2696, April 2017.

[73] D. Car, J. Wang, M. A. Verheijen, E. P. A. M. Bakkers, and S. R. Plissard. Rationally Designed Single-Crystalline Nanowire Networks. *Advanced Materials*, 26:4875–4879, 2014.

[74] J. Kammhuber, M. C. Cassidy, H. Zhang, Ö. Gül, F. Pei, M. W. A. de Moor, B. Nijholt, K. Watanabe, T. Taniguchi, D. Car, S. R. Plissard, E. P. A. M. Bakkers, and L. P. Kouwenhoven. Conductance Quantization at Zero Magnetic Field in InSb Nanowires. *Nano Letters*, 16:3482–3486, June 2016.

[75] R. L. M. Op het Veld, D. Xu, V. Schaller, M. A. Verheijen, S. M. E. Peters, J. Jung, C. Tong, Qingzhen Wang, M. W. A. de Moor, B. Hesselmann, K. Vermeulen, J. D. S. Bommer, J. S. Lee, A. Sarikov, M. Pendharkar, A. Marzegalli, S. Koelling, L. P. Kouwenhoven, L. Miglio, C. J. Palmström, H. Zhang, and E. P. A. M. Bakkers. In-plane selective area InSb–Al nanowire quantum networks. *Communications Physics*, 3:1–7, March 2020.

[76] P. Walker and W. H. Tarn. *CRC Handbook of Metal Etchants*. CRC Press, December 1990.

[77] M. W. A. de Moor. Quantum transport in nanowire networks. 2019.

[78] M. F. Goffman, C. Urbina, H. Pothier, J. Nygård, C. M. Marcus, and P. Krogstrup. Conduction channels of an InAs-Al nanowire Johnson weak link. *New Journal of Physics*, 19:092002, September 2017.

[79] R. Schouten. QTRay. http://qtwork.tudelft.nl/~schouten/ivvi/doc-mod/, 2020.

[80] J. D. S. Bommer, G. Wang, and M. W. A. de Moor. Recalibration lock-in measurement. 2020.

[81] G. Wang, J. Bommer, and M. de Moor. Notes on transport measurements using a lock-in. 2020.

[82] J. A. Sauls. Andreev bound states and their signatures. *Philosophical Transactions of the R.al Society A: Mathematical, Physical and Engineering Sciences*, 376:20180140, August 2018.

[83] N. Read and D. Green. Paired states of fermions in two dimensions with breaking of parity and time-reversal symmetries and the fractional quantum Hall effect. *Physical Review B*, 61:10267–10297, April 2000.

[84] K. Sengupta, I. Žutić, H.-J. Kwon, V. M. Yakovenko, and S. Das Sarma. Midgap edge states and pairing symmetry of quasi-one-dimensional organic superconductors. *Physical Review B*, 63:144531, March 2001.

[85] K. T. Law, P. A. Lee, and T. K. Ng. Majorana Fermion Induced Resonant Andreev Reflection. *Physical Review Letters*, 103:237001, December 2009.

[86] K. Flensberg. Tunneling characteristics of a chain of Majorana bound states. *Physical Review B*, 82:180516, November 2010.

[87] C.-X. Liu, J. D. Sau, T. D. Stanescu, and S. Das Sarma. Andreev bound states versus Majorana bound states in quantum dot-nanowire-superconductor hybrid structures: Trivial versus topological zero-bias conductance peaks. *Physical Review B*, 96:075161, August 2017.

[88] C. Moore, C. Zeng, T. D. Stanescu, and S. Tewari. Quantized zero-bias conductance plateau in semiconductor-superconductor heterostructures without topological Majorana zero modes. *Physical Review B*, 98:155314, October 2018.

[89] C.-X. Liu, J. D. Sau, and S. Das Sarma. Role of dissipation in realistic Majorana nanowires. *Physical Review B*, 95:054502, February 2017.

[90] E. Prada, R. Aguado, and P. San-Jose. Measuring Majorana nonlocality and spin structure with a quantum dot. *Physical Review B*, 96:085418, August 2017.

[91] W. Chang, S. M. Albrecht, T. S. Jespersen, F. Kuemmeth, P. Krogstrup, J. Nygård, and C. M. Marcus. Hard gap in epitaxial semiconductor–superconductor nanowires. *Nature Nanotechnology*, 10:232–236, March 2015.

[92] H. Zhang, Ö. Gül, S. Conesa-Boj, M. P. Nowak, M. Wimmer, K. Zuo, V. Mourik, F. K. de Vries, J. van Veen, M. W. A. de Moor, J. D. S. Bommer, D. J. van Woerkom, D. Car, S. R. Plissard, E. P. A. M. Bakkers, M. Quintero-Pérez, M. C. Cassidy, S. Koelling, S. Goswami, K. Watanabe, T. Taniguchi, and L. P. Kouwenhoven. Ballistic superconductivity in semiconductor nanowires. *Nature Communications*, 8:16025, July 2017.

[93] J. D. S. Bommer. Zero-energy states in Majorana nanowire devices. 2020, 2021.

[94] J. D. S. Bommer, H. Zhang, M. W. A. de Moor, D. Xu, S. Gazibegovic, R. L. M. Op het Veld, J. A. Logan, M. Pendharkar, J. S. Lee, C. J. Palmström, E. P. A. M. Bakkers, and L. P. Kouwenhoven. Zero-bias conductance plateaus due to local majorana states. *to be submitted*, 2021.

[95] A. Grivnin, E. Bor, M. Heiblum, Y. Oreg, and H. Shtrikman. Concomitant opening of a bulk-gap with an emerging possible Majorana zero mode. *Nature Communications*, 10:1940, April 2019.

[96] Y. Huang, J. D. Sau, T. D. Stanescu, and S. Das Sarma. Quasiparticle gaps in multiprobe Majorana nanowires. *Physical Review B*, 98:224512, December 2018.

[97] P. Yu, J. Chen, M. Gomanko, G. Badawy, E. P. A. M. Bakkers, K. Zuo, V. Mourik, and S. M. Frolov. Non-Majorana states yield nearly quantized conductance in proximatized nanowires. *Nature Physics*, pages 1–7, January 2021.

[98] T. Ö. Rosdahl, A. Vuik, M. Kjaergaard, and A. R. Akhmerov. Andreev rectifier: A nonlocal conductance signature of topological phase transitions. *Physical Review B*, 97:045421, January 2018.

[99] G. W. Winkler, A. E. Antipov, B. van Heck, A. A. Soluyanov, L. I. Glazman, M. Wimmer, and R. M. Lutchyn. Unified numerical approach to topological semiconductor-superconductor heterostructures. *Physical Review B*, 99:245408, June 2019.

[100] B. D. Woods, S. Das Sarma, and T. D. Stanescu. Electronic structure of full-shell InAs/Al hybrid semiconductor-superconductor nanowires: Spin-orbit coupling and topological phase space. *Physical Review B*, 99:161118, April 2019.

[101] R. Schouten. QTRay-docs3b. http://qtwork.tudelft.nl/~schouten/ivvi/docmod/docs3b.htm, 2020.

[102] R. Schouten. QTRay-docm1b. http://qtwork.tudelft.nl/~schouten/ivvi/docmod/docm1b.htm, 2020.

[103] C.-X. Liu, F. Setiawan, J. D. Sau, and S. Das Sarma. Phenomenology of the soft gap, zero-bias peak, and zero-mode splitting in ideal Majorana nanowires. *Physical Review B*, 96:054520, August 2017.

[104] F. Setiawan, C.-X. Liu, J. D. Sau, and S. Das Sarma. Electron temperature and tunnel coupling dependence of zero-bias and almost-zero-bias conductance peaks in Majorana nanowires. *Physical Review B*, 96:184520, November 2017.

[105] M. König, S. Wiedmann, C. Brüne, A. Roth, H. Buhmann, L. W. Molenkamp, X.-L. Qi, and S.-C. Zhang. Quantum Spin Hall Insulator State in HgTe Quantum Wells. *Science*, 318:766–770, November 2007.

[106] C.-Z. Chang, J. Zhang, X. Feng, J. Shen, Z. Zhang, M. Guo, K. Li, Y. Ou, P. Wei, L.-L. Wang, Z.-Q. Ji, Y. Feng, S. Ji, X. Chen, J. Jia, X. Dai, Z. Fang, S.-C. Zhang, K. He, Y. Wang, L. Lu, X.-C. Ma, and Q.-K. Xue. Experimental Observation of the Quantum Anomalous Hall Effect in a Magnetic Topological Insulator. *Science*, 340:167–170, April 2013.

[107] R. Willett, J. P. Eisenstein, H. L. Störmer, D. C. Tsui, A. C. Gossard, and J. H. English. Observation of an even-denominator quantum number in the fractional quantum Hall effect. *Physical Review Letters*, 59:1776–1779, October 1987.

[108] W. Pan, J.-S. Xia, V. Shvarts, D. E. Adams, H. L. Stormer, D. C. Tsui, L. N. Pfeiffer, K. W. Baldwin, and K. W. West. Exact Quantization of the Even-Denominator Fractional Quantum Hall State at $\nu = 5/2$ Landau Level Filling Factor. *Physical Review Letters*, 83:3530–3533, October 1999.

[109] C. Nayak, S. H. Simon, A. Stern, M. Freedman, and S. Das Sarma. Non-Abelian anyons and topological quantum computation. *Reviews of Modern Physics*, 80:1083–1159, September 2008.

[110] S. T. Gill, J. Damasco, B. E. Janicek, M. S. Durkin, V. Humbert, S. Gazibegovic, D. Car, E. P. A. M. Bakkers, P. Y. Huang, and N. Mason. Selective-Area Superconductor Epitaxy to Ballistic Semiconductor Nanowires. *Nano Letters*, 18:6121–6128, October 2018.

[111] A. E. Antipov, A. Bargerbos, G. W. Winkler, B. Bauer, E. Rossi, and R. M. Lutchyn. Effects of Gate-Induced Electric Fields on Semiconductor Majorana Nanowires. *Physical Review X*, 8:031041, August 2018.

[112] Proximity and Johnson effects in superconductor-two-dimensional electron gas planar junctions. *Physica C: Superconductivity*, 242:261–266, February 1995.

[113] C. Reeg, D. Loss, and J. Klinovaja. Metallization of a Rashba wire by a superconducting layer in the strong-proximity regime. *Physical Review B*, 97:165425, April 2018.

[114] B. Nijholt and A. R. Akhmerov. Orbital effect of magnetic field on the Majorana phase diagram. *Physical Review B*, 93:235434, June 2016.

[115] C. W. Groth, M. Wimmer, A. R. Akhmerov, and X. Waintal. Kwant: A software package for quantum transport. *New Journal of Physics*, 16:063065, June 2014.

[116] A. Vuik, D. Eeltink, A. R. Akhmerov, and M. Wimmer. Effects of the electrostatic environment on the Majorana nanowire devices. *New Journal of Physics*, 18:033013, March 2016.

[117] A. E. G. Mikkelsen, P. Kotetes, P. Krogstrup, and K. Flensberg. Hybridization at Superconductor-Semiconductor Interfaces. *Physical Review X*, 8:031040, August 2018.

[118] J. Bardeen. Tunneling from a Many-Particle Point of View. *Physical Review Letters*, 6:57–59, January 1961.

[119] R. C. Dynes, V. Narayanamurti, and J. P. Garno. Direct Measurement of Quasiparticle-Lifetime Broadening in a Strong-Coupled Superconductor. *Physical Review Letters*, 41:1509–1512, November 1978.

[120] G. W. Winkler, D. Varjas, R. Skolasinski, A. A. Soluyanov, M. Troyer, and M. Wimmer. Orbital Contributions to the Electron g-factor in Semiconductor Nanowires. *Physical Review Letters*, 119:037701, July 2017.

[121] T. D. Stanescu, R. M. Lutchyn, and S. Das Sarma. Majorana fermions in semiconductor nanowires. *Physical Review B*, 84:144522, October 2011.

[122] S. Vaitiekėnas, M.-T. Deng, J. Nygård, P. Krogstrup, and C. M. Marcus. Effective g-factor of Subgap States in Hybrid Nanowires. *Physical Review Letters*, 121:037703, July 2018.

[123] J. Nitta, T. Akazaki, H. Takayanagi, and T. Enoki. Gate Control of Spin-Orbit Interaction in an Inverted $In_{0.53}Ga_{0.47}As/In_{0.52}Al_{0.48}As$ Heterostructure. *Physical Review Letters*, 78:1335–1338, February 1997.

[124] I. van Weperen, B. Tarasinski, D. Eeltink, V. S. Pribiag, S. R. Plissard, E. P. A. M. Bakkers, L. P. Kouwenhoven, and M. Wimmer. Spin-orbit interaction in InSb nanowires. *Physical Review B*, 91:201413, May 2015.

[125] Z. Scherübl, G. Fülöp, M. H. Madsen, J. Nygård, and S. Csonka. Electrical tuning of Rashba spin-orbit interaction in multigated InAs nanowires. *Physical Review B*, 94:035444, July 2016.

[126] T. D. Stanescu, R. M. Lutchyn, and S. Das Sarma. Dimensional crossover in spin-orbit-coupled semiconductor nanowires with induced superconducting pairing. *Physical Review B*, 87:094518, March 2013.

[127] B. van Heck, J. I. Väyrynen, and L. I. Glazman. Zeeman and spin-orbit effects in the Andreev spectra of nanowire junctions. *Physical Review B*, 96:075404, August 2017.

[128] E. C. T. O'Farrell, A. C. C. Drachmann, M. Hell, A. Fornieri, A. M. Whiticar, E. B. Hansen, S. Gronin, G. C. Gardner, C. Thomas, M. J. Manfra, K. Flensberg, C. M. Marcus, and F. Nichele. Hybridization of Subgap States in One-Dimensional Superconductor-Semiconductor Coulomb Islands. *Physical Review Letters*, 121:256803, December 2018.

[129] S. Mi, D. I. Pikulin, M. Marciani, and C. W. J. Beenakker. X-shaped and Y-shaped Andreev resonance profiles in a superconducting quantum dot. *Journal of Experimental and Theoretical Physics*, 119:1018–1027, December 2014.

[130] R. V. Mishmash, D. Aasen, A. P. Higginbotham, and J. Alicea. Approaching a topological phase transition in Majorana nanowires. *Physical Review B*, 93:245404, June 2016.

[131] S. Nadj-Perge, V. S. Pribiag, J. W. G. van den Berg, K. Zuo, S. R. Plissard, E. P. A. M. Bakkers, S. M. Frolov, and L. P. Kouwenhoven. Spectroscopy of Spin-Orbit Quantum Bits in Indium Antimonide Nanowires. *Physical Review Letters*, 108:166801, April 2012.

[132] J. D. Sau, S. Tewari, and S. Das Sarma. Experimental and materials considerations for the topological superconducting state in electron- and hole-doped semiconductors: Searching for non-Abelian Majorana modes in 1D nanowires and 2D heterostructures. *Physical Review B*, 85:064512, February 2012.

[133] S. R. Plissard, I. van Weperen, D. Car, M. A. Verheijen, G. W. G. Immink, J. Kammhuber, L. J. Cornelissen, D. B. Szombati, A. Geresdi, S. M. Frolov, L. P. Kouwenhoven, and E. P. A. M. Bakkers. Formation and electronic properties of InSb nanocrosses. *Nature Nanotechnology*, 8:859–864, November 2013.

[134] R. Meservey and P. M. Tedrow. Properties of Very Thin Aluminum Films. *Journal of Applied Physics*, 42:51–53, January 1971.

[135] N. W. Ashcroft and N. D. Mermin. *Solid State Physics*. Holt, Rinehart and Winston, 1976.

[136] O. Madelung. *Semiconductors: Group IV Elements and III-V Compounds*. Springer Science & Business Media, December 2012.

[137] I. Vurgaftman, J. R. Meyer, and L. R. Ram-Mohan. Band parameters for III–V compound semiconductors and their alloys. *Journal of Applied Physics*, 89:5815–5875, June 2001.

[138] E. M. T. Fadaly, H. Zhang, S. Conesa-Boj, D. Car, Ö. Gül, S. R. Plissard, R. L. M. Op het Veld, S. Kölling, L. P. Kouwenhoven, and E. P. A. M. Bakkers. Observation of Conductance Quantization in InSb Nanowire Networks. *Nano Letters*, 17:6511–6515, November 2017.

[139] H. Schmid, M. Borg, K. Moselund, L. Gignac, C. M. Breslin, J. Bruley, D. Cutaia, and H. Riel. Template-assisted selective epitaxy of III–V nanoscale devices for coplanar heterogeneous integration with Si. *Applied Physics Letters*, 106:233101, June 2015.

[140] P. Aseev, A. Fursina, F. Boekhout, F. Krizek, J. E. Sestoft, F. Borsoi, S. Heedt, G. Wang, L. Binci, S. Martí-Sánchez, T. Swoboda, R. Koops, E. Uccelli, J. Arbiol, P. Krogstrup, L. P. Kouwenhoven, and P. Caroff. Selectivity Map for Molecular Beam Epitaxy of

Advanced III–V Quantum Nanowire Networks. *Nano Letters*, 19:218–227, January 2019.

[141] F. Krizek, J. E. Sestoft, P. Aseev, S. Marti-Sanchez, S. Vaitiekėnas, L. Casparis, S. A. Khan, Y. Liu, T. Stankevič, A. M. Whiticar, A. Fursina, F. Boekhout, R. Koops, E. Uccelli, L. P. Kouwenhoven, C. M. Marcus, J. Arbiol, and P. Krogstrup. Field effect enhancement in buffered quantum nanowire networks. *Physical Review Materials*, 2:093401, September 2018.

[142] M. Fahed, L. Desplanque, D. Troadec, G. Patriarche, and X. Wallart. Selective area heteroepitaxy of GaSb on GaAs (001) for in-plane InAs nanowire achievement. *Nanotechnology*, 27:505301, November 2016.

[143] M. Friedl, K. Cerveny, P. Weigele, G. Tütüncüoglu, S. Martí-Sánchez, C. Huang, T. Patlatiuk, H. Potts, Z. Sun, M. O. Hill, L. Güniat, W. Kim, M. Zamani, V. G. Dubrovskii, J. Arbiol, L. J. Lauhon, D. M. Zumbühl, and A. Fontcuberta i Morral. Template-Assisted Scalable Nanowire Networks. *Nano Letters*, 18:2666–2671, April 2018.

[144] J. S. Lee, S. Choi, M. Pendharkar, D. J. Pennachio, B. Markman, M. Seas, S. Koelling, M. A. Verheijen, L. Casparis, K. D. Petersson, I. Petkovic, V. Schaller, M. J. W. Rodwell, C. M. Marcus, P. Krogstrup, L. P. Kouwenhoven, E. P. A. M. Bakkers, and C. J. Palmström. Selective-area chemical beam epitaxy of in-plane InAs one-dimensional channels grown on InP(001), InP(111)B, and InP(011) surfaces. *Physical Review Materials*, 3:084606, August 2019.

[145] L. Desplanque, A. Bucamp, D. Troadec, G. Patriarche, and X. Wallart. Selective area molecular beam epitaxy of InSb nanostructures on mismatched substrates. *Journal of Crystal Growth*, 512:6–10, April 2019.

[146] M. E. Straumanis and C. D. Kim. Lattice Parameters, Thermal Expansion Coefficients, Phase Width, and Perfection of the Structure of GaSb and InSb. *Journal of Applied Physics*, 36:3822–3825, December 1965.

[147] P. Aseev, G. Wang, L. Binci, A. Singh, S. Martí-Sánchez, M. Botifoll, L. J. Stek, A. Bordin, J. D. Watson, F. Boekhout, D. Abel, J. Gamble, K. Van Hoogdalem, J. Arbiol, L. P. Kouwenhoven, G. de Lange, and P. Caroff. Ballistic InSb Nanowires and Networks via Metal-Sown Selective Area Growth. *Nano Letters*, 19:9102–9111, December 2019.

[148] B. M. Borg and L.-E. Wernersson. Synthesis and properties of antimonide nanowires. *Nanotechnology*, 24:202001, April 2013.

[149] J. E. Oh, P. K. Bhattacharya, Y. C. Chen, and S. Tsukamoto. Molecular-beam epitaxial growth of high-quality InSb on InP and GaAs substrates. *Journal of Applied Physics*, 66:3618–3621, October 1989.

[150] M. D. Schroer and J. R. Petta. Correlating the Nanostructure and Electronic Properties of InAs Nanowires. *Nano Letters*, 10:1618–1622, May 2010.

[151] G. Badawy, S. Gazibegovic, F. Borsoi, S. Heedt, C.-A. Wang, S. Koelling, M. A. Verheijen, L. P. Kouwenhoven, and E. P. A. M. Bakkers. High Mobility Stemless InSb Nanowires. *Nano Letters*, 19:3575–3582, June 2019.

[152] M. W. A. de Moor, J. D. S. Bommer, D. Xu, G. W. Winkler, A. E. Antipov, A. Bargerbos, G. Wang, N. van Loo, R. L. M. Op het Veld, S. Gazibegovic, D. Car, J. A. Logan, M. Pendharkar, J. S. Lee, E. P. A. M. Bakkers, C. J. Palmström, R. M. Lutchyn, L. P. Kouwenhoven, and H. Zhang. Electric field tunable superconductor-semiconductor coupling in Majorana nanowires. *New Journal of Physics*, 20:103049, October 2018.

[153] B. D. Woods, T. D. Stanescu, and S. Das Sarma. Effective theory approach to the Schrödinger-Poisson problem in semiconductor Majorana devices. *Physical Review B*, 98:035428, July 2018.

[154] C.-K. Chiu, J. D. Sau, and S. Das Sarma. Conductance of a superconducting Coulomb-blockaded Majorana nanowire. *Physical Review B*, 96:054504, August 2017.

[155] Z. Cao, H. Zhang, H.-F. Lü, W.-X. He, H.-Z. Lu, and X.-C. Xie. Decays of Majorana or Andreev Oscillations Induced by Steplike Spin-Orbit Coupling. *Physical Review Letters*, 122:147701, April 2019.

[156] H. Zhang, D. E. Liu, M. Wimmer, and L. P. Kouwenhoven. Next steps of quantum transport in Majorana nanowire devices. *Nature Communications*, 10:5128, November 2019.

[157] C. Thelander, P. Caroff, S. Plissard, A. W. Dey, and K. A. Dick. Effects of Crystal Phase Mixing on the Electrical Properties of InAs Nanowires. *Nano Letters*, 11:2424–2429, June 2011.

[158] S. Vaitiekėnas, G. W. Winkler, B. van Heck, T. Karzig, M.-T. Deng, K. Flensberg, L. I. Glazman, C. Nayak, P. Krogstrup, R. M. Lutchyn, and C. M. Marcus. Flux-induced topological superconductivity in full-shell nanowires. *Science*, 367, March 2020.

[159] M. Valentini, F. Peñaranda, A. Hofmann, M. Brauns, R. Hauschild, P. Krogstrup, P. San-Jose, E. Prada, R. Aguado, and G. Katsaros. Nontopological zero-bias peaks in full-shell nanowires induced by flux-tunable Andreev states. *Science*, 373:82–88, July 2021.

[160] R. M. Lutchyn, G. W. Winkler, B. van Heck, T. Karzig, K. Flensberg, L. I. Glazman, and C. Nayak. Topological superconductivity in full shell proximitized nanowires. *Science*, 367:eaav3392, March 2020.

[161] W. A. Little and R. D. Parks. Observation of Quantum Periodicity in the Transition Temperature of a Superconducting Cylinder. *Physical Review Letters*, 9:9–12, July 1962.

[162] V. V. Schmidt, V. V. S. P. Müller, V. V. Schmidt, P. Müller, I. V. Grigorieva, and A. V. Ustinov. *The Physics of Superconductors: Introduction to Fundamentals and Applications*. Springer, 1997.

[163] N. Taoka, M. Yokoyama, Sang Hyeon K., R. Suzuki, S. Lee, R. Iida, T. Hoshii, W. Jevasuwan, T. Maeda, T. Yasuda, O. Ichikawa, N. Fukuhara, M. Hata, M. Takenaka, and S. Takagi. Impact of Fermi level pinning inside conduction band on electron mobility in InGaAs metal-oxide-semiconductor field-effect transistors. *Applied Physics Letters*, 103:143509, September 2013.

[164] H. D. Trinh, Y. C. Lin, E. Y. Chang, C.-T. Lee, S.-Y. Wang, H. Q. Nguyen, Y. S. Chiu, Q. H. Luc, H.-C. Chang, C.-H. Lin, S. Jang, and C. H. Diaz. Electrical Characteristics of Al_2O_3/InSb MOSCAPs and the Effect of Postdeposition Annealing Temperatures. *IEEE Transactions on Electron Devices*, 60:1555–1560, May 2013.

[165] F. Borsoi, G. P. Mazur, N. van Loo, M. P. Nowak, L. Bourdet, K. Li, S. Korneychuk, A. Fursina, E. Memisevic, G. Badawy, S. Gazibegovic, K. van Hoogdalem, E. P. A. M. Bakkers, L. P. Kouwenhoven, S. Heedt, and M. Quintero-Pérez. Single-shot fabrication of semiconducting-superconducting nanowire devices. *arXiv:2009.06219 [cond-mat]*, September 2020.

[166] R. A. Webb, S. Washburn, C. P. Umbach, and R. B. Laibowitz. Observation of h/e Aharonov-Bohm Oscillations in Normal-Metal Rings. *Physical Review Letters*, 54:2696–2699, June 1985.

[167] Y.V. Nazarov, Y. Nazarov, and Y.M. Blanter. *Quantum Transport: Introduction to Nanoscience*. Cambridge University Press, 2009.

[168] E. N. Economou and C. M. Soukoulis. Static Conductance and Scaling Theory of Localization in One Dimension. *Physical Review Letters*, 46:618–621, March 1981.

[169] B.L. Al'Tshuler, A.G. Aronov, and B.Z. Spivak. The Aharonov-Bohm effect in disordered conductors. *JETP Lett*, 33(2):94–97, 1981.

[170] T. Ihn. *Semiconductor Nanostructures: Quantum States and Electronic Transport*. OUP Oxford, 2010.

[171] G. Seelig and M. Büttiker. Charge-fluctuation-induced dephasing in a gated mesoscopic interferometer. *Physical Review B*, 64:245313, December 2001.

[172] T. Ludwig and A. D. Mirlin. Interaction-induced dephasing of Aharonov-Bohm oscillations. *Physical Review B*, 69:193306, May 2004.

[173] A. E. Hansen, A. Kristensen, S. Pedersen, C. B. Sörensen, and P. E. Lindelof. Mesoscopic decoherence in Aharonov-Bohm rings. *Physical Review B*, 64:045327, July 2001.

[174] P. A. Lee and A. D. Stone. Universal Conductance Fluctuations in Metals. *Physical Review Letters*, 55:1622–1625, October 1985.

[175] C. W. J. Beenakker. Random-matrix theory of quantum transport. *Reviews of Modern Physics*, 69:731–808, July 1997.

[176] M. L. Polianski and P. W. Brouwer. Scattering matrix ensemble for time-dependent transport through a chaotic quantum dot. *Journal of Physics A: Mathematical and General*, 36:3215–3236, March 2003.

[177] C. W. J. Beenakker and B. Michaelis. Stub model for dephasing in a quantum dot. *Journal of Physics A: Mathematical and General*, 38:10639–10646, November 2005.

[178] W. G. van der Wiel, Yu. V. Nazarov, S. de Franceschi, T. Fujisawa, J. M. Elzerman, E. W. G. M. Huizeling, S. Tarucha, and L. P. Kouwenhoven. Electromagnetic Aharonov-Bohm effect in a two-dimensional electron gas ring. *Physical Review B*, 67:033307, January 2003.

[179] G. L. R. Anselmetti, E. A. Martinez, G. C. Ménard, D. Puglia, F. K. Malinowski, J. S. Lee, S. Choi, M. Pendharkar, C. J. Palmström, C. M. Marcus, L. Casparis, and A. P. Higginbotham. End-to-end correlated subgap states in hybrid nanowires. *Physical Review B*, 100:205412, November 2019.

[180] G. C. Ménard, G. L. R. Anselmetti, E. A. Martinez, D. Puglia, F. K. Malinowski, J. S. Lee, S. Choi, M. Pendharkar, C. J. Palmström, K. Flensberg, C. M. Marcus, L. Casparis, and A. P. Higginbotham. Conductance-Matrix Symmetries of a Three-Terminal Hybrid Device. *Physical Review Letters*, 124:036802, January 2020.

[181] E. A. Martinez, A. Pöschl, E. B. Hansen, M. A. Y. van de Poll, S. Vaitiekėnas, A. P. Higginbotham, and L. Casparis. Measurement circuit effects in three-terminal electrical transport measurements. *arXiv:2104.02671 [cond-mat]*, April 2021.

[182] D. Puglia, E. A. Martinez, G. C. Ménard, A. Pöschl, S. Gronin, G. C. Gardner, R. Kallaher, M. J. Manfra, C. M. Marcus, A. P. Higginbotham, and L. Casparis. Closing of the induced gap in a hybrid superconductor-semiconductor nanowire. *Physical Review B*, 103:235201, June 2021.

[183] S. Heedt, M. Quintero-Pérez, F. Borsoi, A. Fursina, N. van Loo, G. P. Mazur, M. P. Nowak, M. Ammerlaan, K. Li, S. Korneychuk, J. Shen, M. A. Y. van de Poll, G. Badawy, S. Gazibegovic, N. de Jong, P. Aseev, K. van Hoogdalem, E. P. A. M. Bakkers, and L. P. Kouwenhoven. Shadow-wall lithography of ballistic superconductor–semiconductor quantum devices. *Nature Communications*, 12:4914, August 2021.

[184] G. P. Mazur, N. van Loo, J. Y. Wang, T. Dvir, G. Wang, A. Khindanov, S. Korneychuk, F. Borsoi, R. C. Dekker, G. Badawy, P. Vinke, S. Gazibegovic, E. P. A. M. Bakkers, M. Quintero-Perez, S. Heedt, and L. P. Kouwenhoven. Spin-mixing enhanced proximity effect in aluminum-based superconductor-semiconductor hybrids. *arXiv:2202.10230 [cond-mat]*, February 2022.

[185] J.-Y. Wang, N. van Loo, G. P. Mazur, V. Levajac, F. K. Malinowski, M. Lemang, F. Borsoi, G. Badawy, S. Gazibegovic, E. P. A. M. Bakkers, M. Quintero-Perez, S. Heedt,

and L. P. Kouwenhoven. Parametric exploration of zero-energy modes in three-terminal InSb-Al nanowire devices. *arXiv:2203.00773 [cond-mat]*, March 2022.

[186] J. Danon, A. B. Hellenes, E. B. Hansen, L. Casparis, A. P. Higginbotham, and K. Flensberg. Nonlocal Conductance Spectroscopy of Andreev Bound States: Symmetry Relations and BCS Charges. *Physical Review Letters*, 124:036801, January 2020.

[187] D. I. Pikulin, B. van Heck, T. Karzig, E. A. Martinez, B. Nijholt, T. Laeven, G. W. Winkler, J. D. Watson, S. Heedt, M. Temurhan, V. Svidenko, R. M. Lutchyn, M. Thomas, G. de Lange, L. Casparis, and C. Nayak. Protocol to identify a topological superconducting phase in a three-terminal device. *arXiv:2103.12217 [cond-mat]*, March 2021.

[188] J. D. Sau and S. Das Sarma. Realizing a robust practical Majorana chain in a quantum-dot-superconductor linear array. *Nature Communications*, 3:964, July 2012.

[189] G. Wang, T. Dvir, N. van Loo, G. P. Mazur, S. Gazibegovic, G. Badawy, E. P. A. M. Bakkers, L. P. Kouwenhoven, and G. de Lange. Non-local measurement of quasiparticle distribution in proximitized semiconductor nanowires using quantum dots. *arXiv:2110.05373 [cond-mat]*, October 2021.

[190] C.-X. Liu, G. Wang, T. Dvir, and M. Wimmer. Tunable crossed Andreev reflection and elastic co-tunneling between quantum dots. *arXiv:2203.00107 [cond-mat]*, February 2022.

[191] G. Wang, N. van Loo, C.-X. Liu, G. Mazur, S. Gazibegovic, G. Badawy, E. P. A. M. Bakkers, M. Wimmer, G. de Lange, and T. Dvir. Tuning singlet vs triplet Cooper-pair splitting in InSb nanowires. In *Bulletin of the American Physical Society*. American Physical Society, 2022.

[192] D. van Driel, G. Wang, A. Bordin, N. van Loo, G. Mazur, S. Gazibegovic, G. Badawy, E. P. A. M. Bakkers, G. de Lange, and T. Dvir. Direct Measurement of the Andreev Bound State Spin and Charge During the Singlet-Doublet Transition. In *Bulletin of the American Physical Society*. American Physical Society, 2022.

[193] T. Dvir, G. Wang, G. Mazur, A. Bordin, B. ten Haaf, G. Badawy, S. Gazibegovic, E. P. A. M. Bakkers, and G. de Lange. Delocalized Andreev bound states and non-topological Majorana excitations in InSb nanowiresc. In *Bulletin of the American Physical Society*. American Physical Society, 2022.

[194] A. Bordin, G. Wang, T. Dvir, B. ten Haaf, D. van Driel, F. Zatelli, N. van Loo, G. Mazur, C.-X. Liu, G. Badawy, S. Gazibegovic, E. P. A. M. Bakkers, M. Wimmer, and G. de Lange. Gate-controlled Elastic Co-Tunneling and Crossed Andreev Reflection mediated by Andreev Bound States. In *Bulletin of the American Physical Society*. American Physical Society, 2022.

ACKNOWLEDGMENTS

Completing the PhD is a long journey and not easy. During my PhD in QuTech, I have met a great many of people and had incredible amount of various experiences. The colorful and irreplaceable memories in Delft will be kept in my mind forever. At the end of my thesis, I would like to express my gratitude to all those who have been offering support to me during my PhD.

It is still vivid in my mind how flattered I was by being invited for an interview with you, **Leo**, and coming to visit QuTech and the beautiful Dutch town – Delft, where I was about to have unforgettable times in the next > 5 years. **Leo**, I would like to show my sincere gratitude to you for the great opportunity to work in your group. You created QuTech with such an ambitious and multicultural atmosphere, and being one of the top players in Quantum research. You never stopped going for new adventures, for instance bringing the Microsoft collaboration to Delft. The tools and resources that you provided are so advantageous in our research. It can also be seen what a special institute QuTech is based on this many people I need to list here, so I can hardly imagine being anywhere else for such a wonderful PhD experience. Your support on finishing my PhD is always inspiring and instructive. Your sparks of physical thoughts taught me how a great physicist should be like. The exchange of ideas and discussions with you improved my understanding of physics a lot. I hope you will scale new heights in your academic career!

Michael, thank you for being my second promotor, and regular check-ups and always offering support during my writing. **Elsa** and **Silvano**, I'm always impressed by the wonderful quality of your works, and thank you for being my committee members. Looking forward to meeting you online, and hope to see you somewhere in the world in the future. **Yaroslav**, **Jan** and **Erik**, thank you for being my committee members. **Jos**, thank you for being the reserve member.

Hao, I would like to thank you for teaching me so much from the start of my PhD all along the two years when I worked in your team.

Guan, we started in the same year and worked together for a couple of periods. It was genuinely enjoyable to work with you. You not only taught me much knowledge to start my Majorana journey, but you are also a true friend with many mutual interests. Thanks for enjoying the concerts and operas with me, and many trips such as in Paris, Malta, Germany, Spain and Sardinia. It's great fun to explore European civilizations with you. I'm so happy for you seeing your great results in your final year. **Nick**, I also worked with you from the very beginning. Your hard working and fun personality is very impressive. Your work has laid essential foundations for many new results in the group. I also remember the beautiful views in Colorado during our road trip. I saw a bigger world and knew myself better through both of you. Thanks for being my paranymphs.

Michiel, I learned a lot from your calm and analytical mind. Your profound knowledge and comprehensive thinking is always deepening and broadening my understand-

ing of physics as well as helping my decision making. We have done great research together. **Jouri**, it's splendid how much you have achieved doing tunneling spectroscopy on nanowires. Thanks for sharing the challenge with me at the beginning of SAG research. Both of you made the ZBP team a great one to work in. Thank you for all the help with experiments and discussions, and best wishes for your career in Microsoft!

Vanessa, it was a great time after you joined the SAG team. I'm so glad that you found your passion and the cause to devote yourself, which many people, including me, should do for their lives but usually don't dare to take the step. I enjoyed many coffee times, ramens and vegan cuisine with you and **Florian**, und natürlich noch *die Walküre*.

Kiefer, **Qing**, **Bart**, we were a wonderful team! It was an honor and a golden time of my PhD to be your supervisor. And we had a memorable trip to Aachen. **Kiefer**, I've learned things in many aspects outside the ivory tower from you. Thanks for your mead, and good luck in Delft Circuits. **Qing**, it's nice that you stayed in QuTech for your PhD so that we could have much more enjoyable interactions. You're having exciting results now, and good luck with the writing process. **Bart**, it's fun to have conversations with you on arts and watch *Samson et Dalila*. Thanks for teaching me *Blender*, and have fun with basketball and your animation projects!

Tom, it's not perfect timing to have much overlap with you on doing experiments. I'm very impressed to see how you brought the previously SAG, now QD team to a completely higher level, and your ability to create unprecedentedly successful new experimental schemes. I'm looking forward to working with you in the future, also with **David van D.** and **Alberto**. **Greg**, how impressive it is to see your great work to miraculously bring the UTS back to life! You established the foundations for the blossoming projects now. Best wishes with your next step in the US or somewhere in the world!

Chunxiao, it's a great pleasure to know you and **Shuang**. When we first met in a restaurant in Los Angeles, I never thought you would be my colleague in Delft, and we could even sit together in a Chinese restaurant that I often enjoyed when I was in Aachen – life gives us magical moments, like in the card game 'eighty points' you taught us. I appreciate your theoretical works very much and hope we have the opportunity to collaborate in the future.

Erik, thank you for the collaboration with us and providing us with high-quality nanowires. Thank you for the warm welcome in Eindhoven and the tour in your cleanroom. **Roy**, we started our PhDs at the same time and it was wonderful to build a cooperative partnership with you. Brainstorming with you and **Jason** on SAG projects was an exciting experience. Also thanks for our nice chats at the final stage of our PhDs and after you started working for ASML. Hope you enjoy the journey in industry! **Sasa** and **Ghada**, your wonderful works on producing VLS nanowires have meant a lot to us.

Chris, I always relish your talks full of humor. I also enjoyed our interactions in sunny Santa Barbara, and watching rocket launching with you and Erik though it was canceled at the last moment. **Joon Sue** and **Mihir**, thanks for the tour in your growth lab and having discussions.

Jakob, even though we only worked together for a short period, you played an important role in introducing me to the lab, teaching me fabrication techniques and guiding me through cryogenic measurements. **Jie**, I always think you are the Wonder Woman in QuTech. You are our ladybro and you are chivalrous. I miss the time when you were in

Delft and wish you a happy life in Beijing. **Jaap**, I enjoyed many coffee chats with you, and *Matthäus-Passion* in Naarden. Thank you for the Dutch translation included in this thesis. **Willemijn**, **Damaz** and **Arno**, I will never forget our road trip in California and Nevada. Good luck with being an astronaut, an engineer or a scientist! **Srijit**, you are an easy-going group leader. Thanks for organizing many Friday night drinks and dinners, and of course darts. Happy to see **Bas** and **Yining** start their research in your group. **Christian M.**, it was nice to share an office with you for a short period, wish you a smooth start in Australia. **Léo**, thanks for performing numerical simulations for my Chapter 7. Best wishes to you and **Mathilde**. **Lin**, great we had many hotpots and coffee breaks together with **Yang**.

Lukas S., you're always energetic for life and work, always eager to take new challenges. Your living style inspires me a lot. As promised, I will provide you with a gourmet map of Delft in the acknowledgments. Here it is!

Di's gourmet map of Delft. a Barbaar. Cozy bar in Prinsenhof. **b** Van der Dussen. Michelin-level fine dining in Delft. **c** Boulangerie Michel. French bakery, baguette-based sandwiches. **d** Café de V. Best Asian fusion in Delft. **e** Chefsbar Centre. Fine dining with monthly updated menu. Good presentation. **f** Chocolaterie De Lelie. Best ice cream in Delft. **g** Charcoal. Southeast Asian BBQ. **h** Delfts Brouwhuis. Gezellig brewery with a variety of beers and good dishes. **i** Stads-Koffyhuis. A touch of Dutch traditional food. **j** Rossio. Mediterranean cuisine. **k** Dolce Amaro. Good Italian restaurant. **l** Il Peperoncino. Very good pizzas and pasta. **m** Café Diner de PeliCaan. Good Mediterranean food, especially high-quality seafood. **n** HANNO. World kitchen. **o** Angkor. Cambodian fine dining. **p** Bij Best. Good brunch with wonderful coffee. **q** Mekhong. Decent Thai food. **r** Kek. Cozy coffee bar with good pastries. **s** Lakila. Spanish and Portuguese snacks with a large variety of drinks. **t** Zaferuw. Persian food. **u** Maharaja. Indian cuisine. **v** Nikkou. (Probably) best ramen in the Netherlands. **w** Moeke. Way-too-big schnitzel. **x** Hummus. Middle Eastern vegetarian restaurant. **y** THUIS by Ladera. Stamppot – Dutch traditional food.

Luca, it was a pleasure working with you in the same team for a while. **Ting**, thank you for many coffee chats and good luck in Taiwan. **Sebastian**, thanks for meeting me in Aachen prior to my interview in Delft. It must be an essential step for me to get my

position in Delft. **James**, the great Scottish, it's always interesting to chat with you. **Alex**, thank you for enjoyable drink times and our conversations on classical music. **Xiao**, our gossiping sessions were a good relaxation after work, and nice to know **Xin**, alumnus of us, as well as other people from Lieven's group.

Kun, hope you're enjoying your new position in Sydney. **Önder** and **Fokko**, welcome back to Delft! My thanks to many others in QuTech, **Marta**, **Vukan**, **Christian P.**, **Filip**, **Michael C.**, **Jiyin**, **Cristina**, **Francesco B.**, **Francesco Z.**, **Prasanna** and **Ivan**, good luck with your research!

Arnold, **Anja** and **Mark**, thank you for your very professional and efficient maintenance on the e-beams and evaporators in the cleanroom. **Olaf**, **Jason**, **Raymond** and **Remco**, thanks for always being ready to help us. The profession of you all is the mainstay of QuTech. **Jenny**, **Csilla**, **Simone** and **Lydia**, thank you for handling any administrative questions.

Jasper, **Daniël** and **Arjan**, thank you for discussing possible industrial opportunities with me! Also thanks to many people who used to work in QuTech, **Lukas G.**, **David van W.**, **Amrita**, **Gijs**, **Nicolò**, **Attila**, **Dominique**, **Nikolai**, **Kevin**, **Elvedin**, **John** and **Maja**.

Many thanks to **Christopf**, **Gerard** and other colleagues in II. Institute of Physics A, RWTH Aachen University in 2015 – 2016. Without you it would be impossible for me to achieve this PhD today. **Gerard**, all the best to your career at TU Delft!

Sophie, **Jing** & **Patrick**, how wonderful we became friends although we have completely different backgrounds. I enjoyed our holidays in Groningen, Amsterdam and Katwijk aan Zee. Hope we can still get together although we are now in different countries. **Haohao**, **Xiaosheng** and **Qi**, it was such a memorable experience to play music together in Aachen as our small "physics orchestra", and to go to many concerts, from Germany to the Netherlands.

I would also like to say a few words on my grandfather, who passed away during completing this thesis. He enlightened me on the love of natural science which ultimately made me a PhD in physics. He also taught me playing the piano, and many hobbies of mine could originate from his influences. He could have seen my defence ceremony if it was done on time. But I guess he would feel happy if seeing this final result.

Finally I would like to express my gratitude to my parents. **Mum & Dad**, your curiosity and tolerance for different cultures also influenced me to take pleasure in cross-cultural experiences. I always feel your strong support all through the years when I pursue my dreams. You gave me much encouragement through the ups and downs during my studies.

CURRICULUM VITÆ

Di XU

04-11-1989	Born in Zhangjiakou, China.
2005 – 2008	Xuanhua No.1 High School, Zhangjiakou, China
2008 – 2010	Undergraduate in Medicine Zhejiang University, China
2010 – 2013	B.Sc. Physics Zhejiang University, China
2013 – 2016	M.Sc. Physics RWTH Aachen University, Germany *Thesis:* Measurement principles for micro- and nanoelectromechanical resonators: down-mixing of a silicon beam oscillator as an example *Promotor:* Prof. Dr. Christoph Stampfer
2016 – 2021	PhD research Delft University of Technology, the Netherlands *Thesis:* Quantum properties in hybrid nanowire devices *Promotor:* Prof. dr. ir. Leo P. Kouwenhoven

LIST OF PUBLICATIONS

JOURNAL PAPERS AND PREPRINTS

7. H. Zhang†, M. W. A. de Moor†, J. D. S. Bommer†, **D. Xu**, G. Wang, N. van Loo, C.X. Liu, S. Gazibegovic, J. A. Logan, D. Car, R. L. M. Veld, P. J. van Veldhoven, S. Koelling, M. A. Verheijen, M. Pendharkar, D. J. Pennachio, B. Shojaei, J. S. Lee, C. J. Palmstrøm, E. P. A. M. Bakkers, S. Das Sarma, L. P. Kouwenhoven, *Large zero-bias peaks in InSb-Al hybrid semiconductor-superconductor nanowire devices*, arXiv preprint arXiv:2101.11456 (2021).

6. R. L. M. Op het Veld†, **D. Xu**†, V. Schaller, M. A. Verheijen, S. M. E. Peters, J. Jung, C. Tong, Q. Wang, M. W. A. de Moor, B. Hesselmann, K. Vermeulen, J. D. S. Bommer, J. S. Lee, A. Sarikov, M. Pendharkar, A. Marzegalli, S. Koelling, L. P. Kouwenhoven, L. Miglio, C. J. Palmstrøm, H. Zhang, E. P. A. M. Bakkers, *In-plane selective area InSb–Al nanowire quantum networks*, Commun. Phys. **3**, 59 (2020).

5. J. Shen†, S. Heedt†, F. Borsoi†, B. van Heck, S. Gazibegovic, R. L. M. Op het Veld, D. Car, J. A. Logan, M. Pendharkar, S. J. J. Ramakers, G. Wang, **D. Xu**, D. Bouman, A. Geresdi, C. J. Palmstrøm, E. P. A. M. Bakkers, L. P. Kouwenhoven, *Parity transitions in the superconducting ground state of hybrid InSb–Al Coulomb islands*, Nat. Commun. **9**, 4801 (2018).

4. M. W. A. de Moor†, J. D. S. Bommer†, **D. Xu**†, G. W. Winkler, A. E Antipov, A. Bargerbos, G. Wang, N. van Loo, R. L. M. Op het Veld, S. Gazibegovic, D. Car, J. A. Logan, M. Pendharkar, J. S. Lee, E. P. A. M. Bakkers, C. J. Palmstrøm, R. M. Lutchyn, L. P. Kouwenhoven, H. Zhang, *Electric field tunable superconductor-semiconductor coupling in Majorana nanowires*, New J. Phys. **20**, 103049 (2018).

3. G. J. Verbiest, H. Janssen, **D. Xu**, X. Ge, M. Goldsche, J. Sonntag, T. Khodkov, L. Banszerus, N. von den Driesch, D. Buca, K. Watanabe, T. Taniguchi, C. Stampfer, *Integrated impedance bridge for absolute capacitance measurements at cryogenic temperatures and finite magnetic fields*, Review of Scientific Instruments **90**, 084706 (2019).

2. G. J. Verbiest, **D. Xu**, M. Goldsche, T. Khodkov, S. Barzanjeh, N. von den Driesch, D. Buca, C. Stampfer, *Tunable mechanical coupling between driven microelectromechanical resonators*, Appl. Phys. Lett. **109**, 143507 (2016).

1. Y. Li, C. Lv, Y. Luo, X. Yang, C. Shen, **D. Xu**, Q. Tao, G. Cao, Z. Xu, *Effect of nonmagnetic zinc impurity on T_c in $LaFe_{1-x}Zn_xPO_{0.94}F_{0.06}$ superconductors*, AIP Advances **2**, 041406 (2012).

PATENT APPLICATION

1. **D. Xu**, H. Zhang, *Method for selectively etching a metal component*, PCT/EP2020/087828, European Patent Office, 23 Dec 2020.

† Equal contribution.